Computational Investigation of Ionic Diffusion in Polymer Electrolytes for Lithium-Ion Batteries

Thesis by

Daniel J. Brooks

In Partial Fulfillment of the Requirements for
the degree of
Doctor of Philosophy

CALIFORNIA INSTITUTE OF TECHNOLOGY
Pasadena, California

2018
(Defended Jan 23, 2018)

To my family.

ACKNOWLEDGEMENTS

I would like to thank my friends, colleagues, and family for their constant support and encouragement during my time in graduate school.

I would like to thank my advisor, Prof. William A. Goddard III, for enabling me to explore the field of quantum chemistry. I have learned many things from the projects that Bill proposed, the suggestions that he made, the questions that he asked, and the resiliency that he displays.

I would also like to thank the members of my thesis committee, Michael R. Hoffman, Mark B. Wise, and Marco Bernardi, for providing valuable direction and advice.

I would like to thank my mentor, Boris V. Merinov, for his guidance, conversation, and wisdom gained from many years of experience. I would like to thank Boris Kozinsky, Jonathan Mailoa, and the rest of the Bosch chemistry group for funding much of this research as well as providing valuable discussions and suggestions.

I would like to thank Asghar Aryanfar, A.J. Colussi, and the rest of the Hoffman group for friendship and the opportunity to explore the dynamics of lithium dendrite growth.

I would also like to thank Saber Naserifar and Vaclav Cvcivek for being excellent colleagues, excellent friends, and excellent mentors.

I would like to thank Frances Houle, Marielle Soniat, and the rest of JCAP for providing me with the opportunity to study diffusion of gas molecules through polymer membranes.

I would like to thank the many other members of the MSC group that I have had the pleasure of interacting with, including Caitlin Scott, Tao Cheng, Wei-Guang Liu, Ross Fu, Hai Xiao, Ho-Cheng Tsai, Yan Choi Lam, Andrea Kirkpatrick, Jason Crowley, Samantha Johnson, Adam Griffith, Sijia Dong, Matthew Gethers, Yufeng Huang, Shane Flynn, Jin Qian, Yalu Chen, Sergey Zybin, Si-Ping Han, Yoosung Jung, Robert "Smith" Nielsen, Hyeyoung Shin, Jamil Tahir-Kheli, Darryl Willick, Ted Yu, Amir Mafi, Mamadou Diallo, Andres Jaramillo-Botero, and any names that I may have missed. I would also like to thank my colleagues Ali Kachmar and Francesco Faglioni. I have learned much from the group, both personally and professionally.

I would also like to thank my former professors Bruce Kusse and Chris Xu for encouraging me to apply to graduate school and guiding me through the process. I would also like to thank Felicia Hunt and Christy Jenstad for their advice and advocacy.

I would like to thank my friends in the CCA program, applied physics class, Magic club, Friday night dinner group, and greater Caltech community for your kindness and support and bringing a smile to my face, even in difficult times.

Last but not least, I would like to thank my parents, Beth and Ian Brooks for their unwavering support and kindness, my brother and sister, Andrew and Laura Brooks, for leading by example, and my girlfriend, Angela Hebberd, for caring so deeply about me.

To the amazing people I have met in the past five and a half years, thank you. I could not have done it without you.

ABSTRACT

Energy storage is a critical problem in the 21st century and improvements in battery technology are required for the next generation of electric cars and electronic devices. Solid polymer electrolytes show promise as a material for use in long-lifetime, high energy density lithium-ion batteries. Improvements in ionic conductivity, however, for the development of commercially viable materials, and, to this end, a series of computational studies of ionic diffusion were performed. First, pulsed charging is examined as a technique for inhibiting the growth of potentially dangerous lithium dendrites. The effective timescale for pulse lengths is determined as a function of cell geometry. Next, the atomistic diffusion mechanism in the leading polymer electrolyte, PEO-LiTFSI, is characterized as a function of temperature, molecular weight, and ionic concentration using molecular dynamics simulations. A novel model for describing coordination of lithium to the polymer structure is developed which describes two types of interchain motion "hops" and "shifts," the former of which is shown to contribute significantly to ionic diffusion. The methodology developed in this study is then applied to a new problem – the adsorption of CO_2 at the surface of semi-permeable polymer membranes. Finally, a new method, PQEq, is developed, which provides an improved description of electrostatic interactions with the inclusion of explicit polarization, Gaussian shielding, and charge equilibration. The dipole interaction energies obtained from PQEq are shown to be in excellent agreement with QM and a preliminary application of PQEq to a polymer electrolyte suggest that it can provide an improved description of ionic diffusion. Taken as a whole, these techniques show promise as tools to explore and characterize novel materials for lithium-ion batteries.

PUBLISHED CONTENT AND CONTRIBUTIONS

A Aryanfar, **DJ Brooks**, BV Merinov, WA Goddard III, AJ Colussi, MR Hoffman. (2014). "Dynamics of lithium dendrite growth and inhibition: Pulsed charging experiments and Monte Carlo calculations". In: *The journal of physical chemistry letters 5* (10), pp. 1721-1726. doi: 10.1021/jz500207a

DJ Brooks developed the Monte Carlo model, carried out the simulations, and prepared the modeling section

DJ Brooks, BV Merinov, WA Goddard III (2018). "Atomistic Description of Ionic Diffusion in PEO-LiTFSI : Effect of Temperature, Molecular Weight, and Ionic concentration". In preparation (2018).

DJ Brooks carried out the simulations, performed the analysis, and wrote the manuscript.

M Soniat, M Tesfaye, **DJ Brooks**, BV Merinov, WA Goddard III, AZ Weber, FA Houle. (2018). "Predictive simulation of non-steady-state transport of gases through rubbery polymer membranes". In: *Polymer 134*, pp.125-142. doi: 10.1016/j.polymer.2017.11.055

DJ Brooks carried out molecular dynamics simulations, described the gas/polymer interface and wrote the corresponding section of the manuscript.

S Naserifar, **DJ Brooks**, WA Goddard III, V Cvicek. (2017). "Polarizable charge equilibration model for predicting accurate electrostatic interactions in molecules and solids". In: *The journal of chemical physics 146* (12), pp. 124117. doi: 10.1063/1.4978891

DJ Brooks contributed to the PQEq implementation, simulations, model training, and writing and revision of the manuscript.

TABLE OF CONTENTS

LIST OF ILLUSTRATIONS AND/OR TABLES

NOMENCLATURE

PEO. Polyethylene oxide. A flexible polymer chain that has a C-C-O backbone.

TFSI. Bis(trifluoromethane)sulfominide. An anion with the structure $N(SO_2CH_3)_2^-$.

PDMS. Polydimethylsiloxane. A polymer chain with a $SiO(CH_3)_2$-O backbone.

QM. Quantum mechanics or a quantum-mechanics based method.

DFT. Density functional theory.

FF. Classical force field.

OPLS. Optimized Potential for Liquid Simulations, a non-reactive force field.

PQEq. Polarizable Charge Equilibration method featuring explicit polarization.

MPA. Mulliken population analysis charges

ESP. Electrostatic potential charges

Introduction

LITHIUM-ION BATTERIES FOR ENERGY STORAGE

Energy storage is a critical problem in the 21st century. As the world population grows, so too does the demand for energy and energy storage materials. The development of the next generation of cars, personal electronics, and renewable energy sources hinges on improvements in battery technology.

A battery, simply defined, consists of one or more electrochemical cells which provide power to external devices.[3] More generally, batteries allow for chemical energy to be converted into electrical energy and vice versa.

All battery cells contain the same basic components. Each battery has an electropositive cathode and an electronegative cathode. Charge-carrying ions travel from one electrode to the other through an ion-conducting and electrically insulating electrolyte material. The battery is charged by applying a positive voltage to the cathode, driving the positive charge carriers to the anode. The potential energy stored in the battery can be released by connecting it to a closed circuit. The electromotive force ($\mathcal{E}$), measured in volts, depends on the difference in electronegativity between the anode and the cathode.

Battery performance depends on two metrics. First, the cell must have a high specific energy, in units of Watt-hour/kg. This is particularly important for portable devices – the range of electric cars and size of electronic devices are fundamentally limited by the size of the battery cell. Second, the cell must be safe, reliable, and long-lasting. In the ideal battery, each charge-discharge cycle would be a completely reversible practice. In practical batteries, however, the cycle is never completely reversible and there is a capacity loss over time[4, 5].

Research aimed at developing better batteries typically focuses on selecting better battery components: cations, anions, cathode materials, anode materials, and electrolytes.

A number of materials, including lead[5] and sodium[6], can serve as a cation in the battery cell. Lithium, however, remains the most widely used cation in high-performance batteries, particularly for portable devices. As lithium is the lightest metal, lithium-based batteries tend to achieve high specific energies[7].

Depending on the chemistry of the battery, a number of anions maybe viable. Smaller anions, such as fluoride[8] have a tendency to clump with lithium and form a precipitate. To a lesser extent, this is also true for mid-sized ions such as tetrafluoroborate (BF_4^-) and hexafluorophosphate (PF_6^-)[9]. Larger ions, such as bis(trifluoromethanesulfonyl)imide ($TFSI^-$)[1, 2] distribute their charge over a larger molecule and are less likely to coordinate strongly to lithium.

The selection of electrode material depends on the use case of the battery. Lithium-metal[10] anodes boast a high specific energy, but degrade after a single charging cycle. For rechargeable lithium batteries, graphite[11] most commonly used as the anode material. Intercalated materials are widely used as cathode materials as well, such as lithium cobalt oxide ($LiCoO_2$)[12] and lithium nickel manganese cobalt oxide ($LiNiMnCoO_2$)[13]. Nanostructured electrode materials are also a topic of active research[14].

A number of electrolytes are in use in batteries today. Generally, there is a tradeoff between conductivity and chemical stability in electrolyte materials: the greater the conductivity, the shorter the lifetime. Liquid electrolytes, such as propylene carbonate, have high ionic conductivities[15], but irreversible chemical processes[16-18] can limit the cycling lifespan of such cells. Additionally, liquid electrolytes are prone to the formation of lithium dendrites[19, 20], which can short circuit and overheat the battery. Many current cells today use a separator[21] to mitigate this problem.

Polymer electrolytes are a promising electrolyte material. A polymer matrix, most commonly poly(ethylene-oxide)[22-24], is placed between the anode and cathode, providing sites for lithium to diffuse while blocking dendrite growth. The primary limitation to polymer electrolytes is the relatively low diffusion coefficient[25]. Discovering ways of increasing ionic diffusion within a polymer is currently a question of great interest. A number of novel mechanisms have been proposed for increasing diffusion in polymer electrolytes, including crosslinkers[26] and plasticizers[27]. Recent experiments have focused on characterizing diffusion in polymer electrolytes as a function of molecular weight and salt concentration[23, 28].

For a fixed battery chemistry, improvements in battery performance can be realized by optimizing other operating conditions, such as temperature[1] or voltage[29]. For example, studies have suggested that charging a battery with a square wave voltage pulse at the appropriate frequency inhibits lithium dendrite growth[19, 29, 30].

Since the chemistry of the battery electrolyte can be complex, some assumptions must be made in order to describe ionic migration. The primary assumption is that changes in ion motion is driven by diffusion, i.e.,

$$\nabla^2 c_{ion} = -\frac{\partial c_{ion}}{\partial t}. \tag{1}$$

For a particular ion, the expected displacement is given by the Einstein-Smoluchowski equation[31],

$$\langle |\vec{r}_{ion}(t)| \rangle = \sqrt{2dDt} \tag{2}$$

where $\vec{r}_{ion}(t)$ is the displacement of the ion, D is the diffusion coefficient, t is time of diffusion and d is the dimension of the space. For d=3, this reduces to:

$$\langle |\vec{r}_{ion}(t)| \rangle = \sqrt{6Dt} \tag{3}$$

The square of equation (3) relates the mean-squared-displacement (MSD) of a trajectory with the diffusion coefficient.

$$\mathrm{MSD}(t) = \langle |\vec{r}_{ion}(t)|^2 \rangle = 6Dt \tag{4}$$

Note that the diffusion assumption in equation (1) holds for ionic motion in sufficiently long trajectories, as over short periods of time, an ion might oscillate back and forth in a local site. These oscillations correspond to a sublinear dependence of MSD(t) on t in loglog space. When equation (4) is used to estimate ionic diffusion coefficients from simulation, care has to be taken to consider simulations long enough to reach the Fickian regime.

The method of modeling diffusion is simply the integration of equation (2). The accuracy of this expression can be improved by including the effect of the electromigration due to the electric field. Note that, due to ionic shielding, this field is largest near the electrode[32, 33]. A complete description of ionic diffusion requires a force-field description of bonds, angles, torsions, and non-bonds. Although useful, traditional force fields make a rather large assumption: that charges are fixed and non-polarizable[34]. Limited work has been done on the development of polarizable force fields for polymer electrolytes[34, 35].

This thesis contains a number of studies aimed at understanding the ionic diffusion in lithium-ion battery materials. In Chapter I, lithium dendrite growth is analyzed using a simple Monte Carlo model with electromigration term. The study shows that pulsed charging over intervals of ~1ms inhibits dendrite growth due to the relaxation of concentration gradients. In Chapter II, a force field simulation of ionic diffusion in PEO-LiTFSI is performed as a function of ion concentration, molecular weight and temperature. The relative diffusion coefficients are shown to be in good agreement with experiment. The most and least diffusive lithium atoms are analyzed and a novel model for characterizing chain hopping suggests that both the motion of the polymer backbone and interchain hopping contribute to ionic diffusion. The methodology developed in chapter II was also applied to a description of the CO_2 adsorption process in semi-permeable polymer membranes, as described in Appendix B. In Chapter III, a polarizable charge equilibration scheme (PQEq) is developed. The model, which describes atomic charges as polarizable Gaussian shells, is shown to produce charges in good agreement with QM methods. Furthermore, PQEq interaction energies are shown to be significantly closer to QM than fixed charge methods over a cyclohexane-based training set. Initial PQEq simulations of ionic diffusion in PEO-LiTFSI look promise, but additional study in needed. These results serve as a platform for future studies of ionic diffusion in lithium-ion batteries, as shown in Appendix E.

Chapter I

DYNAMICS OF LITHIUM DENDRITE GROWTH AND INHIBITION: PULSED CHARGING EXPERIMENTS AND MONTE CARLO CALCULATIONS

With contributions from Asghar Aryanfar, Boris V. Merinov, William A. Goddard III, Agustin J. Colussi, and Michael R. Hoffman

Acknowledgement: The main part of this chapter is published in the Journal of Physical Chemistry Letters, 2014, 5(10), pp1721-1726.

Abstract

Short-circuiting via dendrites compromises the reliability of Li-metal batteries. Dendrites ensue from instabilities inherent to electrodeposition that should be amenable to dynamic control. Here, we report that by charging a scaled coin-cell prototype with 1ms pulses followed by 3ms rest periods, the average dendrite length is shortened ~2.5 times relative to those grown under continuous charging. Monte Carlo simulations dealing with Li^+ diffusion and electromigration reveal that experiments involving 20ms pulses were ineffective because Li^+ migration in the strong electric fields converging to dendrite tips generates extended depleted layers that cannot be replenished by diffusion during rest periods. Because the application of pulse much shorter than the characteristic time τ_c~O(~1ms) for polarizing electric double layers in our system would approach DC charging, we suggest that dendrite propagation can be inhibited, albeit not suppressed, by pulse charging within appropriate frequency ranges.

Introduction

The specific high energy and power capacities of lithium metal (Li^0) batteries are ideally suited to portable devices and are valuable as storage units for intermittent renewable energy sources[36-42]. Li^0, the lightest and most electropositive metal, would be the optimal anode material for rechargeable batteries if it were not for the fact that such devices fail unexpectedly by short-circuiting via the dendrites that grow across electrodes upon recharging[19, 43]. This phenomenon poses a major safety issue because it triggers a series of adverse events that start with overheating, which is potentially followed by the thermal decomposition and ultimately the ignition of the organic solvents used in such devices[44-46].

Li^0 dendrites have been imaged, probed, and monitored with a wide array of techniques[39, 40, 47]. Moreover, their formation has been analyzed[33, 48] and simulated at various levels of realism[19, 49, 50]. Numerous empirical and semiempirical strategies have been employed for mitigating the formation of Li^0 dendrites that were mostly based on modifications of electrode materials and morphologies and variations of operational conditions[37]. Thus, reports can be found on the effects of current density[51-53], electrode surface morphology[44], solvent and electrolyte composition[54-57], electrolyte concentration[51], evolution time[58], the use of powder electrodes[20], and adhesive lamellar block copolymer barriers[59] on dendrite growth. We suggest that further progress in this field should accrue from the deeper insights into the mechanism of dendrite propagation that could be gained by increasingly realistic and properly designed experiments and modeling calculations[56, 60]. We considered that Li^0 dendrite nucleation and propagation are intrinsic to electrodeposition as a dynamic process under nonequilibrium conditions[40,

[48]. Furthermore, in contrast with purely diffusive crystal growth, that Li-ion (Li^+) electromigration is an essential feature of electrolytic dendrite growth[61]. More specifically, we envisioned that runaway dendrite propagation could be arrested by the relaxation of the steep Li^+ concentration gradients that develop around dendrite tips during charging. This is not a new strategy[62], but to our knowledge the quantitative *statistical* impact of pulses of variable duration on dendrite length has not been reported before. Herein, we report experiments focusing on dendrite growth in a scaled coin cell prototype fitted with Li^0 electrodes charged with rectangular cathodic pulses of variable frequencies in the kilohertz range. We preserve the geometry and aspect ratio of commercial coin cells in our prototype, the dimensions of which facilitate the visual observation of dendrites. The effects of pulsing on stochastic phenomena such as dendrite nucleation and growth are quantified for the first time on the basis of statistical averages of observed dendrite length distributions. We also present novel coarse-grained Monte Carlo model calculations that, by dealing explicitly with Li^+ migration in time-dependent nonuniform electric fields, provide valuable insights into the underlying phenomena. We believe our findings could motivate the design of safer charging protocols for commercial batteries. Current efforts in our laboratory aim at such a goal.

Methods

We performed our experiments in a manually fabricated electrolytic cell that provides for in situ observation of the dendrites grown on the perimeter of the electrodes at any stage (Figure 1). The cell consists of two Li^0 foil disc electrodes (1.59cm diameter) separated 0.32cm by a transparent acrylic ring. The cell was filled with 0.4cm^3 of 1M $LiClO_4$ in propylene carbonate (PC) as electrolyte. We conducted all operations in an argon-filled (H_2O, O_2<0.5 ppm) glovebox. Arrays of multiple such cells were simultaneously electrolyzed with trains of 2mAcm^{-2} pulses of variable t_{ON} durations and $\gamma = t_{OFF}/t_{ON}$ idle ratios generated by a programmable multichannel charger. After the passage of 48mAh (173 Coulombs) through the cells, we measured the lengths of 45 equidistant dendrites grown on the cells perimeters by means of Leica M205FA optical microscope through the acrylic separator. Because dendrites propagate unimpeded in our device—that is, in the absence of a porous separator—our experiments are conducted under conditions for controlling dendrite propagation that are more adverse than those in actual commercial cells. Further details can be found in Experimental Details in Appendix A.

Results

The lengths and multiplicities [λ_i, p_i] of the 45 dendrites measured in series of experiments performed at t_{ON} = 1 and 20ms, γ = 0 (DC), 1, 2, and 3, are shown as histograms in Appendix A. Dendrite lengths typically spanned the 200 μm–3000 μm range. Their average length α defined by equation 1

$$\alpha = \frac{\int p_i \lambda_i}{\int p_i} \tag{2}$$

represents a figure of merit more appropriate than the length of a single dendrite chosen arbitrarily for appraising the effect of pulsing on the outcome of stochastic processes. The resulting α values, normalized to the largest α in each set of experiments, are shown as blue bars as functions of γ for t_{ON}=1 and 20ms pulses in Figure 2. It is immediately apparent that the application of [t_{ON}=1ms; t_{OFF}=3ms] pulse trains reduces average dendrite lengths by ~2.4 times relative to DC charging, whereas t_{ON}=20ms pulses are rather ineffective at any γ.

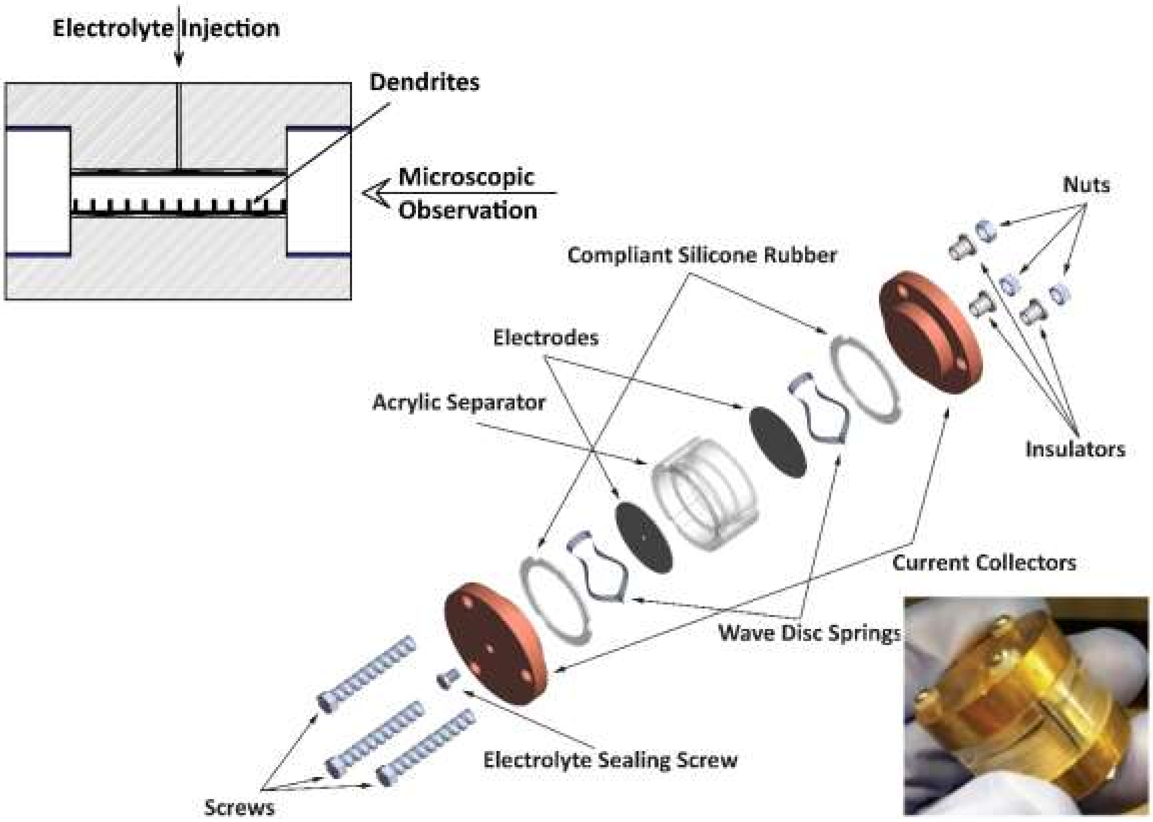

Figure 1: Top down: cross-sectional view, expanded view, and outer photograph of the cell

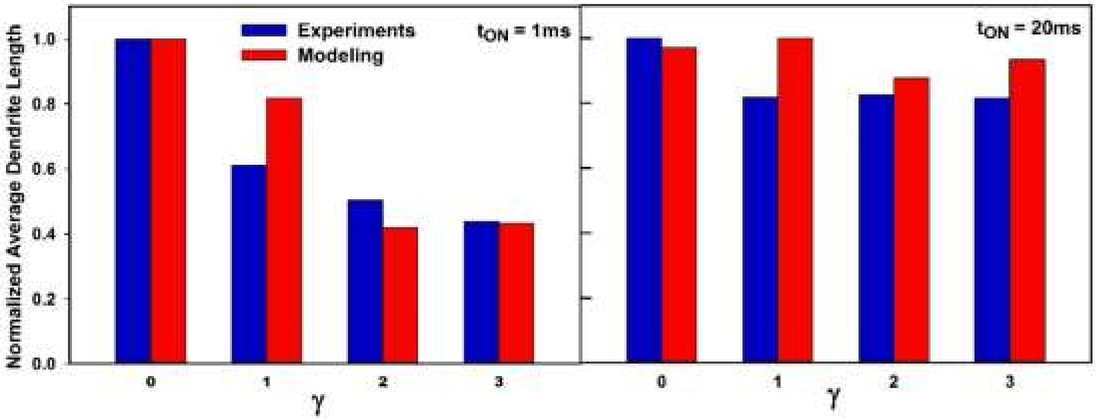

Figure 2: Pulsed charging effects on the average dendrite length, α, sampled over a population of 45 dendrites. The idle ratio is denoted by $\gamma = t_{OFF}/t_{ON}$.

Basic arguments help clarify the physical meaning of the $t_{ON} \sim 1$ ms time scale. The mean diffusive (MSD) displacement of Li^+ ions, MSD = $(2\ D_+\ t)^{1/2}$ (where D_+ is the experimental diffusion coefficient of Li^+ in PC), defines the average thickness of the depletion layers created (via Faradaic reduction of Li^+ at the cathode) that could be replenished by diffusion during t rest periods[33]. Notice that MSD is a function of time$^{1/2}$ and depends on a property of the system (D_+), that is, it is independent of operating conditions such as current density. From the Einstein relationship, $D_+ = \mu_+ (RT/F)$[63] (μ_+ is the mobility of Li^+ in PC), the electric fields $|E|_c$ at which Li^+ electromigration displacements, EMD = $\mu_+ |E|_c\ t$, that would match MSD are given by equation 3:

$$|E|_c = \sqrt{\frac{2RT}{F}} * \frac{1}{\sqrt{\mu_+ t}} \tag{3}$$

Thus, with $(2\ RT/F) = 50$mV at 300K, $\mu_+ = 1 \times 10^{-4}$ cm^{2}V^{-1}s^{-1}, and $t = 1$ms, we obtain $|E|_c = 707$ V cm^{-1}, which is considerably stronger than the initial field between the flat parallel electrodes: $|E|_0 \sim V_0/L = 9.4$Vcm^{-1}. Cathode flatness and field homogeneity, however, are destroyed upon the inception of dendrites, whose sharp (i.e., large radii of curvature) tips induce strong local fields[33, 64]. Under such conditions, Li^+ will preferentially migrate to the tips of advancing dendrites rather than to flat or concave sectors of the cathode surface[33, 48, 65-67]. Because the stochastic nature of dendrite propagation necessarily generates a distribution of tip curvatures, the mean field condition EMD ≤ MSD at specified t_{ON} values is realized by a subset of the population of dendrites. On sharper dendrites the inequality EMD > MSD will apply at the end of t_{ON} pulses. Thus, larger $|E|_c$ values would extend the EMD ≤ MSD conditions to dendrites possessing sharper tips, that is, to a larger set of dendrites that could be controlled by pulsing. Note the weak $|E|_c \propto \mu_+^{-1/2} \propto \eta^{-1/2}$ dependence on solvent viscosity η.

From this perspective, because $|E|_c \propto t^{-1/2}$, the application of longer charging pulses will increase the width of the depletion layers over a larger subset of dendrites to such an extent that such layers could not be replenished during rest periods. The preceding analysis clearly suggests that shorter t_{ON} periods could be increasingly beneficial. Could t_{ON} be shortened indefinitely? No, because charging at sufficiently high frequencies will approach DC conditions. The transition from pulsed to DC charging will take place whenever t_{ON} becomes shorter than the characteristic times τ_c of the transients associated with the capacitive polarization of electrochemical double layers. This is so because under t_{ON} pulses shorter than τ_c most of the initial current will be capacitive, that is, polarization will significantly precede the onset of Faradaic interfacial electron transfer. A rule-of-thumb for estimating τ_c on "blocking" electrodes via eq 3[32, 68-71]

$$\tau_C = \frac{\lambda_D L}{D_+} \tag{4}$$

leads to τ_c~3.3ms. In eq 3, $\lambda_D=(\varepsilon(k_BT/2)z^2e^2C_0)^{1/2}$ is the Debye screening length, L the interelectrode gap, and D^+ the Li^+ diffusion coefficient. In our system, with C_0 = 1M Li^+ solutions in PC (ε=65), $D_+=2.58\times10^{-6}cm^2s^{-1}$, at 298 K, λ_D=0.27. Because the double layer capacitance must be discharged via Faradaic currents in the ensuing rest periods[29], it is apparent that the decreasing amplitude of polarization oscillations under trains of t_{ON} pulses much shorter than $\sim \tau_c$ will gradually converge to DC charging.

In summary, shorter t_{ON} pulses are beneficial for inhibiting dendrite propagation but are bound by the condition $t_{\mathrm{ON}} \geq \tau_c$. The underlying reason is that shorter t_{ON} pulses inhibit dendrite at earlier propagation stages where the curvatures of most dendrite tips have not reached the magnitude at which local electric fields would lead to the EMD > MSD runaway condition. Notice that the stage at which dendrite propagation can be controlled by pulsing relates to the curvature of tip dendrites, which is a morphological condition independent of current density. Higher current densities, however, will shorten the induction periods preceding dendrite nucleation[66].

These ideas were cast and tested in a coarse-grain Monte Carlo model that, in accord with the preceding arguments, deals explicitly with ion diffusion, electromigration, and deposition. It should be emphasized that our model is more realistic than those previously reported[19] because it takes into account the important fact that dendritic growth is critically dependent on the strong electric fields that develop about the dendrites tips upon charging[72]. The key role of electromigration in dendrite propagation has been dramatically demonstrated by the smooth Li^0 cathode surfaces produced in the presence of low concentrations of nonreducible cations, such as Cs^+ that, by preferentially accumulating on dendrite tips, neutralize local electric fields and deflect Li^+ toward the flat cathode regions[38]. Given the typically small overpotentials for metal ion reduction on metallic electrodes[63], we consider that the effect of the applied external voltage on dendrite growth operates via the enhancement of Li^+ migration rather than accelerating Li^+ reduction. In other words, the population of electroactive Li^+ species within the partially depleted double layers surrounding the cathode should be established by the competition of ion diffusion versus electromigration rather than Li^+ deposition. Note furthermore that in our model dendrite nucleation is a purely statistical phenomenon, that is, nucleation occurs spontaneously because there is a finite probability that two or more Li^+ ions are successively reduced at a given spot on the cathode surface. Once a dendrite appears, a powerful positive feedback mechanism sets in. The enhanced electric field at the tip of the sharp dendrites draws in Li^+ ions faster, thereby accelerating dendrite growth/propagation and depleting the solution of Li^+ in its vicinity. The concentration gradients observed nearby growing dendrites are therefore deemed a consequence of the onset of dendrites. In our view, simultaneity does not imply causality[73, 74], that is, we consider that Li^+ depletion around dendrites is more of an effect rather than the cause of dendrite nucleation. Note, however, that experimentally indistinguishable mechanisms of dendrite *nucleation* are compatible with our interpretation that the effects of pulsing on dendrite *propagation* arise from the competition between ion diffusion and electromigration. Because of the computational cost of atomistic modeling, we simulate processes in a 2D domain that is smaller than the section of the actual cell. We chose its dimensions ($L^* \times L^* = 16.7$ nm × 16.7 nm, Table 1) to exceed the depth of actual depletion boundary layers at the cathode. Because our calculations aim at reproducing the frequency response of our experiments, simulation time was set to real time. Therefore, to constrain within our domain the diffusional displacements occurring in real time, we used an appropriately scaled diffusion coefficient D_+^*. The adopted $D_+^* = 1.4 \times 10^{-10}$ cm^2/s $= 5.6 \times 10^{-5}\, D_+$ value leads to MSD*

~ 0.3 L^* after 1ms. The Einstein's relationship above ensures that this choice sets the scaled mobility at $\mu_+^* = D_+^* (F/RT) = 5.6 \times 10^{-9}$ cm^2/(V s). Then, in order to have EMD* = $\mu_+^* |E|^* t \sim$ MSD*, the scaled electric field must be $|E|^* = (V_{\text{anode}} - V_{\text{cathode}})^*/\text{MSD}^* = |E|_0/5.6 \times 10^{-5} = 1.7 \times 10^5$Vcm^{-1}, from which we obtain $(V_{\text{anode}} - V_{\text{cathode}})^* = \text{MSD}^* \cdot 1.7 \times 10^5$ V cm^{-1} = 85mV. The two-dimensional Monte Carlo algorithm implemented on this basis calculates the trajectories of individual Li$^+$ ions via random diffusion and electromigration under time and position-dependent electric fields.

Table 1: Parameters Used in the Monte Carlo Calculations

Domain size L	16.7nm × 16.7nm
Δt (integration step)	$1\mu s$
V_{cathode}	0V
V_{anode}	85mV
D_+ (Li$^+$ diffusion coefficient)	1.4 x 10^{-10} cm^2/s
μ_+ (Li$^+$ mobility)	5.6 x 10^{-9} cm^2/(V*s)
Li$^+$ radius	1.2Å
Free Li$^+$ ions	50
Maximum Li^0 atoms	600

By assuming that Li$^+$ ions reach stationary velocities instantaneously, their mean displacements are given by

$$\vec{r_i}(t + \Delta t) - \vec{r_i}(t) = \sqrt{2D_+\Delta t}\hat{g} + \mu_+\vec{E}\Delta t \qquad (5)$$

The first and second terms on the right hand size of eq 3 are the mean displacements due to ionic diffusion and electromigration, respectively. $\hat{g}$ is a normalized 2D vector representing random motion via diffusion, Δt is the computational time interval, and $\vec{E}$ is the electric field vector. By normalizing displacements relative to the interelectrode separation, L, eq 4 transforms into eq 5

$$\vec{\xi}(t+\Delta t)=\vec{\xi}(t)+\theta\hat{g}+\vec{\eta}. \tag{6}$$

Dendrite lengths λ_i were evaluated as their height $\alpha_i(t)$ above the surface of the electrode:

$$\lambda_i(t)=\max_{k=1:n}\vec{\xi}_k(t)*\boldsymbol{j}. \tag{7}$$

where $\boldsymbol{j}$ is the unit vector normal to the surface of the electrode and n is the total number of lithium atoms incorporated into the dendrite.

By using the Einstein relationship above, the equation of motion becomes

$$\vec{r}(t+\Delta t)-\vec{r}(t)=\sqrt{2D_+\Delta t}\hat{g}+\frac{F}{RT}D_+\Delta t\vec{E}, \tag{8}$$

a function of $D_+\Delta t$.

By neglecting electrostatic ion–ion interactions, given that they are effectively screened because $\lambda_D = 0.27$ nm is smaller than the average interionic separation $R_{i,j} = 1.2$ nm, is computed using Laplace's equation:

$$\nabla^2\phi=\frac{\partial^2\phi}{\partial x^2}+\frac{\partial^2\phi}{\partial y^2}=0. \tag{9}$$

It is obvious that this approximation prevents our model to account for charge polarization, that is, the partial segregation of anions from cations under applied fields. Thus, in our calculations the electric field is instantaneously determined by the evolving geometry of the equipotential dendritic cathode. Note that the concentration gradients that develop in actual depleted boundary layers would lead to even greater electric field enhancements than reported herein. We were forced to adopt the approximation implicit in eq 8 because the inclusion of ion–ion interactions and charge imbalances would be forbiddingly onerous in calculations based on Monte Carlo algorithms. We consider, however, that the inclusion of a variable electric field represents a significant advance over previous models[19].

Calculated dendrite heights were quantified by dividing the x axis (parallel to the surface of the cathode) in four sectors. Here, "dendrite height" in each sector is the height of the Li^0 atoms furthest from the electrode. To ensure good statistics, each simulation was run 100 times, for a total of 400 measurements per data point. The key experimental result, that is, that longer t_{OFF} rest periods are significantly more effective in reducing α after t_{ON}=1ms than t_{ON}=20ms charging pulses, is clearly confirmed by calculations (Figure 2 and Appendix A). Figure 3 displays the results of sample simulations. Metallic dendrites grow with random morphologies into equipotential structures held at $V = 0$V, thereby perturbing the uniform electric field prevailing at the beginning of the experiments. The high-curvature dendrite tips act as powerful attractors for the electric vector field, which by accelerating Li^+ toward their surfaces depletes the electrolyte and self-enhances its intensity. This positive feedback mechanism has its counterpart in the electrolyte regions engulfed by dendrites because, by being surrounded with equipotential surfaces, Gauss's theorem ensures that the electric fields will nearly vanish therein[63]. It should be emphasized that the key feature is that ion displacements from electromigration are proportional to τ_{ON}, whereas diffusive ones increase as $\tau_{ON}^{1/2}$. Above some critical τ_{ON} value, the depth of the deplete layers will increase to the point at which they could not be replenished during the ensuing rest periods of any duration.

These phenomena are visualized from the computational results shown in Figures 3–6. Figure 4 displays the dendrite morphologies created by pulsing at various γ's. Calculations for longer t_{OFF} values show marginal improvements because $\partial[Li^+]/\partial y$ gradients remain largely unaffected in simulations for $\gamma > 3$. Figure 5 shows typical morphologies of dendrites consisting of a given number of deposited Li^0.

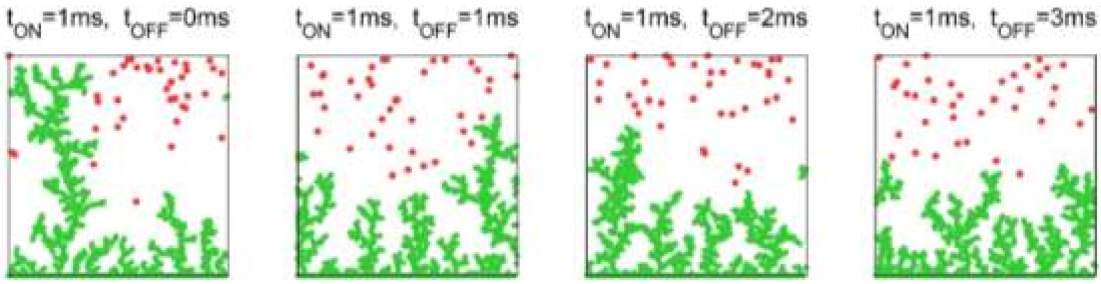

Figure 3: Left to right: dendrite morphologies for DC charging, charging with t_{ON}=1ms pulses at $\gamma = t_{OFF}/t_{ON}$ = 1, 2 and 3. Green dots: Li^0. Red dots: Li^+.

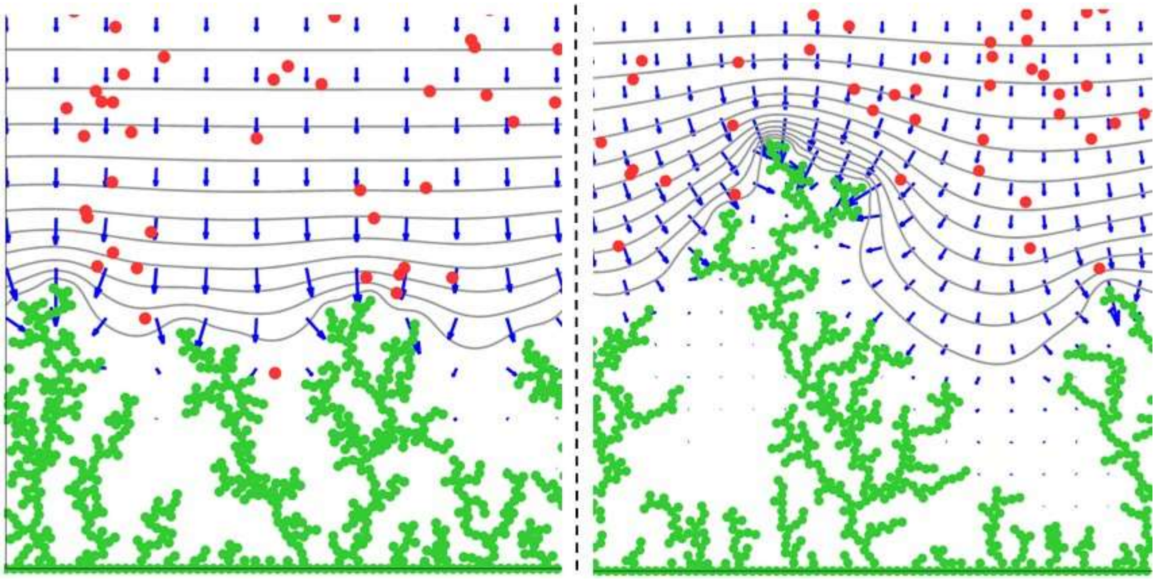

Figure 4: Simulations for charging with t_{ON} = 1 ms (left) and t_{ON} = 20 ms (right) at $\gamma = t_{OFF}/t_{ON} = 3$. Green dots: Li^0. Red dots: Li^+. Gray lines: equipotential contours. Blue vectors: the electric field.

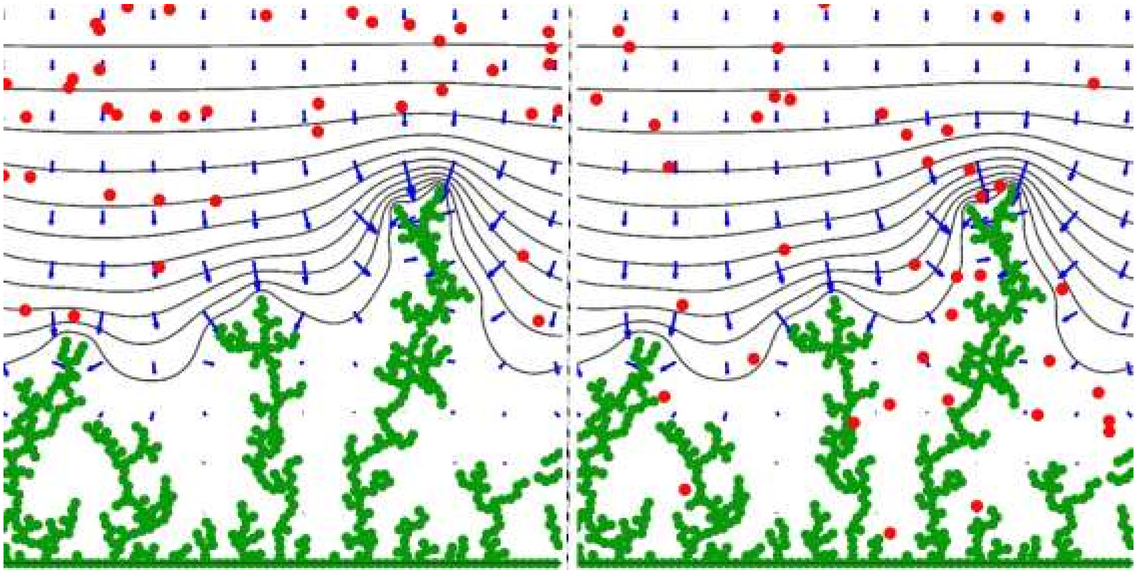

Figure 5: Simulations for charging with t_{ON} = 1 ms, γ = 1 pulses. Left: after a charging pulse. Right: at the end of the successive rest period (right). Green dots: Li^0. Red dots: Li+. Gray lines: equipotential contours. Blue vectors: the electric field.

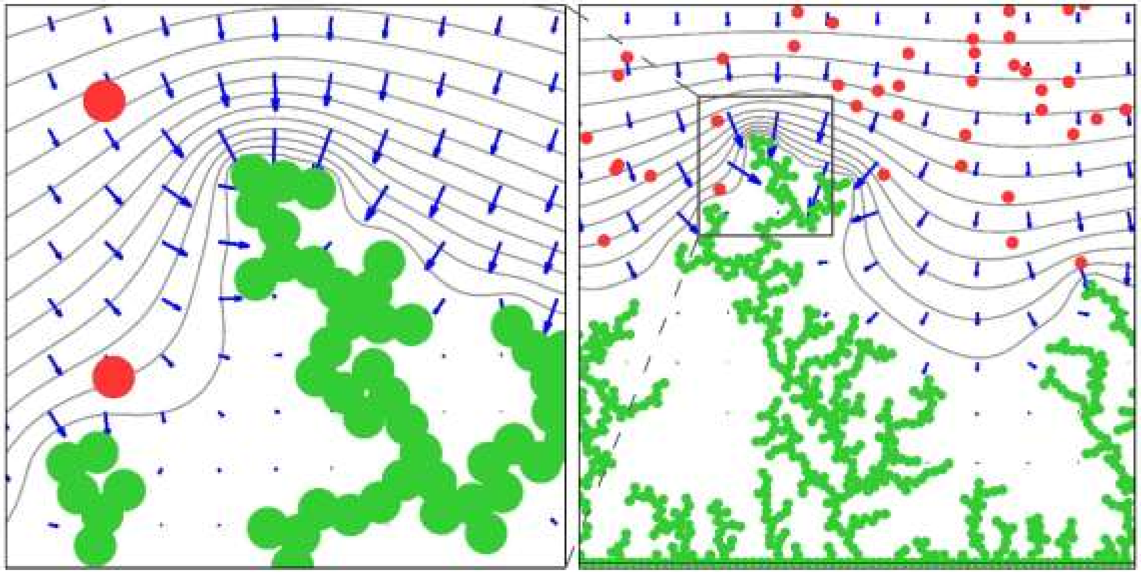

Figure 6: Zooming in the tip of the leading dendrite produced by charging with t_{ON}=20ms, $\gamma=t_{OFF}/t_{ON}$=3 pulses at 243ms, i.e., at the end of simulation time. Green dots: Li_0. Red dots: Li^+. Gray lines: equipotential contours. Blue vectors: the electric field.

Conclusions

In conclusion, we have demonstrated (1) that by charging our lithium metal cell with t_{ON} = 1 ms, $\gamma = t_{OFF}/t_{ON} = 3$ pulse trains, the average dendrite length α is significantly reduced (by ~70%) relative to DC charging and (2) that such pulses are nearly optimal for dendrite inhibition because they are commensurate with the relaxation time τ_c~3 ms for the diffusive charging of the electrochemical double layers in our system. Monte Carlo simulations dealing explicitly with lithium ion diffusion, electromigration in time-dependent electric fields, and deposition at the cathode are able to reproduce the experimental trends of t_{ON} on average dendrite lengths. Further work along these lines is underway.

Chapter II

ATOMISTIC DESCRIPTION OF IONIC DIFFUSION IN PEO-LITFSI: EFFECT OF TEMPERATURE, MOLECULAR WEIGHT, AND IONIC CONCENTRATION

With contributions from Boris V. Merinov and William A. Goddard III

Acknowledgement: Manuscript under preparation (2018).

Abstract

Understanding the ionic diffusion mechanism in polymer electrolytes is critical to the development of better lithium-ion batteries. A molecular dynamics-based characterization of diffusion in PEO/LiTFSI is presented across a range of temperatures, molecular weights and ion concentrations, with relative diffusion coefficients shown to be in good agreement with experimental measurements. To determine the atomistic diffusion mechanism, the chain coordination of lithium atoms is then analyzed across a range of temperatures. The most diffusive lithium atoms are shown to exhibit frequent interchain hopping, whereas the least diffusive lithium atoms frequently oscillate or "shift" coordination between two or more chains. Interestingly, these interchain shifts are shown to contribute little to overall diffusion mechanism and may actually reduce the segmental motion of the polymer, which is shown to contribute significantly to lithium diffusion. These results suggest that novel polymer materials with both a flexible backbone and a low barrier for interchain diffusion are promising for use in the next generation of solid polymer electrolytes.

Introduction

Solid polymer electrolytes are promising materials in the development of high lifetime and energy density lithium-ion batteries[24]. Originally designed for use in portable electronic devices[75], lithium-ion batteries now show promise as energy storage devices for renewable energy sources such as solar and wind power, which produce intermittent power, as well as electric vehicles. Recently, the availability of lithium-ion batteries for residential use has increased with the release of home batteries like the Tesla Powerwall.

The typical, commercially available, lithium-ion battery consists of an organic liquid electrolyte paired with a graphite anode and intercalated transition-metal-oxide cathode[76]. Although high ionic conductivities can be obtained from liquid electrolytes, a high rate of reactions[77] limits both the lifespan and safety of these systems. Specifically, the formation of dead lithium crystals[78] can lead to capacity loss over repeated cycling, and the propagation of lithium dendrites[30, 44, 54] can lead to short circuits and, potentially, combustion of the battery cell.

Solid polymer electrolytes mitigate the effects of these problematic reactions by guiding lithium diffusion along a series of coordination sites along the polymer chains, slowing side-reactions and greatly increasing the potential lifespan and range of safe operating conditions of the battery cell[79]. Although a range of polymer backbones have been studied, poly(ethylene oxide) (PEO)-based structures are currently the leading candidates for use in lithium-ion batteries due to the flexibility of the polymer chains and presence of strong ether coordination sites[22]. Improvements in ionic conductivity, however, are needed for the widespread application of solid polymer electrolytes. Thus, a large research effort is underway to improve the ionic conductivity of PEO-based polymers while maintaining the mechanical strength[1, 2, 24] of the PEO backbone.

The properties PEO-based structures depend strongly on the molecular weight of each chain. Lower molecular weight structures tend to be more flexible and enable larger ionic diffusion coefficients, albeit with reduced mechanical stability. To address this, a number of modifications to the PEO structure have attempted to improve the stability of the backbone, including the creation of block copolymers[80, 81], comb-like[82, 83] and crosslinked[84, 85] polymer structures. For sufficiently large molecular weights, the diffusion coefficient and diffusion mechanism is independent of chain length, as well as the nature of polymer end groups[22].

The crystallization of lithium salts in polymer electrolytes can limit the effective number of charge carriers, and thus the conductivity, within polymer electrolytes. Although a number of anions, such as $LiPF_6$[86], $LiClO_4$[87, 88], and $LiBF_4$[89, 90] have been studied, bis(trifluorométhy-sulfonyl-imide) (TFSI) remains the leading anion candidate, in part, due to its diffuse charge distribution and resistance to clumping[24].

An early description of the diffusion dynamics in polymer electrolytes was provided by the Dynamic Bond Percolation (DBP) model developed by Ratner[91, 92], which can be used to describe diffusion of through a disordered medium that contains a series of coordination sites. The key assumption of the model is the presence of a renewal time, τ_R, over which the neighboring coordination sites are updated due to motion of the polymer backbone. The model demonstrates that ionic motion is always diffusive for timescales longer than the renewal time (t >> τ_R).

A Rouse-based model for ionic diffusion was developed by Maitra[93] and later extended by Borodin and Diddens[94, 95]. This model builds upon the description of renewal events in DBP by introducing a timescale τ_1 associated with intrachain motion along a chain, τ_2 which describes the relaxation time of the polymer chain for segmental motion, and τ_3 as the waiting time between interchain hops. The overall ionic diffusion rate can be expressed as a combination of these three events[93].

A growing body of experiments are being run on PEO-LiTFSI-based polymer systems. Recently, Balsara[23] measured Li^+ and $TFSI^-$ conductivities across a range of molecular weights (M_w=0.6-100 kg/mol) and ionic concentrations (r=0.02-0.08) using pulsed field gradient nuclear magnetic resonance (NMR). Pożyczka[28] recently studied the bulk ionic conductivity as the well as the transference number, t_+, of PEO-LiTFSI across a range of ionic concentrations using impedance spectroscopy. Although, this range of molecular weights and ionic concentrations is of great practical interest, limited molecular dynamics simulations have been carried out across this regime.

In this work, a comprehensive study of ionic diffusion is performed across the range of molecular weights, ion concentrations, and temperatures is performed and the relative diffusion coefficients are shown to be in good agreement with experiment[23]. An analysis of chain coordination reveals that polymer backbone, intrachain, and interchain motion contribute to lithium diffusion, consistent with the Rouse model. An analysis of polymer backbone motion suggests that the presence of lithium reduces segmental chain motion, particularly when the lithium is coordinated to multiple chains. The implication of this finding on the development of new polymer materials is discussed.

Methods

Force field parameters were assigned using the Desmond[96] system builder with the OPLS2005FF[97]. A timestep of 1fs was used for short range interactions and a timestep of 3fs was used for long range interactions, with the Desmond u-series method used to account long range Coulomb interactions after a cutoff of 9Å. In agreement with charges from the QM-based electrostatic potential (ESP) method, ionic charges of ±0.7 were used. A Berendsen thermostat with a time constant of τ=1ps was used for NVT diffusion simulations.

A series of polymer structures were created in an amorphous builder and each structure was equilibrated with a series of minimization, NVT, NPT, and scaled-effective solvent (SES)[98] equilibration steps in order to fully relax the polymer chains. Full details of the equilibration procedure are available in Appendix C. Structures were generated over a range of ionic concentrations (r=0.02, 0.04, 0.06, 0.08 Li:EO). For the r=0.02 case, structures were also constructed across a range of chain lengths (N=23, 45, 100, 450). To maintain a near-constant (N=1000) number of monomers in the simulations, the cells were constructed with m=43, 22, 10 and 2 chains, respectively. Simulations for these structures were performed over a range of temperatures (360K, 400K, 440K, and 480K). Although there is some difference in diffusion for the methyl-terminated chains in our simulations and the hydroxyl-terminated chains studied by Balsara, the difference is negligible at higher molecular weights N>50[22]. The simulations at 400K, 440K, and 480K were run for 115ns, while the simulations at 360K were run for 400ns to reach a regime characterized by Fickian diffusion. The polymer structure for r=0.02, N=100 at the end of the 400ns diffusion simulation is shown in figure 1.

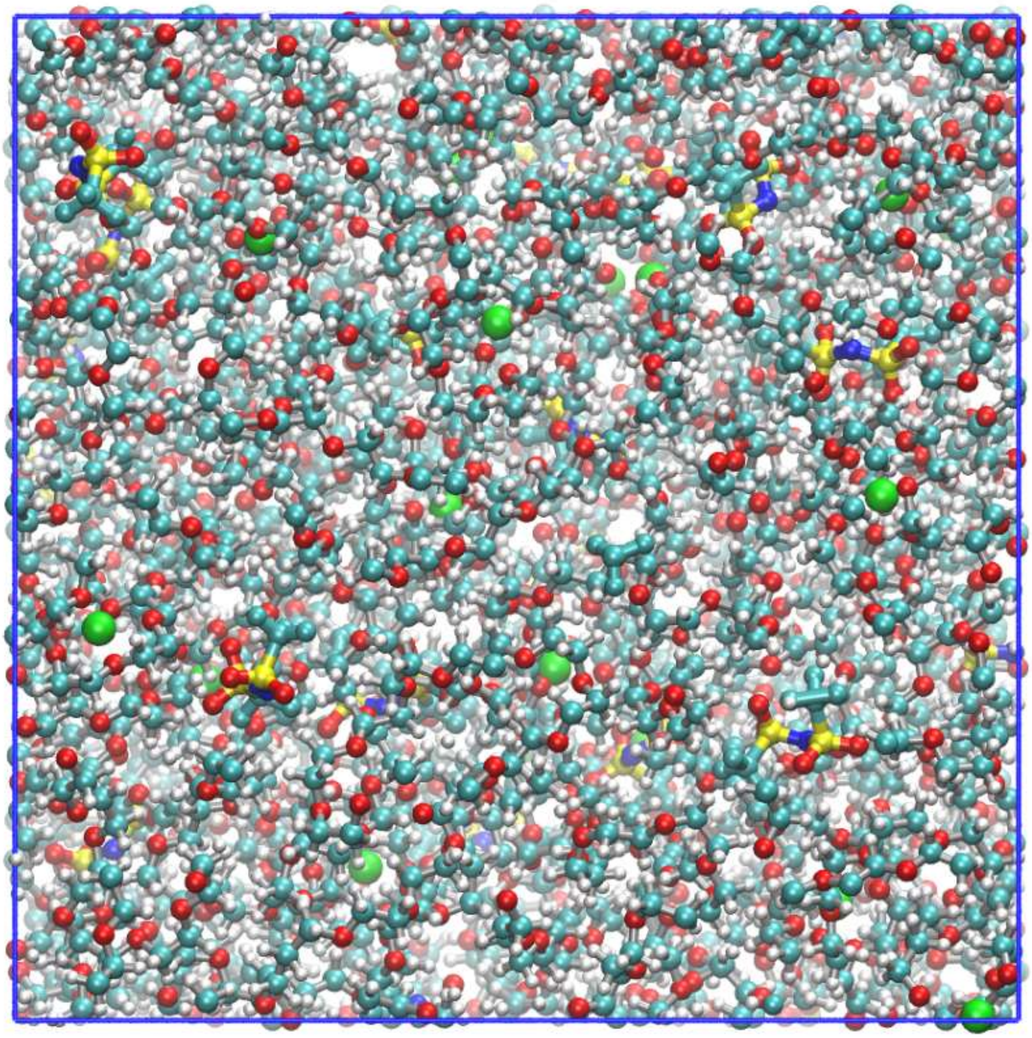

Figure 1: A typical PEO structure consisting of 10 chains of PEO length N=100 monomers and 20 LiTFSI after 400ns of dynamics at 360K. At this concentration, the lithium atoms are shown to coordinate primarily to oxygen along the PEO chains. Lithium atoms are shown in green, TFSI nitrogen is displayed in blue, sulfur in yellow, oxygen in red, and CF_3 in

teal. The PEO chain is identified with bonds shown in grey, oxygen in red, carbon in teal, and hydrogen are shown in white.

The ionic diffusion coefficient, D_{ion}, was derived from the ionic mean-squared displacement (MSD) curve using the 3D diffusion relation:

$$MSD_{ion}(t) \equiv \overrightarrow{r(t)}_{ion}^{2} = 6D_{ion}t. \quad (1)$$

Since this relation only holds for Fickian diffusion, care was taken to identify the Fickian regime of the MSD curve. The largest domain, t, where the loglog slope is nearly unity (within a tolerance of ±0.1) is selected as the fitting region, with a minimum width of one tenth of the total simulation time to ensure good statistics. An example fit is shown in Figure 2. The remainder of the MSD curves are shown in Figure S3 of Appendix C.

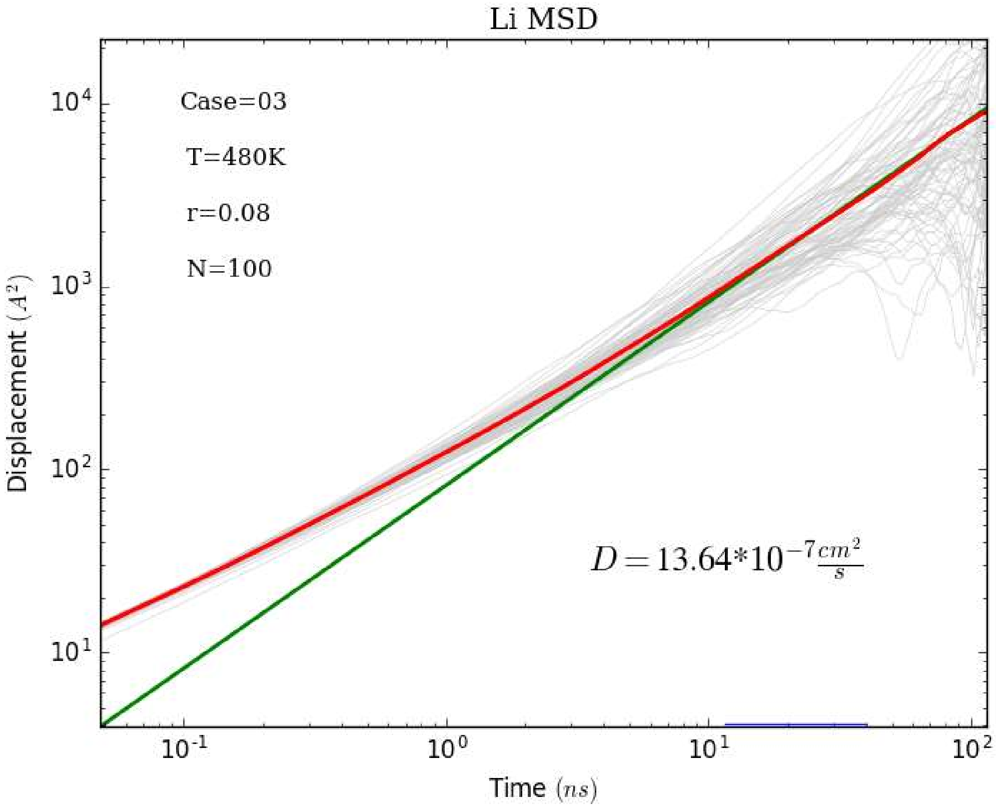

Figure 2: Mean-squared-displacement (MSD) plot of lithium ions diffusing through a PEO polymer matrix with a chain length of N=100 monomers over a 115ns simulation. To ensure a description of true, Fickian, diffusion, the diffusion coefficient is obtained by fitting the MSD curve (red) to a line, 6Dt (green), over the region where the loglog MSD slope is closest to 1. A complete listing of MSD plots can be found in figure S4 of Appendix C.

In order to obtain insight into the atomistic nature of diffusion, a model for lithium coordination is developed. An individual lithium atom is described as coordinated to an oxygen if it is within 2.5Å, roughly the outer width of the first Li-O coordination shell[2]. A lithium atom's position along a chain is tracked by assigning an index to polymer oxygen 1-100, as shown in Figure 3, and defining a lithium position along a chain as the mean index of the coordinated oxygens. The chain a lithium is most coordinated to is tracked as the chain with the greatest number of coordinated oxygen. In the event of a tie, the chain with the smallest lithium-oxygen distance is considered to be the most coordinated chain.

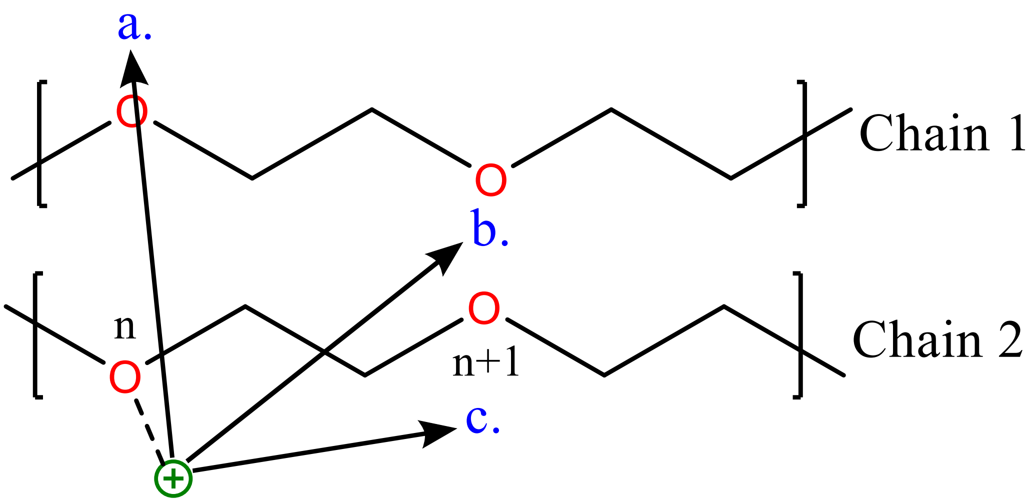

Figure 3: A schematic summarizing the three outcomes of lithium motion: interchain "hops", interchain "shifts", and intrachain motion, represented by sites a, b, and c, respectively. A "hop" occurs when a lithium atom changes chain coordination *and* fully coordinates to a single new chain. A "shift" occurs when a lithium atom changes chain coordination, but remains "stuck" and coordinated to multiple chains. Intrachain motion occurs when lithium's most coordinated chain remains constant and is characterized by a shift, Δn, of the mean lithium-oxygen coordination site. Note that the typical lithium atom is coordinated to 4-5 oxygens, so the shift in coordination can be fractional.

Changes in coordination are tracked over 0.25ns intervals and characterized as intrachain motion, interchain hopping or interchain shifting. For intrachain diffusion, when a lithium atom remained coordinated to the same chain, we measured whether a lithium atom remained fixed $\Delta n=0$, shifted up to one oxygen site $\Delta n\leq 1$, shifted up to two oxygen sites $\Delta n\leq 2$, or shifted more than two oxygen sites $\Delta n>2$. For interchain diffusion, when a lithium atom's most coordinated chain changed, the possible outcomes were an interchain hop, where lithium was only coordinated to a single chain at the end, or a interchain shift, where lithium remained coordinated to at least two chains.

Results

To understand the nature of local sites in the polymer structure, the coordination of lithium is analyzed. A plot of the lithium-oxygen radial distribution function is shown in figure 4. The peak in coordination is observed at 2.12Å, in good agreement the 2.1Å peak observed in a neutron scattering study[1]. The integrated radial distribution function shows that lithium coordinates to an average 4-5 oxygen within a distance of 2.5Å.An example of a lithium coordination site is shown in figure 5.

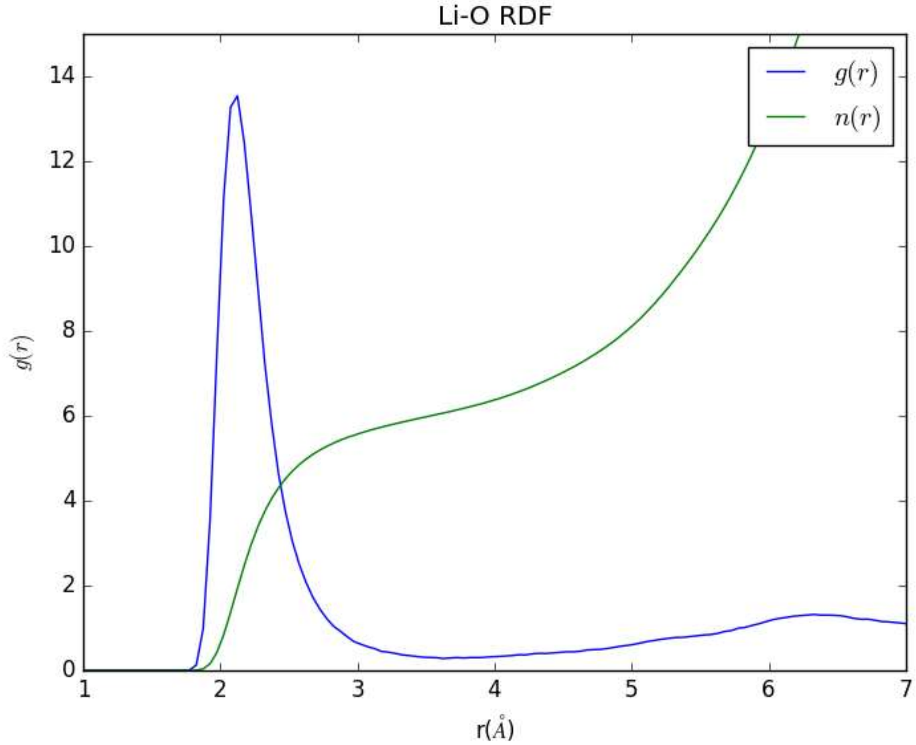

Figure 4: Shows the Li-O radial distribution function for the system containing 10 PEO chains of length 100 monomers and at r=0.02 Li:EO at 360K averaged every 100ps over a 400ns trajectory. The inner Li-O coordination peak is located at 2.12Å, in good agreement with

measurements made with neutron scattering[2]. Additionally, the density of the structure, $1.125\frac{g}{cm^3}$ is shown to be in the experimental range[1, 22, 23].

The local site of a lithium atom in the r=0.02/N=100 structure at 360K is shown in Figure 5. The lithium atom coordinates strongly (r<2.5Å) to 3 polymer oxygen, less than the average of 3-4. Interestingly, these oxygen atoms belong to two separate polymer chains, making this a relatively rare "shift" coordination in the context of the coordination model. A full discussion of lithium coordination is provided later in the text.

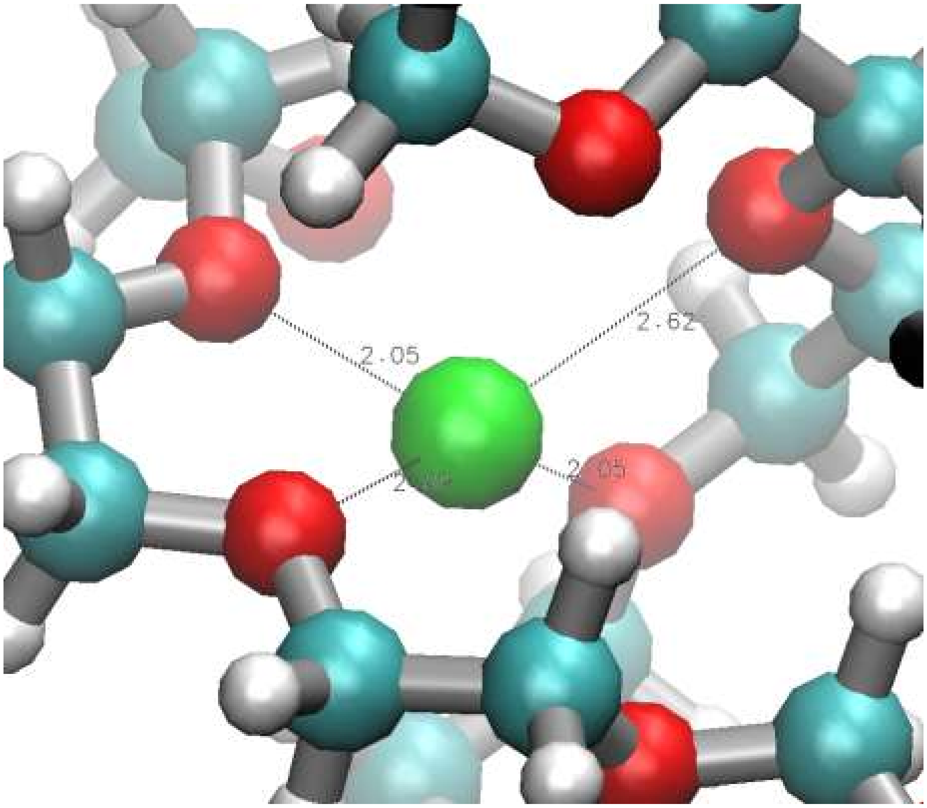

Figure 5: Shows the local coordination of lithium (green) to PEO oxygen atoms (red) at the end of the 400ns 360K/20LiTFSI/N=100 simulation. In this case, the lithium is coordinated to oxygen along two different PEO chains, corresponding to a shift event in the hopping model.

Next, the diffusion coefficients for lithium and TFSI are analyzed as a function of temperature, molecular weight, and chain length. First, the computed diffusion coefficients for lithium and TFSI as a function of chain length for N=23, 48, 100, 450 monomers are shown in Figure 6. In both experiment and theory, the ionic diffusion coefficient is shown to drop with increasing chain length, with a sharp drop between 23 and 100 monomers and a plateau between 100 and 450 monomers, likely due to increased polymer motion of flexible chain length. An analysis of polymer oxygen motion in table 1 confirms this description.

Although there is excellent agreement between the relative diffusion coefficients obtained from theory and experiment, the theoretical values are systematically smaller than NMR data by a factor of 3. This systematic shift is observed in a number of diffusion studies and could be due to ionic charges[99] or nature of the NMR measurement. Ionic diffusion coefficients obtained from more recent experiments by Pożyczka are a factor of 5 lower than NMR, which put the computed diffusion coefficients in the experimental range. A full discussion of experimental diffusion measurements is provided in Appendix C.

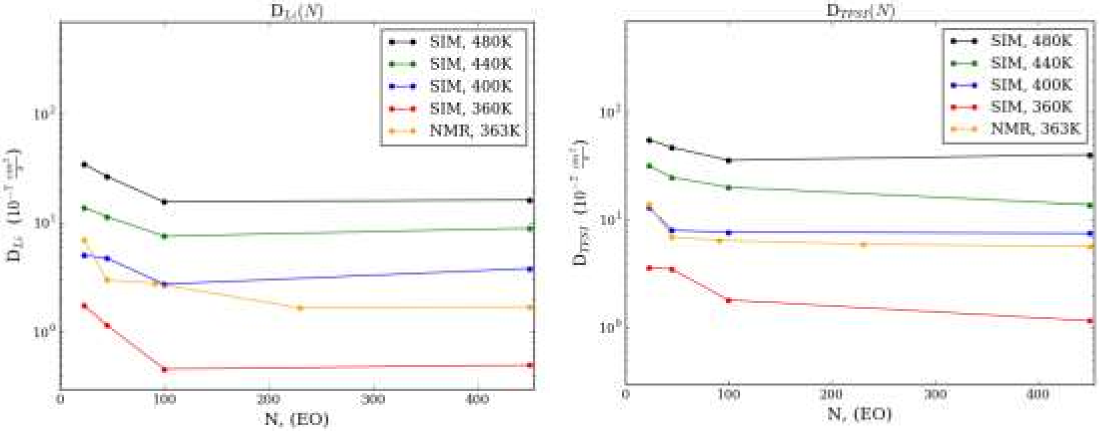

Figure 6: Li and TFSI diffusion coefficients as a function of chain length N. Diffusion coefficients obtained from 400ns simulations at 360K are shown in red, and diffusion coefficients from 400K, 440K, and 480K simulations are shown in blue, green, and black respectively. Diffusion coefficients obtained from NMR measurements at 363K are shown in orange. Shorter chain lengths are shown to lead to larger ionic diffusion coefficients, with a particularly large increase occurring between chain lengths of N=23 and N=100 monomers.

The ionic diffusion coefficients for lithium and TFSI as a function of ionic concentration are shown in Figure 7. The ionic diffusion coefficients drop slightly from r=0.02 to 0.08. In the literature, this drop decrease has been attributed partially as an increase in the number of salt clusters[28]. An analysis of oxygen and polymer displacements, in Figure 14 and Table 1, suggest that the presence of lithium ions may slow the segmental motion of the polymer chains and thus the process of lithium diffusion.

In both experiment and theory, the diffusion coefficient slightly drops with increasing r, but interestingly, a peak is observed at r=0.04. Although the reported experiments by Balsara[23] do not have a peak at this concentration, a recent set of IS measurements[28] indicate such a peak, recent measurements by Pożyczka[28] suggest a peak in ionic conductivity between r=0.02 and r=0.06.

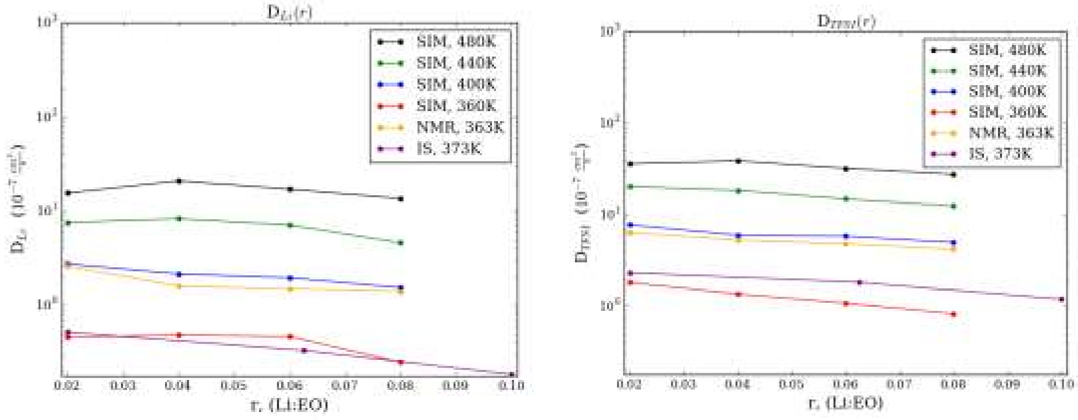

Figure 7: Li and TFSI diffusion coefficients over a range of concentrations, r=0.02, 0.04, 0.06, and 0.08 (Li:EO). Diffusion coefficients obtained from molecular dynamics simulations at 360K, 400K, 440K, and 480K are shown in red, blue, green, and black, respectively. Diffusion coefficients obtained from NMR experiments at 363K are shown in orange and IS experiments at 373K are shown in purple. The overall diffusion coefficient is shown to decrease slightly with ionic concentration. The computed diffusion coefficients lie within the experimental range.

The activation energies for lithium and TFSI diffusion are shown in figure 8 as a function of chain length and ionic concentration. These values are in the range reported by Gorecki[1], and suggest that the computed diffusion coefficients are transferable across a range of temperatures.

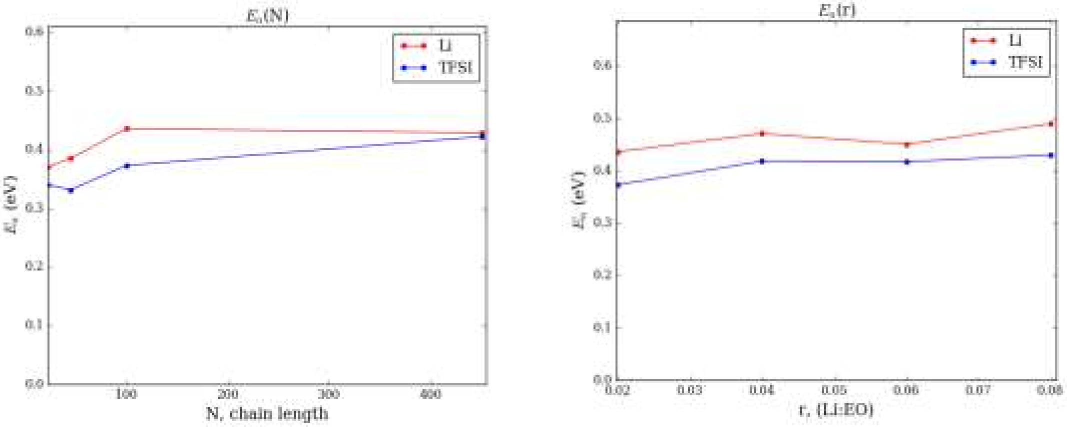

Figure 8: Li and TFSI activation energies over a range of chain lengths, N=23, 45, 100, 450, and concentrations r=0.02, 0.04, 0.06 and 0.08 Li:EO. The computed activation energy depends weakly on chain length and concentration within this regime, in agreement with experimental measurements[1].

To understand the atomistic nature of diffusion, the coordination model is then used to analyze the atoms with the largest and smallest mean-squared-displacements (MSD) over the simulation time. These atoms are denoted as the most and least diffusive lithium. The chain coordination of the most diffusive lithium atom in the r=0.02 Li:EO, N=100 simulation at 360K is plotted as a function of time in Figure 9. The structure on the right shows the real space position of this single lithium atom evolving over time, over 0.25ns intervals. The lithium resides on the 8th chain for around 30ns before hopping to the 9th chain, then the 5th. Overall, the most diffusive lithium moves 59.3Å in 400ns and coordinates to a total of seven chains.

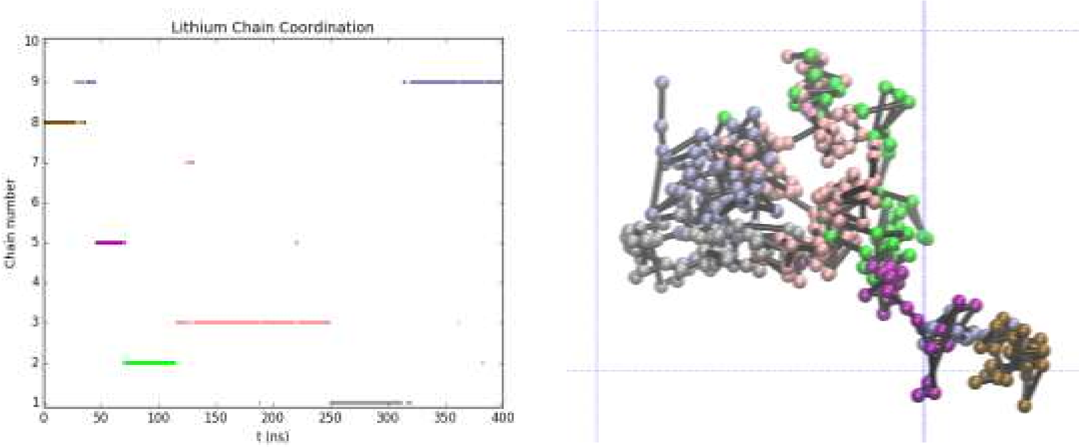
Most Diffusive Lithium, 360K/20LiTFSI

Figure 9: Examines the coordination and displacement behavior of the single most diffusive lithium atom in the 360K/20LiTFSI/N=100 simulation as a function of time. The plot on the left shows the most coordinated chain as a function of time throughout the 400ns simulation.

The structure on the right displays the real positions of the lithium at points spaced every 1ns in the trajectory. Over the duration of the simulation, this lithium atom diffuses a total of 59.3Å and coordinates to a total of 7 chains.

For comparison, the coordination behavior of the least diffusive lithium atom in this simulation is shown in figure 10. This lithium atom only diffuses a total of 12.2Å and coordinates to the 8th chain for most of the simulation, occasionally shifting between chains.

These results suggest that there is considerable variability in the diffusional behavior of individual ions. The more diffusive lithium in this case more frequently hopped between chains, whereas the less diffusive lithium atom only temporarily shifted between chains. A complete analysis of diffusion as a function of coordination change is shown in figure 13.

Least Diffusive Lithium, 360K/20LiTFSI

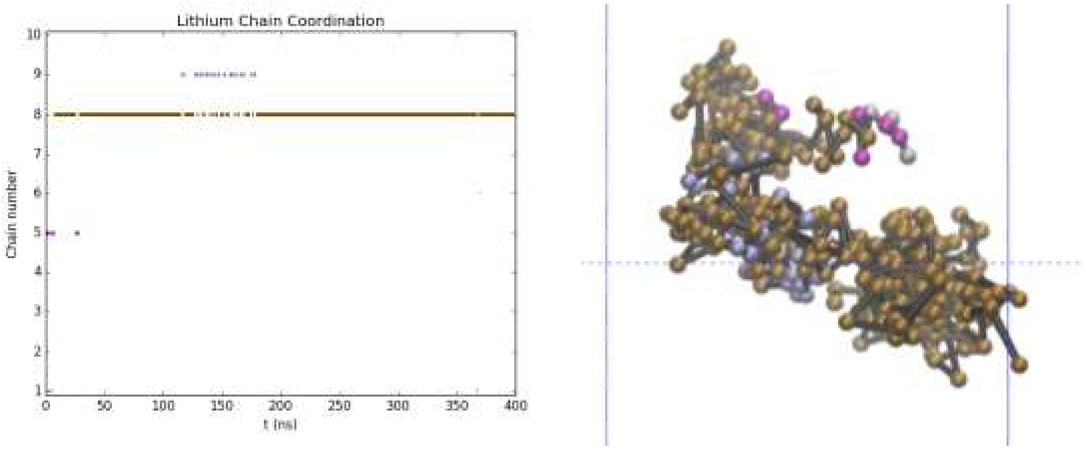

Figure 10: Examines the coordination and displacement behavior of the single least diffusive lithium atom in the r=0.02Li:EO, N=100 simulation at 360K as a function of time. The plot on the left shows the most coordinated chain as a function of time throughout the 400ns simulation. The structure on the right displays the real positions of the lithium at points spaced every 1ns in the trajectory. Over the duration of the simulation, this lithium atom

diffuses a total of 12.2Å and remains primarily coordinated to chain #8 for the majority of the simulation.

This analysis was repeated for the most and least diffusive lithium atoms for the r=0.02 Li:EO, N=100 simulation at 480K and the results are shown in figures 11 and 12. At this temperature, numerous interchain hops are observed over the 115ns trajectory and the total displacements of the lithium are 115.4Å and 45.5Å, respectively. These results suggest a change in the mechanism for diffusion at higher temperatures, as lithium are more able to overcome the barriers for interchain diffusion. This mechanism is analyzed in terms of the hopping model, shown in figure 3, in the discussion section.

Most Diffusive Lithium, 480K/20LiTFSI

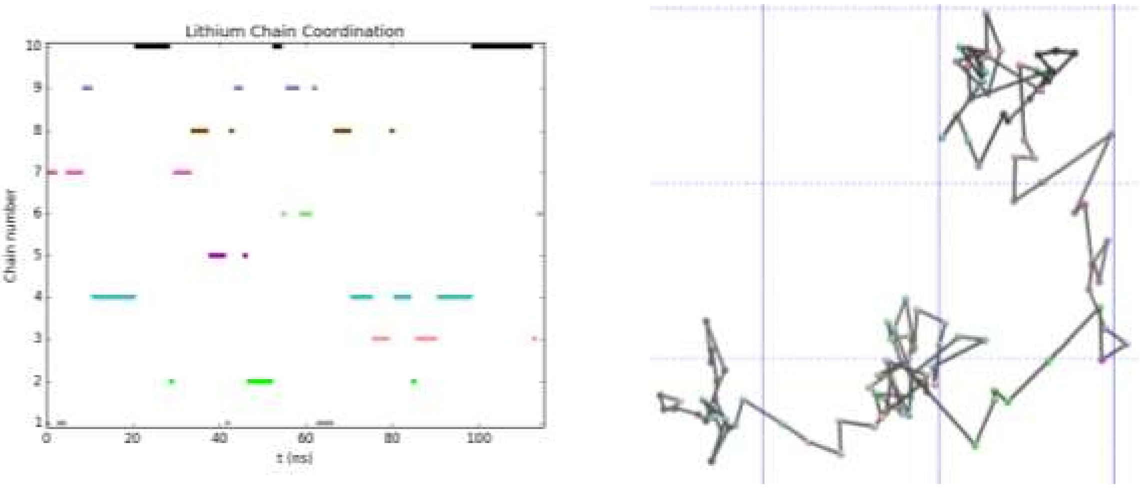

Figure 11: Examines the coordination and displacement behavior of the single most diffusive lithium atom in the 480K/20LiTFSI/N=100 simulation as a function of time. The plot on the left shows the most coordinated chain as a function of time throughout the 115ns simulation. The structure on the right displays the real positions of the lithium at points spaced every 1ns in the trajectory. Over the duration of the simulation, this lithium atom diffuses a total of diffuses a total of 115.4Å with frequent hops between all 10 PEO chains.

Least Diffusive Lithium, 480K/20LiTFSI

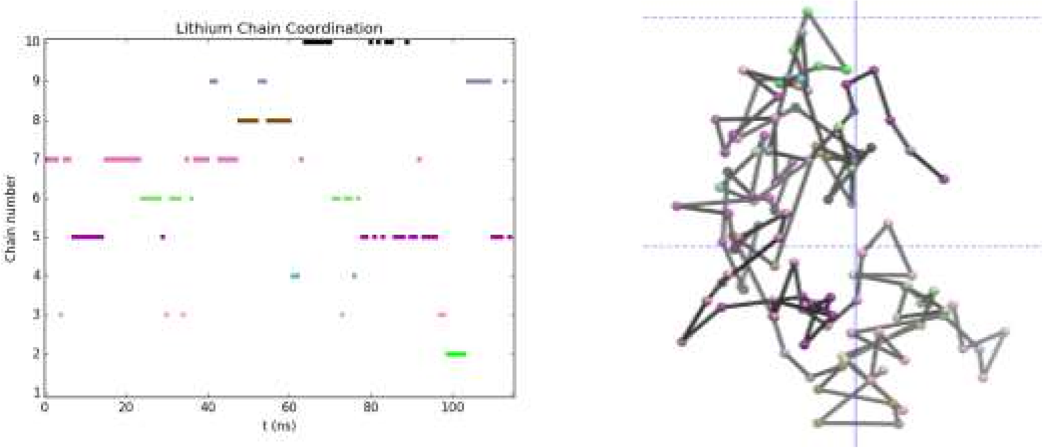

Figure 12: Examines the coordination and displacement behavior of the single least diffusive lithium atom in the r=0.02, N=100 simulation at 480K as a function of time. The plot on the left shows the most coordinated chain as a function of time throughout the 115ns simulation. The structure on the right displays the real positions of the lithium at points spaced every 0.25ns in the trajectory. Over the duration of the simulation, this lithium atom diffuses a total of diffuses a total of 45.5Å with frequent hopping between all 10 PEO chains.

Discussion

The changes in chain coordination of the most and least diffusive lithium atoms suggest a connection between chain coordination and total lithium displacement. In order to examine this, changes in lithium coordination are tracked every Δt=0.25ns in the trajectory. The hopping model, shown in figure 3, describes lithium motion as intrachain diffusion, interchain "hops" between chains, and interchain "shifts" when lithum remains coordinated to multiple chains.

An analysis of the lithium coordination frequency is shown as a function of temperature in figure 13. A small number of lithium atoms undergo no change in coordination, Δn=0.

Small intrachain hops, Δn≤1, correspond to slight changes in the lithium-oxygen coordination shell and are the frequent transition at lower temperatures T=360K, 400K, 440K. Increases in temperature are correlated with an increased frequency of large intrachain hops, Δn>2 and interchain hops, which suggests that an activation barrier is associated with these processes. Interestingly, the frequency of shifts is seen to be independent of temperature, suggesting that this coordination pattern is geometric in nature rather than energy-mediated. The lithium displacements corresponding to these processes are shown in figure 14.

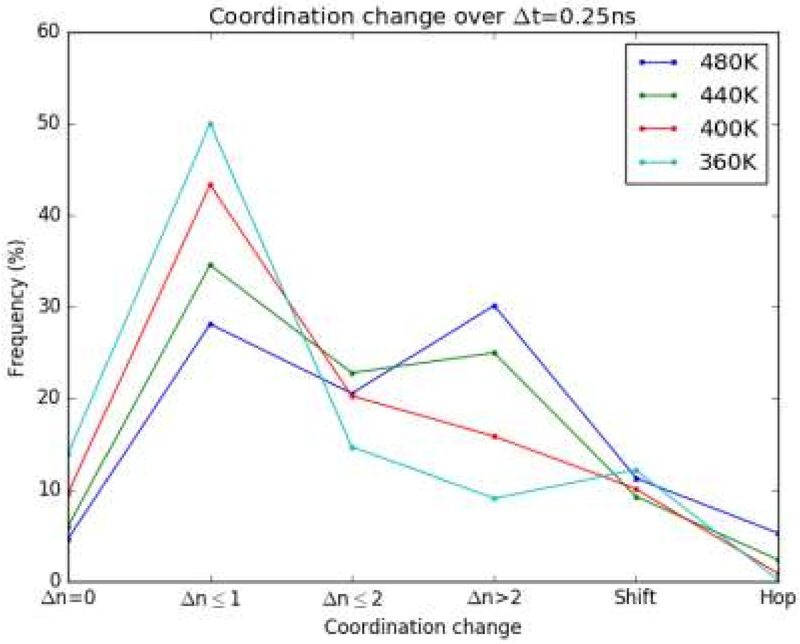

Figure 13: Frequency of lithium coordination changes as a function of temperature. Small intrachain hops, Δn≤1, are most frequent at lower temperatures T=360K, 400K, 440K. Increases in temperature are correlated with an increased frequency of large intrachain hops, Δn>2 and interchain hops. Interestingly, the frequency of shifts is seen to be independent of temperature, suggesting that this coordination pattern is geometric in nature

rather than energy-mediated. The lithium displacements corresponding to these processes are shown in figure 14.

The displacements associated with each of these diffusion processes are shown in figure 14. For no change in coordination, the lithium displacements, Δn=0 caused by the segmental motion of the polymer chains. This segmental motion is shown to be the dominant contributor to ionic diffusion over short timescales. Intrachain changes in coordination along a chain (Δn>0) contribute to the overall lithium diffusion, but intrachain hops alone are not enough to reach the Fickian diffusion limit. Interchain hops, on the other hand are correlated with the largest increases in lithium motion and contribute significantly to the diffusion process. Taken together, these results suggest that the atomistic nature of lithium diffusion is consistent with the Rouse[93] model formulation – the segmental motion of polymer chains drives is associated significant vehicular diffusion. Frequent lithium intrachain hops and infrequent interchain hops contribute to the overall diffusion process.

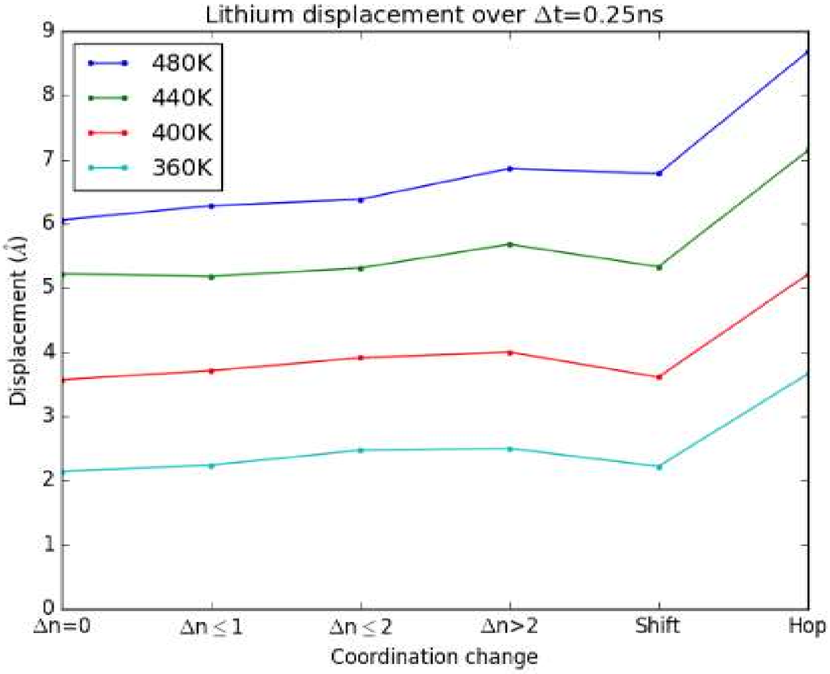

Figure 14: Average lithium displacements associated with coordination change. The Δn=0 displacement is associated with the vehicular motion of the polymer backbone. The increase in average displacements for Δn>0 is associated with intrachain diffusion along a chain. Interchain hopping is associated with significantly increased diffusion.

In order to examine the nature of segmental motion of the polymer chain, the displacement of individual oxygen atoms are analyzed. As polymer displacements can differ as a function of chain position, the two extreme cases are considered – oxygen atoms located at the center of the chain (n=50, 51) and oxygen atoms located at the edge of the chain (n=1, 100). The results of this analysis are shown in table 1. Across all temperatures, it is shown that the oxygen atoms near the edge of the polymer chain diffuse ~30% more than the oxygen atoms at the center of the chain. This suggests increased polymer flexibility and motion for shorter chains, consistent with the results of the diffusion simulations.

Oxygen Displacements (Δt=0.25ns)

Displacement	Center	Edge
360K	3.0Å	3.8Å
400K	4.8Å	6.3Å
440K	6.5Å	8.8Å
480K	7.6Å	10.4Å

Table 1: Shows real space oxygen of polymer backbone oxygen over timescales of Δt=0.25ns. Average displacements are taken for the two oxygen sites closest to center (n=50, 51) and edge (n=1, 100) of a length N=100 polymer chain. These results suggest an increase in segmental motion at the edges of the polymer chain. These results also suggest that the presence of lithium ions may slow the segmental motion of the polymer as the displacements of the polymer chain is significantly less than the Δn=0 motion of lithium at a fixed site along the chain.

Interestingly, it is observed that the oxygen along a polymer chain diffuse significantly more, on average, than the lithium atoms at a fixed position along a chain (Δn=0), as seen in figure 14. This suggests that the presence of lithium ions may constrain the motion of the polymer and reduce the segmental motion of the polymer associated with the thermal reptation of the polymer. This effect could explain the reduction in ionic diffusion coefficients observed at higher ionic concentrations.

The reduction in chain motion in the presence of lithium ions also suggests that lithium coordinated to multiple chains (i.e. shifting), may slow the overall rate of segmental diffusion in the polymer. This is consistent with the increased number of shift transitions associated with the least diffusive lithium ions in figures 10 and 12. This suggests that the nature of lithium coordination between chains may play an important role in ionic diffusion.

Conclusions

Taken as a whole, these results show that both the motion of polymer backbone and interchain hopping make the largest instantaneous contributions to polymer diffusion. Intrachain motion makes a smaller instantaneous contribution to diffusion, but is the most probable mode near the battery operating temperature around 360K. An analysis of oxygen displacements suggests that the presence of lithium may slow polymer reptation, particularly when the lithium is coordinated to multiple chains. The results also suggest that lithium atoms can reside between chains and that interchain hops must involve *both* coordination to a new chain *and* detachment from its previous chain in order to facilitate greater ionic diffusion. Additionally, reasonably accurate relative ionic diffusion coefficients, consistent with experimental data, were obtained across a range of ion concentrations, temperatures, and molecular weights. The obtained results validate that this methodology shows promise for predicting the structure and ionic conductivity of new and novel polymer materials.

Chapter III

POLARIZABLE CHARGE EQUILIBRATION METHOD (PQEQ)

With contributions from Saber Naserifar, William A. Goddard III, and Vaclav Cvcivek

Acknowledgement: The main part of this chapter is published in the Journal of Chemical Physics, 2017, 146(12), pp124117.

Abstract

Electrostatic interactions play a critical role in determining the properties, structures, and dynamics of chemical, biochemical, and material systems. These interactions are described well at the level of quantum mechanics (QM) but not so well for the various models used in force field simulations of these systems. We propose and validate a new general methodology, denoted PQEq, to predict rapidly and dynamically the atomic charges and polarization underlying the electrostatic interactions. Here the polarization is described using an atomic sized Gaussian shaped electron density that can polarize away from the core in response to internal and external electric fields, while at the same time adjusting the charge on each core (described as a Gaussian function) so as to achieve a constant chemical potential across all atoms of the system. The parameters for PQEq are derived from experimental atomic properties of all elements up to Nobelium (atomic no. =102). We validate PQEq by comparing to QM interaction energy as probe dipoles are brought along various directions up to 30 molecules containing H, C, N, O, F, Si, P, S, and Cl atoms. We find that PQEq predicts interaction energies in excellent agreement with QM, much better than other common charge models such as obtained from QM using Mulliken or ESP charges and those from standard force fields (OPLS and AMBER). Since PQEq increases the accuracy of

electrostatic interactions and the response to external electric fields we expect that PQEq will be useful for a large range of applications including ligand docking to proteins, catalytic reactions, electrocatalysis, ferroelectrics, and the growth of ceramics and films, where it could be incorporated into standard force fields such as OPLS, AMBER, CHARMM, Dreiding, ReaxFF, and UFF.

1. Introduction

For practical simulations of dynamical processes, such as ligands binding to proteins, nucleic acids, and polymers responding to externals fields and stresses, catalysts reacting with substrates, and external fields driving electrochemical reactions, it is necessary to go far beyond the time and length scales of QM through the use of a force field (FF) to describe the structures and forces as they evolve. A critical issue in all such multiscale models is how to accurately describe electrostatic interactions. One common approach is to break the system into fragments, perform QM calculations on each one, and then obtain partial charges from Electrostatic Potential fitting (ESP)[100], Mulliken Population Analysis (MPA)[101] or other QM charge assignment models[102]. Additional discussion on these models can be found in the Supplementary Materials. One disadvantage with these approaches is that the charges are fixed and not allowed to adjust to changes in the electrostatic environment that occur during dynamics. It can also be burdensome to perform the QM calculations to obtain charges, for example, for the millions of ligands used in Virtual Screening (VS) applications. The charge equilibration (QEq)[103] method introduced by Rappé and Goddard in 1991 provides an alternative fast way to predict charges for systems too large for

QM. Indeed, carrying out the QEq calculation along an MD trajectory takes into account some changes in polarization during dynamics. Advantages of QEq are that the 3 parameters per atom are derived from atomic ionization energies (valence averaged) and from covalent radii so that they are available for the whole periodic table (through Lr, atomic no. =103). Also, because the charge on each atom is distributed over a Slater orbital having the size of the atom, QEq can be used to predict charges between bonded atoms to describe the changes during reactions. This made QEq useful for defining a general FF (UFF)[104] for inorganic-organic systems and for reactive FFs (ReaxFF)[105, 106]. However, it has not been demonstrated whether QEq is as accurate as ESP or MPA in reproducing QM energies nor that the predicted changes in polarization during dynamics agree with QM.

Describing the changes in polarization within a molecule or solid during dynamics or in response to an external electric field is crucial in many applications[107-109]. Consequently, many strategies have been proposed for including polarization into FFs particularly for liquid water and its interactions with ions[110-113], for modeling of proteins[114-118], DNA[119], enzymatic reactions[120], protein–ligand docking[121, 122], peptides[123], and in small-molecule systems[124-132]. Polarization is also important in ion channels and aqueous solution[111, 133-135], superionic systems[136], piezoelectric and ferroelectrics materials[137-139], lithium batteries[140], crystal defects and surface energies[141-143], lattice vibrational frequencies calculations[143, 144], dynamic dielectric response or Raman light scattering[144, 145], hydration energy calculations[146], carbon nanotubes[147], and predicting organic crystal structure [148-

[151]. This need has led to a number of approaches that have been discussed thoroughly in several reviews[107, 108, 110, 152-154]. Our perspectives about these methods is summarized in the Appendix D.

In this paper, we propose a new polarizable charge equilibration scheme that builds upon the success of QEq and includes polarization in a generic way that can be easily extended for the entire periodic table. This polarizable charge equilibration model (PQEq) allows charges and polarization to readjust dynamically to attain a constant chemical potential during the simulation. Here the polarization is described by an atomic sized Gaussian shaped electron density cloud that can polarize away from the atomic core in response to internal and external electric fields. The charges on the cores are also described by Gaussian functions and charge can flow from one atom to another based on the QEq charge equilibration scheme. The total electrostatic energy is expressed as a sum of internal atomic energy plus pairwise shielded Coulombic interactions. PQEq uses the same covalent bond radii and atomic ionization energies previously used in QEq. An additional atomic polarization parameter is based on the literature value for atomic polarizability. Thus, the parameters for PQEq are well defined for all elements up to Nobelium (atomic no. =102).

For validation, we perform a series of high quality QM calculations for 30 structures using cyclohexane and benzene scaffolds containing H, C, N, O, F, Si, P, S, and Cl atoms. The interaction energy was computed by bringing a pair of ±1 point charges (probe dipole) towards each structure along several axes. We show that PQEq produces interaction energies in excellent agreement with QM. In addition, we optimize a parameter set (PQEq1) that increases the accuracy in the interaction energies for these particular compounds. Here, and for the rest of the paper, the total interaction energy between the dipole and target structure is referred to as the interaction energy. For fixed charge models, this interaction is just the electrostatic energy between the dipole and fixed charges (i.e. no polarization). For PQEq, with charge updates and shell polarization turned on, this interaction energy now also reflects the change in energy from polarization.

We then compare the PQEq interaction energies with other common charge models such as Mulliken or ESP charges obtained from QM and those from standard force fields (OPLS[155-158] and AMBER[159-161]). We find that the fixed charge methods do not describe the induced polarization in the system.

Based on these results, we believe that PQEq can be used to improve the description of electrostatic interactions for systems in which polarization is important. It can be incorporated into existing force fields such as OPLS, AMBER, CHARMM[162-164], Dreiding, ReaxFF, and UFF, but it may be necessary to modify some parameters to account for the change in the charge model. This could be useful for a large range of applications including ligand docking to proteins, catalytic reactions, electrocatalysis, ferroelectrics, and growth of ceramics and films.

2. Methods

2.1 Polarizable Charge Equilibration (PQEq) model

The PQEq model combines the QEq[103] charge equilibration model with the shell (Drude oscillator) model[114, 129, 138, 165, 166]. The key difference from previous shell models is that PQEq does not use point charges. Rather the shell electron is described as a Gaussian function having the same size as the core charge. This leads to shielding as the shell electron interacts with its core and with other atoms so that the singularities in point charge descriptions are avoided. The polarization of the shell away from its core in response to the electrostatic field of all other charges and any external field accounts for polarization dynamically. Here we take the mass of the shell to be zero so that it responds adiabatically as the atoms move about in the MD.

For a system of N atoms, each atom, i, is partitioned into two charged sites (core and shell). The core (ρ_{ic}) consists of two parts; ρ_i with a variable total charge (q_i) and ρ_{iZ} with a fixed total charge (Z_i). The shell (ρ_{is}) has a fixed total charge of $-Z_i$. The shell and core of an atom are connected by an isotropic harmonic spring with force constant K_s (see Figure 1),

$$\delta E = \frac{1}{2} K_s (\delta R)^2, \tag{1}$$

where δR is the distance between the core and shell. Equation 1 leads to an atomic or shell polarizability of

$$\eta = C_{unit} \frac{Z^2}{K_s}, \tag{2}$$

$$K_s = C_{unit} \frac{Z^2}{\eta}, \tag{3}$$

where Z is the shell charge and C_{unit} = 332.0637 is a unit conversion factor that expresses energy in kcal/mol, distance in angstroms (Å), and η as Å^3. This conversion constant is C_{unit} =14.3994 for energies expressed in eV. The η values derived from the atomic polarizability can be computed using high quality *ab-initio* calculations or measured for single atom polarization in response to an external electric field. We use the values tabulated by Miller[167].

Defining the total charge (core plus shell) on atom *i* as q_i, the individual charges on the core and shell are

$$\begin{aligned} q_{ic} &= q_i + Z_i, \\ q_{is} &= -Z_i. \end{aligned} \tag{10}$$

The net atomic charge at the core ($q_{is} + q_{ic} = q_i$) is variable and adjusts to keep the chemical potential constant. There is positive fixed charge (Z_i) at the core at position $\vec{r}_{ic}$(i.e. $\vec{r}_i$) and a negative fixed charge ($-Z_i$) is at the shell position $\vec{r}_{is}$. The displacement of shell *i* with respect to its core, $\vec{r}_{is,ic}$, is defined as $\vec{r}_{is} - \vec{r}_{ic}$. The charge density of both the core and the shell is described by a 1s Gaussian charge distribution,

$$\rho_{ic}(\vec{r}) = \rho_i(\vec{r}) + \rho_{iZ}(\vec{r}), \tag{11}$$

$$\rho_{is}(\vec{r}) = \rho_{i\bar{Z}}(\vec{r}), \tag{12}$$

$$\rho_i(\vec{r}) = \left(\frac{\alpha_i}{\pi}\right)^{3/2} q_i \exp\left(-\alpha_i |\vec{r} - \vec{r}_{ic}|^2\right), \tag{13}$$

$$\rho_{iZ}(\vec{r}) = \left(\frac{\alpha_{iZ}}{\pi}\right)^{3/2} Z_i \exp\left(-\alpha_{iZ} |\vec{r} - \vec{r}_{ic}|^2\right), \tag{14}$$

$$\rho_{i\bar{Z}}(\vec{r}) = -\left(\frac{\alpha_{iZ}}{\pi}\right)^{3/2} Z_i \exp\left(-\alpha_{iZ} |r - r_{is}|^2\right), \tag{15}$$

where α_{ik} , the width of the distribution, is given by

$$\alpha_{ik} = \frac{\lambda}{2R_{ik}^{2}}. \tag{10}$$

Here, R_{ik} is the covalent atomic radius in Å units and λ is a parameter that converts the overlap of two Gaussian charges to the effective shielding. We determined the value of λ by comparing PQEq and QM electrostatic interaction energies (see below). The PQEq model uses equal atomic and shell radii (i.e. $R_i=R_{ic}=R_{is}$) for each atom i so that the above equations simplify to

$$\rho_{ic}(\vec{r}) = \rho_i(\vec{r}) + \rho_{iZ}(\vec{r}) = \left(\frac{\alpha_i}{\pi}\right)^{3/2}(q_i + Z_i)\exp\left(-\alpha_i\left|\vec{r}-\vec{r}_{ic}\right|^2\right), \tag{16}$$

$$\rho_{is}(\vec{r}) = -\left(\frac{\alpha_i}{\pi}\right)^{3/2} Z_i \exp\left(-\alpha_i\left|\vec{r}-\vec{r}_{is}\right|^2\right). \tag{17}$$

This charge distribution has the shape of a spherical 1s Gaussian shape with a width determined by the atomic radius of the atom. The core and shell of each atom has a Columbic interaction with the cores and shells of every other atom in the system. We allow the atomic charges (q_i) to respond to the electrostatic environment based on the QEq scheme[103, 139]. The position of the shell is then calculated by balancing the sum of all electrostatic forces on the shell with the spring force (see below). A shell charge of Z_i=1 is used for all atoms.

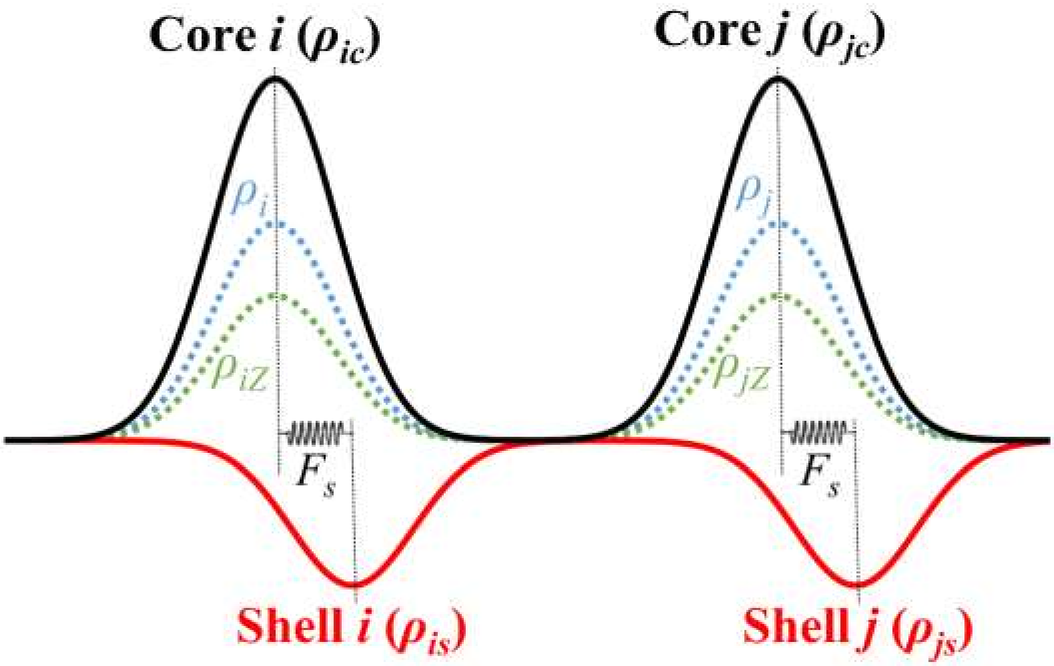

Figure 1: Partition of a two-atom system into core and shell for the PQEq model. Both cores and shells are described by spherical 1s Gaussian charge distributions. The core (ρ_{ic}) consists of two parts; ρ_i with a variable total charge (q_i) and ρ_{iZ} with a fixed total charge (Z_i). The shell (ρ_{is}) has a fixed total charge of -Z_i. The shell and core of an atom interact with each other through a harmonic spring force. Cores and shells of different atoms interact with each other through Coulombic interactions as well. The atomic charge on each core (q_i) is allowed flow within the system until the atomic chemical potentials are equalized.

2.2 Electrostatic Energy

The electrostatic energy between two Gaussian charges is given by $C_{ik,jl}(\vec{r})q_{ik}q_{jl}$,

where

$$C_{ik,jl}(\vec{\cdot}\;, \qquad r \;\; \left(\sqrt{\frac{\alpha_{ik}\alpha_{jl}}{\alpha_{ik}+\alpha_{jl}}}r\right). \tag{18}$$

Here *i* and *j* are the atomic indices, and *k* and *l* represent the core (c) and shell (s), respectively. In the case of $\vec{r}_{ik}=\vec{r}_{jl}$, $C_{ik,jl}$ is equal to

$$C^0_{ik,jl} = \lim_{r \to 0} C_{ik,jl}(\vec{r}) = \frac{2}{\sqrt{\pi}} \sqrt{\frac{\alpha_{ik}\alpha_{jl}}{\alpha_{ik} + \alpha_{jl}}}. \tag{19}$$

A well-known problem in other shell and induced dipole[120, 168] models is that they suffer from a polarization catastrophe when the shells or dipoles are placed too close together. The Gaussian shielding present in PQEq addresses this issue as the Coulombic interaction energy remains finite, even in the limit of zero interatomic distance.

We describe the PQEq electrostatic energy, $E(\{\vec{r}_{ic}, \vec{r}_{is}, q_i\})$, as a sum of an intra-atomic electrostatic energy $E_i(\{\vec{r}_{ic}, \vec{r}_{is}, q_i\})$ and interatomic pairwise Coulomb interactions,

$$E(\{\vec{r}_{ic}, \vec{r}_{is}, q_i\}) = \sum_i^N E_i(\vec{r}_{is,ic}, q_i) + \sum_{i>j} C_{ik,jl}(\vec{r}_{ik,jl}) q_{ik} q_{jl}. \tag{20}$$

The internal energy (E_i) is a function of the electronic polarization and total charge on the atom.

$$E_i(\vec{r}_{is,ic}, q_i) = E_i(0, q_i) + \left[E_i(\vec{r}_{is,ic}, q_i) - E_i(0, q_i)\right] \tag{21}$$

The first term on the right hand side of Equation 21, $E_i(0, q_i)$ is the energy required to create a charge, q_i, assuming zero polarization and neutral atomic state as the reference point. We use a Taylor expansion to express this energy term as

$$E_i(0, q_i) = E_i^0 + q_i \left(\frac{\partial E}{\partial q}\right)_{i0} + \frac{1}{2} q_i^2 \left(\frac{\partial^2 E}{\partial q^2}\right)_{i0} + \ldots \tag{22}$$

and truncate it after second-order terms. The original QEq method[103] included a radius dependent scaling parameter for hydrogen atom in order to better fit the dipole moment for both alkali hydrides (e.g., LiH) and halogen hydrides (e.g., HF). This leads to a nonharmonic dependence of energy, which in our experience can lead to unstable systems, so PQEq eschews this complication.

We use three conditions to determine the rest of the parameters as follows:

$$E_i\left(0,+1\right)=E_i^0+\left(\frac{\partial E}{\partial q}\right)_{i0}+\frac{1}{2}\left(\frac{\partial^2 E}{\partial q^2}\right)_{i0}, \tag{23}$$

$$E_i\left(0,0\right)=E_i^0, \tag{24}$$

$$E_i\left(0,-1\right)=E_i^0-\left(\frac{\partial E}{\partial q}\right)_{i0}+\frac{1}{2}\left(\frac{\partial^2 E}{\partial q^2}\right)_{i0}. \tag{25}$$

Here, $E_i\left(0,+1\right)$ is the ionization potential (IP), which is the energy required to remove one electron from the atom, and $E_i\left(0,-1\right)$ is the electron affinity (EA), which is the energy gained when an atom receives one additional electron. Both IP and EA are well known experimentally for nearly all elements. We use the same values as determined by Rappé and Goddard[103] in which the experimental IP and EA are averaged over the ground state atomic configuration in order to reflect the averaging introduced by bonding to other atoms. Thus, for nitrogen atom the IP and EA are derived using the averages over the ^{4}S, ^{2}D, and ^{2}P states associated with the $(2s)^2(2p)^3$ configuration and the ^{3}P, ^{1}D, and ^{1}S states associated with the $(2s)^2(2p)^2$ and $(2s)^2(2p)^4$ configurations of the ions. Solving Equations 23-25 for the unknowns yields

$$\chi_i^0=\tfrac{1}{2}\left(IP+EA\right)=\left(\frac{\partial E}{\partial q}\right)_{i0}, \tag{26}$$

$$J_{ii}^{0} = IP - EA = \left(\frac{\partial^2 E}{\partial q^2} \right)_{i0} , \tag{27}$$

where χ_i^0 is the Mulliken electronegativity[169] of atom i and J_{ii}^0 is the idempotential (hardness) or electron capacity of atom i, which resists electron flow to or from an atom. We replace the second term on the right hand side of Equation 21 with the Coulombic interaction between core and shell of atom i plus a spring interaction between the core and shell of atom i. Therefore, Equation 20 can be written as,

$$E_i\left(\vec{r}_{is,ic}, q_i\right) = E_i^0 + \chi_i^0 q_i + \frac{1}{2} J_{ii}^0 q_i^2 + O\left(q_i^3\right) + \frac{1}{2} K_s r_{ic,is}^2 . \tag{23}$$

Ignoring the $O\left(q_i^3\right)$ term in Equation 23, the electrostatic energy of the system is given by

$$E\ \left(\{\vec{r}_{ic}, \vec{r}_{is}, q_i\}\right) = \sum_{i}^{N} \left\{ E_i^0 + \chi_i^0 q_i + \frac{1}{2} J_{ii}^0 q_i^2 + \frac{1}{2} K_s r_{ic,is}^2 \right\} + \sum_{ik>jl} C_{ik,jl}\left(\vec{r}_{ik,jl}\right) q_{ik} q_{jl} , \tag{24}$$

where the second sum is the pairwise shielded Coulomb interaction energy between all cores and shells, which can be expanded to give the total electrostatic energy as

$$\begin{aligned} E\left(\{\vec{r}_{ic}, \vec{r}_{is}, q_i\}\right) &= \sum_{i}^{N} \left\{ E_i^0 + \chi_i^0 q_i + \frac{1}{2} J_{ii}^0 q_i^2 + \frac{1}{2} K_s r_{ic,is}^2 \right\} \\ &+ \sum_{i>j} \left[C(\vec{r}_{ic,jc}) q_{ic} q_{jc} - C(\vec{r}_{ic,js}) q_{ic} Z_j - C(\vec{r}_{is,jc}) q_{jc} Z_i + C(\vec{r}_{is,js}) Z_i Z_j \right] . \end{aligned} \tag{28}$$

2.3 The Charge Equilibration Condition

A serious problem in most classical MD/MM applications is that fixed charges are assigned to each atom. Such fixed charges (even the most reliable ones from *ab-initio* calculations) do not respond to the changes in the electrostatic environment, which decreases the accuracy. This problem becomes paramount for reactive force fields (e.g. ReaxFF[106]) where the bond connectivities of atoms change during reactive MD simulations, requiring updates of the atomic charges (ideally at each time step). As in QEq, the PQEq model allows the charge distribution on the various atoms to change as the electrostatic environment changes during the dynamics. The optimum charge distribution is computed from the conditions that the chemical potentials ($\partial E / \partial q_i$) are equal for all of the atoms (which provides *N-1* conditions where *N* is the number of atoms) and that the total charge is conserved

$$\sum_i (q_{ic} + q_{is}) = \sum_i q_i = Q, \tag{29}$$

where Q is the total charge of the system. We use Lagrange multipliers to guarantee this constraint as the charges are optimized. The energy expressions with the Lagrange multiplier, μ, is

$$E_\mu\left(\{\vec{r}_{ic}, \vec{r}_{is}, q_i, \mu\}\right) = E\left(\{\vec{r}_{ic}, \vec{r}_{is}, q_i\}\right) - \mu \sum_i q_i. \tag{30}$$

Setting the derivative of Equation 30 equal to zero yields

$$-\frac{\partial E_\mu}{\partial q_i} = 0 \rightarrow \sum_j H_{ij} q_j = -A_i + \mu, \tag{31}$$

$$H_{ij} = J_{ii}^0 \delta_{ij} + (1 - \delta_{ij}) C(\vec{r}_{ic,jc}), \tag{32}$$

$$A_i = \chi_i^0 + \sum_{i>j} \left[C(\vec{r}_{ic,jc}) - C(\vec{r}_{ic,js}) \right] Z_j, \tag{33}$$

where H_{ij} is an N by N matrix and δ_{ij} is the Kronecker delta function. The diagonal elements of H_{ij} matrix ($\delta_{ij} = 1$) denote the idempotential of the atoms while the off-diagonal elements represent the Coulombic interactions between the variable charge part of the cores (i.e. q_i). A_i in Equation 33 is a vector of length N. The first term of A_i is the electronegativity of the atom. The second term is the Coulombic interaction coefficient between the core and shell of the atom i. The third term is the sum of Coulombic interaction coefficient between variable charge part of core i (i.e., q_i) and the fixed charge component of all other cores and shells (i.e., Z_j and $-Z_j$). Note that in Equation 33, A_i is a fixed quantity for each atom during the charge minimization, which reduces to $A_i = \chi_i^0$ if polarization is not included, as in the QEq model[103, 170]. In Equations 31-33, the Lagrange multiplier μ is the chemical potential that constrains the sum of the atomic charges to be equal to the total charge of Q. Solving Equations 31-33 leads to

$$q_i = \sum_j H^{-1}{}_{ij}(-A_j + \mu 1_j). \tag{34}$$

Applying Equation 29 we get

$$\sum_i q_i = -\sum_i \sum_j H^{-1}{}_{ij} A_j + \sum_i \sum_j H^{-1}{}_{ij} \mu = Q, \tag{35}$$

which is solved to obtain μ

$$\mu = \frac{Q + \sum_i \sum_j H^{-1}{}_{ij} A_j}{\sum_i \sum_j H^{-1}{}_{ij} 1_j} = \frac{\sum_i \tilde{q}}{\sum_i \hat{q}_i}, \tag{36}$$

where $\tilde{q}_i$ and $\hat{q}_i$ are fictitious charges. In practice, we solve Equation 36 by partitioning it into two sub equations. Setting the derivative of Equation 36 to zero results in

$$\sum_j H_{ij} \tilde{q}_j = -A_i, \tag{37}$$

$$\sum_j H_{ij} \hat{q}_j = -1. \tag{38}$$

Finally, the instantaneous total charges on each atom (q_i=q_{ic}+q_{is}) can be written as

$$q_i = \tilde{q}_i - \mu \hat{q}_i . \qquad (39)$$

The above formulation for PQEq omits the presence of external electric fields, which is included in the Supplementary Materials. A frequency-dependent response can be obtained from time-dependent fields.

2.4 Preconditioned Conjugate Gradient (PCG) Solution of the Charge Equilibration Equations

Exactly solving for the charges that satisfy the QEq condition involves inverting an *N* by *N* matrix, which scales as $O(N^3)$. Since this is required every time step[103], this process is computationally too expensive to be practical for large systems. A practical solution to this problem is the PCG method implemented in the PuReMD[171, 172] and LAMMPS[173] software packages.

We use PCG to solve Equations 37 and 38. The efficiency and convergence of this iterative conjugate-gradient (CG) method depends on the spectrum of the coefficient matrix. The PCG method uses a second matrix (preconditioner) to transform the coefficient matrix to obtain improved spectral properties. This preconditioner involves an incomplete factorization of the coefficient matrix. In particular, incomplete LU factorization (ILU) (where L and U are lower and upper triangular) can be used for solving this sparse linear systems[174]. For QEq, Aktulga et al. studied the performance, stability, and accuracy of the ILU-based preconditioners for various model systems[172]. They showed that ILU-based preconditioners dramatically reduces the number of iterations while allowing the same L and U factors to be used effectively as preconditioners over several steps, due to the slow changes in the simulation environment. We extended this ILU-based preconditioner method to PQEq and coupled it with shell relaxation (see next section) to calculate the PQEq charges while updating the shell position.

2.5 Shell Relaxation

In our formulation of the PQEq dynamics, we choose to displace the core of each atom together with its shells as a rigid body during every timestep of the dynamics. After moving core plus shell, the first step of the next iteration is to calculate the electrostatic field on every particle and to solve the PQEq equations (using the PCG method) for the new charges. Next, we fix the core positions and update the positions of all shells simultaneously using a one-step relaxation as follows. If necessary, this process of updating atomic charges and shell relaxation with fixed cores can be repeated for several iterations to attain self-consistency for troublesome geometries. However, we find that one cycle is normally sufficient to reach equilibrium for each timestep after the first.

The shell position for each atom is obtained by balancing the effect of the electrostatic field due to all external atoms with intra-atomic interactions involving only the core and its shell. These forces are calculated by taking the derivative of the electrostatic energy (Equation 28) with respect to the shell position,

$$F_{intra} = -\frac{\partial}{\partial r_{is}}\left(\frac{1}{2}K_s r_{ic,is}^2\right), \tag{40}$$

$$F_{external} = -\frac{\partial}{\partial r_{is}}\sum_j\left[C(\vec{r}_{ic,jc})q_{ic}q_{jc} - C(\vec{r}_{ic,js})q_{ic}Z_j - C(\vec{r}_{is,jc})q_{jc}Z_i + C(\vec{r}_{is,js})Z_iZ_j\right] \tag{41}$$

We solve Equations 40 and 41 to find the optimal position of shells (r_{is}) using a single iteration of the Newton-Raphson method. Since the shell is typically very close to its core (usually < 0.1 Å), we neglect the effect of the external core and shell charges on this second derivative to avoid inverting the Hessian. We assume here that the shell is massless, so that it relaxes instantaneously to its zero-force position, with no inertial delay. Therefore, we estimate the new position of the shell by assuming that F_{intra} and $F_{external}$ are collinear. Thus, the new position of the shell is computed by,

$$r_{is,new} = r_{is,old} - \frac{E'(r_{is,old})}{E''(r_{is,old})} = r_{is,old} + \frac{\left(F_{intra} + F_{external}\right)\big|_{r_{is,old}}}{\partial^2 E/\partial r_{is}^2\big|_{r_{is,old}}}, \tag{42}$$

$$\frac{\partial^2 E}{\partial r_{is}^2} = \frac{\partial^2}{\partial r^2{}_{is}}\left(\frac{1}{2}K_s r_{ic,is}^2\right). \tag{43}$$

Although, this problem is not strictly one-dimensional, we use the above second derivative allowing the shell to rotate into the direction in which the external field acts.

3. QM Interaction Energy for Validation

In order to validate the accuracy of PQEq and to perform optimization of the model (if needed), we must decide the criteria to use for comparison and optimization. The normal practice in most FFs is to use QM charges. We discuss in

Supplementary Materials that QM charges are not reliable for this purpose. Instead, we use the QM interaction energy. We probe each of the 30 molecules in our validation set with a pair of ±1 point charges separated by 1 Å to describe the interaction with dipole and higher order multipoles. For convenience, we refer to this pair of point charges as an electric dipole. The interaction energy from QM is shown as a function of distance and used as the reference energy.

We selected scan axes along a variety of symmetry directions to provide insight about how the polarization depends on the elements. Care was taken to avoid close contacts with the nearby atoms. Figure 2 shows an example for cyclohexane molecule of electric dipole scans along several different directions. These scans are performed towards a backbone atom (d1 and d2), along a bond (d3 and d4), perpendicular to a bond (d5), and toward the center of mass of the structure (d6). For all calculations, we use the standard B3LYP hybrid flavor of DFT, including both the generalized gradient approximation and a component of the exact Hartree–Fock (HF) exchange[175-179]. These calculations were performed with the 6-311G(d,p) (or 6-311G**++) basis set[180].

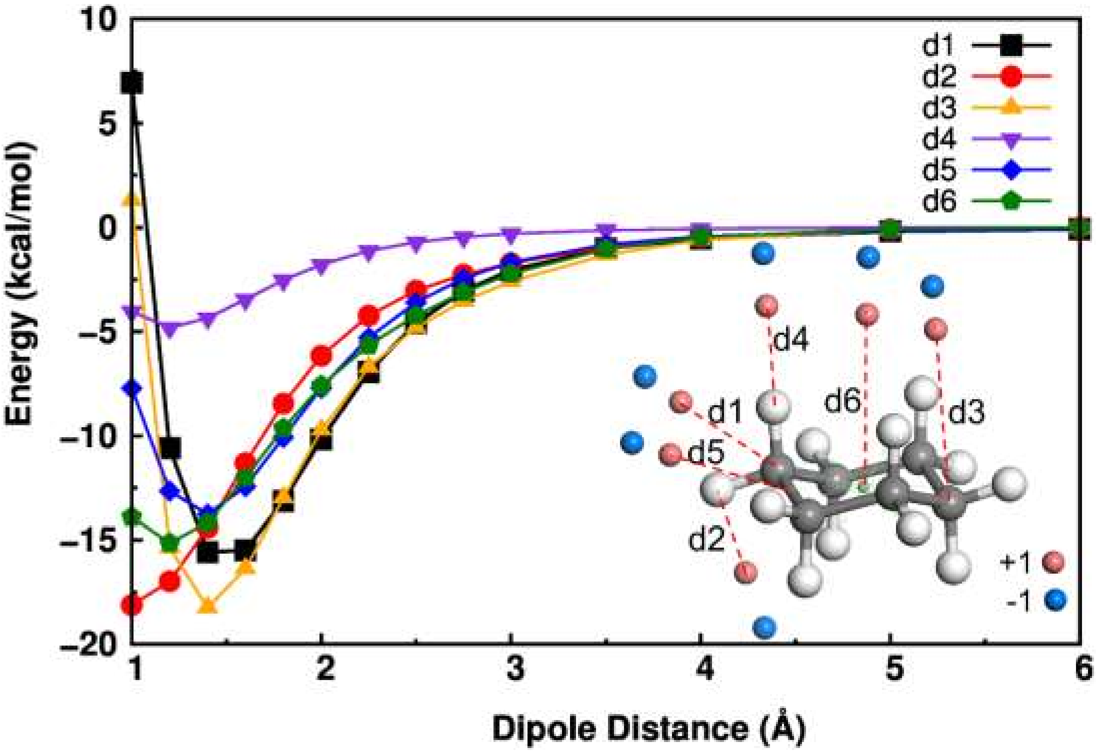

Figure 2: Interaction energies from bringing an electric dipole toward the cyclohexane molecule along various directions including: toward C and H atoms (d1 and d2), along a C-H bond (d3 and d4), perpendicular to a C-C bond (d5), and toward the center of mass (d6). The positive (red) and negative (blue) heads of the dipole form an angle of 180° (dotted line) with the reference point. The corresponding directions are labeled on the molecular configuration shown in the inset of the figure. Note that for most directions, the QM energies increase below 1.5 Å due to non-electrostatic effects.

4. PQEq Database

We used a set of 30 molecular structures in our validation of the PQEq model. We designed this data set to cover H, C, N, O, F, Si, P, S, and Cl elements in a balanced manner. These structures are depicted in Figure S3 of the Supplementary Materials. We use cyclohexane and benzene rings as the framework for these molecular structures, replacing C and H with the above atoms. This framework provides a reasonable number of atoms and bond types for studying charge transfer and polarization effects. The molecular structures are at their equilibrium geometries optimized using QM with same DFT method and basis set described above. Then, the electric dipole is scanned along various directions with respect to these molecular structures. The scan directions were selected after extensive preliminary calculations to probe properly the amount of polarization and electrostatic potential change during the scan. We excluded cases that resulted in less than 2 kcal/mol change in the energy throughout the scan. We also avoided scanning directions that could lead to very close interaction of the dipole with nearby atoms. In addition, to avoid non-electrostatic interactions arising from Pauli principle repulsion at close distances we scan only up to the inflection point (attractive forces) of the electrostatic potential curve. We find this distance to be near 2.5 Å for most of the cases so that the electric dipole is scanned from 10.0 Å up to 2.5 Å with respect to the reference point for all cases.

The above considerations resulted in a total of 68 scans for the above molecular structures. The change of QM electric dipole energy with the distance for each case is shown in Figure S4 of Appendix D.

5. Results

5.1 Parametrization of PQEq Model

In this paper, we present two sets of PQEq parameters. The first set (denoted as PQEq) uses the same χ, J, and R_{cs} parameters as in the QEq method[103] which were obtained from standard bond radii and experimental ionization energies. These are available for all elements of the periodic table up to Lawrencium (Lr) (atomic no.

=103). Using Equation 3, we derived the K_s values based on experimental or high quality *ab-initio* calculations of atomic polarizabilities in the presence of an external electric field. These values are available up to Nobelium (No) (atomic no. =102)[167]. The exception is for H atom where we use IP=11.02 eV and EA=1.96 eV to define χ and J as did Rappé and Goddard[103] and we take the K_s value for H from the Karasawa and Goddard calculation for the polarizability of Polyvinylidene-fluoride crystal that they fitted to a shell-model[138]. Our results in the next section show that this default PQEq parameter set, with no additional optimization predicts interaction energies from QM very well.

For the second series of parameters (PQEq1), we performed a constrained optimization of the atomic χ and J parameters with respect to the QM derived energy for all 68 cases. We used CG optimization to minimize the difference between the energies computed by PQEq1 and QM. The total error is defined as the weighted mean square error (MSE),

$$Error = \sum_i \omega_i \left(E_{QM} - E_{PQEq1} \right)^2, \tag{44}$$

where ω_i is the weight and E_{PQEq} and E_{QM} are the energies computed by PQEq1 and QM, respectively. Constraints were applied to ensure that the parameters obey the general trends of the periodic table. That is, we require that within a row of the periodic table the atoms should become more electronegative as we move to the right. Similarly, we require atoms become more electronegative as we move down a column in the periodic table. This was enforced at each step of the optimization. These constraints defend against overfitting and ensure better transferability of the final parameter set. We find the total error in Equation 44 to decrease from 1219.29 to 471.55 during the PQEq1 optimization. Thus for this class of systems the PQEq1 parameters should provide a more accurate description of the electrostatics. The changes in parameter values are generally small. The maximum change in the PQEq1 parameters is for Fluorine (F) atom, which led to a 19.96 percent change in the χ parameter. The comparison between the parameters before and after optimization is shown in Table S3 in the Supplementary Materials. The PQEq and PQEq1 parameters are tabulated in Table S1 and Table S2 in the Supplementary Materials, respectively. We also provide the electronic versions of these files.

5.2 Electric Dipole Energy

Figure 3 shows the comparison (one for each atom type) between the interaction energies computed by QM, PQEq, and PQEq1 for the scan of the electric dipole at different distances. Here, the interaction energy includes the polarization effect during the scan. The dipole scan directions are shown with the dotted lines on the molecular structure schematics for each case. Comparisons for additional cases are shown in Figure S4 of Appendix D.

Based on these results, we choose the effective shielding parameter in the Equation 10 to be λ=0.4628. This value is close to the corresponding number in QEq model (0.4913) using Slater-type orbitals[103]. The results show good agreement of PQEq with QM. This suggests that the PQEq general parameter set can accurately describe the electrostatic potential for a variety of molecular structures and environments. Thus, we expect good transferability of the PQEq model to new materials. This often has been a challenge for previous FFs and charge calculation models. As expected, the results from PQEq1 parameter set show better agreement with QM and may be useful for other systems contain similar structures as in our database. In particular, PQEq1 provides a dramatic improvement for molecules containing Fluorine element, as seen in Figure 3e

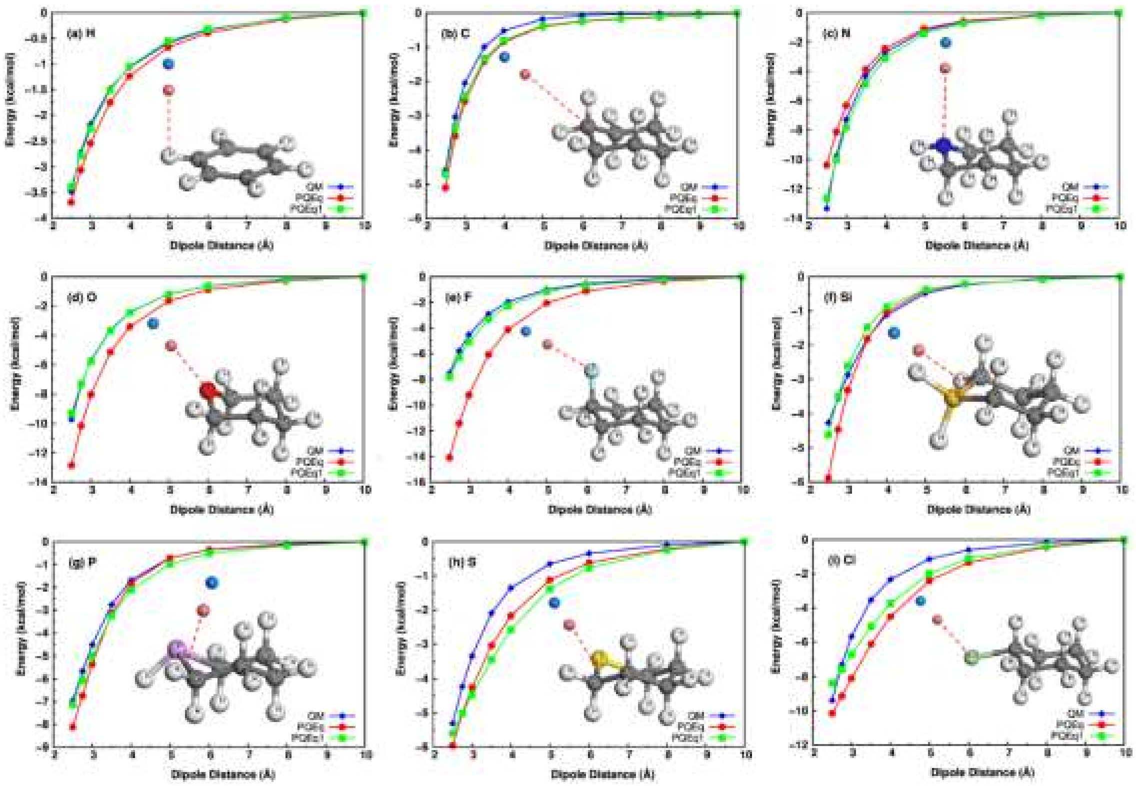

Figure 3: Interaction energies of an electric dipole near database molecular structures computed by QM (blue), PQEq (red), and PQEq1 (green). One case is presented for each atom type; (a) H, (b) C, (c) N, (d) O, (e) N and O, (e) F, (f) Si, (g) P, (h) S, and (i) Cl. The inset of each subfigure shows the molecular structure configuration with the scan direction (dotted line) of the electric dipole. The ±1 electric dipole is shown with small solid spheres. The positive (red) and negative (blue) heads of the dipole form an angle of 180° (dotted line) with the reference point.

5.3 Partial Charge Calculation

The energy comparison is the crucial criterion to test the accuracy of the PQEq model, but we are also concerned to determine if the computed charges are consistent with chemical intuition. This is particularly important for using PQEq partial atomic charges in the electrostatic potential term of FFs that have been developed with different charge model. We compute the partial atomic charges for all of the molecular structures using PQEq and PQEq1 parameter sets and compare them with ESP and MPA charges.

For the MPA and ESP charge calculations, we use several flavors of DFT including B3LYP[176], M06[181], and PBE[182] with several Gaussian basis sets including 6-311G, polarizable 6-311G**, polarizable and diffusive 6-311G**++ [180, 183-186]. The results for two selected cases are shown in Figure 4 and for additional cases in Figure S5 in the Appendix D. We find for all cases that the PQEq and PQEq1 charges are in the range of ESP and MPA charges. It is well known that ESP and MPA charges sometime lead to unintuitive charge assignments (see section 2 of the Appendix D), but we have not found such cases with PQEq and PQEq1.

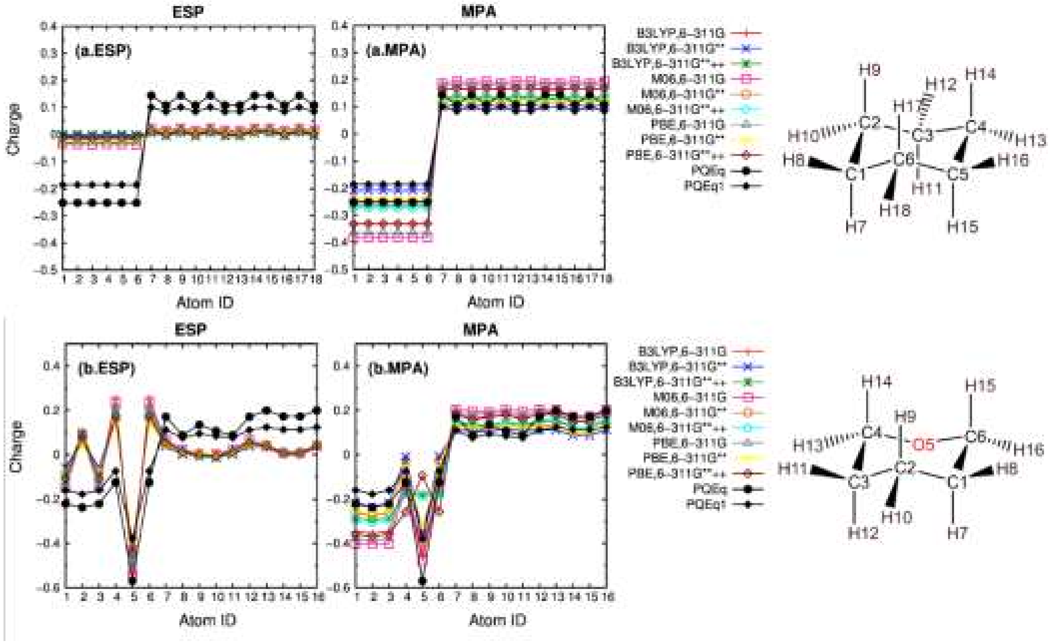

Figure 4: Partial charge comparison between QM (ESP and MPA), PQEq, and PQEq1 in (a) C_6H_{12}, (b) $C_5H_{10}O$ molecules. The ESP (left) and MPA (right) charges were computed using several basis sets and DFT functionals. The PQEq and PQEq1 charges are plotted in each figure for a better comparison. The position of each atom for the corresponding ID is shown on the molecular structure schematic on the right.

5.4 Charge Fluctuations and Shell Stability during High Temperature Dynamics

To test the stability of the PQEq model for MD/MM simulations, we examined the reactive MD simulations of the hexahydro-1,3,5-trinitro-1,3,5-s-triazine (RDX)[187] crystal at high temperatures using ReaxFF-lg[188] reactive force field. These calculations use the LAMMPS[173] MD simulation package with our implementation of the PQEq methodology. First, we minimized the total energy of the crystal (168 atoms) using the CG method. Then, we equilibrated this structure using the (*NVT*) ensemble at 50 K for 2ps. Then, we carried out MD-*NVT* simulations using a heating rate of 0.7 K/fs, during which the temperature increased from 50 to 3500 K. Finally, the structure was maintained at 3500 K for ~50 ps using MD-*NVT* simulations. See section 9 of the Appendix D for more details of the simulations. Under these conditions, bonds are broken with the fragments interacting to form new bonds. We consider this a good test case for PQEq. Indeed, we find that PQEq provides a stable description of the complex evolution of the dynamics as bonds break and rearrange. There are smooth changes of the temperature (T), potential energy (E_p), and electrostatic energy (E_{PQEq}) of the RDX crystal during the simulation (Figure S8 in Appendix D). We note that at 3500 K both E_p and E_{PQEq} decrease for several ps due to fast chemical reactions at this high temperature and then reach an equilibrium. We find that the atomic charges and shell positions fluctuate in response to the changes in the electrostatic environment as they were updated every time step. The changes with time of the charges and shell positions are shown in figure 5. The shell positions remain stable with respect to the core with up to 0.05 Å displacement from the core. This shows that the K_s values derived from the literature atomic polarizabilities are useful for simulation of these elements at high temperatures. The value of K_s should be tested for other elements prior to dynamics, particularly at high temperatures.

In addition, we performed a series of MD simulations to demonstrate the stability of PQEq during dynamics. For this purpose, we utilized MD-*NVT* simulations as above to heat the system from 50 to 3500 K and maintained the temperature at 3500 K for 5 ps. After this step, we performed a MD-*NVE* simulation for 20 ps. We observed reasonable dynamics throughout the simulation. One point that requires attention is the small drift in energy during the MD-*NVE* simulation, a known problem with the ReaxFF force field used here.

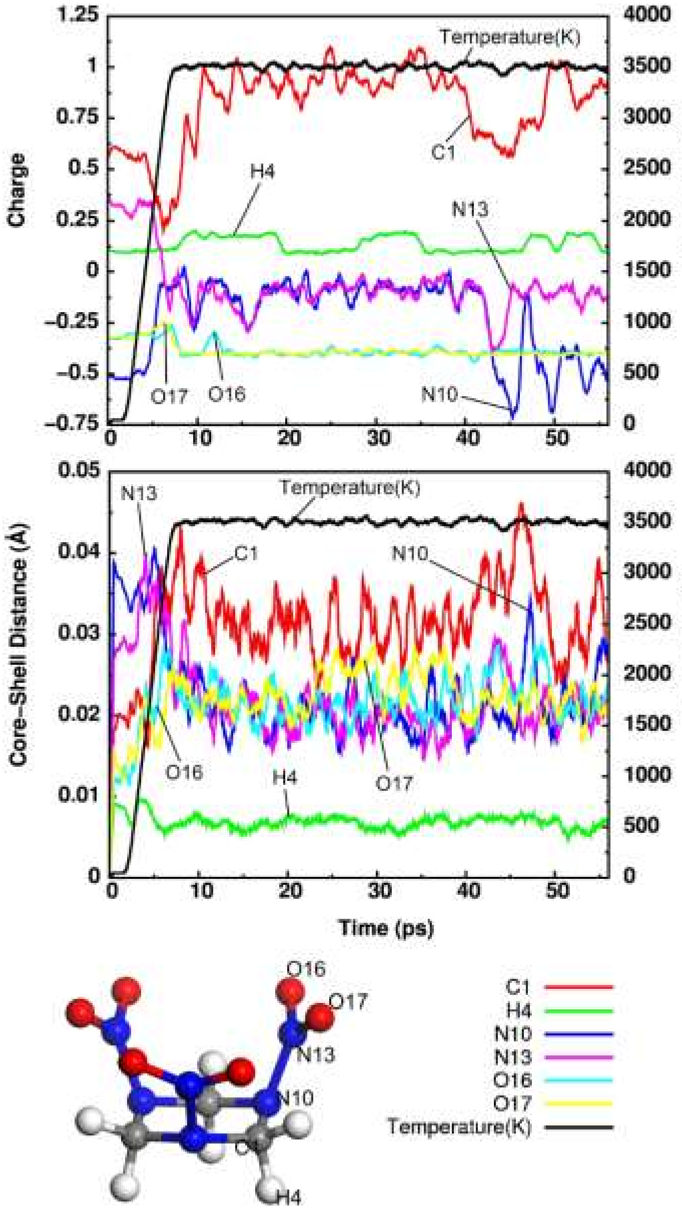

Figure 5: The variations of charge, core-shell distance, and temperature with time for selected atoms in the RDX crystal during the ReaxFF-*lg* MD simulations up to 3500 K. This core-shell distance is the distance of the atom’s shell from its own core. The

position of each atom in the figures is shown on the molecular structure of RDX.

6. Discussion

In this section, we compare the dipole interaction energies from QM, PQEq, and PQEq1 with the results from ESP, MPA, OPLS, AMBER, PQEq0, QEq, and QEq0. In this section:

PQEq0 refers to PQEq with the charges fixed prior to the introduction of the dipole. Here, some part of the polarization energy is included via the shell polarization.

QEq keeps the shell fixed to the core and equilibrates the charge as the dipole is scanned. Here, the charge updates capture part of the polarization energy.

QEq0 keeps the shell fixed to the core and the charges fixed prior to the introduction of the dipole. In this case no polarization is included.

For ESP, MPA, OPLS, and AMBER, PQEq0, and QEq0, we first compute the charges for each molecular structure in the absence of the electric dipole and then fix the charges to calculate the interaction energy at different distances of the electric dipole from the molecule.

The OPLS and AMBER FFs are often used for simulations of large organic and protein systems. These charges are fixed and assigned based on the type of the atoms and its bonding type. AMBER and CHARMM have standard charges for standard amino acids and nucleic acid bases, but for other molecules the charges are assigned from QM using MPA or ESP. Thus we also include the ESP and MPA charges computed using the B3LYP flavor of DFT and 6-311G** basis set. The results for six selected cases are shown in figure 6.

The importance of polarization is clearly shown in figures 6a-c where the scans are performed towards backbone C atom in cyclohexane (figure 6a), toward H atom and perpendicular to the benzene ring (figure 6b), and toward the C-Si bond middle point in a cyclohexane-based molecule (figure 6c). Here only PQEq, PQEq1, and QEq predict interaction energies in good agreement with QM. Fixed charge methods sometimes fail to predict the correct sign of the interaction energy as shown in 6a and 6c. For the remaining cases in Figure 6, the scans are performed towards N (figure 6d) and O (figure 6e) atoms in cyclohexane-based molecules and towards O (figure 6f) atom in the plane of nitrobenzene molecule. For these polar systems involving N and O atoms, the fixed charge models account for some of the polarization occurs along the bonds of polar to nonpolar atoms. We see here that PQEq1 does an excellent job of fitting QM, whereas PQEq is accurate for N but overestimates the polarization for O. This suggests that the reference polarizability for O may be too large.

We note here that QEq0 leads to an accuracy similar to the ESP or MPA obtained from QM. Thus for assigning fixed charges for use in MD, there is no longer a need to do QM, which can save considerable expense for applications such as virtual screening over millions of molecules or simulations on very large molecules.

In existing software codes, such as NAMD[189], CHARMM[190], and DESMOND[191], major changes would be needed to recalculate the charges along the MD trajectory . However, including just the shell polarization would be fairly simple to add to current software packages. This would allow the accuracy of PQEq0, which captures 21.8%, 55.6%, and 62.6% of the total polarization energies in figure 6a, 6b, and 6c, respectively. Therefore, PQEq0 could provide dramatically improved descriptions of the polarization in very large systems (the shell polarization requires only a one step update in shell position each iteration). However, some re-optimization of the force field parameters might be needed when PQEq methodology is used to replace the charge model in other force fields.

PQEq and PQEq0 should be particularly interesting for MD simulations of highly polarizable systems such as ferroelectrics and electrochemical systems with solvents and applied fields.

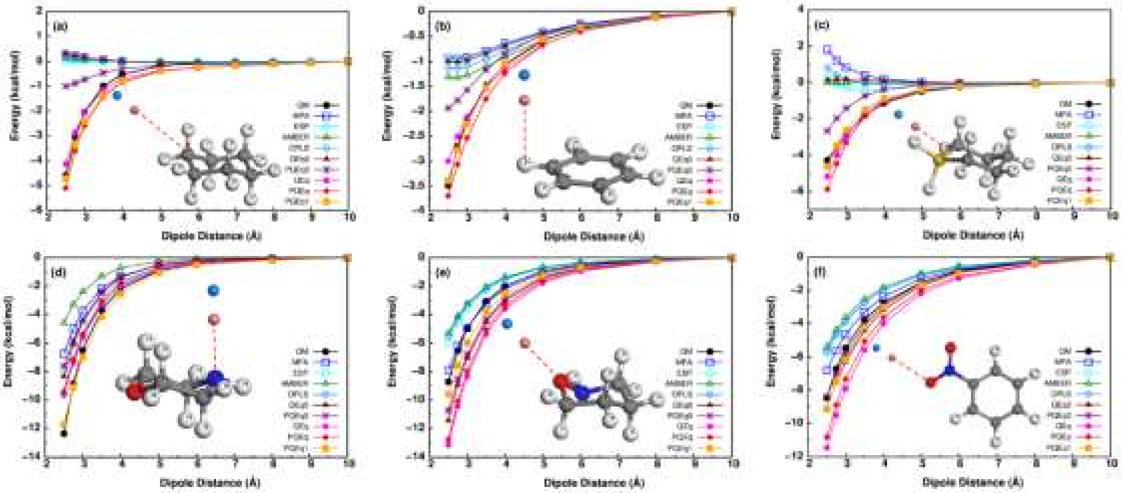

Figure 6: Interaction energies as an electric dipole is brought up to selected molecular structures computed by QM, PQEq, PQEq1, PQEq0, and QEq0, compared with the interactions from fixed charge models: ESP, MPA, OPLS, and AMBER. Here, PQEq0 refers to PQEq with the charges fixed prior to the introduction of the dipole. QEq keeps the shell fixed to the core and equilibrates the charge as the dipole is scanned. QEq0 keeps the shell fixed to the core and the charges fixed prior to the introduction of the dipole. The inset of each subfigure shows the molecular structure configuration with the scan direction (dotted line).

7. Conclusions

We show that the PQEq polarizable charge equilibration method provides accurate descriptions of the electrostatic interactions for MD simulations. This PQEq model uses atomic sized Gaussian shaped core and shell densities connected with an isotropic harmonic spring. The atomic parameters of PQEq are obtained from standard atomic ionization energies, standard covalent radii, and literature atomic polarizabilities, which we provide here up to Nobelium (atomic no. = 102). Thus, no parameters have been optimized.

We validated the accuracy of PQEq by comparing the electrostatic polarization energies as an electric dipole is brought up to the molecule for 30 molecules (68 cases) involving H, C, N, O, F, Si, P, S, and Cl atoms. We find that PQEq is in good agreement with QM. We also considered the PQEq1 model in which the atomic parameters (χ and J) are optimized against QM polarization energy. This led to improvements especially for Fluorine element.

We also presented the results for various fixed charge models: ESP, MPA, AMBER, OPLS, QEq0, and PQEq0. These methods are generally similar and much less accurate than the polarized models. However, we see that PQEq0 is capable of capturing significant parts of the polarization with just adjustments of the shell polarization while keeping the charges fixed. Thus, PQEq0 can offer significantly improved accuracy compared to other fixed charge models. We expect that PQEq and PQEq0 will be useful for many applications including ligand docking to proteins, catalytic reactions, electrocatalysis, ferroelectrics, fuel cells, lithium ion batteries, and the growth of ceramics and films.

Chapter III, Part 2

DEVELOPMENT OF PQEQ FOR PEO-LITFSI

With contributions from Saber Naserifar and Ali Kachmar

Introduction

Polarization effects can play an important role in highly charges ionic systems. Tradition force fields, however, used a fixed charge model which neglects the effect of polarization. There is a great interest, then, in the application of PQEq to PEO-LiTFSI improve the description of ionic diffusion in polymer electrolytes.

Although PQEq has been applied to provide a robust description of charges in organic materials[192], little study has been performed on salt and ion clusters. In this section, therefore, a set of PQEq-LiTFSI parameters are presented for use in polymer electrolytes.

PQEq-LiTFSI Parameter Set

An initial set of parameters for PQEq simulations of LiTFSI is shown in table S1.

Element	χ	J	R_{cs}	K_2
N	7.787	10.803	0.715	301.876
O	8.308	14.661	0.669	414.045
F	6.703	17.277	0.706	596.165
S	2.751	8.286	1.047	114.505
Li	1.900	14.530	0.759	11994.000
C	5.508	9.812	0.759	198.8405
H	4.725	15.573	0.371	2037.201

Table S1. PQEq parameters for the PQEq-LiTFSI parameter set. Energies are expressed in ($\frac{\text{kcal}}{\text{mol}}$) and lengths are expressed in Å.

Validation of Mulliken Charges

In order to understand the nature of PQEq- charges in a polymer structure, a representative PEO_{10}-LiTFSI cell was constructed an equilibrated using the OPLS2005 force field with lattice parameters of 10.53Åx10.53Åx10.53Å. A long timescale simulation was performed (600ps) using the CP2K program with the PBE functional and the DZVP-MOLOPT-ST-GTH basis set. The initial structure is shown in figure S1.

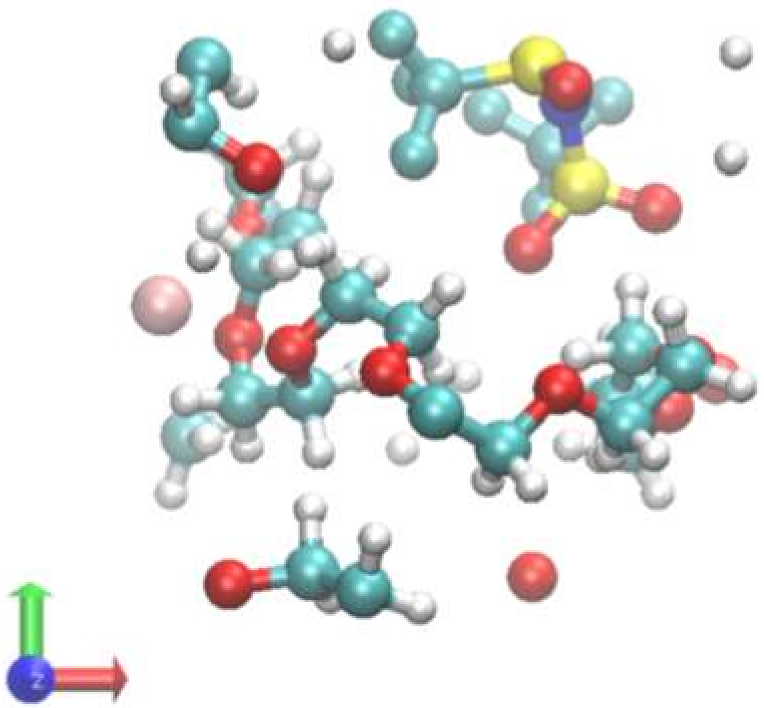

Figure S1. A representative PEO_{10}LiTFSI structure, with lithium shown in pink. A 600ps QM simulation was performed using this cell in order to understand the nature of charges in the polymer structure.

A comparison of Mulliken charges obtained from the QM simulation and PQEq-LiTFSI are shown in figure S2. The charges are shown to be in good agreement.

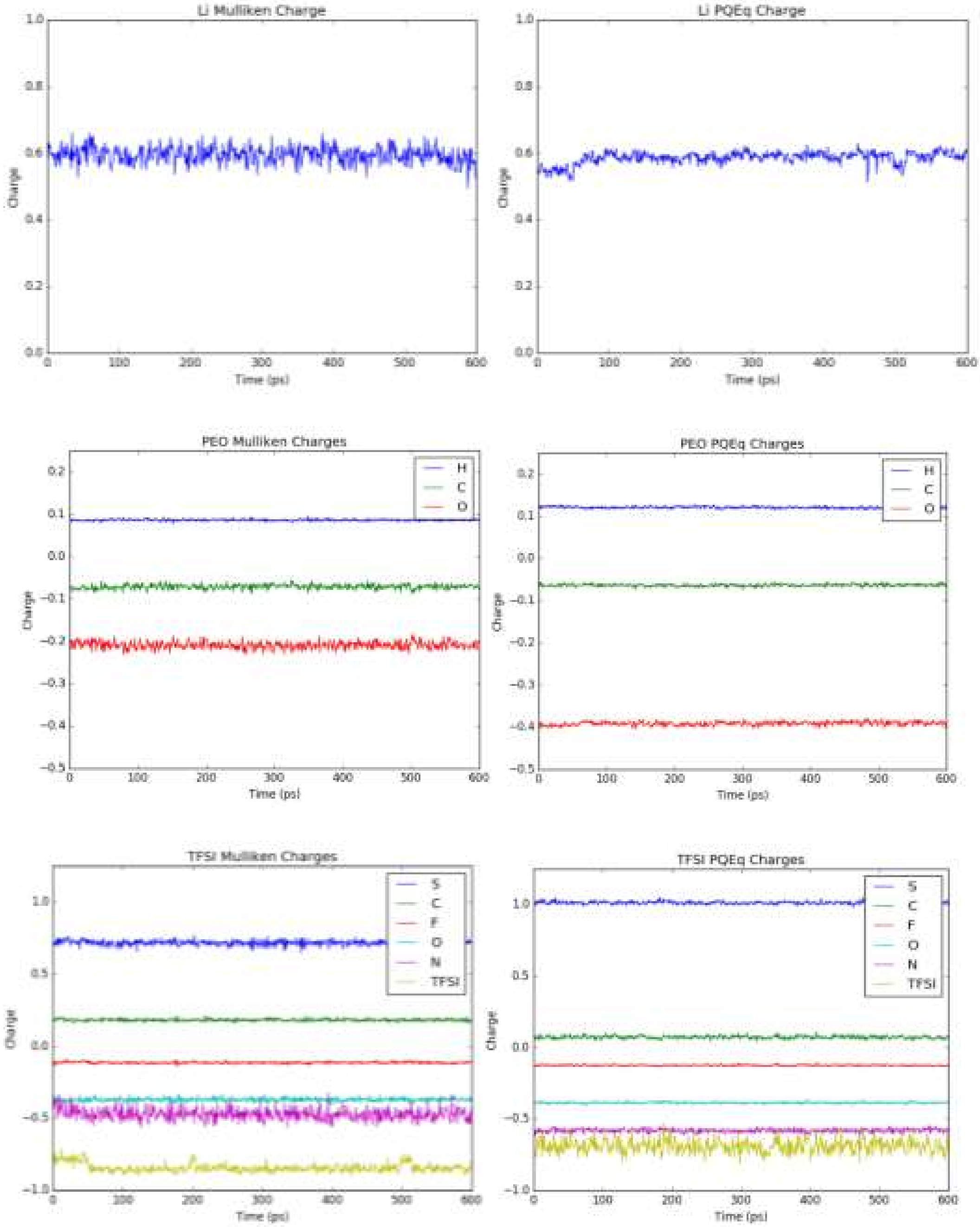

Figure S2. Mulliken charges (left) and PQEq-PEOLiTFSI charges (right) for lithium, PEO, and TFSI, respectively. The PQEq charges are shown to be in good agreement with QM.

Diffusion Simulations:

PQEq simulations of ionic diffusion were performed over a range of molecular weights, r=0.02, r=0.04, r=0.08. Bond, angle, torsion, and Lennard-Jones were taken from the OPLS2005 force field, with the addition of optimized Li-O Lennard-Jones parameters of σ_{Li-O}=2.3Å and ε_{Li-O}=0.06kcal/mol. The PQEq-LiTFSI model was used to replace the fixed charge description of electrostatics with an outer cutoff of 10Å. OPLS exclusions of (0.0, 0.0, 0.5) were used. Integration was performed at 480K with a Berendsen thermostat with time constant 0.1ps.

Additionally, it was found that a damping factor was necessary to control high frequency charge fluctuations on the lithium atoms. Charges at a timestep t are computed as a fraction, λ=0.001, of the computed charge q_c and a fraction (1- λ) of the previous charge q_{t-1}:

$$q_t = \lambda q_c + (1 - \lambda) q_{t-1} \tag{1}$$

Shell positions are updated using the same scheme:

$$\vec{r}_t = \lambda \vec{r}_c + (1 - \lambda) \vec{r}_{t-1} \tag{2}$$

This corresponds to a damping time of $t_{damp} = \frac{1}{\lambda}$ timesteps = 1ps. Using the diffusion relation, an effective damping length can be computed as $r_{damp} = \sqrt{6Dt_d} \sim 0.3$Å for lithium at 480K. Thus, the lithium charge damped over short timescales, while allowing charge updates over the longer timescales associated with updates in lithium sites. A full analysis of damped lithium motion for the PQEq and QEq models is provided in Appendix E.

The results from these diffusion simulations are shown in Figure S3:

PQEq Diffusion, r=0.02, N=100, T=480K

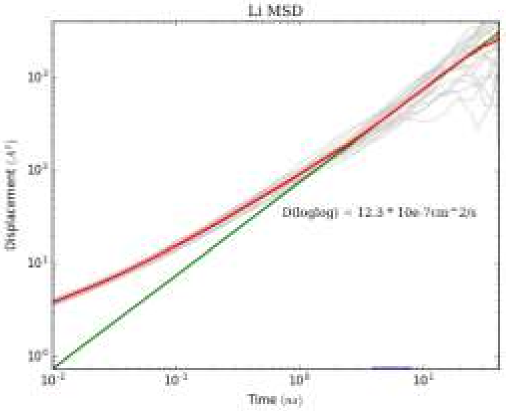

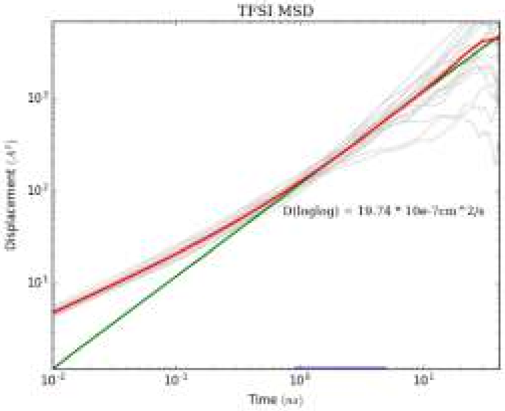

PQEq Diffusion, r=0.04, N=100, T=480K

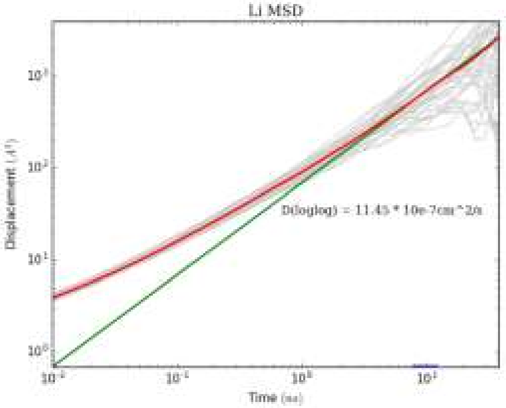

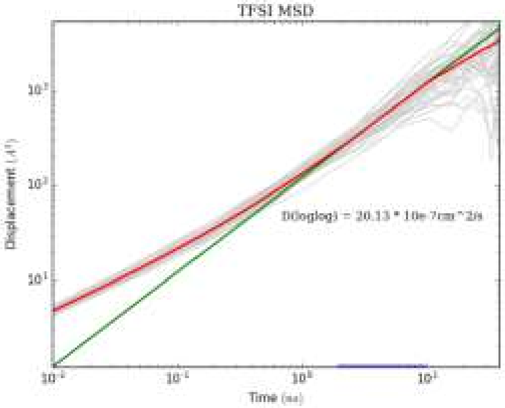

PQEq Diffusion, r=0.08, N=100, T=480K

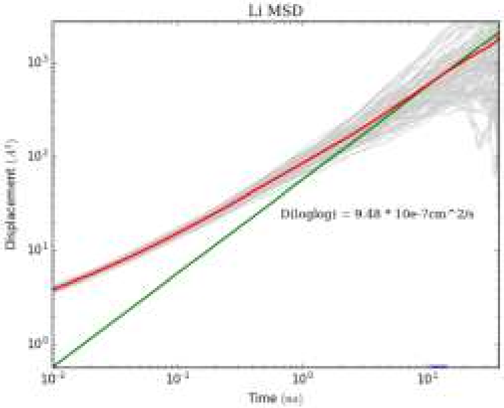

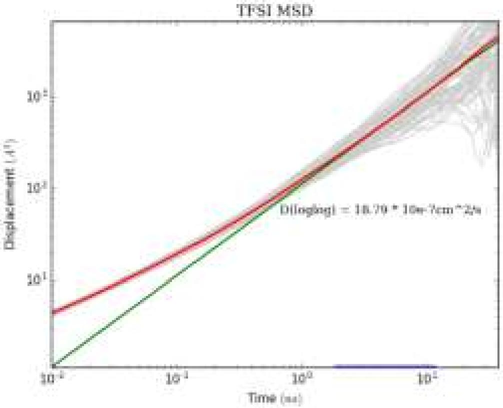

PQEq Diffusion, r=0.02, N=23, T=480K, t=29ns

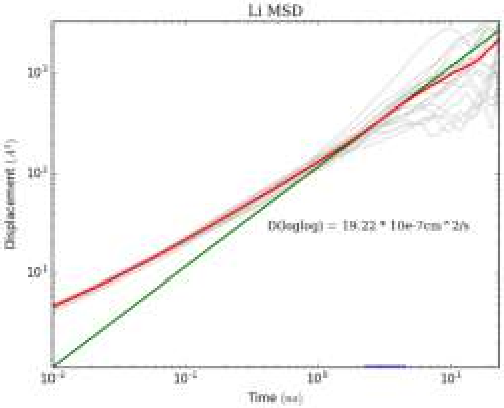

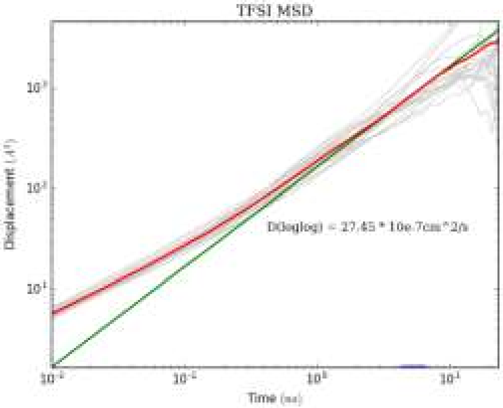

PQEq Diffusion as a function of molecular weight

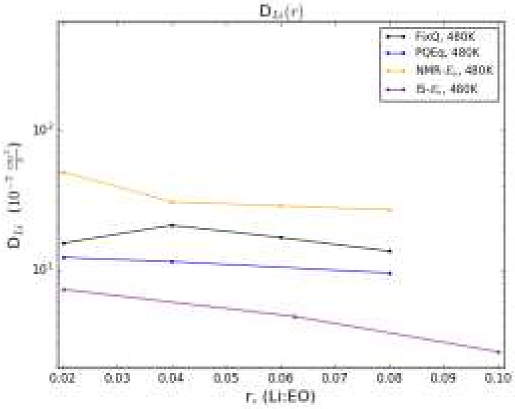

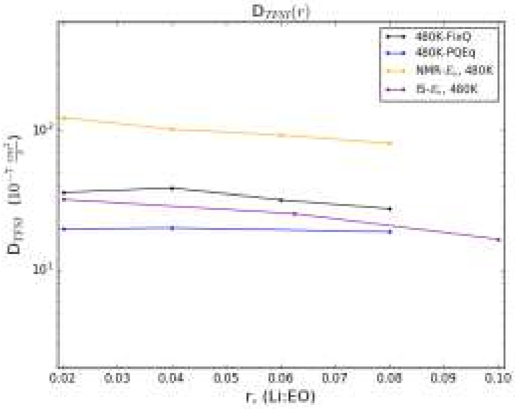

Figure S3. Diffusion coefficients obtained from fixed charge and PQEq simulations of diffusion at 480K. The PQEq method is shown describe the monotonic decrease in conductivity with concentration with the fixed charge model. A comparison with NMR and IS experiments is made assuming an activation energy of 0.38eV. A PQEq simulation run at low molecular weight, (N=29), yields a higher diffusion coefficient than N=100, in agreement with NMR data. Although initial results look promising, additional PQEq simulations are required at lower temperatures for a direct validation against experiment.

Conclusions and Future Prospects:

PQEq shows promise as a method for improving the description of electrostatics in simulations of ionic diffusion. Initial PQEq simulations show an improvement over the fixed charge model by predicting an monotonic decrease in the ionic diffusive coefficients with increasing molecular weight.

There is much future work to be completed with regards to PQEq. First, role of high-frequency charge fluctuations and the dependence of the damping factor on temperature must be explored. Second, as the cost of PQEq calculations limits them to higher temperatures, a robust method for comparing to experiment must developed. Third, the applicability of the PQEq description of electrostatics must be applied to a range of polymer systems and operating conditions.

Here, we have derived a set of PQEq parameters that produce Mulliken charges in reasonable agreement with QM and diffusion coefficient that better capture the trend in diffusivity with molecular weight. Much work remains, however, and we hope that this work will serve as a platform for future PQEq simulations of ionic diffusion in the search for better battery materials.

Appendix A

PULSED CHARGING SUPPORTING INFORMATION

Acknowledgement: The main part of this chapter is published in the Journal of Physical Chemistry Letters, 2014, 5(10), pp1721-1726.

Experimental Details

The cell separator was crafted from an acrylic plate by means of universal ILS9 laser cutter and interelectrode distance was precision-machined to 1/8”. Current collectors were machined from copper rod alloy 110 (1” dia.) with protrusion of compatible with separator depression for an effective sealing. The cathode current collector was threaded (1/32” dia.) for electrolyte injection. Ring gaskets (9/16” ID, 5/8” OD) were chopped out from silicone rubber sheet (McMaster-Carr, Plain Back, 0.02" thick). All cell components were washed with deionized water and isopropyl alcohol and dried under vacuum at 60°C for 48 hours and were transferred to argon-filled glovebox (H_2O, $O_2 < 0.5$ ppm).

Lithium foil (Aldrich, 99.9% on trace metal basis) 0.38 mm thick was punched (5/8” dia.) to be used as electrode. The counter lithium electrode was punched (1/32” dia.) in the middle for later electrolyte injection. Lithium oxide layers were scraped out via a sharp blade and dimethyl carbonate (DMC). The clean electrodes were flattened by being rolled via a glass tube. Both electrodes were intercalated in the separator. Wave disc springs (McMaster-Carr, high-carbon steel, 0.413" ID, 0.622" OD, 0.006" thick) were planted after electrodes to fill the possible gap in fabrication. Silicone rubber rings were laid between current collectors and separator to provide airtight sealing. The components were sandwiched with insulated screws. The electrolyte was injected into the cell afterwards and the hole was plugged through a small screw lined with Teflon tape.

Lithium perchlorate (Aldrich, battery grade, 99.99% trace metal basis) was dried for 24 hours in a vacuum oven at 100°C and dissolved in propylene carbonate (Aldrich, 99.7% Anhydrous) and 1 molar lithium perchlorate in propylene carbonate was synthesized through stoichiometric mixing to be used as electrolyte.

The demo cell was fabricated with representative electrodes and electrolyte and was cycled with the rate of 1mA/cm^2 and C/5, for 400 cycles inside the glovebox and for the most of the period, stable voltage regime was recorded without drying out the liquid electrolyte. The small voltage and current variations are attributed to lithium electrode surface reorganization to different morphologies.

Multiples cells were fabricated and subsequently charged with Bio-logic instruments (SP-50, VSP) and Neware battery tester (BTS-5V10mA, Shenzhen, China). The cells were flushed in perimeter via isopropyl alcohol after each experiment for dendrite measurements and various morphologies of dendrites were observed (Figure 1’).

Figure 1': Observed dendrites which reach the counter electrode and short the cell.

Modeling Details:

In order to describe the experimental conditions as faithfully as possible, the following assumptions were made:

I. We have assumed periodic boundary conditions (PBC) in x direction. Therefore, every Li^+ exiting the domain boundaries automatically enters the domain from the opposite side, i.e.,

$$if\ x > a \rightarrow x = x - a \qquad (1)$$

$$if\ x < 0 \rightarrow x = x + a \qquad (2)$$

where a is the length of the cell.

II. For mimicking the electrolyte concentration in the experiment, we set the number of free ions in the model such that the average interionic distances would be close. In the 1 M $LiClO_4$ in PC, the average interionic distance is 11.8 Å. Setting the same initial interionic distance for the model, we obtain the *maximum* number of free ions as (166.7/11.8 + 1)^2=229. As dendrites advance into the electrolyte, the free domain becomes smaller and, therefore, in order to preserve the average interionic distance the number of free ions should decrease as well. Accordingly, we chose such number at 50. As the ions diffuse independently, the results generated by the model are not sensitive to changes in the number of ions.

III. The absolute diffusion coefficient was scaled in order to maintain close transition times between experiments and our model. We define *maximum transition time* as the mean time it takes for ions to diffuse through the largest distance in the cell. The 1-dimensional diffusion distance is defined as:

$$\Delta x = \sqrt{2D\Delta t} \qquad \text{(E1')}$$

From Table 1, the modeling domain length is 167Å. Following the work of Mayers[19], taking D_{Li} as $1.4 * 10^{-14} \frac{m^2}{s}$ gives a maximum transition time as 9.9 ms. For the experiments, we first obtain the distance in the vicinity of the electrode the considerable variations in the concentrations occur[33]:

$$x_1 = \left(((9 * 64 * 8.85 * 10^{-12} * 3.175 * 10^{-3} * \frac{16}{(32 * 1.38 * 10^{-23} * 300 * 1000 * 6.022 * 10^{23})} \right)^{\frac{1}{3}} \cong 1.5\mu m$$

From this, we obtain an experimental maximum transition time across the electrical double layer of 4.36ms which is in the same order as the corresponding modeling parameter. In both experiment and theory, 1ms << maximum transition time << 20ms.

IV. About 2% of simulations shorted the counter electrode during simulations. In those cases, we stopped the run and analyzed the dendrite measurements from the obtained dendrite until then. The average number of attached atoms in those simulations was 540 (versus 600 in normal condition).

The dendritic growth during charge is the result of gradients in electrochemical potential parameters such as electrostatic field around the equipotential electrode surface, diffusion coefficient and mobility of solvent[63] as well as electrode surface morphology[11].

Let the position of each Li$^+$ at time t and t+Δt be $\vec{r_i}(t)$ and $\vec{r_i}(\mathrm{t} + \Delta\mathrm{t})$, respectively. During the interval Δt, Li$^+$ ions will perform random walks due to collisions with the solvent and/or migration under the applied electric field.

The value for the diffusion coefficient employed in the simulations corresponds to the measured current flow of lithium cations in propylene-carbonate based solutions[193] and its mobility is calculated from Einstein-Stokes equation (Table 1).

When a Li^+ ion comes within a distance d_{att} of a Li^0 on the surface or dendrite, it attaches to the structure. In this case, it is pushed a distance d_{att} from nearby Li^0 atoms becomes a Li^0 atom on the dendrite. We define the dendrite equipotential surface as points within a distance $r_{surface}$ of lithium atoms attached to the electrode. To ensure a smooth surface, $r_{surface}$ is taken to be slightly larger than the radius of a Lithium atom ($1.3r_0$) and is held at the same electric potential as dendrite. In the rare case where the Li^+ is still too close to an atom after n=50 pushes, it is returned to its position one time-step before it approached the Li^0. Every time a Li^+ is annihilated as Li^0 at the dendritic sites and lithium electrode surface, another lithium ion is added randomly in a thin layer at the top of the domain.

Although the experiments were done in galvanostatic condition, we observed a stable voltage regime mostly in the range of 3.5V and 4.5V. Therefore, we did the simulations based on an equivalent potentiostatic condition. Ee assign the boundary conditions as follows:

$$\Phi_{anode} = V_- \quad \text{(E2')}$$

$$\Phi_{cathode} = V_+ \quad \text{(E3')}$$

When the electrode is off, we have:

$$\Phi_{cathode} = \Phi_{anode}. \quad \text{(E4')}$$

Thus, there is no electrostatic field in the cell domain.

We assume the Solid Electrolyte Interphase (SEI) is composed of sufficient lithium metal atoms and that the dendrite can be considered an equipotential; therefore we have

$$\Phi_{dendrite} = V_{-}. \qquad \text{(E5')}$$

The Poisson equation describing the potential distribution Li$^+$ transport as follows[63]:

$$\frac{\partial^2 \Phi}{\partial x^2} + \frac{\partial^2 \Phi}{\partial y^2} = \frac{-e(z_c c_c - z_a c_a)}{\varepsilon_r \varepsilon_0}. \qquad \text{(E6')}$$

Φ is the potential, ε_0 and ε_r are the vacuum and relative electrolyte permittivity, z_c, z_a are cationic and anionic valence numbers, and C_c and C_a are cationic and anionic concentrations.

The following finite difference method was used:

1. Impose an arbitrary potential in any point in the inter-electrode space. The simplest case is uniform distribution from V_{-} to V_{+}.
2. Apply neighbor-based discrete Poisson relation to each point until the values in all space converge to a constant value or the errors between two subsequent iterations becomes smaller than the acceptable assigned voltage error.

The electrostatic field is numerically computed using the finite difference scheme:

$$\vec{E}_{i,j} = -\frac{\Phi_{i+1,j} - \Phi_{i-1,j}}{2\Delta x}\hat{x} - \frac{\Phi_{i,j+1} - \Phi_{i,j-1}}{2\Delta y}\hat{y}. \qquad \text{(E7')}$$

In addition to the observed ionic concentration gradients, the large electrostatic field that occurs near the dendrite tips contributes to increases lithium deposition rates and thus the propagation of dendrite growth[38].

Appendix B

PREDICTIVE SIMULATION OF NON-STEADY-STATE TRANSPORT OF GASES THROUGH A POLYMER MEMBRANE

With contributions from Marielle Soniat, Meron Tesfaye, Boris V. Merinov, William A. Goddard, III, Adam Z. Weber, and Frances Houle.

Acknowledgement: This chapter describes the molecular dynamics contribution to work published in *Polymer*, (2018), 134, pp125-142.

Abstract

A multiscale, physically-based, reaction-diffusion kinetics model is developed for non-steady-state transport of simple gases through a rubbery polymer. Experimental data from the literature, new measurements of non-steady-state permeation and a molecular dynamics simulation of a gas-polymer sticking probability for a typical system are used to construct and validate the model framework. Using no adjustable parameters, the model successfully reproduces time-dependent experimental data for two distinct systems: (1) O_2 quenching of a phosphorescent dye embedded in poly(n-butyl(amino) thionylphosphazene), and (2) O_2, N_2, CH_4, and CO_2 transport through poly(dimethyl siloxane). The calculations show that in the pre-steady-state regime, permeation is only correctly described if the sorbed gas concentration in the polymer is dynamically determined by the rise in pressure. The framework is used to predict selectivity targets for two applications involving rubbery membranes: CO_2 capture from air and blocking of methane cross-over in an aged solar fuels

device. This appendix describes molecular dynamics simulations which describe the adsorption process at the polymer-gas interface.

Methods – Molecular Dynamics

In most continuum models, gas uptake and desorption at the surface of a polymer membrane are considered to be instantaneous, with bulk transport being the controlling factor in permeation rate. However, to build a predictive model, it is necessary to use physically-derived rate constants for all processes. The dynamics of gas-rubbery polymer collisions are not well studied, so we have selected CO_2 among the gases used in this work, N_2, O_2, CH_4, and CO_2, for a thorough investigation of the uptake process using molecular dynamics (MD) simulations. All of the gases are weakly interacting with the polymers they permeate, so we assume that the sticking coefficient obtained from the study of CO_2 can be applied to all the gases studied in this work.

Simulations are performed using the Desmond MD simulation package[194-196] and the OPLS-2005 force field.[197] A time-step of 1 fs is used for short-range interactions and a 3 fs time-step is used for long-ranged interactions. Long-ranged electrostatics are computed using the Ewald summation. A short-ranged Coulomb cutoff of 9 Å is used. Center of mass motion is removed at each time step in the adsorption simulations.

The initial PDMS structure is generated using an extension of the protocol established in chapter II for PEO-LiTFSI. An initial low-density ($\rho = 0.0245$ kg/m^3) structure is created using an amorphous builder. This polymer structure has 25 chains of PDMS of 100-monomer length, for a total of 25,053 atoms. To ensure that there are no overlapping atoms in the structure, 100 steps of energy minimization and 10 ps of dynamics in the NVT ensemble[198] at 10 K are performed (using a time constant of 0.1 ps for the thermostat). The density of the structure is increased by running 500 ps of dynamics in the NPT ensemble using the algorithm of Martyna, Tobias, and Klein (MTK) with a 1 ps time constant for the barostat.[199] To ensure entanglement of the polymer chains, a Scaled Effective Solvent (SES)[200] equilibration step is performed in which long-ranged van der Waals and Coulomb interactions scaled to 20% of their original values, and dynamics are run for 2000 ps in the NVT ensemble with a Nosé-Hoover thermostat. Finally, with van der Waals and electrostatic interactions at their full strength, energy minimization is performed for 300 ps and the lattice parameters of the structure are again relaxed with 200 ps of NPT dynamics.

The above procedure results in a roughly 70-Å thick slab of PDMS created with dimensions of 6.79 × 6.79 × 6.79 nm^3. This procedure results in a bulk density of ≈0.985 kg/m^3, which is above the experimental reference value of 0.970 kg/m^3,[201] but below the experimental sample densities of 1.06 to 1.08 kg/m^3 obtained in this study (see Section II.C.). To create a PDMS surface, the length of the cell is increased by 200 Å in the x-direction to generate a region of empty space. All polymer chains are kept intact. The surface is then equilibrated for 3000 ps in the NVT ensemble using the Berendsen thermostat at 300 K. The density near the surface is reduced to ≈0.94 kg/m^3 due to surface roughness.

The surface is described using the method of Willard and Chandler[202]. Each polymer atom, at location $\vec{r}_i(t)$, is assigned a Gaussian shell with width of $d = 3.0$Å. This creates a "coarse-grained polymer density," $f(\vec{r})$, with units of Å^{-3},

$$f(\vec{r}) = \sum_{\vec{r}_i} \frac{1}{d^3(2\pi)^{3/2}} e^{\frac{-(\vec{r}-\vec{r}_i)^2}{2}}, \tag{45}$$

where this coarse-grained density reaches half its bulk value, f = 0.035, a surface is constructed on a 1-Å grid. The parameters for Gaussian width and grid fineness control the smoothness of the surface. Several combinations are tested to determine the sensitivity of sticking coefficient results to these parameters. The Willard and Chandler surface definition is selected over other commonly used methods, such as the “10-90” definition or the Gibbs dividing surface, because it provides information about the instantaneous, local interface. A change of ±0.01 in the f at which the surface is constructed results in a ≈1.2 Å shift in the surface. This magnitude of shift in the surface location has a minimal effect on the sticking coefficient. Since most desorbed molecules are far from the surface, the choice of surface region primarily affects the distinction between absorbed and adsorbed molecules. Thus, upper bound for the sticking coefficient, the fraction of absorbed and adsorbed molecules, is insensitive to the choice of surface.

The final, equilibrated structure and its instantaneous surface are shown in Figure 1.

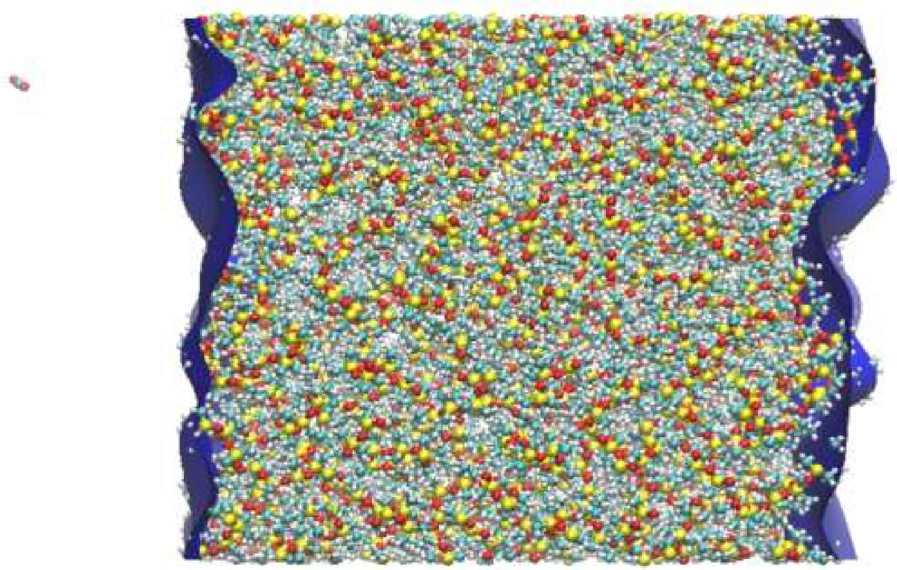

Figure 1: The structure of poly(dimethyl siloxane) (PDMS) in the molecular dynamics simulations. Hydrogen atoms are shown in white, carbon in light blue, oxygen in red and silicon in yellow. The instantaneous interface is shown in dark blue. The CO_2 molecule (upper left hand corner of the image) is sent towards the surface of the PDMS polymer structure for an adsorption simulation.

CO_2 absorption, adsorption, and desorption events are tracked using a procedure based on the molecular adsorption studies of Julin *et al*.[203, 204] A CO_2 molecule is introduced at a distance of approximately 15 Å from the surface and is assigned a velocity from the Maxwell-Boltzmann distribution at 300 K, with the constraint that the x-component of the velocity vector lies within a 45-degree cone normal to the surface. After 100 ps of NVE simulation, the outcome (adsorption, absorption, desorption) is recorded based on the position of the CO_2 molecule relative to the surface region, which is defined as points within 4 Å, i.e. twice the van der Waals radius, of the instantaneous surface. Justification of the 4-Å cutoff is given in the results section.

Results – Molecular Dynamics

Few data are available on sticking coefficients to of weakly interacting gases to PDMS or other rubbery polymers; therefore, we use molecular dynamics simulations to estimate reasonable values. We found that the sticking process is not kinetically limiting during construction of the permeation model for PDMS, similar to the finding for O_2 in C4PTP, so we have performed calculations for a single gas, CO_2, and assume that its sticking coefficient on PDMS is applicable to the other gases investigated. A series of 250 simulations of CO_2 impacts onto a PDMS surface was performed, and the results are shown in Figure 2 and summarized in Table 1. Some care must be taken in how the classification of type of event is interpreted: the distinction between an adsorbed and absorbed molecule is arbitrary, especially for atoms just below the interface, and the fate of molecules adsorbed on the surface is not clear from the finite simulation time. Thus, sticking in these simulations has a lower bound of 30%, equal to the fraction of absorbed molecules, and an upper bound of 50%, equal to the fraction of absorbed plus adsorbed molecules. The minimum sticking coefficient of 30% is used in the reaction-diffusion simulations for all gas molecules.

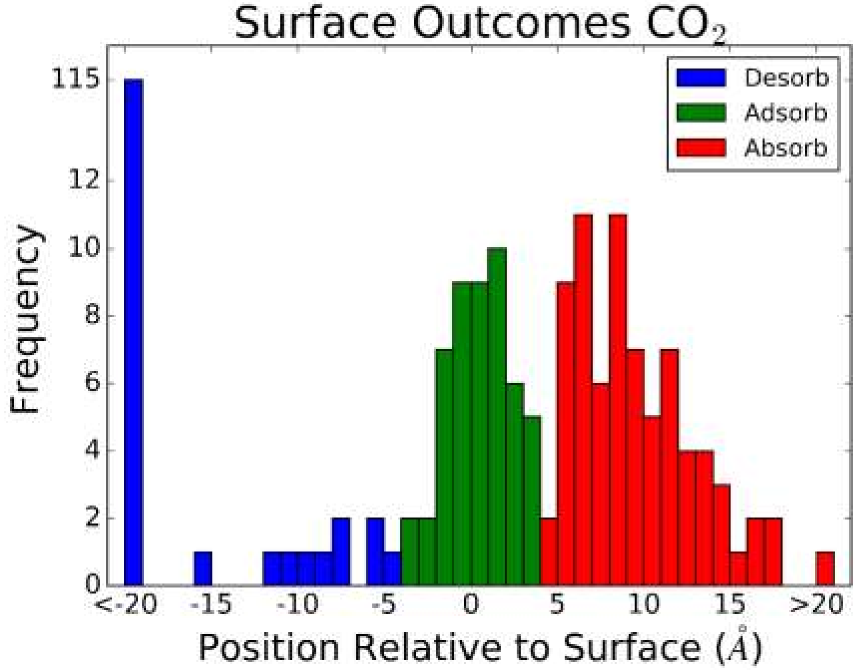
Surface Outcomes CO_2
Desorb
Adsorb
Absorb
Frequency
115
12
10
8
6
4
2
0
<-20
-15
-10
-5
0
5
10
15
>20
Position Relative to Surface (Å)

(a)

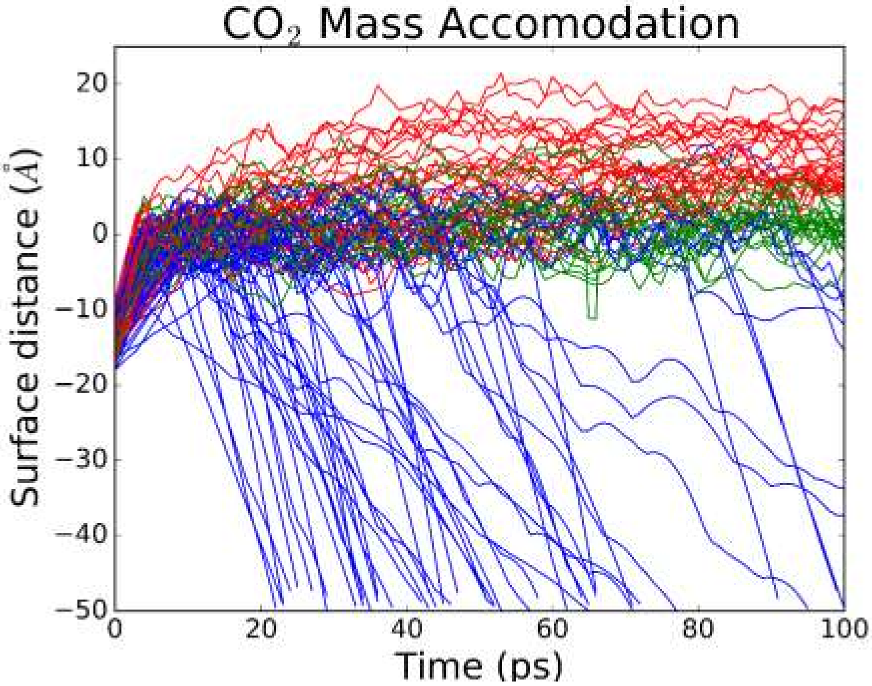
CO_2 Mass Accomodation
Surface distance (Å)
20
10
0
−10
−20
−30
−40
−50
0
20
40
60
80
100
Time (ps)

(b)

Figure 2: Results of molecular dynamics simulations for CO_2 sticking to PDMS. The surface is defined as position 0 with positive position indicating the region occupied by polymer and negative position indicating the empty region. Absorbed molecules are plotted in red, adsorbed molecules in green, and scattered and desorbed molecules in blue. (a) Histogram showing the distribution of outcomes from all 250 simulations. Note that the far left blue bar represents desorption in 115 simulations. (b) Distance from the final Willard surface as a function of time for 100 randomly selected trajectories.

Table 1: Results of molecular dynamics study of sticking of CO_2 to a PDMS surface.

Events	**Absorb**	**Adsorb**	**Desorb**	**Total**
Number	75	50	125	250
Percent	30	20	50	100

The most similar system that has been studied experimentally is the scattering of the O_2 gas from the surface of the hydrocarbons squalane and dodecane.[205] At incident energies of 8 kJ/mol, twice the average kinetic energy for gas molecules in this study, the oxygen molecules fully transfer their excess energy to the hydrocarbon surface,[205] indicating a sticking probability near 100%. A MD study of carbon dioxide[206] colliding with hydrocarbon self-assembled monolayers (SAMs) also shows a large sticking probability of ≈70% when the SAMs are terminated with $-CH_3$ or -OH functional groups. The sticking probability falls to ≈40% for SAMs terminated with $-CF_3$. The reason for such a high sticking probability is explained in a MD study of argon colliding with hydrocarbon SAMs terminated with $-CH_3$ and $-CF_3$. The SAMs terminated with $-CH_3$ are able to redistribute the energy of the incoming molecule on the same timescale as the impact of the atom with the surface by recruiting a large number of low-frequency (inter-chain) vibrational modes; the SAM's terminated with -CF_3 redistribute the energy more slowly along high-frequency (intra-chain) vibrational modes, resulting in a lower sticking probability.[207] PDMS contains a large number of low-frequency interactions, and so an energy transfer mechanism similar to -CH_3 terminated SAMs may apply. Thus, we conclude that a sticking probability of 30 to 50% is reasonable for a light, inert gas molecule at ambient temperature colliding with a flexible polymer surface. Further study of this type of system, and systems in which there are stronger interactions between the gas and the polymer, would be useful.

The absorption mechanism observed in the MD simulations involves CO_2 interacting with a gap between the polymer chains during a gas-surface collision or while transiently physisorbed, and passing directly into the polymer bulk. The simulations did not show that CO_2 has a strongly preferred adsorption site, i.e. atom type, on the PDMS surface. This is expected for gas-polymer combinations with weak interactions and supports our assumption that every surface atom is an available binding site in the reaction-diffusion simulations. If strong hydrogen bonding were possible, the surface area available for adsorption would be reduced.[208, 209] On the other hand, if roughness were significant the surface sites available would be greater than assumed. The MD simulations show that the ratio of the instantaneous surface area to the nominal surface area is 1.1, indicating that the actual rough surface area is only 10% greater than the ideally smooth surface assumed in the reaction-diffusion simulations.

Appendix C

SUPPLMENTARY MATERIAL – FIXED CHARGE MOLECULAR DYNAMICS SIMULATIONS

Determination Ionic Charges on LiTFSI

Although, the optimized potential for liquid simulations (OPLS2005) force field provides a robust description of organic liquids and polymer materials[156], care must be taken when considering ionic charges[210].

Simulations of ionic diffusion require charges less[99] than the purely ionic charge of ±1 in order to account for shielding effects. A series of ESP calculations on a representative PEO_4-LiTFSI structure at the B3LYP/6-31G** level of theory yielded ESP charges on lithium in the range of +0.60 to +0.70 due to charge transfer effects.

Thus, ionic charges ±0.7 were selected for use in the simulation. The TFSI charges were taken from ESP charges on an isolated $TFSI^-$ molecule, scaled by a factor of 0.7 in order to maintain a neutral system. Charges on the polymer were taken directly from the OPLS2005FF[97].

A list of charges used in the molecular dynamics simulations in figure S1.

PEO

Atom	FF
C	+0.14
H	-0.03
O	-0.40

Li$^+$

Atom	FF
Li	+0.70

TFSI$^-$

Atom	FF
O	-0.34
S	+0.61
N	-0.45
C	+0.22
F	-0.09

Figure S1: Molecular dynamics charges on PEO and LiTFSI. Polymer charges are from the OPLS2005 FF and LiTFSI charges are determined from ESP charges obtained from DFT calculations.

These charges are also in reasonable agreement with Mulliken charges and a set of charges later developed using the PQEq[192] method.

Experimental Measurements of Ionic Diffusion using Nuclear Magnetic Resonance (NMR) and Impedance Spectroscopy (IS)

Although the absolute diffusion coefficient obtained from polymer simulations are often systematically offset from experiment[210, 211], the relative diffusion coefficients are widely used for predicting physical trends[211]. In these simulations, the obtained ionic diffusion coefficients are systematically smaller than NMR measurements obtained by Balsara in a recent study[23] by roughly a factor of three. More recent impedance spectroscopy (IS), by Pożyczka[28], measurements yield ionic diffusivities, via the Nernst-Einstein equation and transference number, roughly 5 times lower than those measured by Balsara. A comparison of these measurements is shown in figure S2.

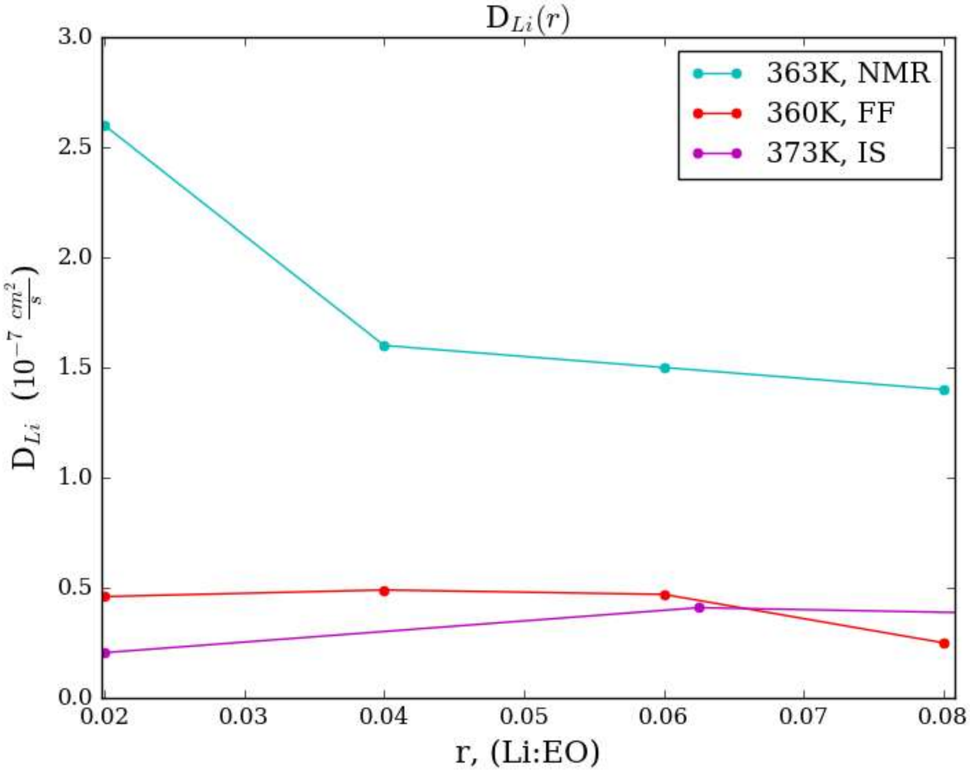

Figure S2: Diffusion coefficient obtained from NMR measurements (teal) and impedance spectroscopy measurements (purple) are shown to differ by a factor of 5.18 at T=360K,r=0.02. The data obtained from this force field (red) lies within the experimental range.

A number of factors could account for the differences in the diffusion coefficient, most notably assumption about the number of charge carriers present in solution[23]. Overall, however, the relative diffusion coefficients obtained with all three methods are shown to be in good agreement. Interestingly, a peak in ionic conductivity is observed near r=0.06

Li:EO in both the work of Pożyczka and at higher temperatures in the molecular dynamics simulations. The significance of this peak is discussed in the main text.

Equilibration Procedure for Polymer Cells

As polymer structures are fundamentally amorphous structures, care must be taken to ensure that the polymer chains have been provided sufficient time to relax into an equilibrium structure. Here, each structure is equilibrated using a standard procedure[212] based on the Scaled-Effective-Solvent method[98, 212], which allows polymer allows for the rapid relaxation of polymer chains. The steps in the initial equilibration procedure are as follows:

1. Construct a PEO-Li-TFSI structure at 60% of the experimental density in an amorphous builder
2. Minimize for 300 steps to prevent interchain clashes
3. Run NVT at 10K for 20ps
4. Run NPT at 300K for 200ps to equilibrate the lattice parameters of the cell
5. Minimize for 300 steps, again, to prevent interchain clashes
6. 500ps of NVT at 300K with non-bond (Coulomb, van der Waals) interactions scaled down to 20% of their original value (f=.2) to allow the polymer chains to rapidly relax
7. Minimize for 300 steps, again to prevent interchain clashes

8. Run NPT at 300K for 100ps to re-equilibrate the lattice parameters at 300K

The equilibrated structure from step 8 is then used as the initial structure for simulations at 360K, 400K, 440K, and 480K. To account for the higher temperature, two additional steps of equilibration are performed.

9. Run 1ns of NPT at the target temperature to equilibrate lattice parameters

10. Run 10ns of NVT at the target temperature to equilibrate polymer

After the equilibration process is completed, a production simulation is run for 115-400ns.

The polymer cells created via this procedure were shown to be well equilibrated for molecular dynamics simulation, and are both in experimental density range[23]{Gorecki, 1995 #106;Mao, 2000 #70} for r=0.02/N=100 at 360K of 1.125$\frac{g}{cm^3}$ and provide a good description of the Li-O radial distribution function[1]. Further discussion is available in the main text.

1. Mean-Squared-Displacement Plots for All Simulations

The mean-squared displacement plots for all simulations are shown below. The mean-squared-displacement (in units of Å^2) is defined as the average squared displacement of the center of mass of the ion over all points in the trajectory separated by the corresponding time (in ns). The MSD curves for individual ions are shown as grey lines and the average of the collection of ions is shown as a red curve. The Fickian regime of the MSD is identified as largest continuous group of times where the loglog slope is with 0.1 units of 1.0. To ensure a robust fit, if the Fickian regime (shown in blue) is less than 10% of the totally trajectory length, it is evenly extended to 10% of the trajectory in the ±t directions. This method yielded results in agreement with other fitting schemes, such as apparent diffusion coefficient[211], while ensuring that diffusion coefficients are obtained from truly Fickian diffusion.

Figure S3 (below): Diffusion coefficients for all molecular dynamics simulations as a function of temperature, molecular weight and ionic concentration.

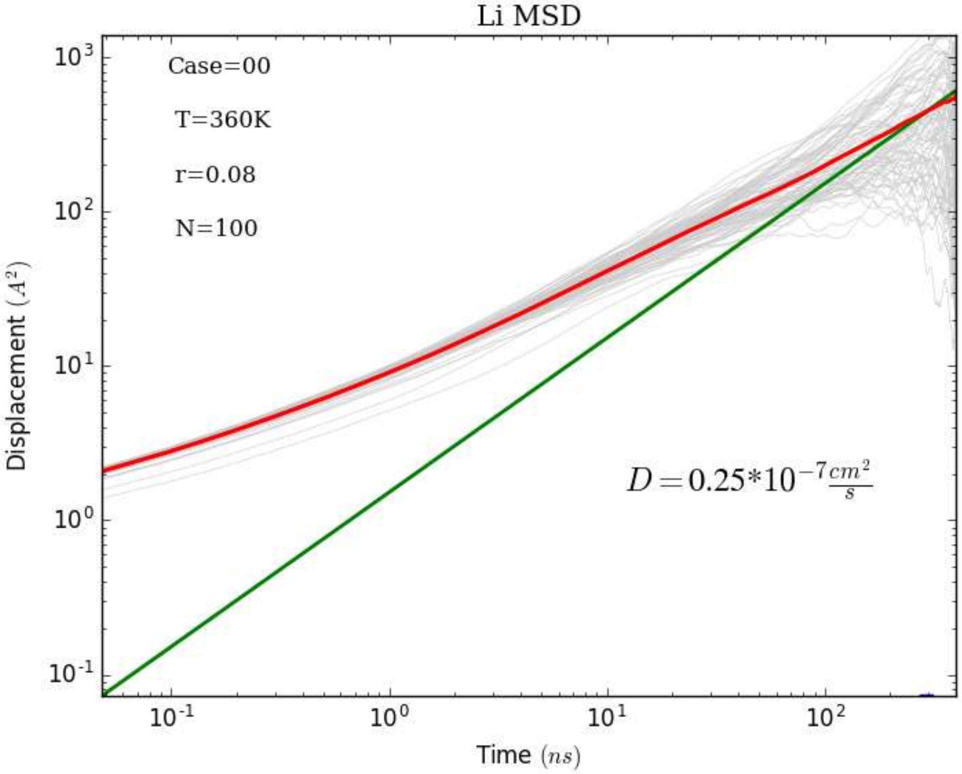
Li MSD
Case=00
T=360K
r=0.08
N=100
$D = 0.25*10^{-7}\frac{cm^2}{s}$
Displacement (A^2)
Time (ns)
10^{-1}
10^{0}
10^{1}
10^{2}
10^{3}

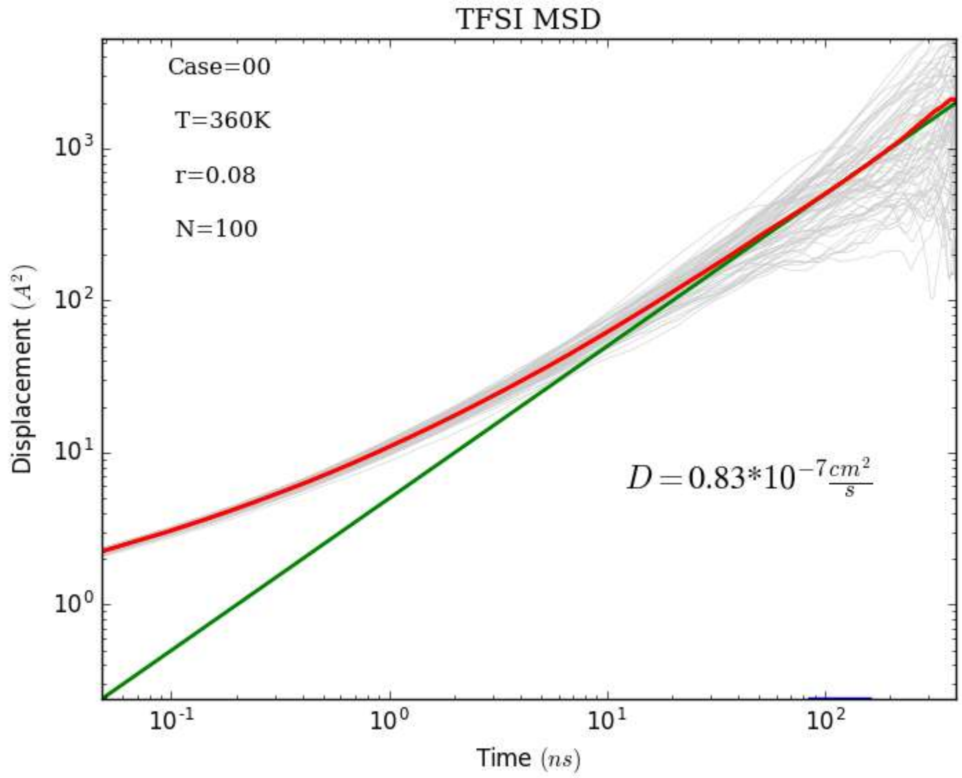
TFSI MSD
Case=00
T=360K
r=0.08
N=100
$D = 0.83*10^{-7}\frac{cm^2}{s}$
Displacement (A^2)
Time (ns)
10^{-1}
10^{0}
10^{1}
10^{2}
10^{3}

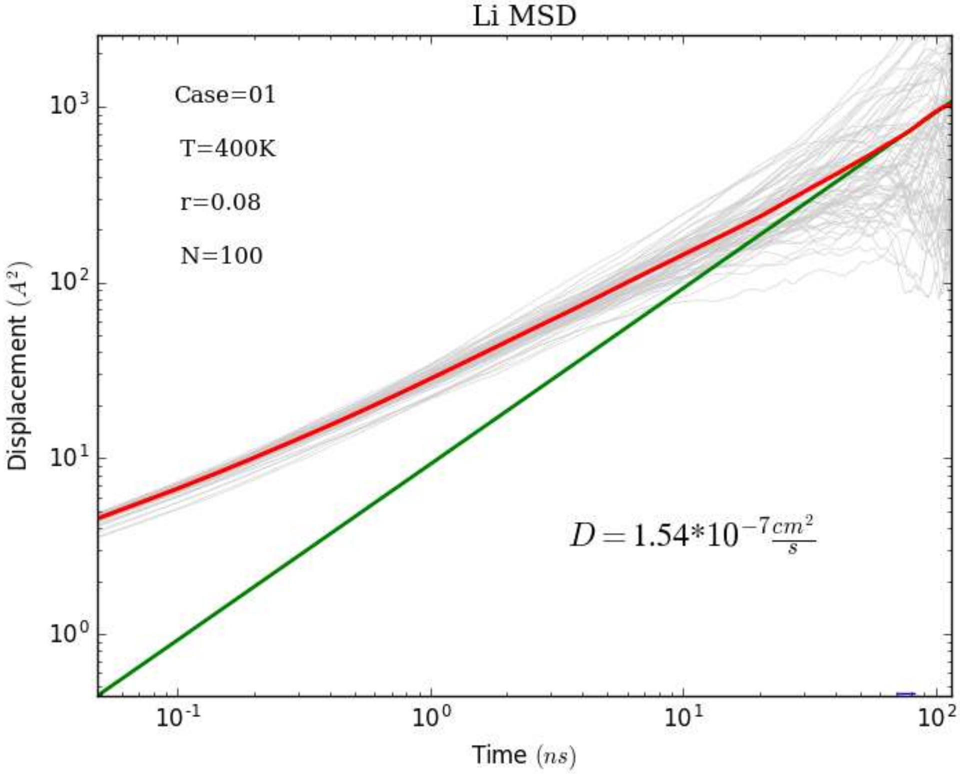
Li MSD
Case=01
T=400K
r=0.08
N=100
$D = 1.54*10^{-7}\frac{cm^2}{s}$
Displacement (A^2)
10^0
10^1
10^2
10^3
Time (ns)
10^{-1}
10^0
10^1
10^2

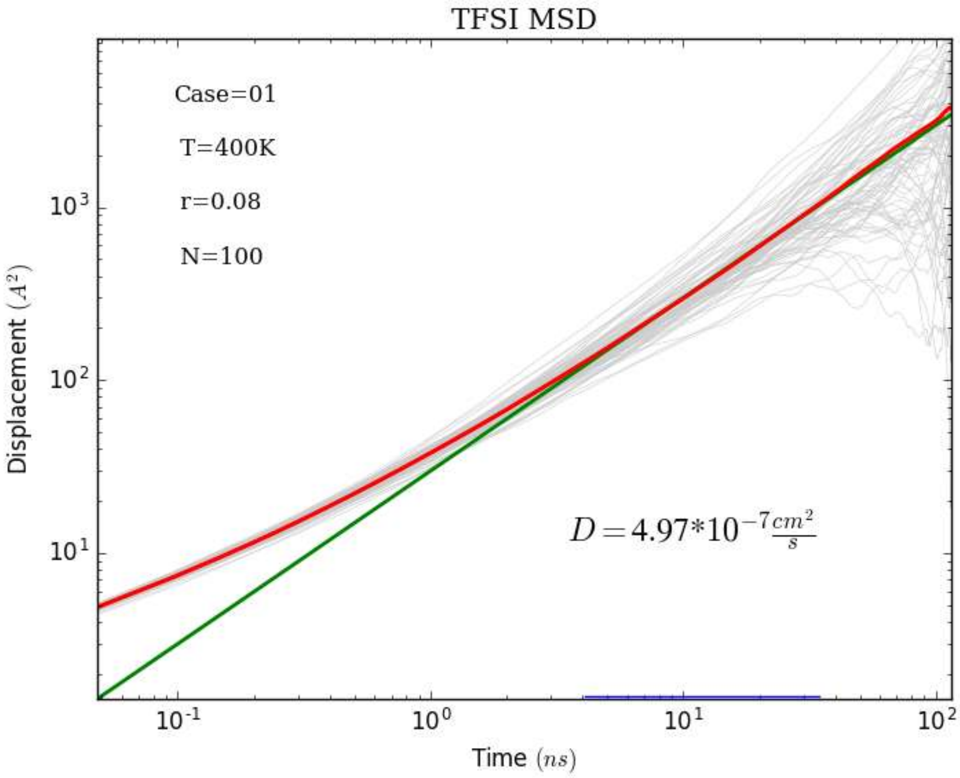
TFSI MSD
Case=01
T=400K
r=0.08
N=100
$D = 4.97*10^{-7}\frac{cm^2}{s}$
Displacement (A^2)
10^1
10^2
10^3
Time (ns)
10^{-1}
10^0
10^1
10^2

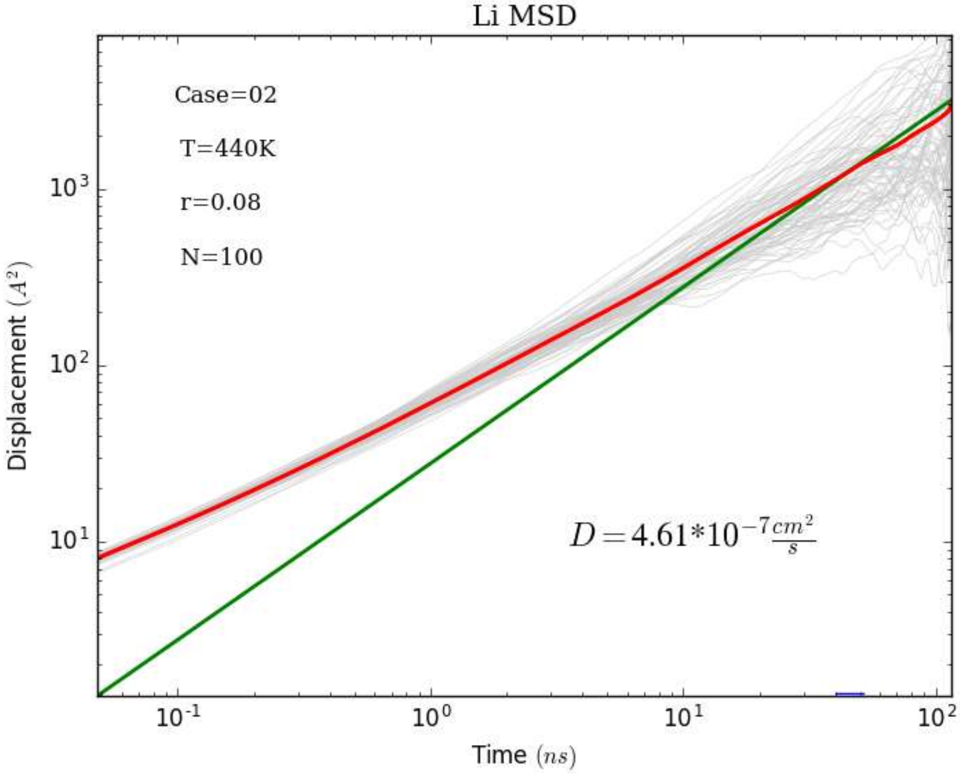
Li MSD

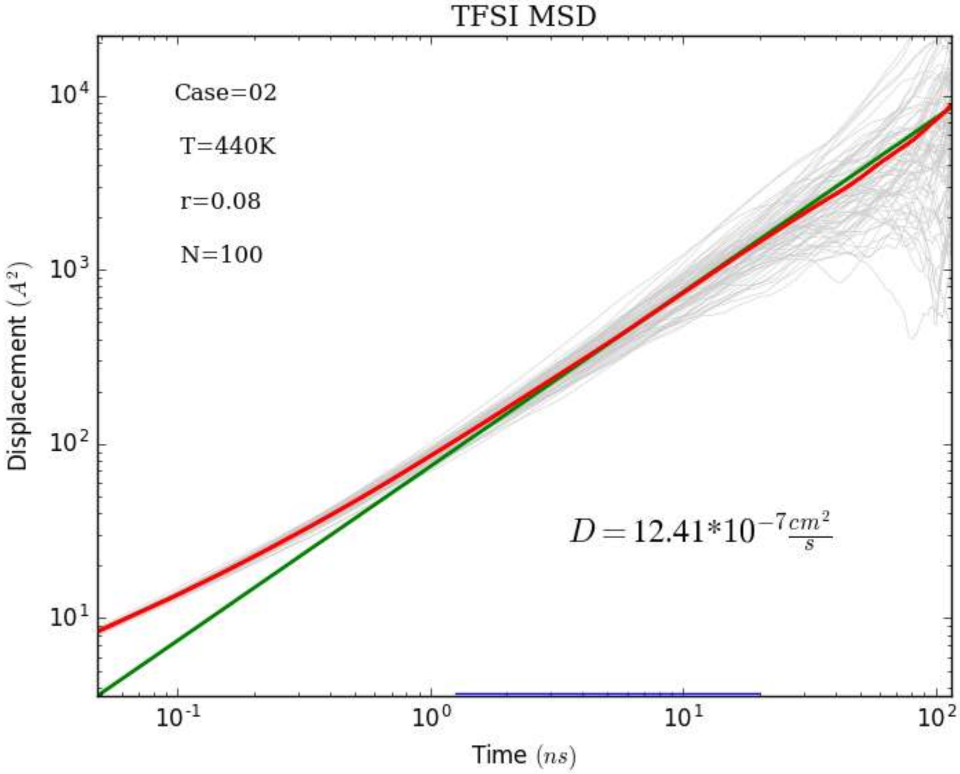
TFSI MSD

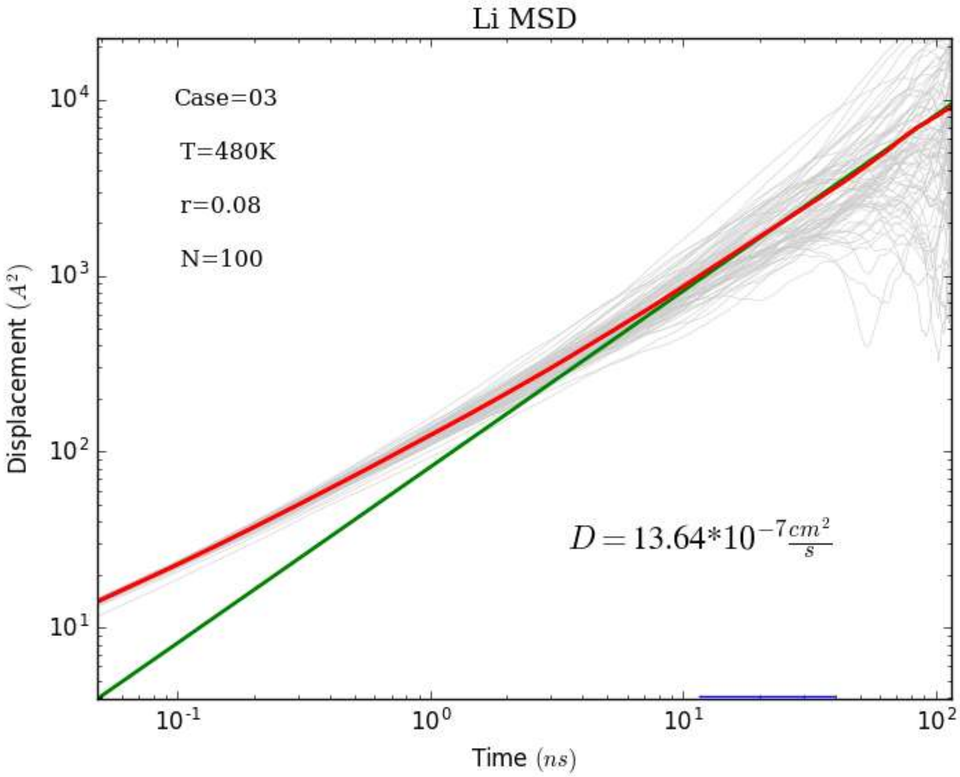
Li MSD
Case=03
T=480K
r=0.08
N=100
$D = 13.64*10^{-7}\frac{cm^2}{s}$
Displacement (A^2)
Time (ns)
10^1
10^2
10^3
10^4
10^{-1}
10^0
10^1
10^2

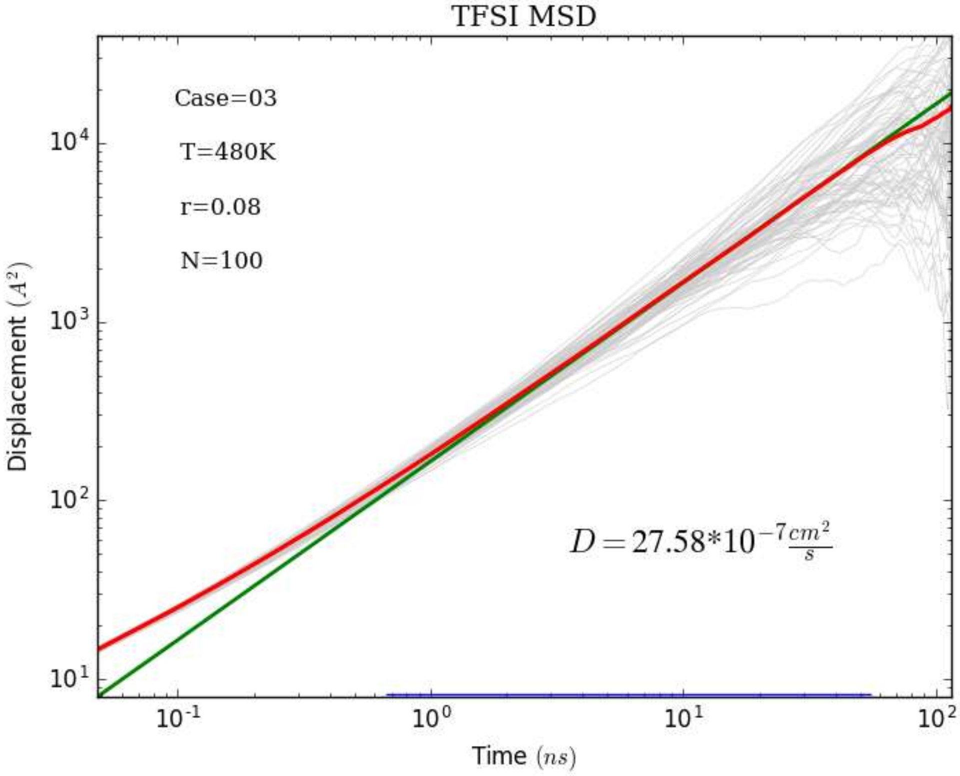
TFSI MSD
Case=03
T=480K
r=0.08
N=100
$D = 27.58*10^{-7}\frac{cm^2}{s}$
Displacement (A^2)
Time (ns)
10^1
10^2
10^3
10^4
10^{-1}
10^0
10^1
10^2

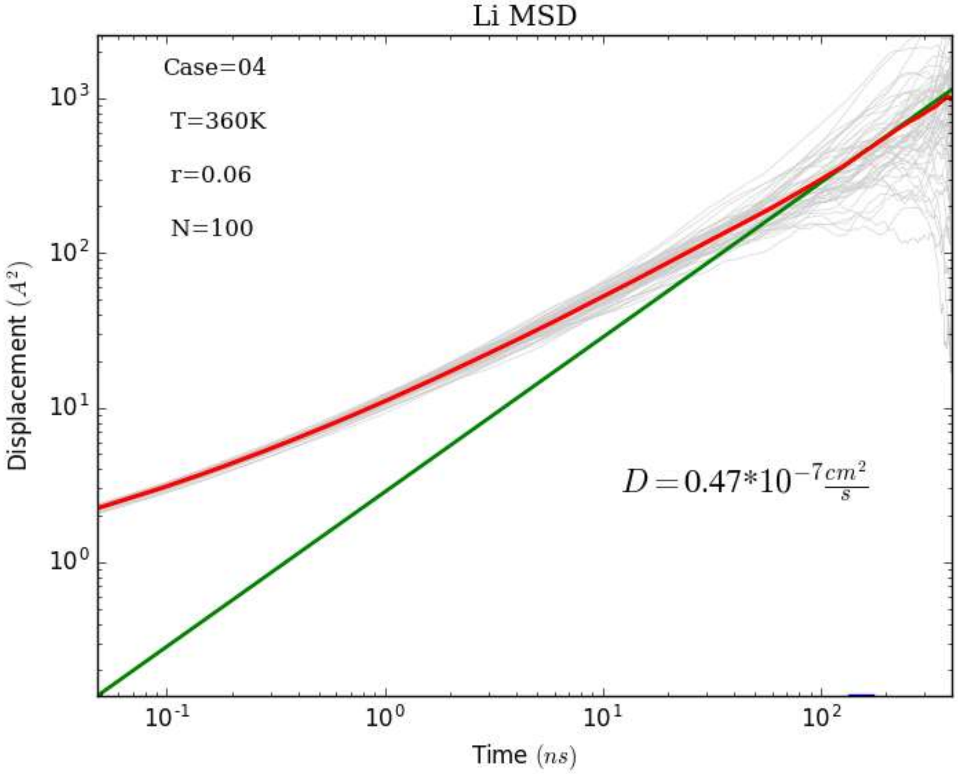
Li MSD
Case=04
T=360K
r=0.06
N=100
$D = 0.47 * 10^{-7} \frac{cm^2}{s}$
Displacement (A^2)
Time (ns)
10^3
10^2
10^1
10^0
10^{-1}
10^0
10^1
10^2

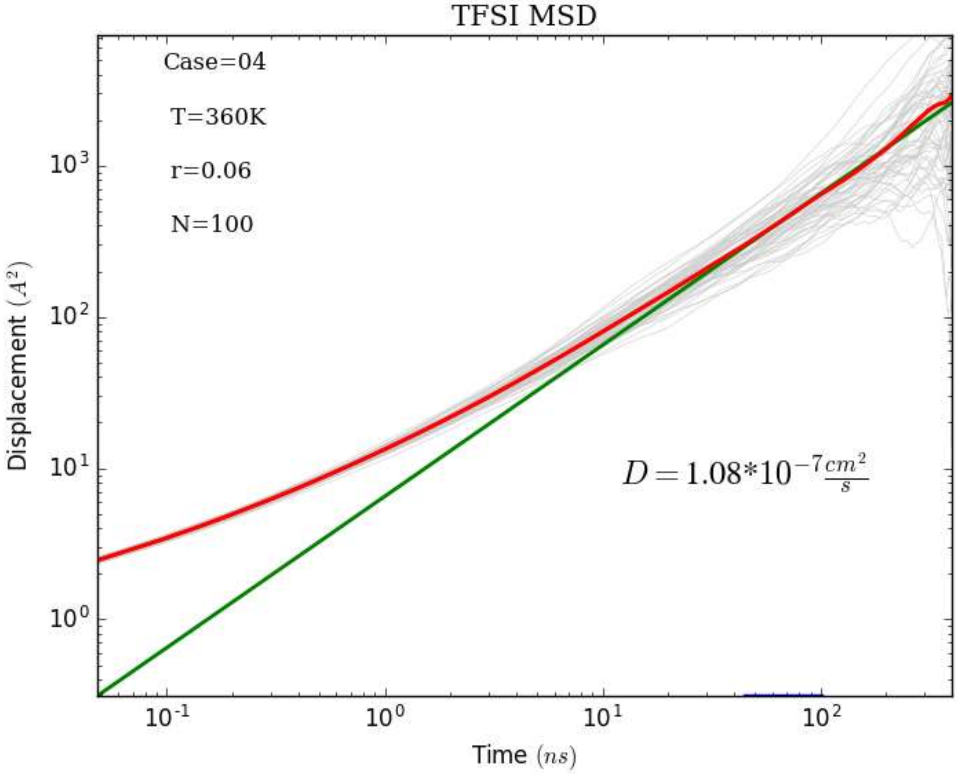
TFSI MSD
Case=04
T=360K
r=0.06
N=100
$D = 1.08 * 10^{-7} \frac{cm^2}{s}$
Displacement (A^2)
Time (ns)
10^3
10^2
10^1
10^0
10^{-1}
10^0
10^1
10^2

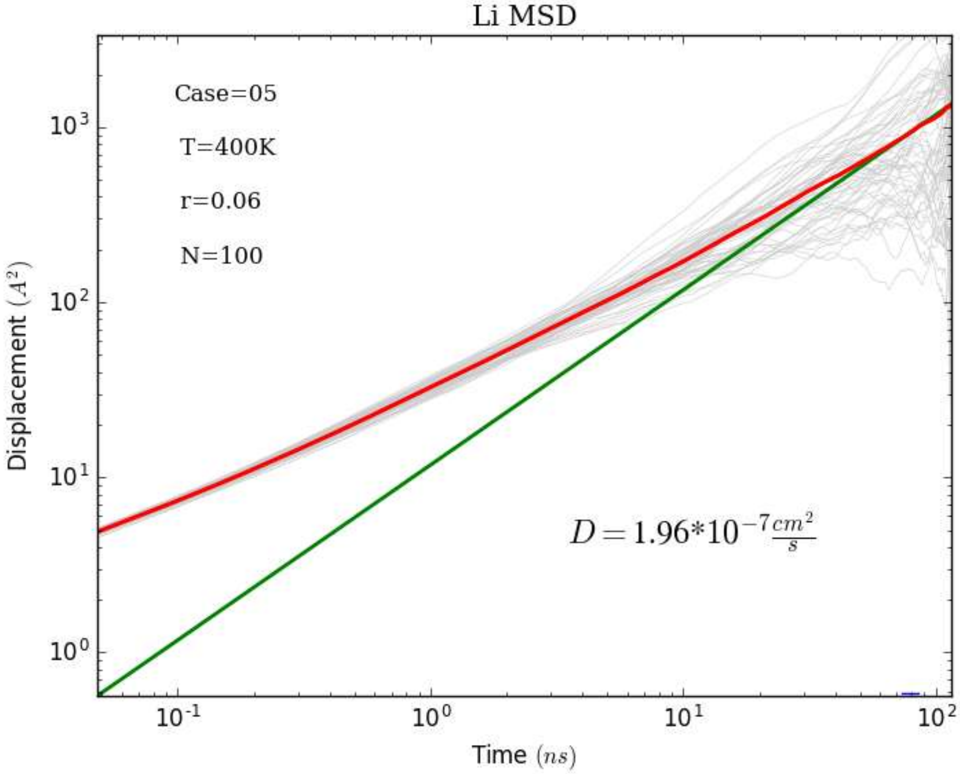
Li MSD
Case=05
T=400K
r=0.06
N=100
$D = 1.96*10^{-7}\frac{cm^2}{s}$
Displacement (A^2)
10^0
10^1
10^2
10^3
Time (ns)
10^{-1}
10^0
10^1
10^2

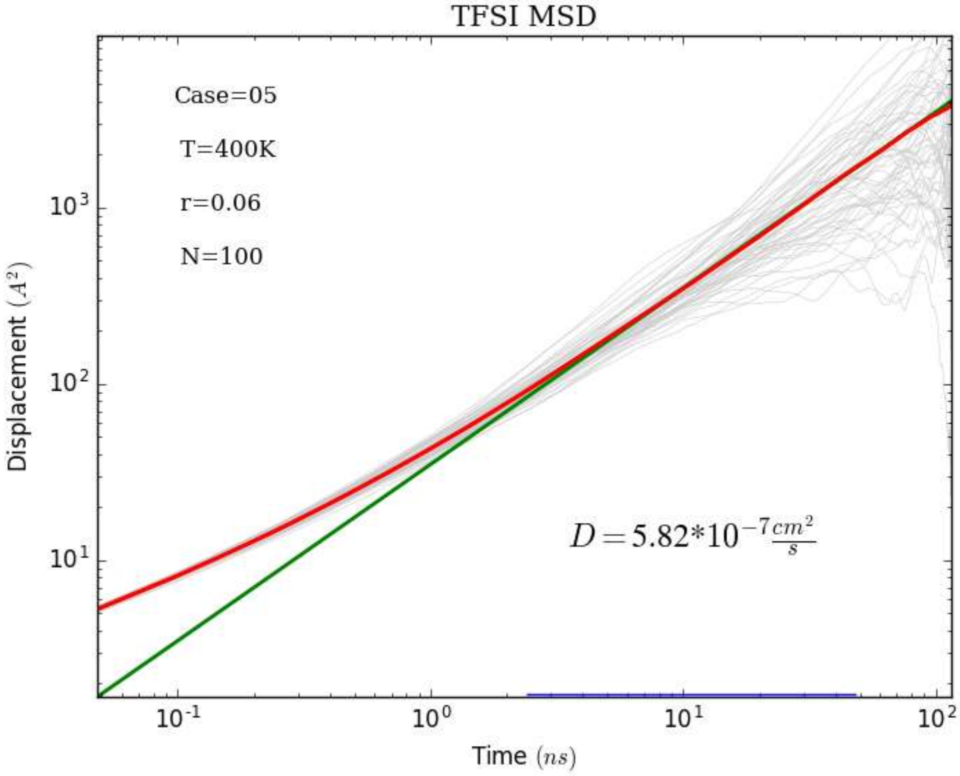
TFSI MSD
Case=05
T=400K
r=0.06
N=100
$D = 5.82*10^{-7}\frac{cm^2}{s}$
Displacement (A^2)
10^1
10^2
10^3
Time (ns)
10^{-1}
10^0
10^1
10^2

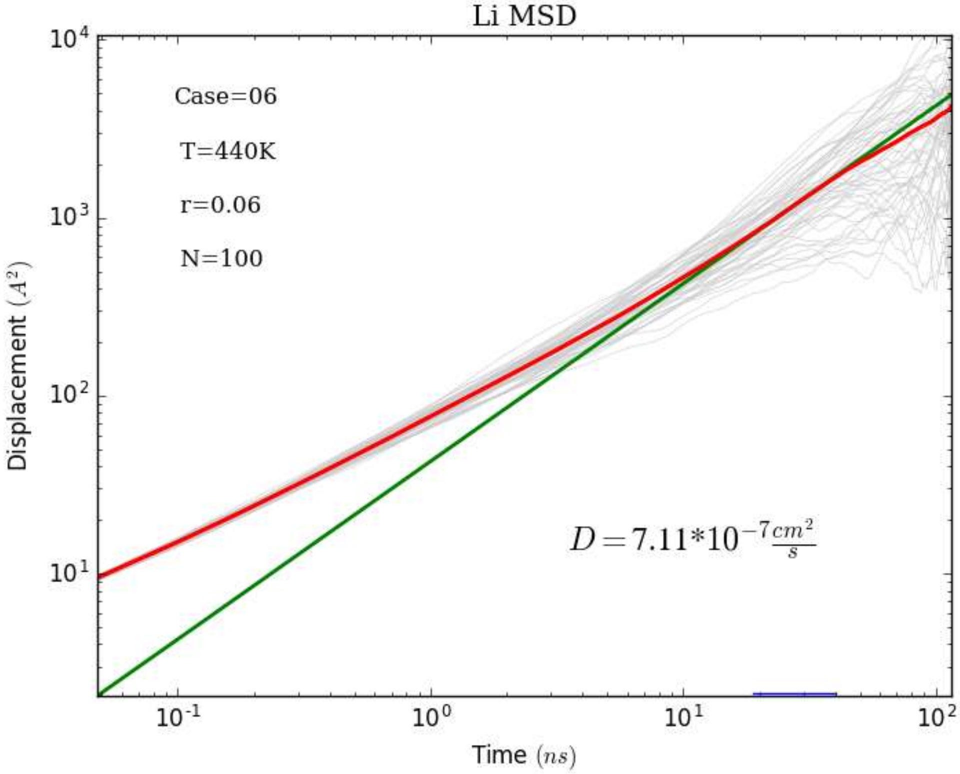
Li MSD

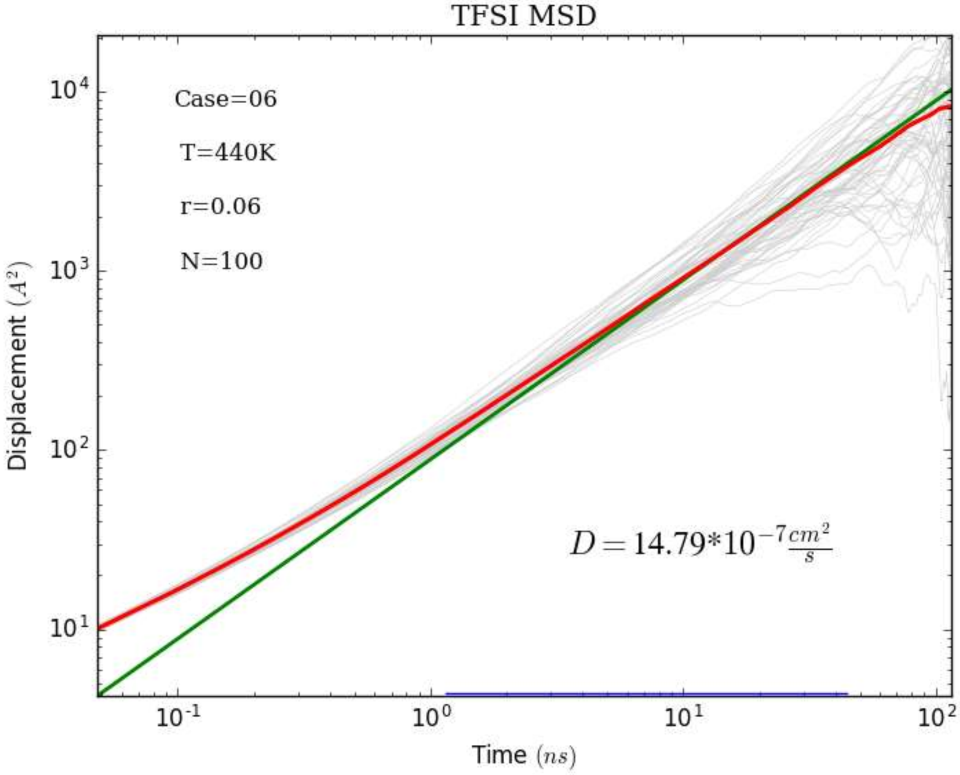
TFSI MSD

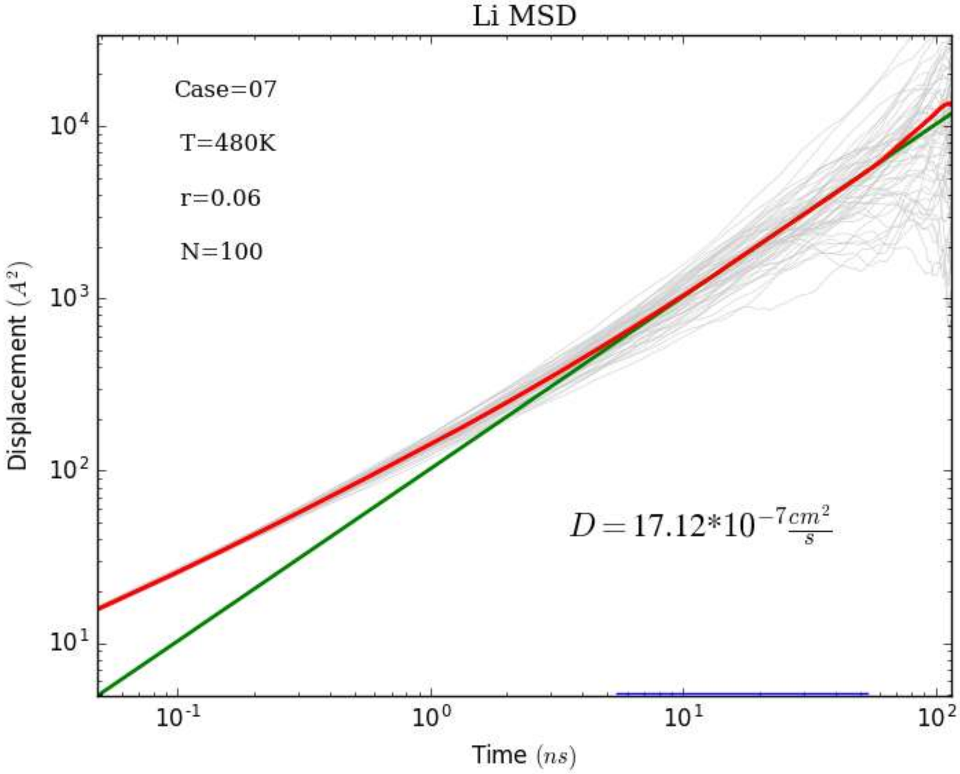
Li MSD

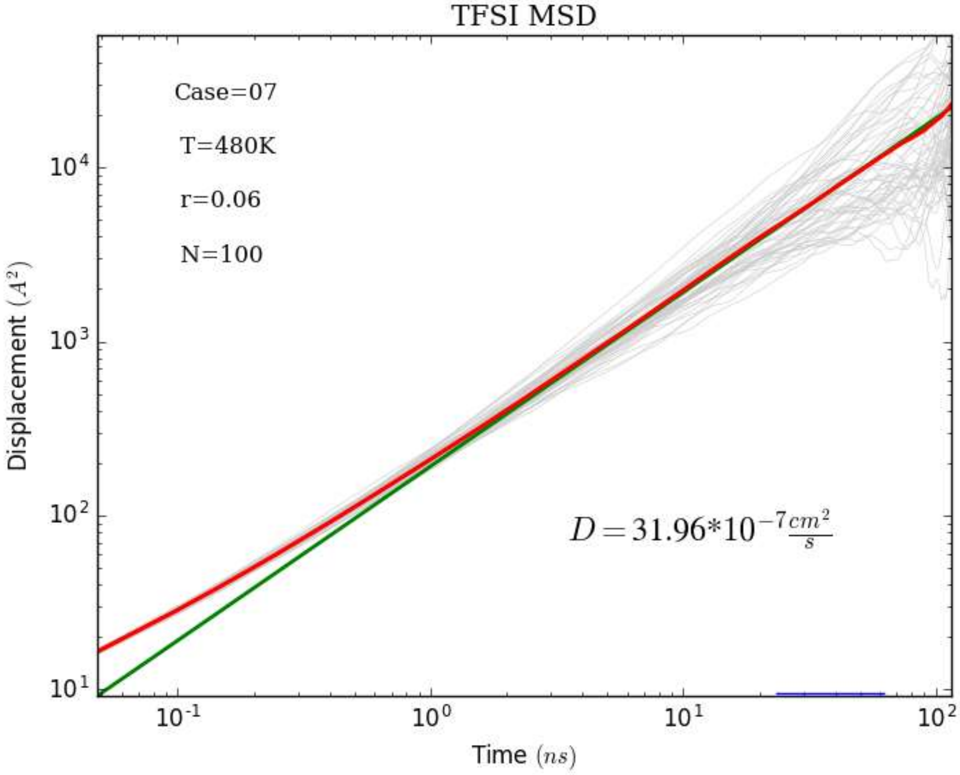
TFSI MSD

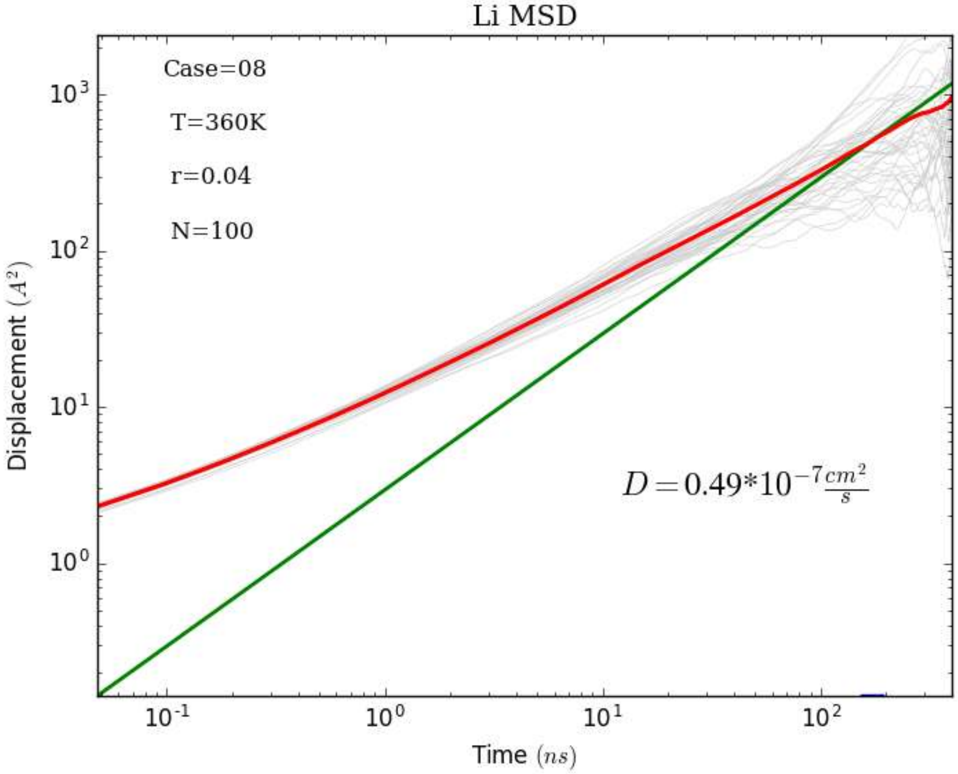
Li MSD
Case=08
T=360K
r=0.04
N=100
$D = 0.49 * 10^{-7} \frac{cm^2}{s}$
Displacement (A^2)
Time (ns)
10^3
10^2
10^1
10^0
10^{-1}
10^0
10^1
10^2

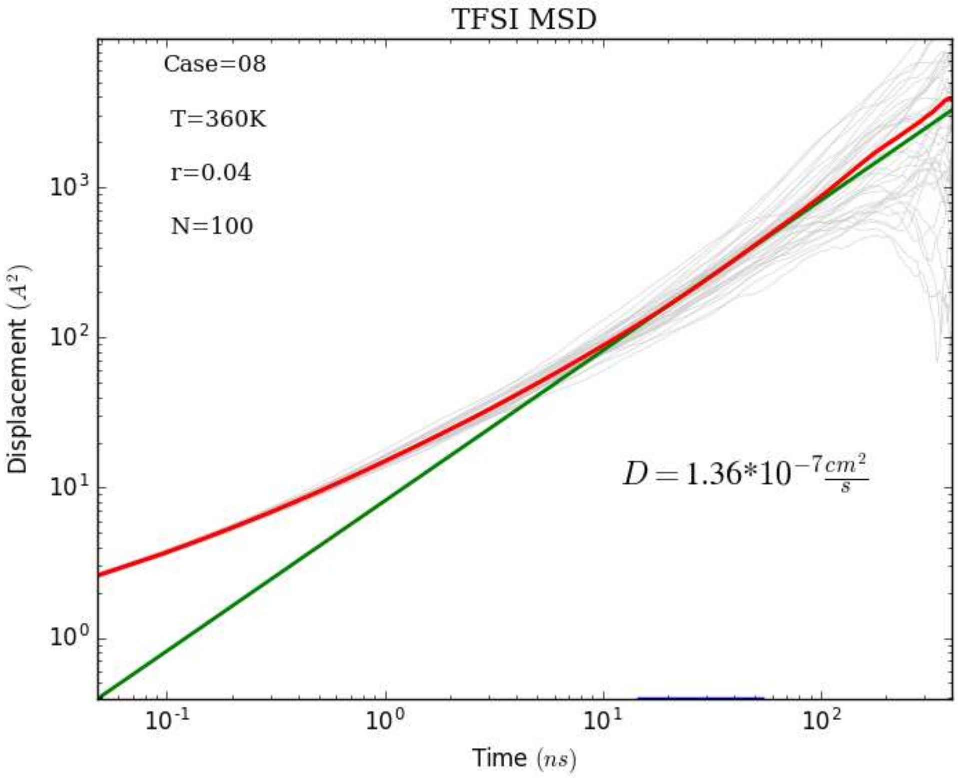
TFSI MSD
Case=08
T=360K
r=0.04
N=100
$D = 1.36 * 10^{-7} \frac{cm^2}{s}$
Displacement (A^2)
Time (ns)
10^3
10^2
10^1
10^0
10^{-1}
10^0
10^1
10^2

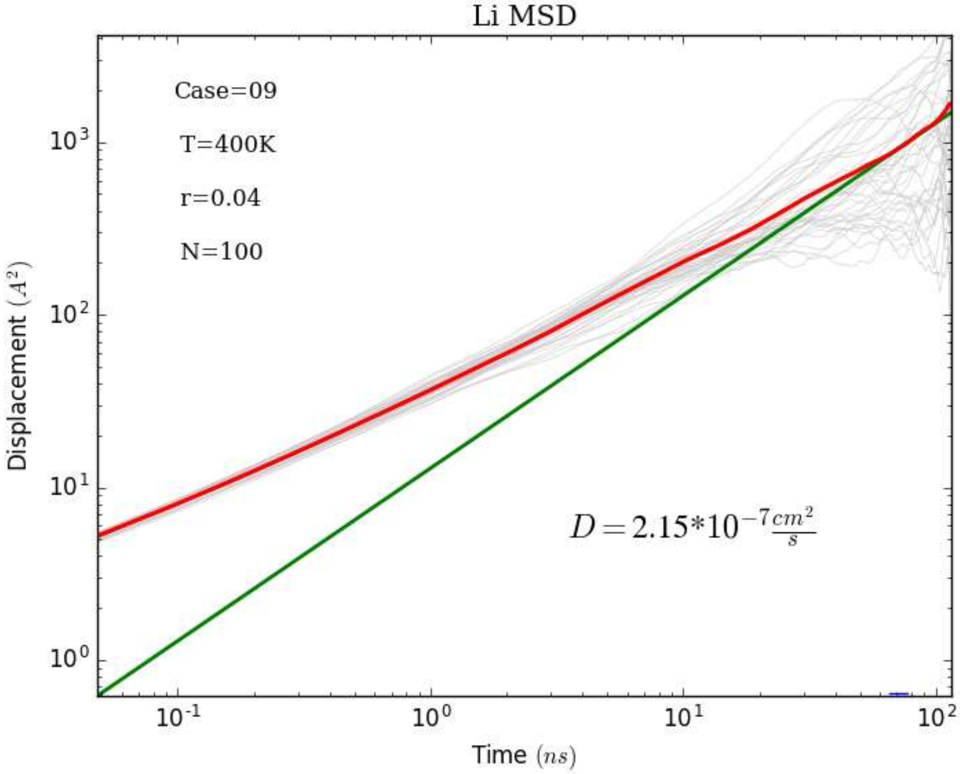
Li MSD
Case=09
T=400K
r=0.04
N=100
$D = 2.15*10^{-7}\frac{cm^2}{s}$
Displacement (A^2)
10^0
10^1
10^2
10^3
Time (ns)
10^{-1}
10^0
10^1
10^2

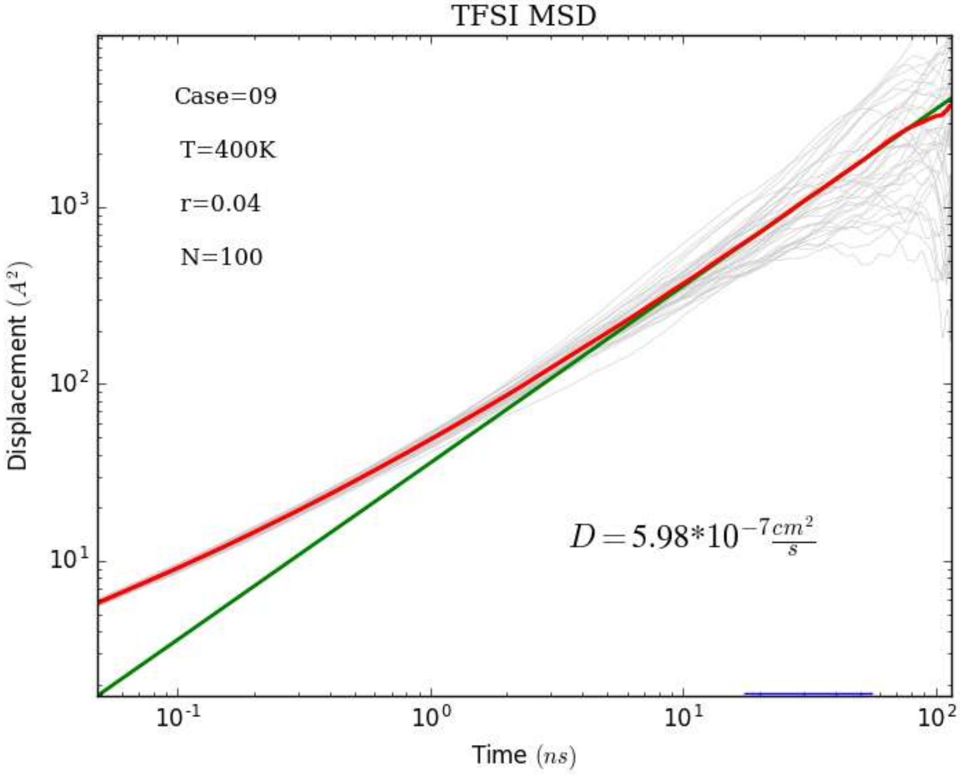
TFSI MSD
Case=09
T=400K
r=0.04
N=100
$D = 5.98*10^{-7}\frac{cm^2}{s}$
Displacement (A^2)
10^1
10^2
10^3
Time (ns)
10^{-1}
10^0
10^1
10^2

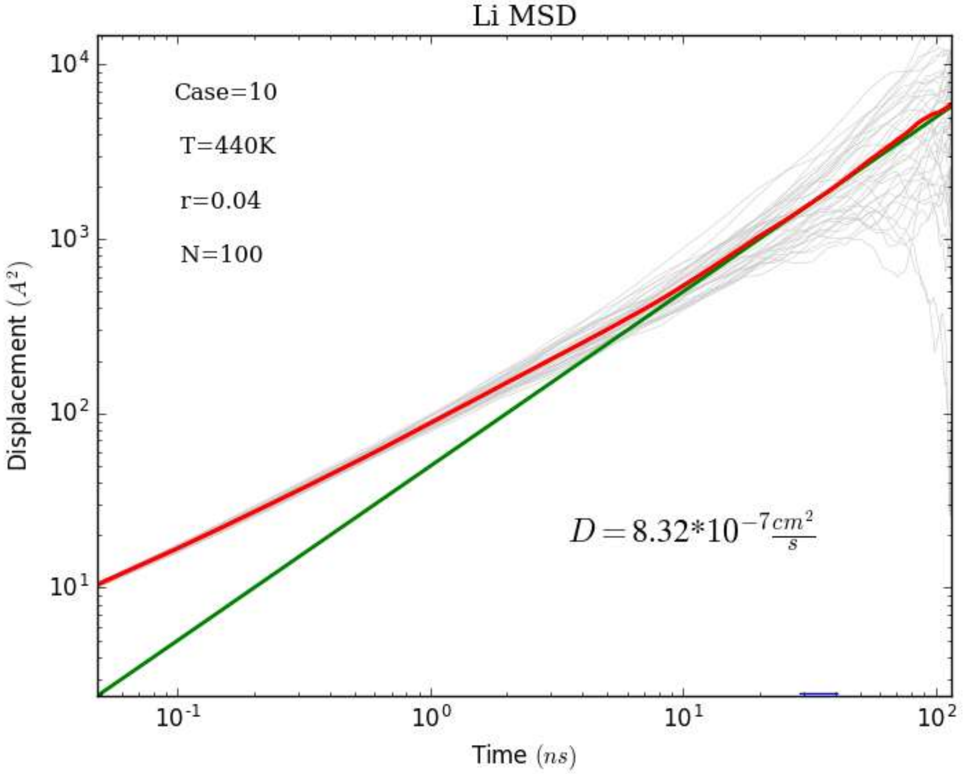
Li MSD

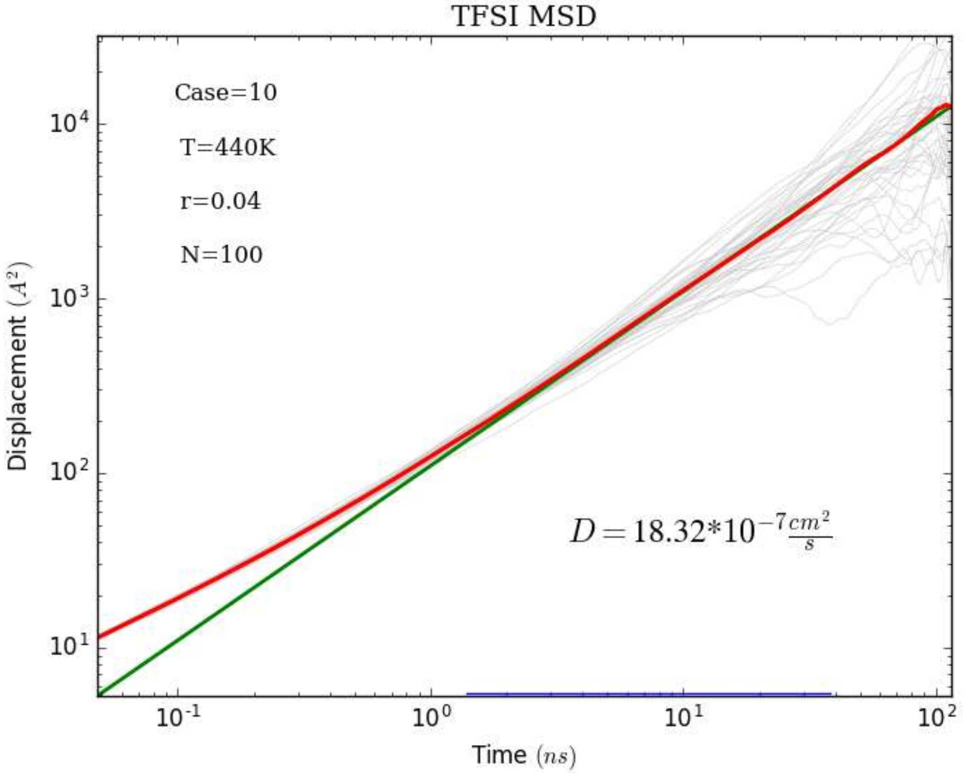
TFSI MSD

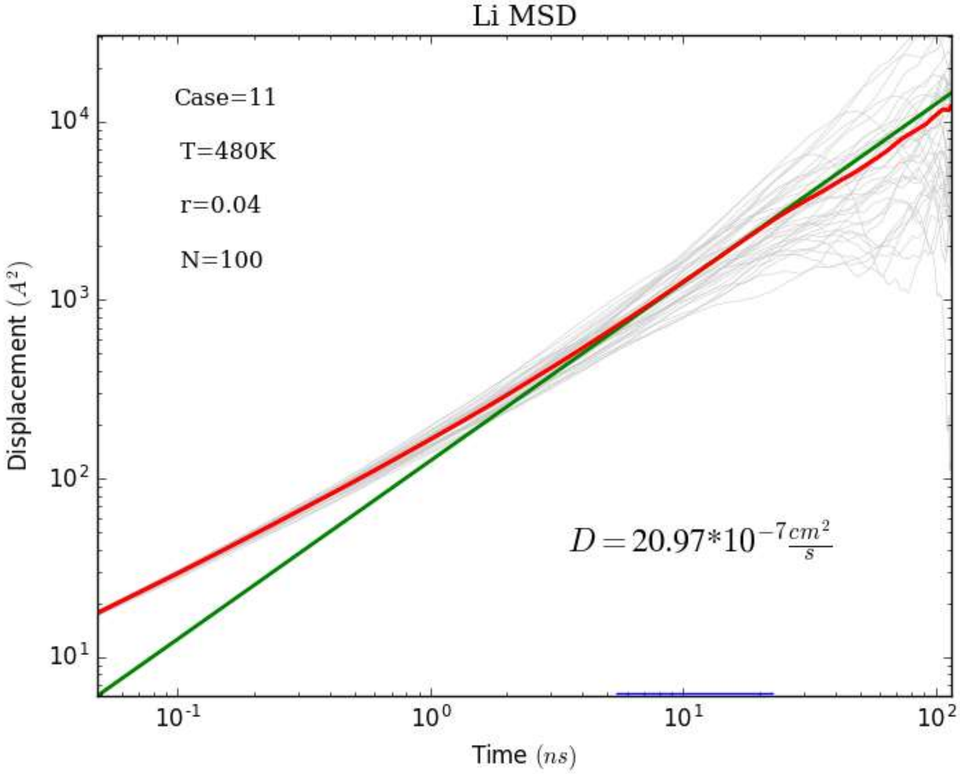
Li MSD
Case=11
T=480K
r=0.04
N=100
$D = 20.97*10^{-7}\frac{cm^2}{s}$
Displacement (A^2)
10^1
10^2
10^3
10^4
Time (ns)
10^{-1}
10^0
10^1
10^2

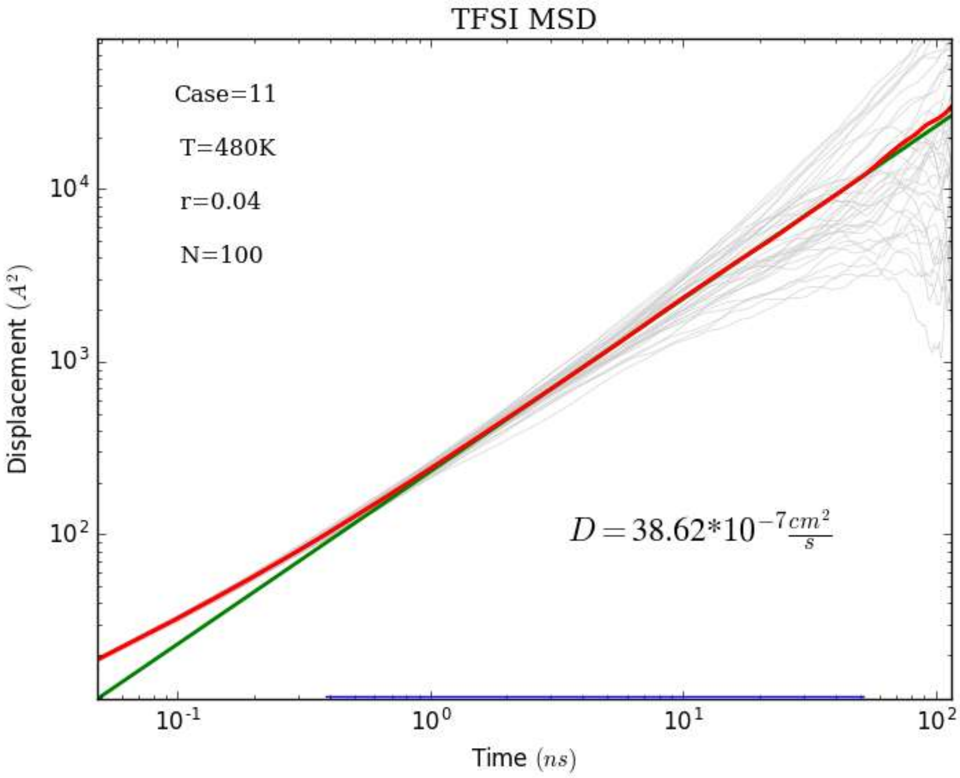
TFSI MSD
Case=11
T=480K
r=0.04
N=100
$D = 38.62*10^{-7}\frac{cm^2}{s}$
Displacement (A^2)
10^2
10^3
10^4
Time (ns)
10^{-1}
10^0
10^1
10^2

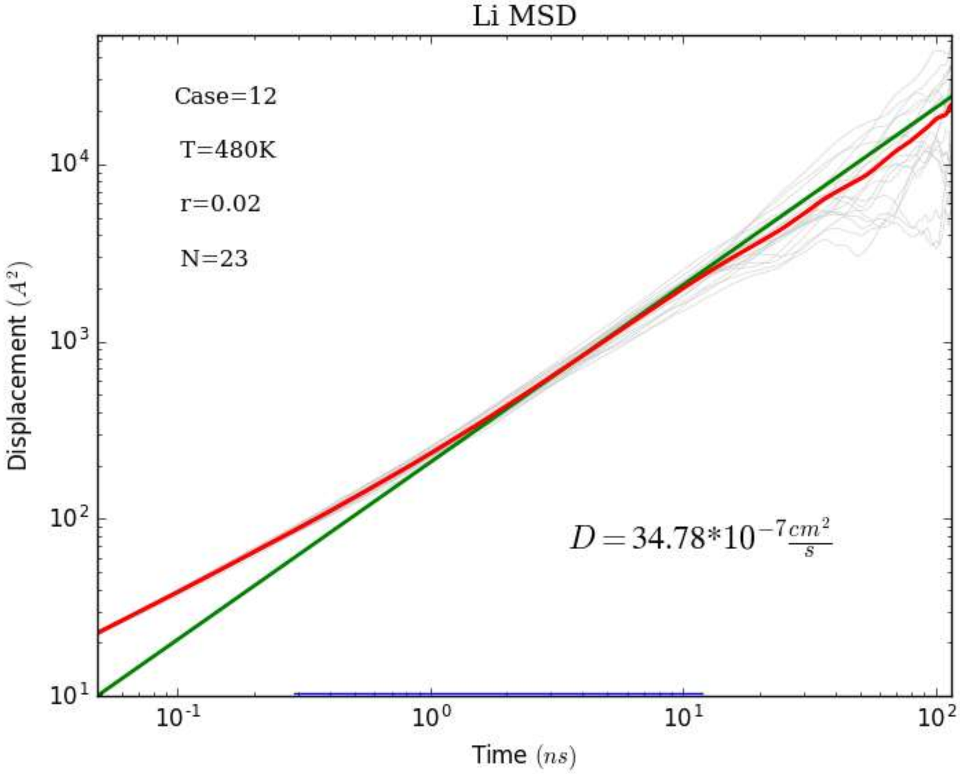
Li MSD
Case=12
T=480K
r=0.02
N=23
$D = 34.78*10^{-7}\frac{cm^2}{s}$
Displacement (A^2)
10^1
10^2
10^3
10^4
Time (ns)
10^{-1}
10^0
10^1
10^2

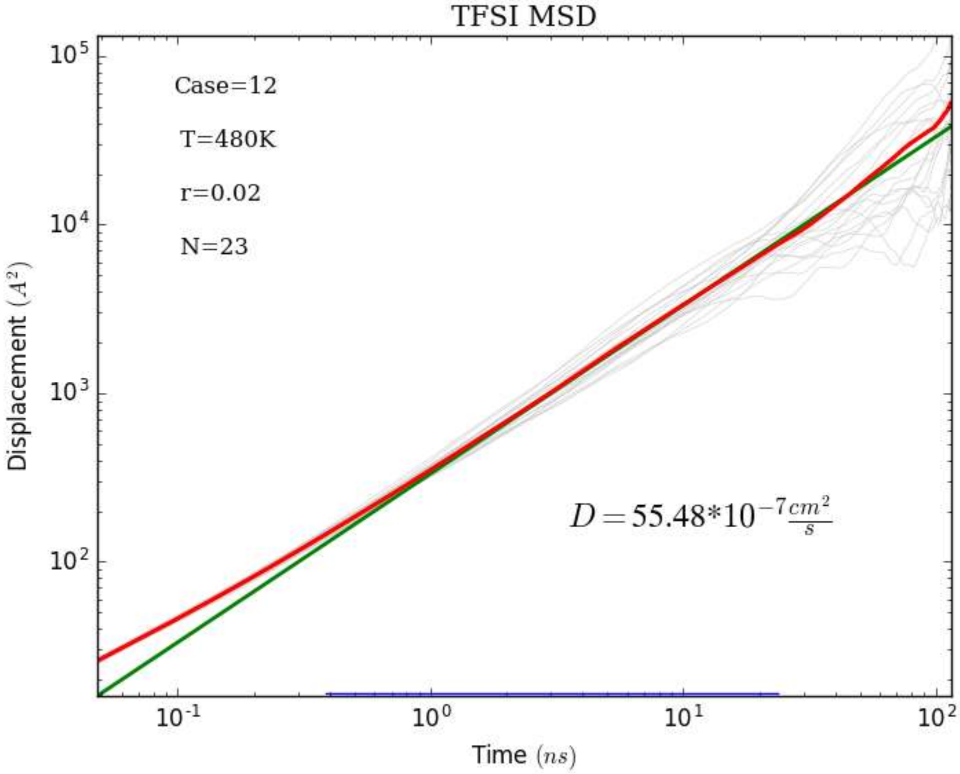
TFSI MSD
Case=12
T=480K
r=0.02
N=23
$D = 55.48*10^{-7}\frac{cm^2}{s}$
Displacement (A^2)
10^2
10^3
10^4
10^5
Time (ns)
10^{-1}
10^0
10^1
10^2

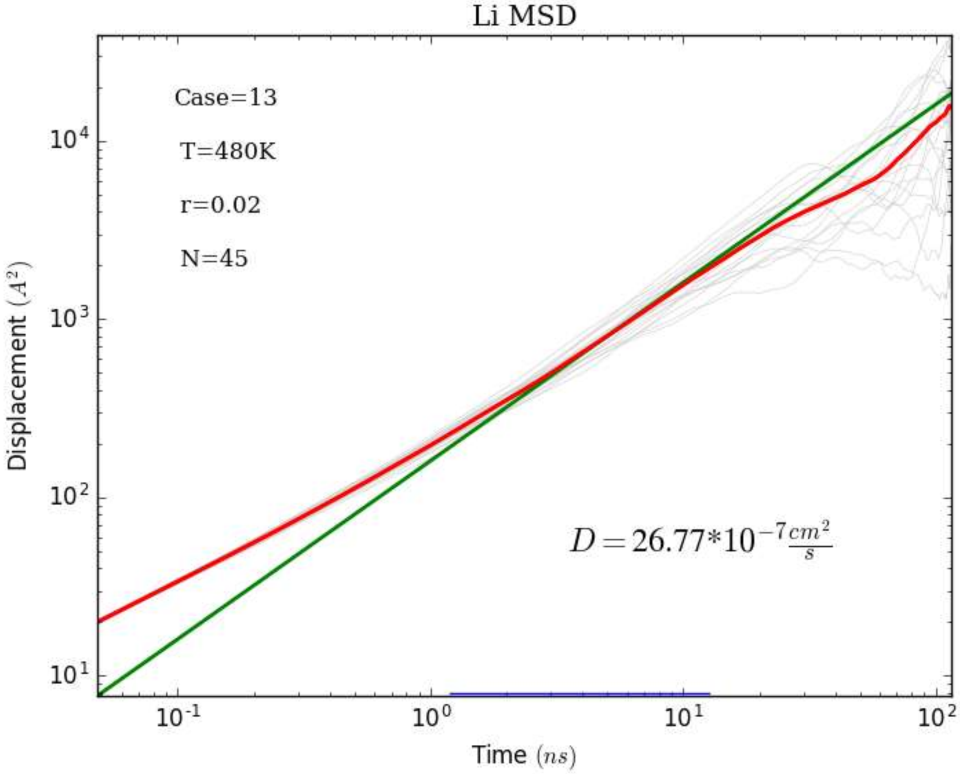
Li MSD
Case=13
T=480K
r=0.02
N=45
$D = 26.77 * 10^{-7} \frac{cm^2}{s}$
Displacement (A^2)
10^1
10^2
10^3
10^4
Time (ns)
10^{-1}
10^0
10^1
10^2

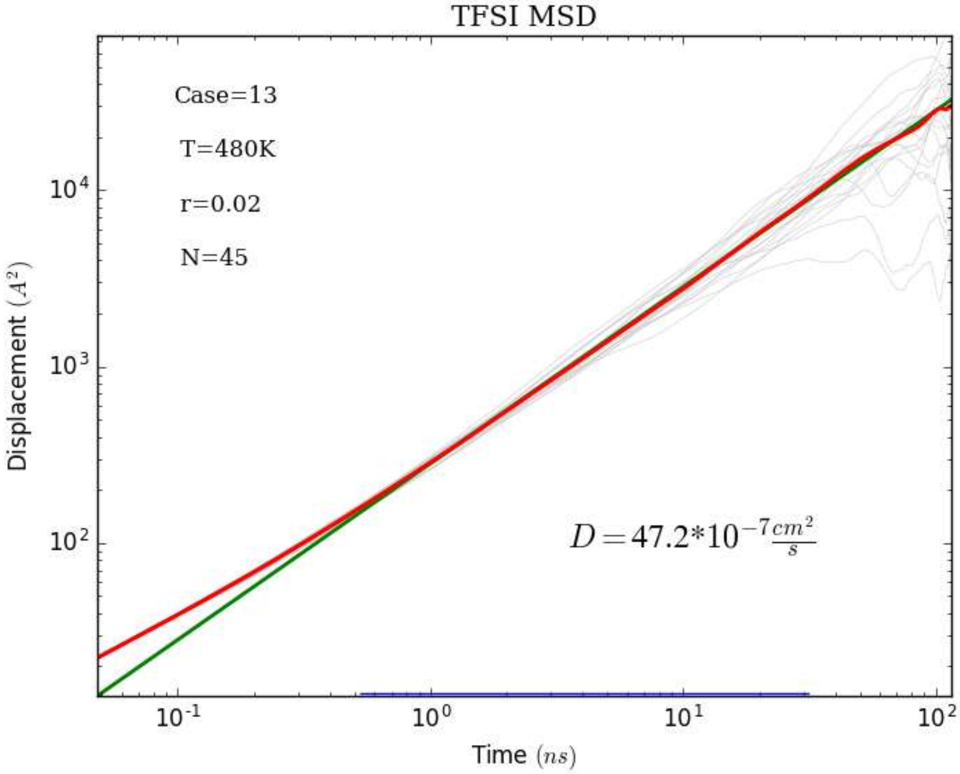
TFSI MSD
Case=13
T=480K
r=0.02
N=45
$D = 47.2 * 10^{-7} \frac{cm^2}{s}$
Displacement (A^2)
10^2
10^3
10^4
Time (ns)
10^{-1}
10^0
10^1
10^2

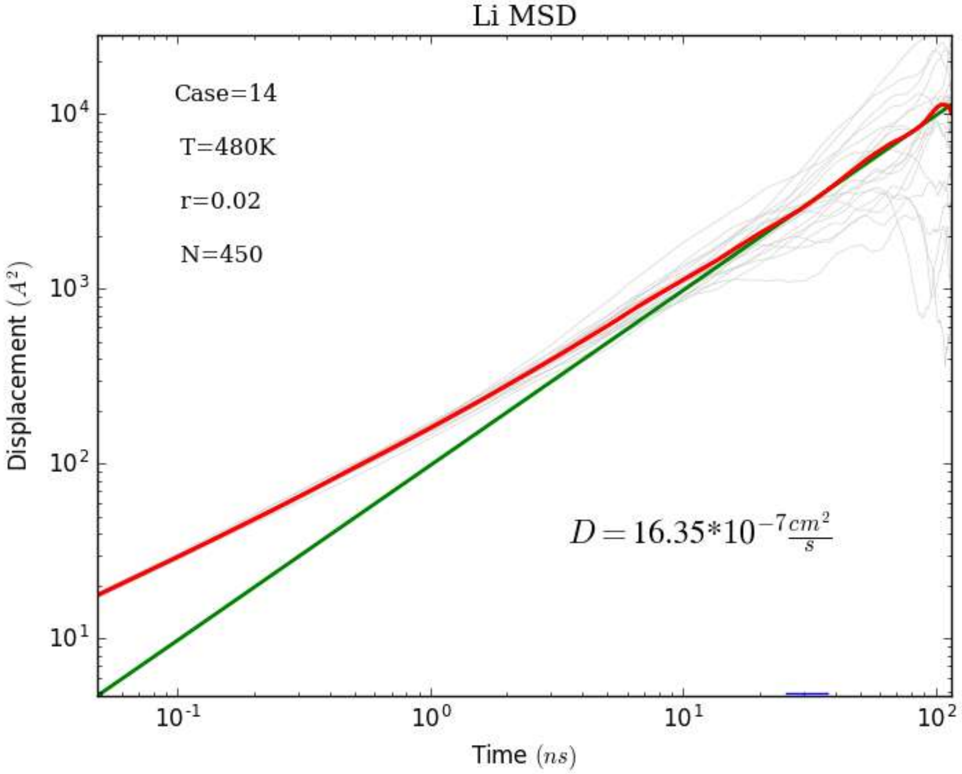
Li MSD
Case=14
T=480K
r=0.02
N=450
$D=16.35*10^{-7}\frac{cm^2}{s}$
Displacement (A^2)
10^4
10^3
10^2
10^1
10^{-1}
10^0
10^1
10^2
Time (ns)

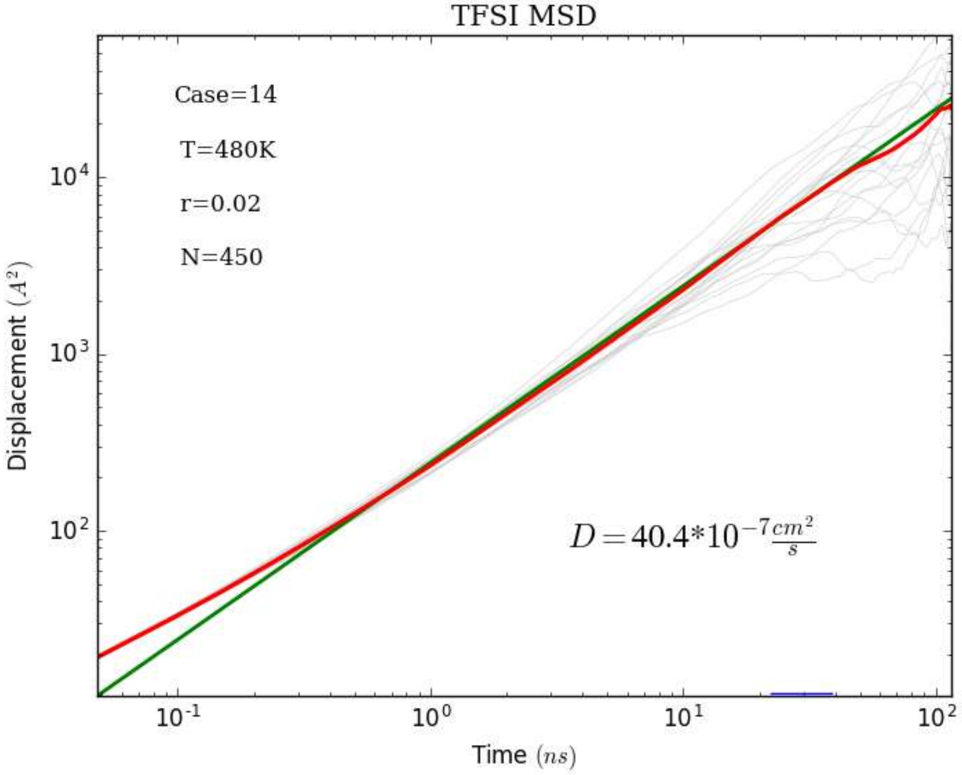
TFSI MSD
Case=14
T=480K
r=0.02
N=450
$D=40.4*10^{-7}\frac{cm^2}{s}$
Displacement (A^2)
10^4
10^3
10^2
10^{-1}
10^0
10^1
10^2
Time (ns)

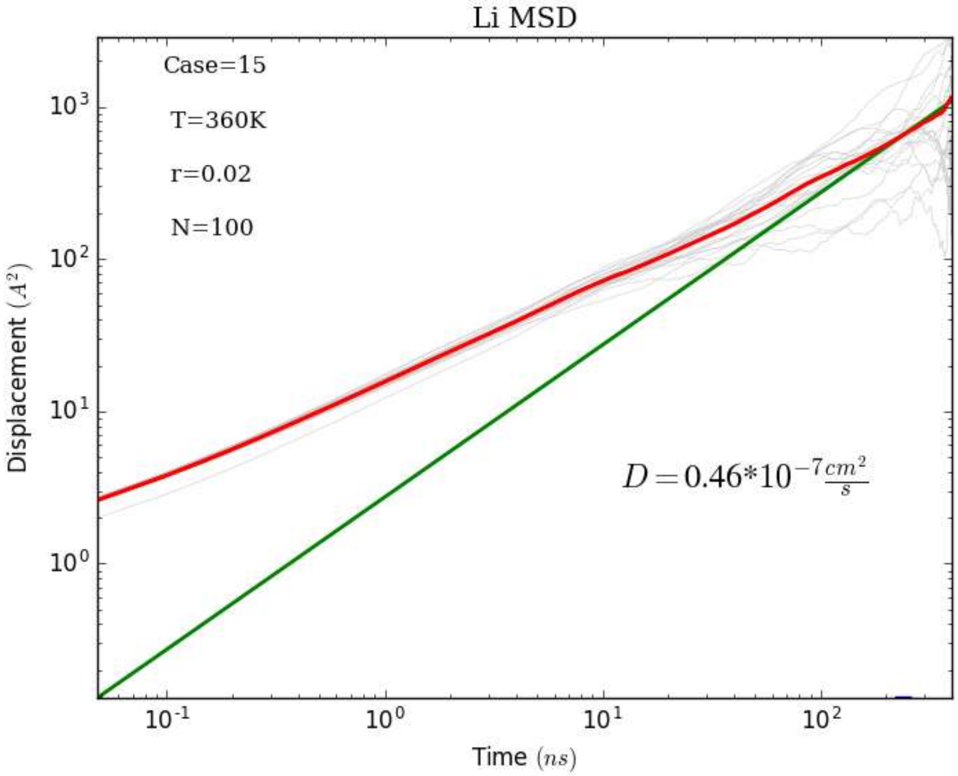
Li MSD
Case=15
T=360K
r=0.02
N=100
$D=0.46*10^{-7}\frac{cm^2}{s}$
Displacement (A^2)
10^3
10^2
10^1
10^0
Time (ns)
10^{-1}
10^0
10^1
10^2

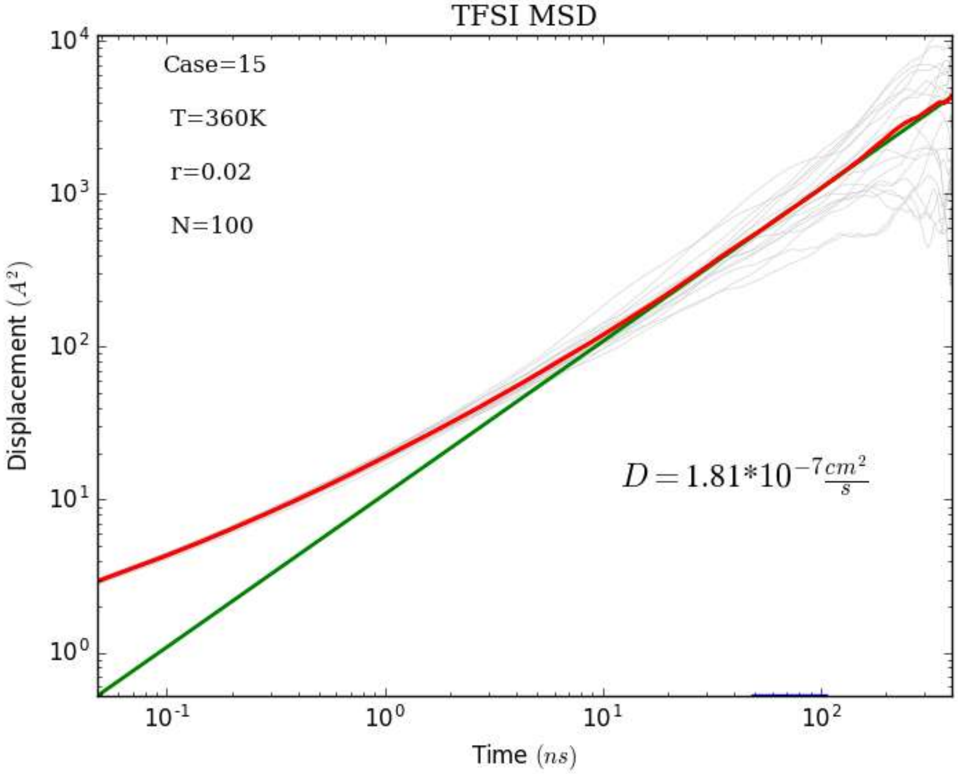
TFSI MSD
Case=15
T=360K
r=0.02
N=100
$D=1.81*10^{-7}\frac{cm^2}{s}$
Displacement (A^2)
10^4
10^3
10^2
10^1
10^0
Time (ns)
10^{-1}
10^0
10^1
10^2

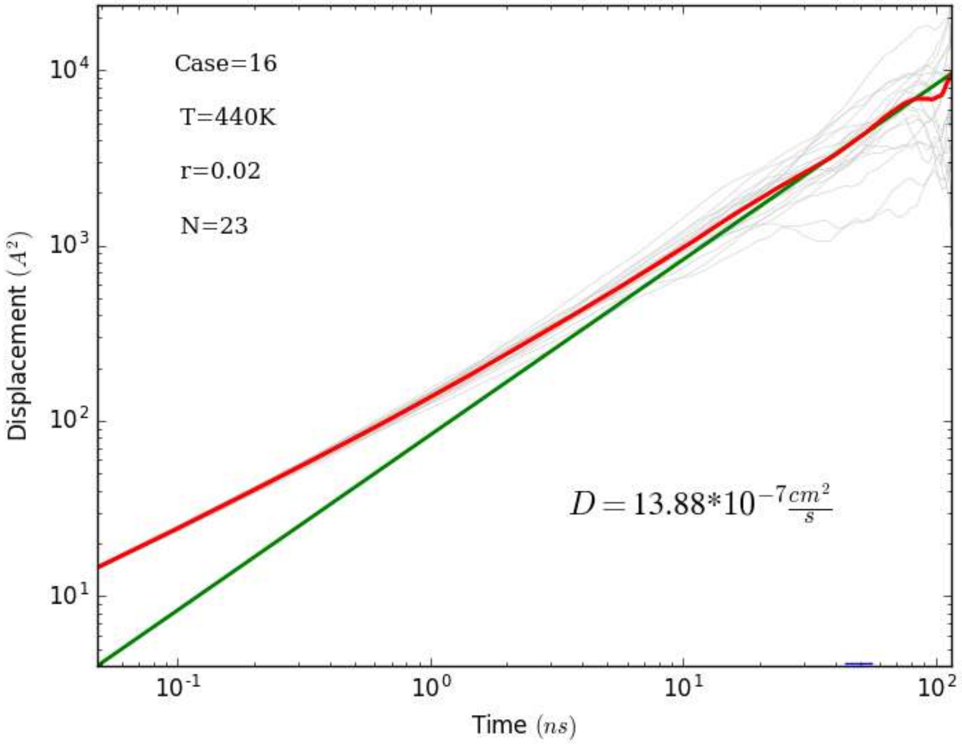
Li MSD

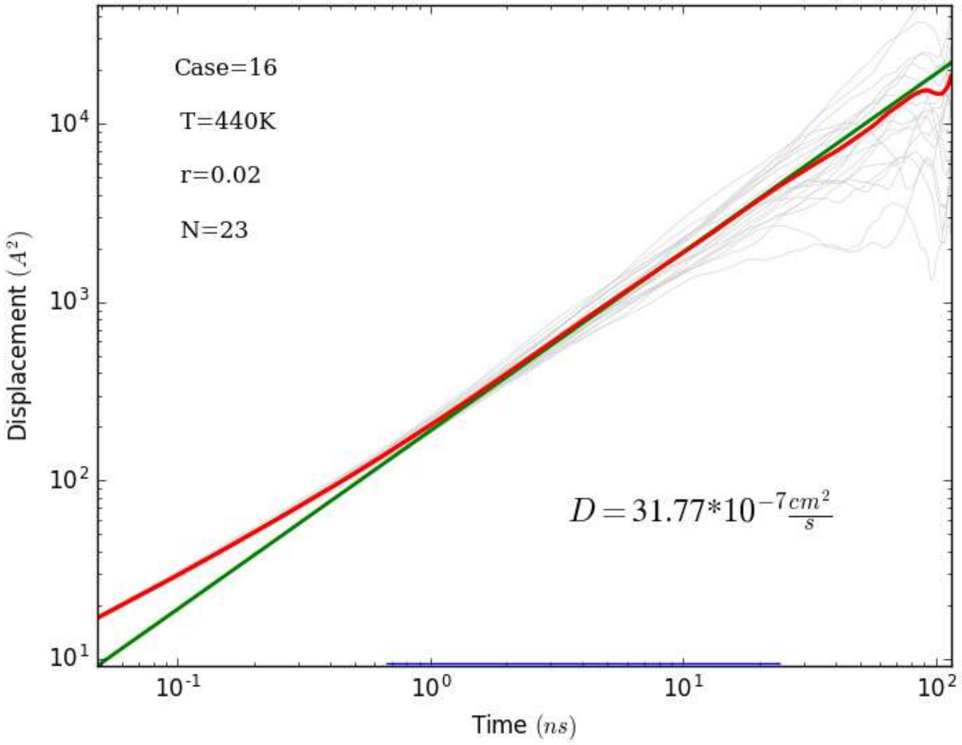
TFSI MSD

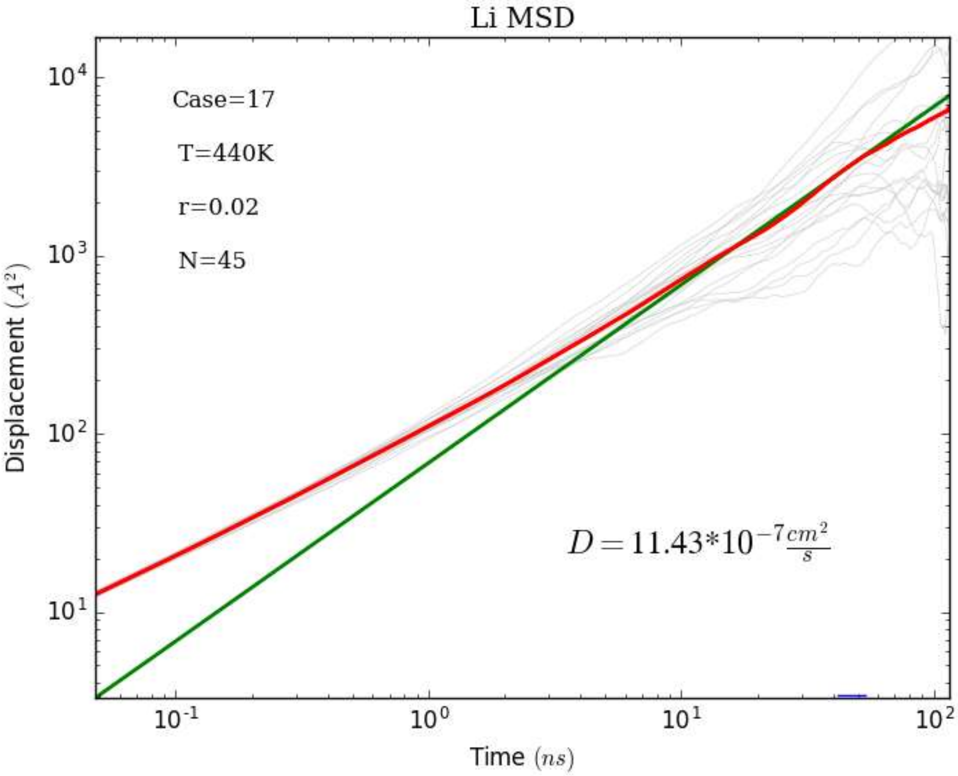
Li MSD
Case=17
T=440K
r=0.02
N=45
$D=11.43*10^{-7}\frac{cm^2}{s}$
Displacement (A^2)
Time (ns)
10^1
10^2
10^3
10^4
10^{-1}
10^0
10^1
10^2

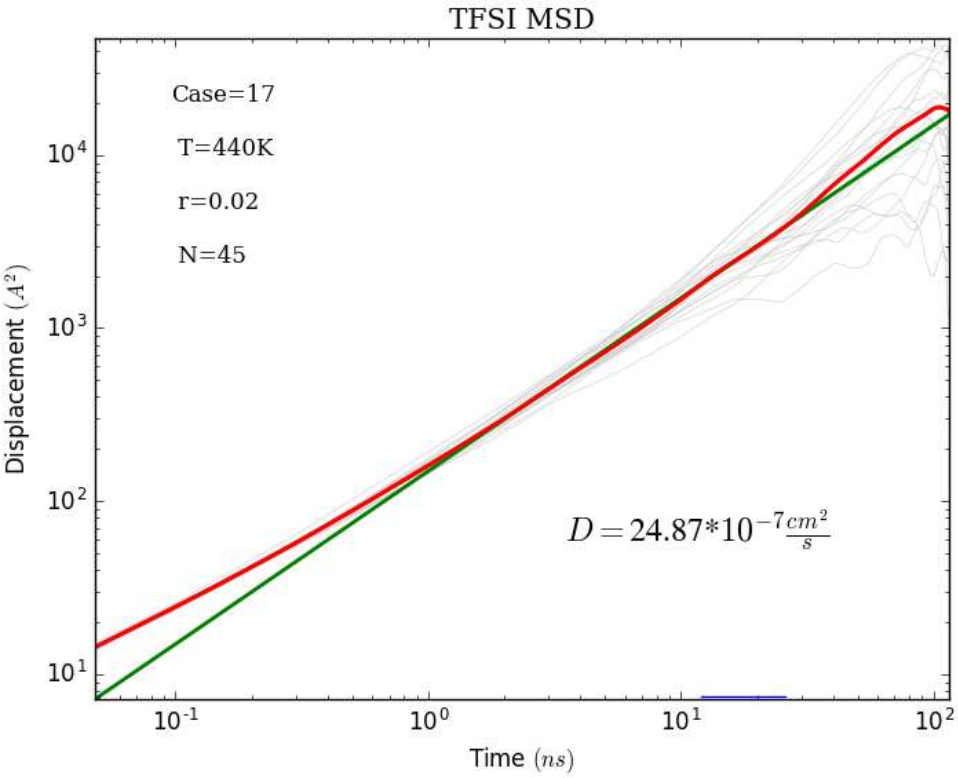
TFSI MSD
Case=17
T=440K
r=0.02
N=45
$D=24.87*10^{-7}\frac{cm^2}{s}$
Displacement (A^2)
Time (ns)
10^1
10^2
10^3
10^4
10^{-1}
10^0
10^1
10^2

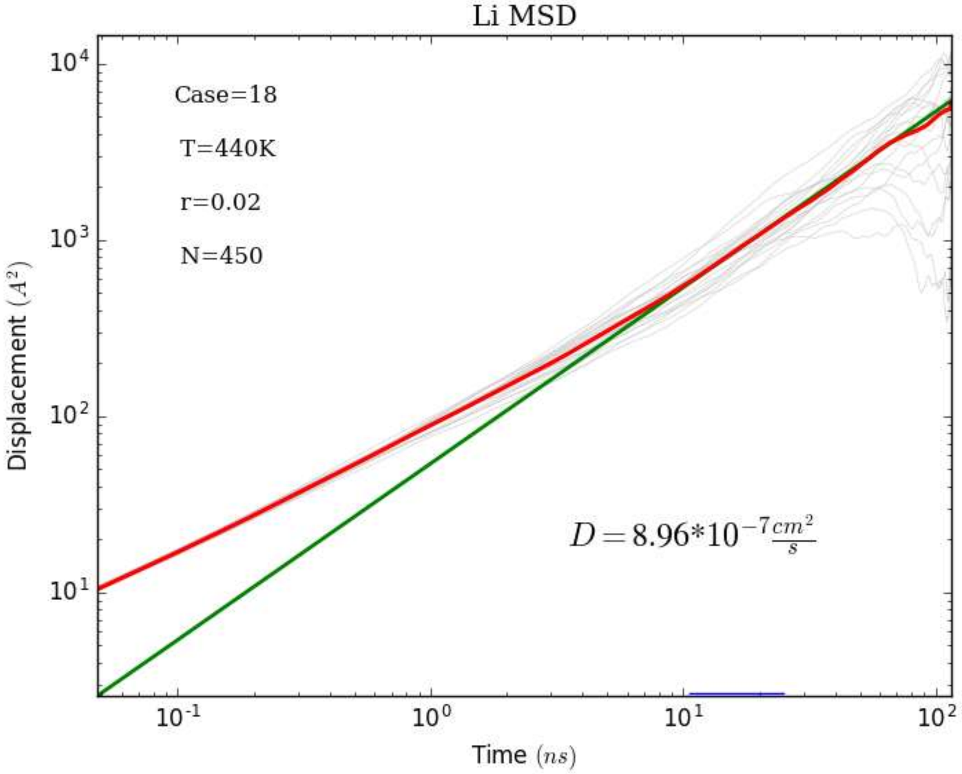
Li MSD
Case=18
T=440K
r=0.02
N=450
$D=8.96*10^{-7}\frac{cm^2}{s}$
Displacement (A^2)
Time (ns)
10^4
10^3
10^2
10^1
10^{-1}
10^0
10^1
10^2

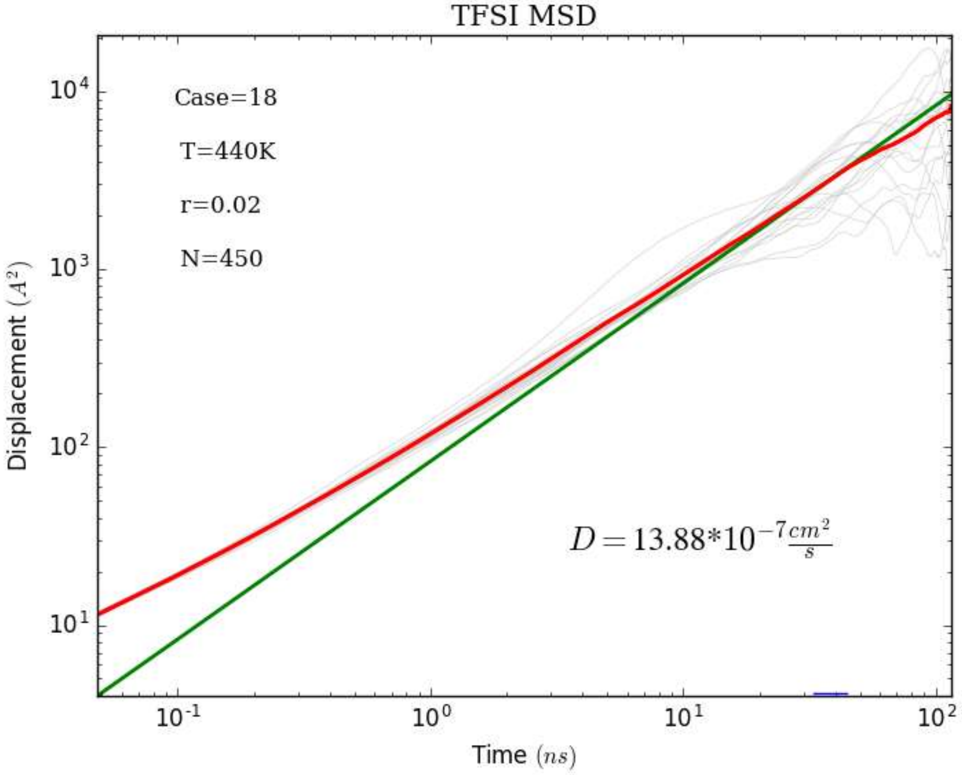
TFSI MSD
Case=18
T=440K
r=0.02
N=450
$D=13.88*10^{-7}\frac{cm^2}{s}$
Displacement (A^2)
Time (ns)
10^4
10^3
10^2
10^1
10^{-1}
10^0
10^1
10^2

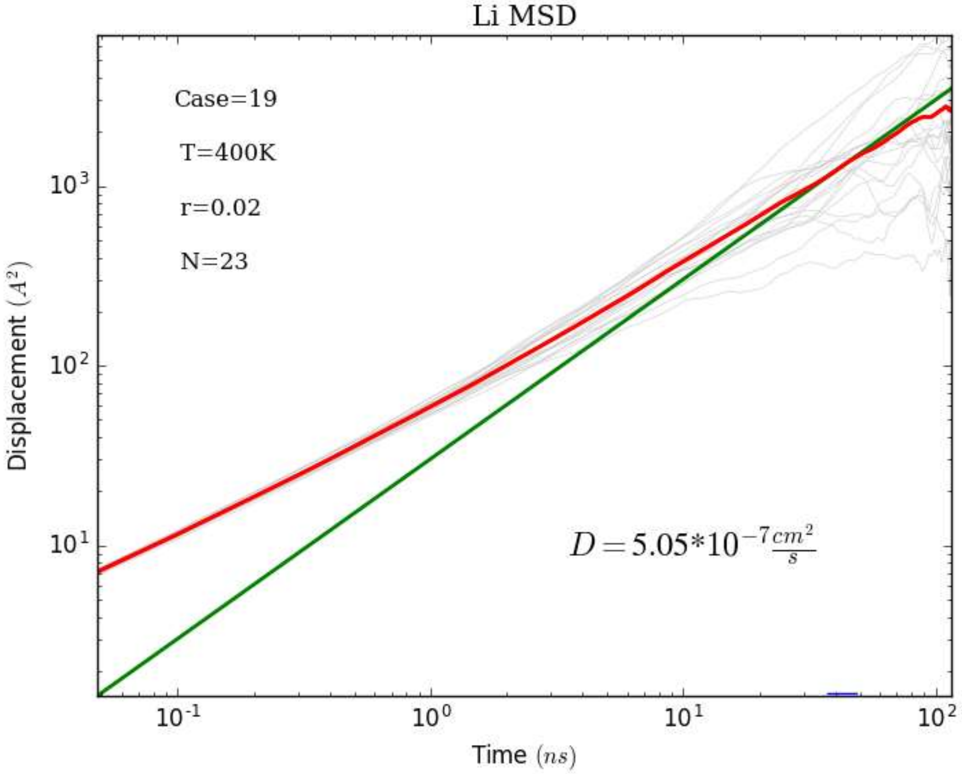
Li MSD
Case=19
T=400K
r=0.02
N=23
$D = 5.05*10^{-7}\frac{cm^2}{s}$
Displacement (A^2)
10^1
10^2
10^3
Time (ns)
10^{-1}
10^0
10^1
10^2

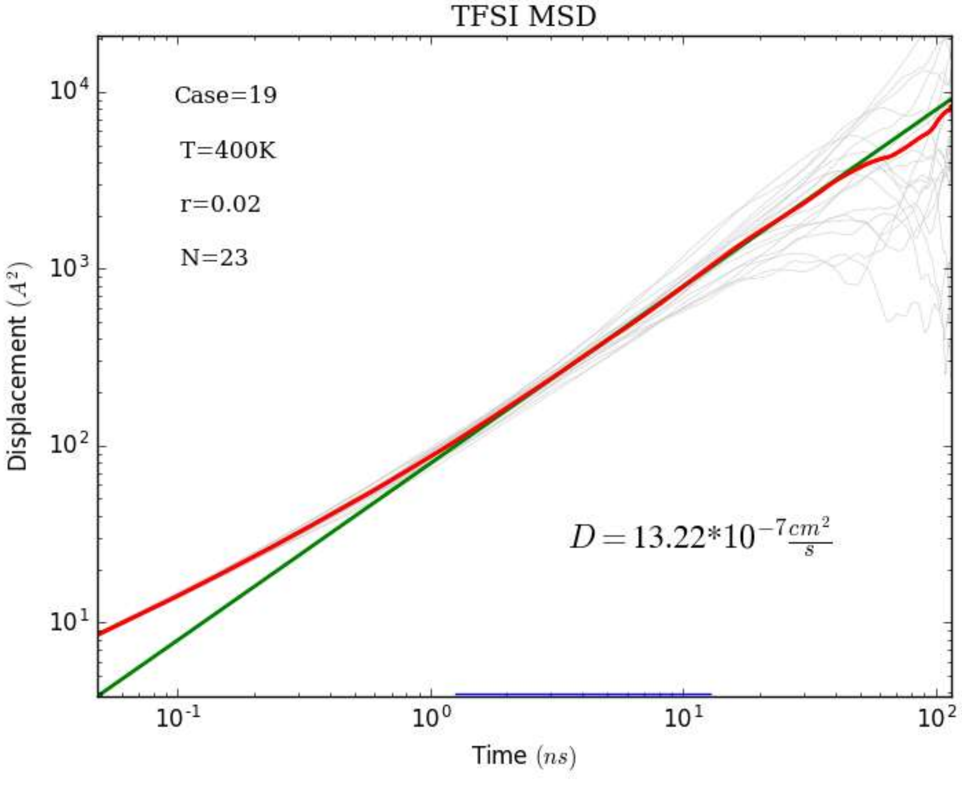
TFSI MSD
Case=19
T=400K
r=0.02
N=23
$D = 13.22*10^{-7}\frac{cm^2}{s}$
Displacement (A^2)
10^1
10^2
10^3
10^4
Time (ns)
10^{-1}
10^0
10^1
10^2

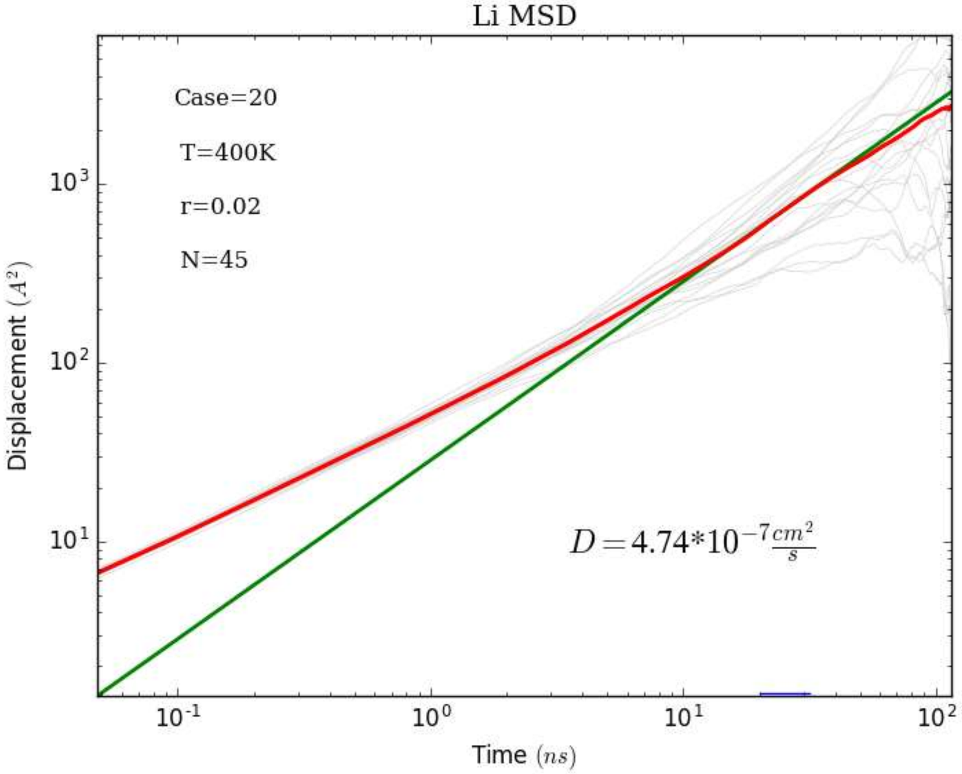
Li MSD
Case=20
T=400K
r=0.02
N=45
$D = 4.74*10^{-7}\frac{cm^2}{s}$
Displacement (A^2)
10^1
10^2
10^3
Time (ns)
10^{-1}
10^0
10^1
10^2

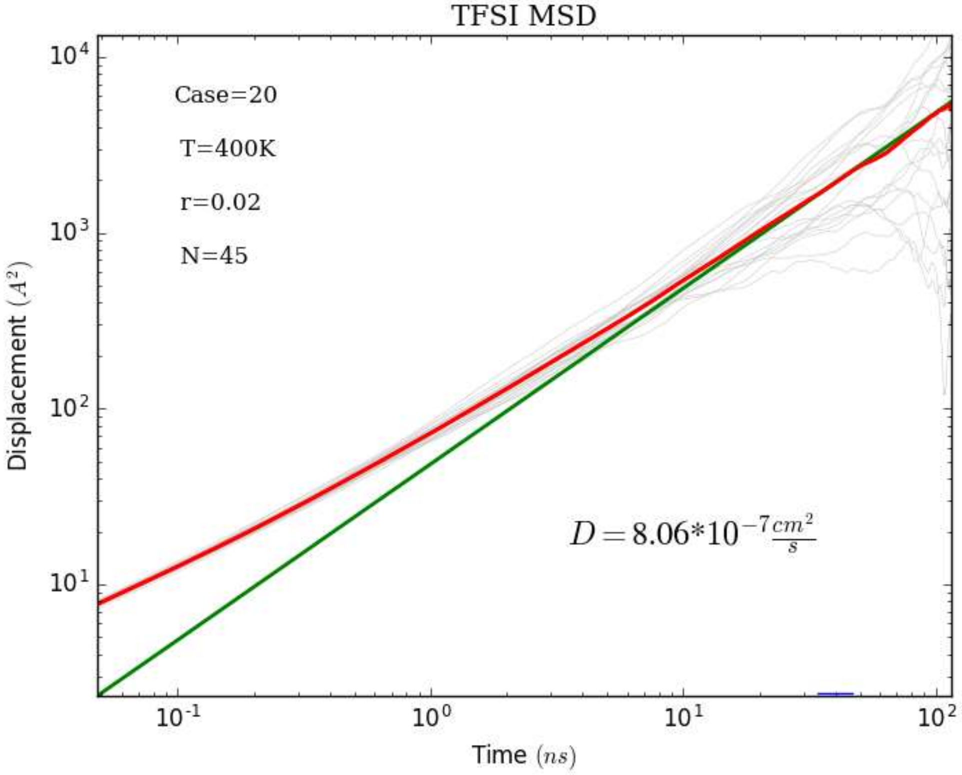
TFSI MSD
Case=20
T=400K
r=0.02
N=45
$D = 8.06*10^{-7}\frac{cm^2}{s}$
Displacement (A^2)
10^1
10^2
10^3
10^4
Time (ns)
10^{-1}
10^0
10^1
10^2

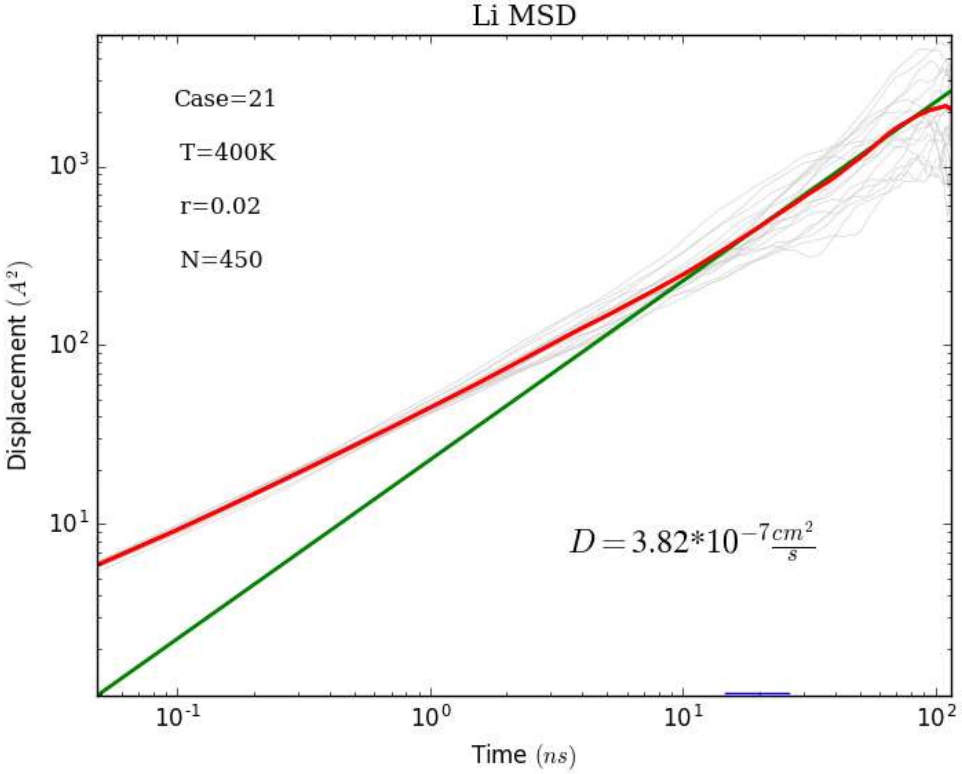

Li MSD
Case=21
T=400K
r=0.02
N=450
$D = 3.82 * 10^{-7} \frac{cm^2}{s}$
Displacement (A^2)
Time (ns)
10^1
10^2
10^3
10^{-1}
10^0
10^1
10^2

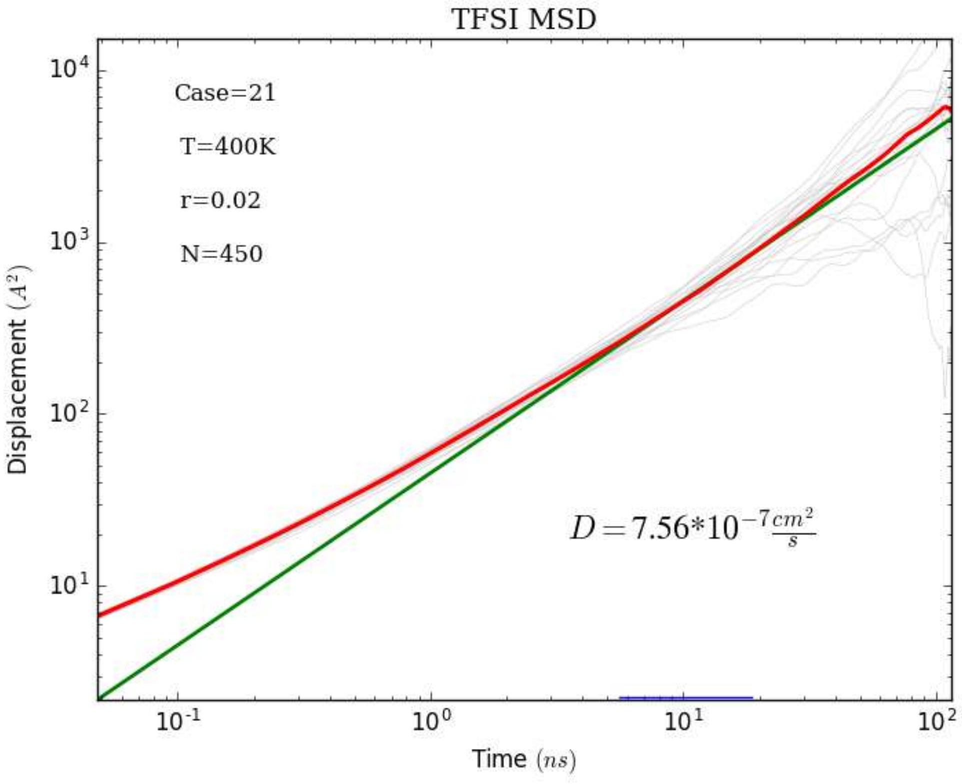

TFSI MSD
Case=21
T=400K
r=0.02
N=450
$D = 7.56 * 10^{-7} \frac{cm^2}{s}$
Displacement (A^2)
Time (ns)
10^1
10^2
10^3
10^4
10^{-1}
10^0
10^1
10^2

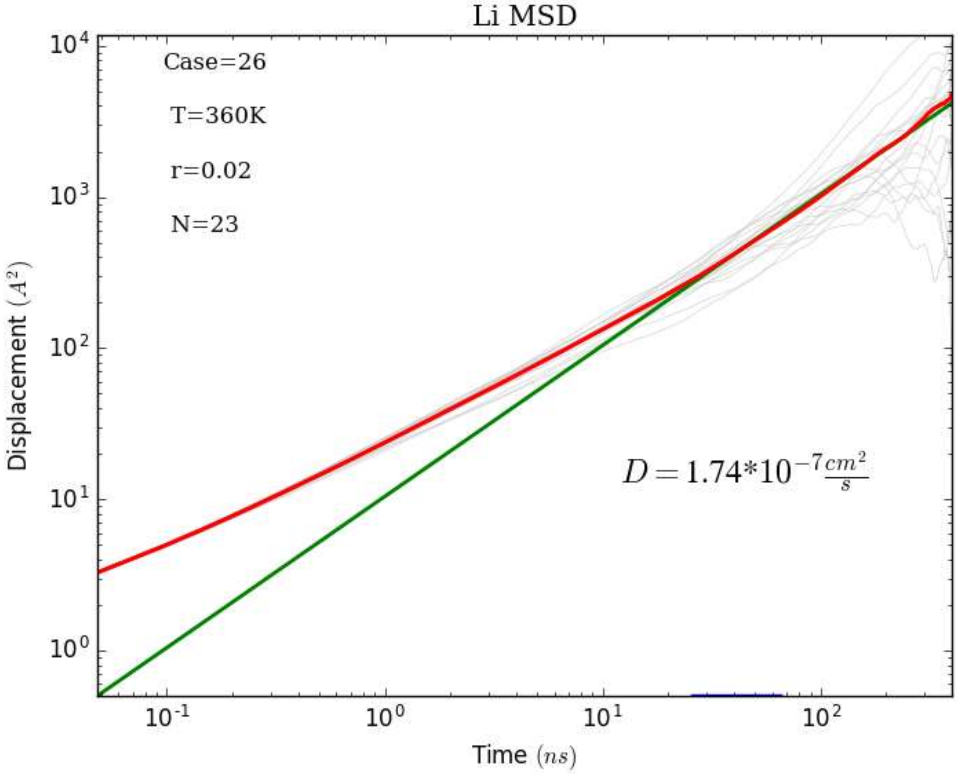
Li MSD
Case=26
T=360K
r=0.02
N=23
$D = 1.74 * 10^{-7} \frac{cm^2}{s}$
Displacement (A^2)
10^4
10^3
10^2
10^1
10^0
Time (ns)
10^{-1}
10^0
10^1
10^2

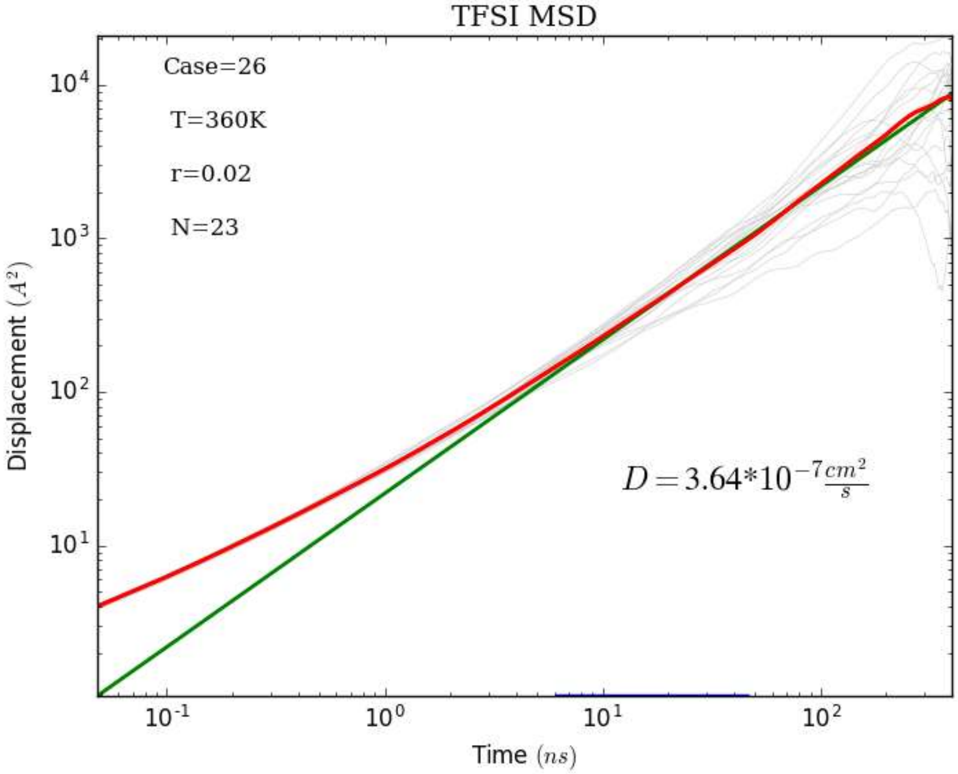
TFSI MSD
Case=26
T=360K
r=0.02
N=23
$D = 3.64 * 10^{-7} \frac{cm^2}{s}$
Displacement (A^2)
10^4
10^3
10^2
10^1
Time (ns)
10^{-1}
10^0
10^1
10^2

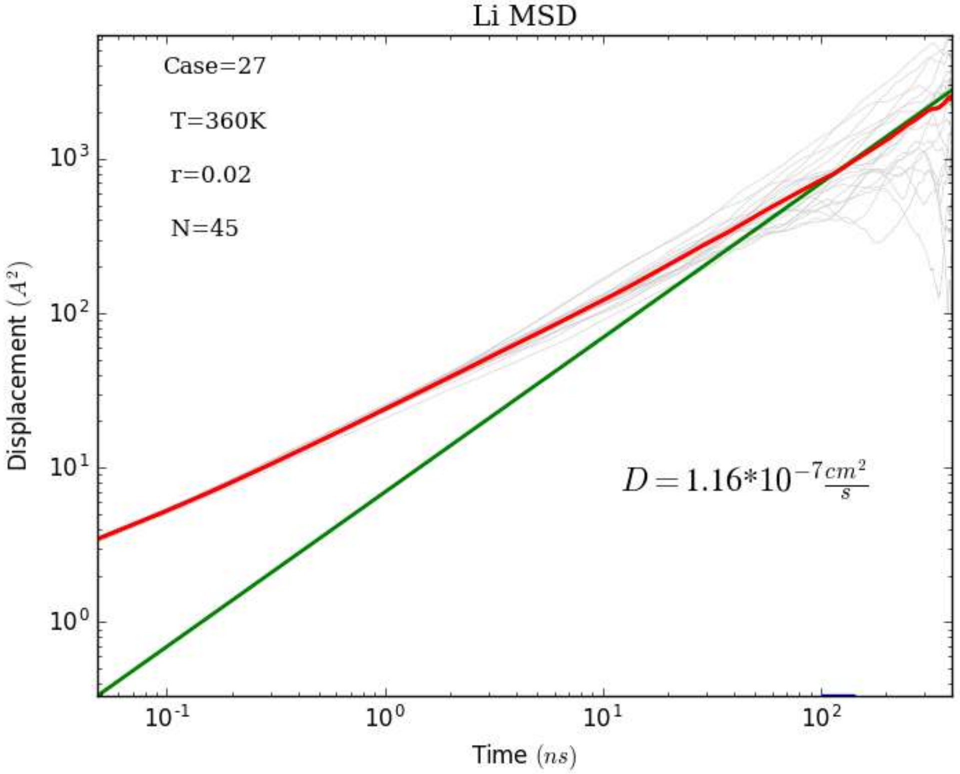

Li MSD

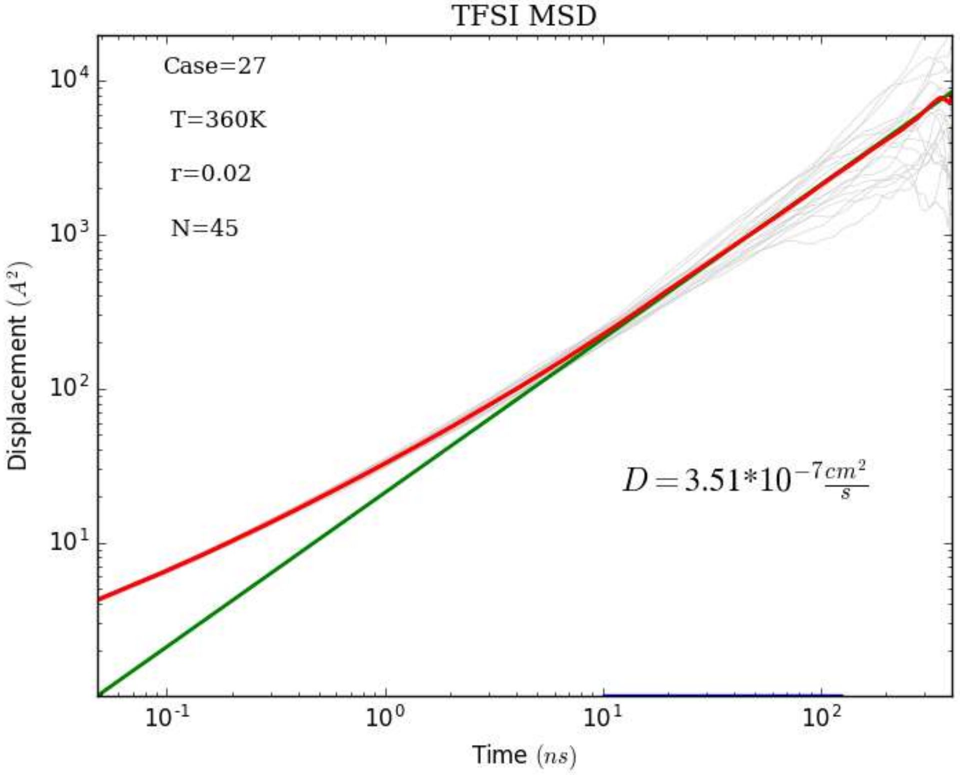

TFSI MSD

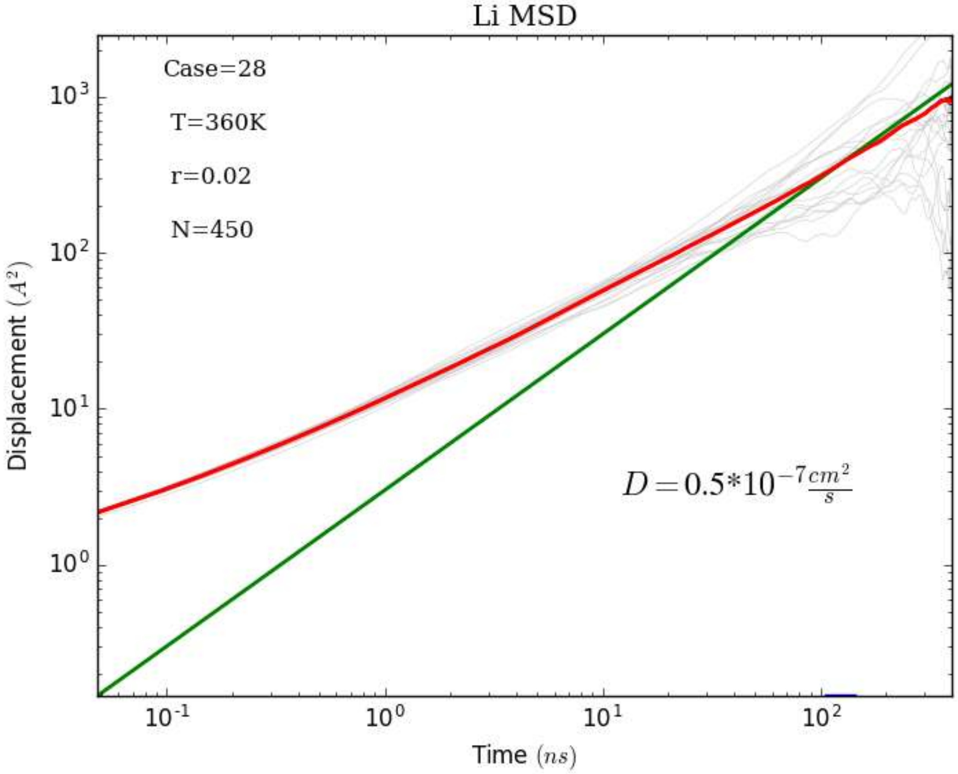
Li MSD
Case=28
T=360K
r=0.02
N=450
$D = 0.5*10^{-7}\frac{cm^2}{s}$
Displacement (A^2)
Time (ns)
10^0
10^1
10^2
10^3
10^{-1}
10^0
10^1
10^2

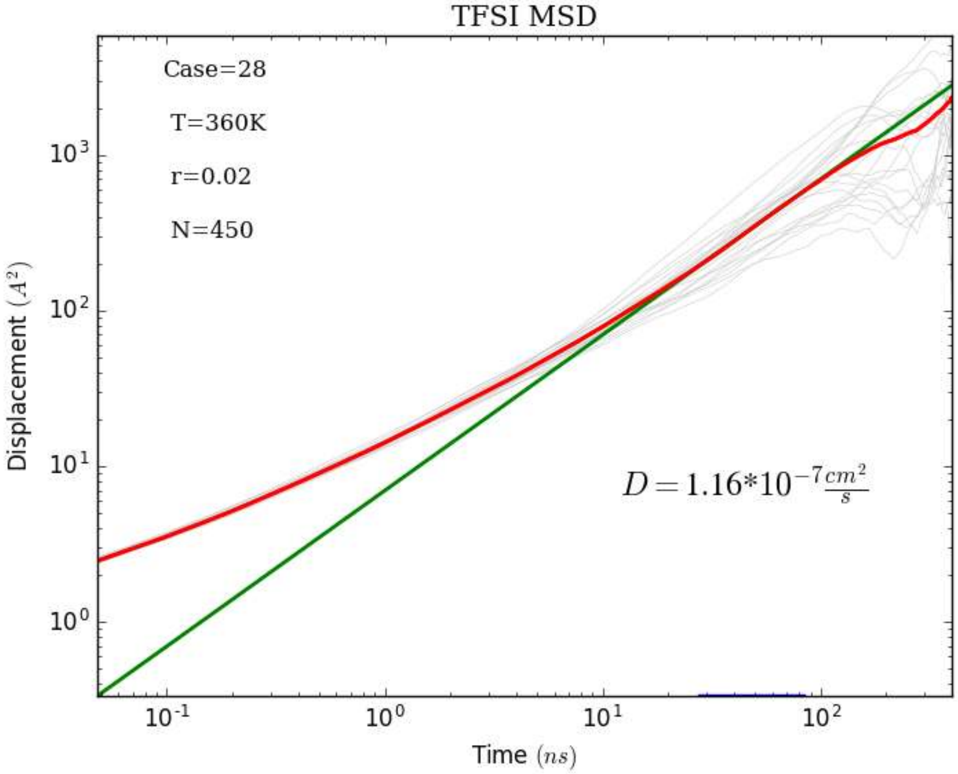
TFSI MSD
Case=28
T=360K
r=0.02
N=450
$D = 1.16*10^{-7}\frac{cm^2}{s}$
Displacement (A^2)
Time (ns)
10^0
10^1
10^2
10^3
10^{-1}
10^0
10^1
10^2

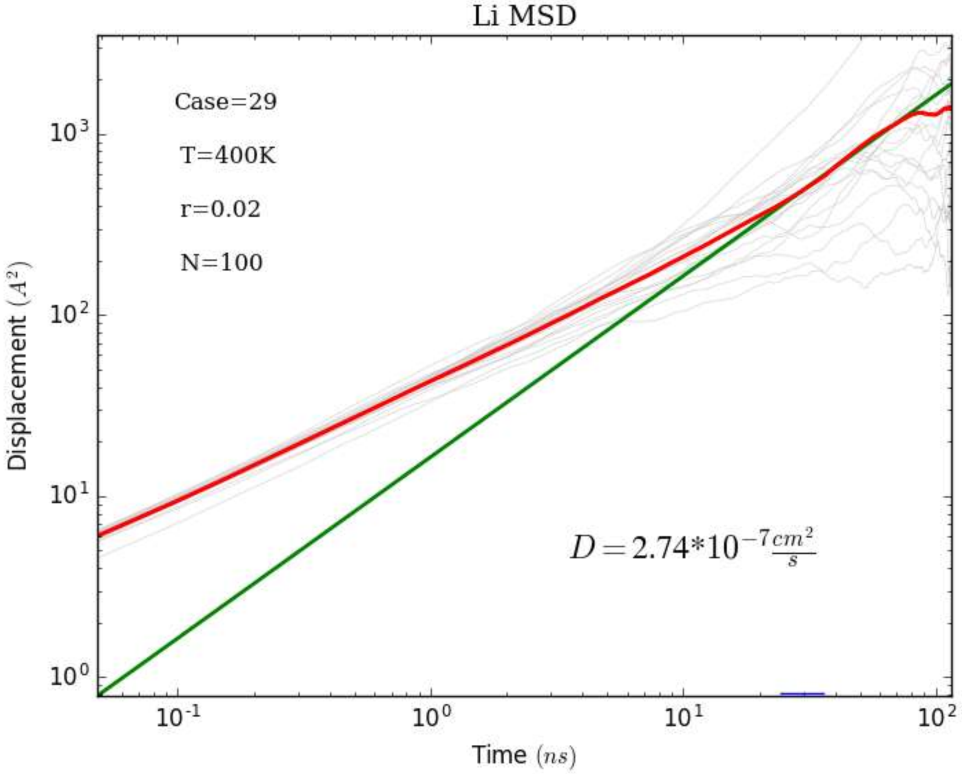
Li MSD
Case=29
T=400K
r=0.02
N=100
$D = 2.74*10^{-7}\frac{cm^2}{s}$
Displacement (A^2)
Time (ns)
10^0
10^1
10^2
10^3
10^{-1}
10^0
10^1
10^2

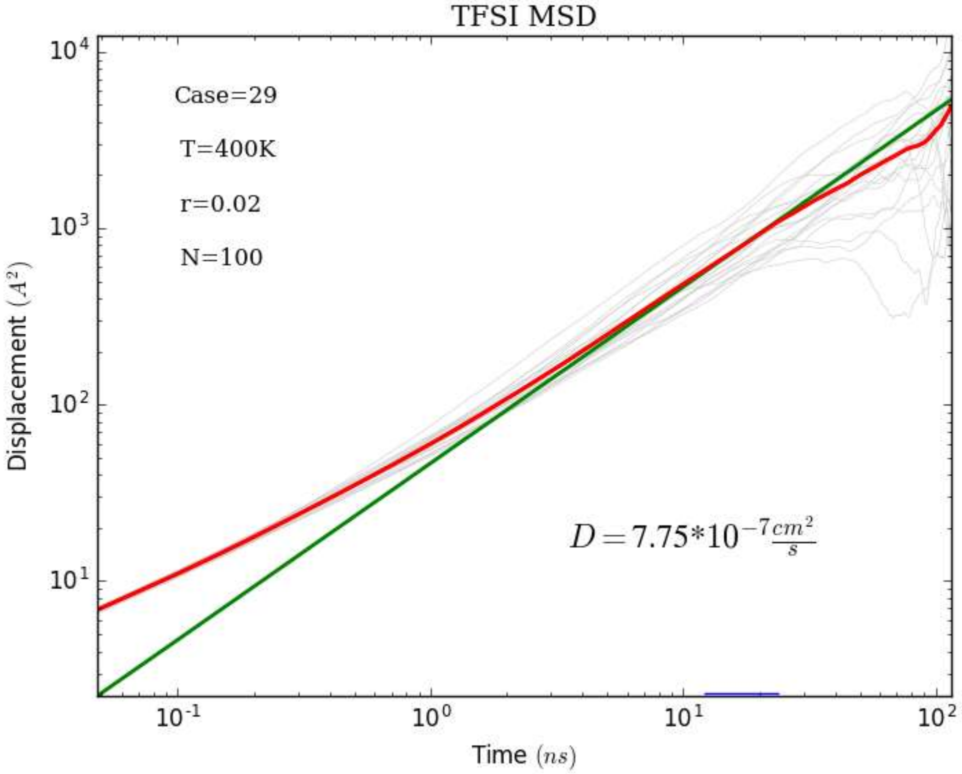
TFSI MSD
Case=29
T=400K
r=0.02
N=100
$D = 7.75*10^{-7}\frac{cm^2}{s}$
Displacement (A^2)
Time (ns)
10^1
10^2
10^3
10^4
10^{-1}
10^0
10^1
10^2

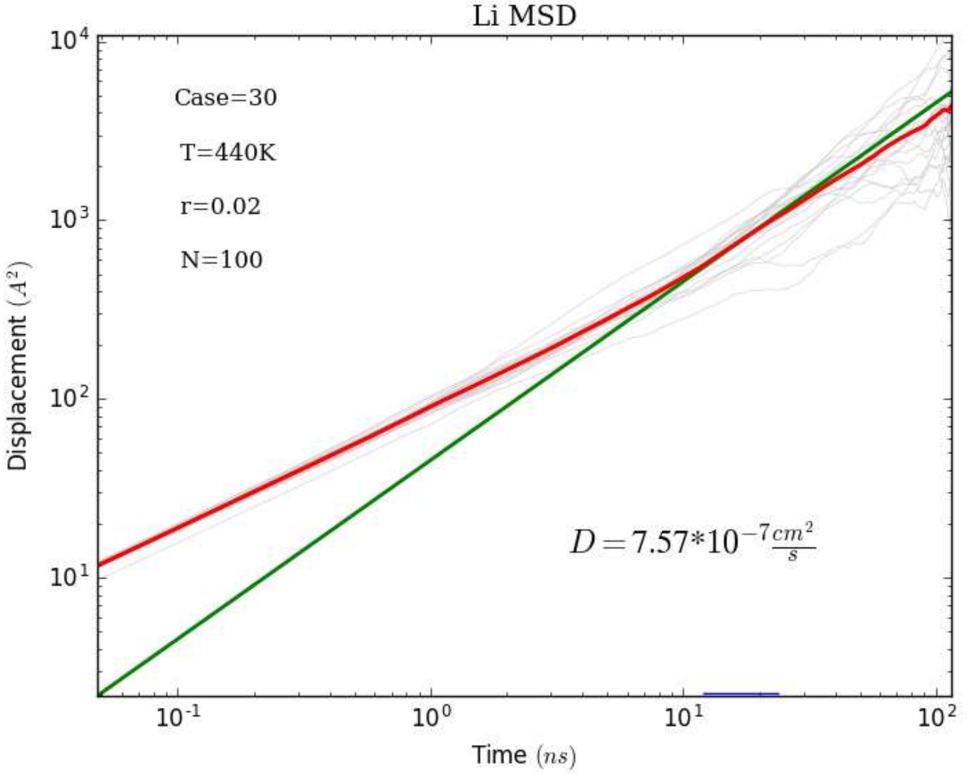
Li MSD
Case=30
T=440K
r=0.02
N=100
$D=7.57*10^{-7}\frac{cm^2}{s}$
Displacement (A^2)
Time (ns)
10^4
10^3
10^2
10^1
10^{-1}
10^0
10^1
10^2

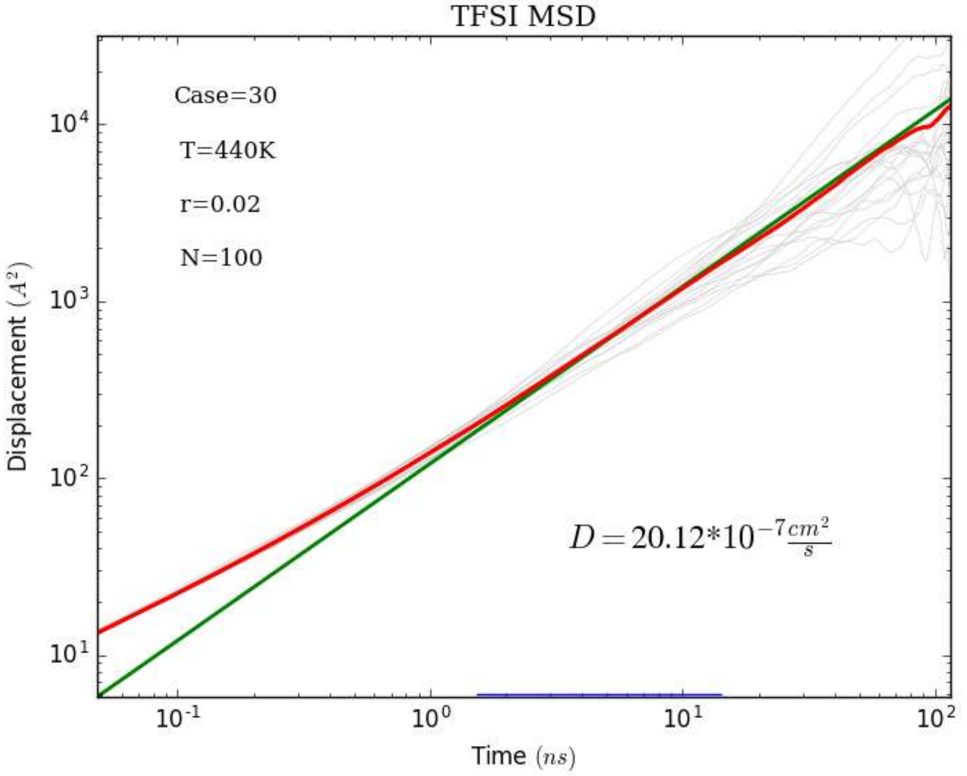
TFSI MSD
Case=30
T=440K
r=0.02
N=100
$D=20.12*10^{-7}\frac{cm^2}{s}$
Displacement (A^2)
Time (ns)
10^4
10^3
10^2
10^1
10^{-1}
10^0
10^1
10^2

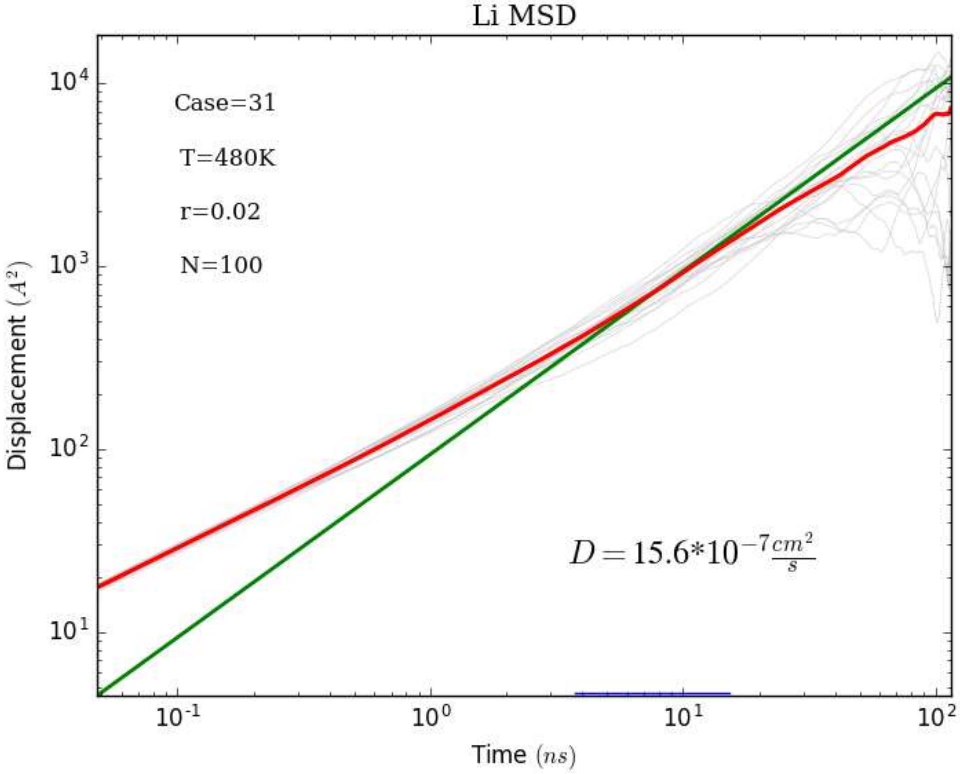
Li MSD
Case=31
T=480K
r=0.02
N=100
$D = 15.6 * 10^{-7} \frac{cm^2}{s}$
Displacement (A^2)
10^1
10^2
10^3
10^4
Time (ns)
10^{-1}
10^0
10^1
10^2

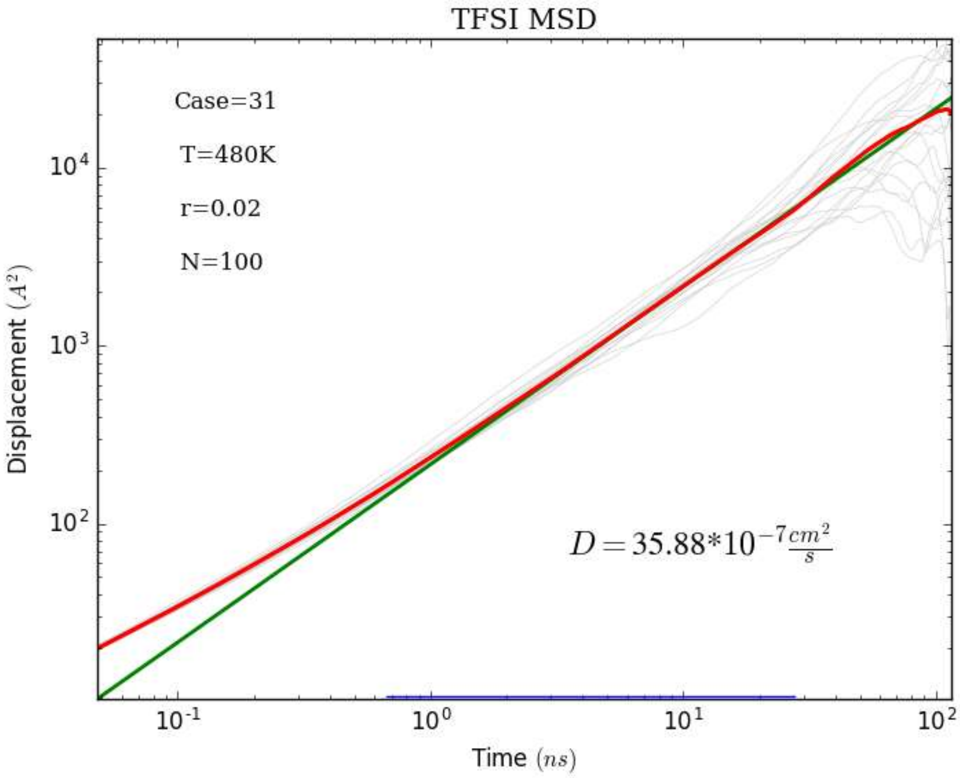
TFSI MSD
Case=31
T=480K
r=0.02
N=100
$D = 35.88 * 10^{-7} \frac{cm^2}{s}$
Displacement (A^2)
10^2
10^3
10^4
Time (ns)
10^{-1}
10^0
10^1
10^2

Appendix D

PQEQ METHOD SUPPORTING INFORMATION

With contributions from Saber Naserifar, William A. Goddard III, and Vaclav Cvcivek

Acknowledgement: The main part of this chapter is published in the Journal of Chemical Physics, 2017, 146(12), pp124117.

1. PQEq and Polarization Models

The first step in any Force Field (FF) simulation, is to establish how to calculate electrostatic interactions. The standard method is to extract partial atomic charges from quantum mechanics (QM) electron densities. There are several different methods to convert QM electron densities to partial atomic charges[100, 101, 104, 213-230]. For organic and biological systems the charges are extracted from QM electron densities using either the Electrostatic Potential (ESP) outside the molecule or the Mulliken Population Approximation (MPA) involving analysis of the occupied molecular orbitals. For macromolecular systems such as polymers, proteins, and nucleic acids, it is too expensive to do QM on the full system, so the QM is done for finite fragments to extract partial atomic charges from QM electron densities. Examples include such FFs are AMBER[159-161], CHARMM[162-164], OPLS[156-158], GROMOS[231, 232], and MMFF[157, 161], which are widely used in biological Molecular Dynamics (MD) and Molecular Mechanics (MM) simulations. This approach becomes cumbersome, for example, for virtual screening of large, million molecule, data bases, where one needs a simpler way to define charges. For inorganics systems QM studies are less useful because the charges depend on the environment and for metal alloys there is no generally accepted way to put charge into the FFs.

Thus, we need a fast accurate method to predict partial atomic charges without carrying out full-scale QM calculations. This was the motivation for Rappé and Goddard to develop the QEq method[103]. QEq uses generic parameters defined for the whole periodic table (up to Lawrencium, Z=103) in terms of valence average ionization energies and standard bond radii. The concept is that the energy of an atom depends on the internal charge plus electrostatic interactions with other atoms, shielded by describing the charge in terms of a local (Slater) orbital having the size of a bond radius to allow electrostatic interactions between bonded atoms, which is very important for inorganic and metallic systems. The internal energy of the atom was assumed to be harmonic so that the parameters could be calculated directly from the atomic ionization potential (IP) and electron affinity (EA), after averaging to reflect the atomic state after forming bond. Then, the charge for any specific geometry was calculated using the condition that the chemical potential be equal on all atoms.

The QEq methods has been used in numerous MD simulations[105, 233-242] and is a part of the generic Universal Force Field (UFF) of Rappé and Goddard[104] and the ReaxFF reactive force field of van Duin and Goddard[106]. However, it was not clear how QEq charges well matched QM. In this paper, we provide a criterion for assessing the accuracy, by calculating the QM energy as point dipole is brought up to a molecule along various axes. QEq when charges are relaxed provide an excellent agreement with QM (see section 8). Adjusting charges comes at a cost; however as described in the paper the precondition Conjugate Gradient method (PCG), minimizes these costs. Fixing the charges of the molecule and keeping the charges fixed, we find that QEq does about the same as fixed charged based on ESP and MPA and is comparable to various fixed charge FFs such as Amber, CHARMM and OPLS. Of course for many systems it is important to allow charges to vary during the MD. In addition, describing the changes in polarization within a molecule or solid during dynamics or in response to an external electric field is crucial in many systems. For example, in ferroelectrics the charges can switch under mechanical stresses. Similarly, in chemical reactions the bond breaking processes change the charge, particularly if reduction-oxidation reactions (Redox) are involved.

Many methods have been proposed for incorporating the electronic polarization effect explicitly in MD/MM simulations[108, 152, 153]. There are four general approaches:

i) shell (Drude oscillator) model[111, 113-115, 124-129, 135, 146, 153, 165, 166, 243-245],

ii) fluctuating charge (FQ) model [104, 107, 112, 117, 154, 168, 239, 246-264],

iii) induced dipole model[118-120, 140, 147-151, 168, 186, 265-275], and

iv) QM-based models[121-123, 130, 152, 276-280].

The details of these methods with their application are given elsewhere[107, 108, 152-154, 281]. Despite the large number of studies performed on polarizable charge equilibration, no general consensus has been reached on a universal applicable model[109].

PQEq combines two well-known models explicit polarization: an electron shell plus QEq variable charge and adds the concept that the core and shell charges are localized over the size of the atom (described with a Gaussian functions). This physical polarization model resolves many of the existing problems in other polarization and charge calculation models.

In this section, we briefly discuss the above explicit polarization models and compare them with PQEq.

i. Shell Model

The shell model[165] is based on the classical Drude oscillator model[166], also referred to as the charge-on-spring method[129]. In this method, an "auxiliary" mobile Drude particle, with or without mass[153], with a fixed charge is attached to atomic center by means of a harmonic spring. The Drude particle accounts for polarization by moving off-center in response to an external electric field. The shell model has been applied in numerous studies, such as modeling of water molecule and other small-molecule systems[124-129], polarization in ion channels[111, 135], hydration of K^+ ions[244], and also for larger systems such as protein systems[113-115, 243], hydration energy calculation[146], systems with monovalent and divalent ions[245]. Results using the shell model have been shown to agree reasonably well with available QM and experimental data, showing its potential for describing such complex systems[153]. However, the shell model suffers from a polarization catastrophe when the atomic centers and/or shells get too close together, leading to overpolarization[153].

PQEq solves the polarization catastrophe problem using a finite sized Gaussian charge distribution, rather than a point charge. As atomic charges and/or shells get very close to each other, even for the extreme case of two atoms or shells at the same point, the shielding of the Gaussians leads to finite interaction energies, avoiding the polarization catastrophe. For the size of the Gaussian functions we use standard bond radii.

ii. Fluctuating Charge (FQ) Model

The FQ models allow the charges to flow between atoms until the chemical potential and electronegativities of the atoms reach to an equilibrium. This, in principle, provides a way to include the polarizability by dynamic coupling of the charge distribution of molecules to the electrostatic environment. The FQ models have been used in several FFs including the universal force field (UFF)[104], CHARMM-FQ[107, 117, 257], ReaxFF, and several other FFs[112, 117, 154, 168, 239, 246-248, 251, 256, 258-260, 262]. A variety of methods to describe the charge fluctuations have been developed. For example, the original charge equilibration model (QEq) with Slater type orbitals[103], the electronegativity equalization method (EEM)[252, 253], partial equalization of orbital electronegativity (PEOE) method[249, 250, 255, 282], split charge equilibration (SQE) method[254], and so on[261, 263, 264, 283-285]. These models were derived based on intuition motivated by rigorous QM calculations. The FQ approach provides a computationally attractive way to include polarization. Of course, such charge equilibration models are essential for reactive MD, where we must allow bond connectivities to change during the MD, requiring frequent updates of the atomic charges. Some FQ methods involve model parameters that must be determined prior to any charge calculation. Here, the parametrization is usually done by fitting the parameters to some reference charges using arbitrary optimization methods. This could result in a set of completely nonphysical parameters, which makes it hard to extend and apply for the new systems. The QEq method avoids this problem by basing the parameters (χ, J, and R_c) on valence averaged IP and EA plus standard atomic radii[103]. The PQEq model differs from the original QEq model by using a Gaussian type orbital to describe the atomic charge distribution rather than Slater type orbital for shielding between atoms. The fact that there was no need to change any of the QEq parameters (χ, J, and R_c) suggests that the exact shape is not so important.

In this paper, we show that some improvements in the accuracy can be made by optimizing the parameters (leading to PQEq1), which might be important for certain classes of materials (protein, nucleic acids, carbohydrates, ferroelectrics). However, we consider the default parameters as adequate for most purposes.

iii. Induced Dipole Model

The induced dipole model incorporates explicit induced dipoles at each of the atomic centers[120, 168] and has been used in several FFs such as polarizable versions of AMBER[186, 274] and OPLS[269], as well in PIPF-CHARMM[275], NEMO[266], SIBFA[268], EFP[267], AMOEBA[270], and QMPFF3[265] to study a wide range of systems such as solvation effect, Lithium battery[140], modeling of DNA strand[119], and carbon nanotubes[147], etc. Similar to shell model, the induced dipole model also suffers from a polarization catastrophe. If the dipoles are positioned too close together, they lead to an infinite polarizability[286, 287]. Some works have tried to solve this problem[288-291] but they do not completely grantee the problem of overpolarization[292, 293].

iv. QM-based Model

Another strategy is to performing the QM calculation only on a small part of the system whose polarization is important with the remainder described with some charge model[152]. This QM/MM methodology is used for large molecular systems to combine QM (for small regions) and MM (for most of the atoms or degrees of freedom). This approach has been used in applications such to model enzymatic reactions inside the binding site of proteins, protein–ligand docking [121, 122], water[130], and peptides[123]. There are several published reviews about application and implementation of this method[122, 276, 277, 279, 280]. QM/MM can become prohibitively expensive if the QM region is too large. To overcome on this problem, there have been attempts to parameterize FF potentials with QM data to predict the forces and multipoles of large systems[278] but this may lead to numerous parameters with little physical meaning introduced into the potentials[108].

2. The Limitations of Point Charges from QM Calculations

The normal practice in most of the FFs is to use QM charges obtained for molecules or fragments of the whole system as reference data points. These QM charges are computed by converting the electron density to partial atomic charges based on electron population analysis (EPA). There are variety of methods for doing EPA since partial atomic charges are not observable characteristics of the molecules. The EPA methods can be classified into three groups. In group I methods, the charges are obtained by direct partitioning of the molecular wave function into atomic contributions based on an arbitrary, orbital-based scheme such as Mulliken population analysis (MPA)[101], Löwdin population analysis (LPA)[220, 224], renormalized LPA (RLPA)[228], and Natural population analysis (NPA)[226]. In group II methods, charges are computed based on analysis of a physical observable (e.g., dipole moment and electrostatic potential), which is calculated from the electronic wave function. Examples of group II are electrostatic potential (ESP)[100, 215, 219, 229], restricted ESP[214, 218], ESP for periodic systems[216, 225], generalized atomic polar tensor (GAPT)[217], atoms-in-molecules (AIM)[213], and Voronoi deformation density (VDD)[221]. In group III methods, charges are derived through a semi-empirical mapping of the initial charges (from groups I and II) in order to reproduce an experimentally determined observable, for example, charge models 1-3 (CM1-3)[222, 223, 227, 230]. However, there are limitations to each class of methods. Group I methods can have problems with orbital-based population analysis, group II methods can produce an ill-conditioned conformational dependence of the partial charges, and group III methods are reliant on the availability of experimental data [294]. In particular, the limitations of the widely used MPA and ESP methods are discussed here.

With MPA, a very arbitrary partition is made of the molecular orbital contributions to the net charge by putting half of the shared electron equally between the atoms that sharing basis functions reside. This rule can introduce errors in final charges for atoms that have very different electronegativities and ignores the role of lone pairs. For example, in a simple molecule like CCl_4 one expects the electronegative Cl atom to take on a smaller charge compare to C atom. MPA, however, gives partial charges of +0.09 and -0.36 for Cl and C respectively, using the standard B3LYP functional and 6-31G** basis set. The original MPA methods also uses the non-orthogonal basis set which can lead to some undesirable results. In addition, the charges computed from MPA depend on the basis set that is used. Figure S1 shows how MPA charges for different DFT functionals and basis sets for a cyclohexane molecule. Using a very complete basis set might seem to be a solution for this problem but it actually could result in unphysically large charges. Several other QM methods such as NPA, LPA, and RLPA have tried to resolve the problems with MPA method but they also reflect their own errors[294].

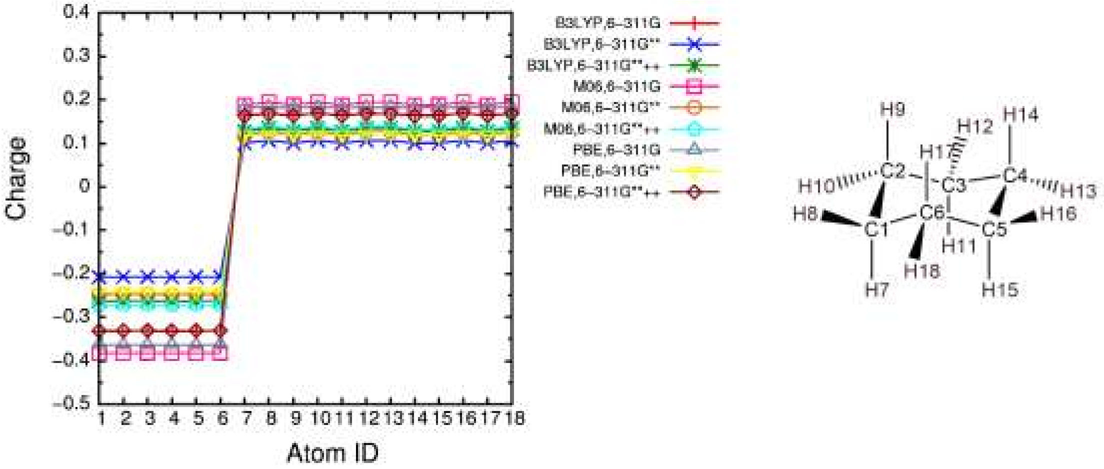

Figure S1: MPA partial charge comparison using different basis sets and DFT functionals for cyclohexane molecule. The position of each atom for the corresponding ID is shown on the molecular structure schematic on the right.

The ESP method fits partial charges to the electrostatic potential obtained from QM. This method performs well for simple geometries. For complex geometries, the fitting procedure can become ill-conditioned, with small changes in geometry leading to large changes in charges, particularly for atoms that are far from the van der Waals (VDW) molecular surface. This is clearly shown in Figure S2,**Figure S2**: The comparison between the potential energies computed using QM (black), Dreiding FF using ESP (red), and Dreiding FF using MPA (blue) charges. The HF molecule is scanned with respect to the oxygen atom in the isoxazole molecule. The ESP fails to compute the charges correctly when intermolecular interaction of molecules becomes important inside the VDW surface. where an HF molecule is scanned with respect to the oxygen atom in the isoxazole molecule. The charges at each distance are computed by using both MPA and ESP method and then used in conjunction with the Dreiding FF[295] to plot the potential energies versus the QM energy. In this case, ESP fails to compute the charges correctly when intermolecular interaction of molecules becomes important inside the VDW surface of isoxazole and HF molecules. More details regarding the limitations of MPA, ESP, and other charge calculation methods can be found elsewhere[294, 296, 297].

In order to validate the accuracy of PQEq and to provide a criterion for optimization of the parameters, we need to decide what criteria to use for comparison and optimization. In order to provide a meaningful comparison with QM, we propose using the polarization of QM electrostatic potential energy.

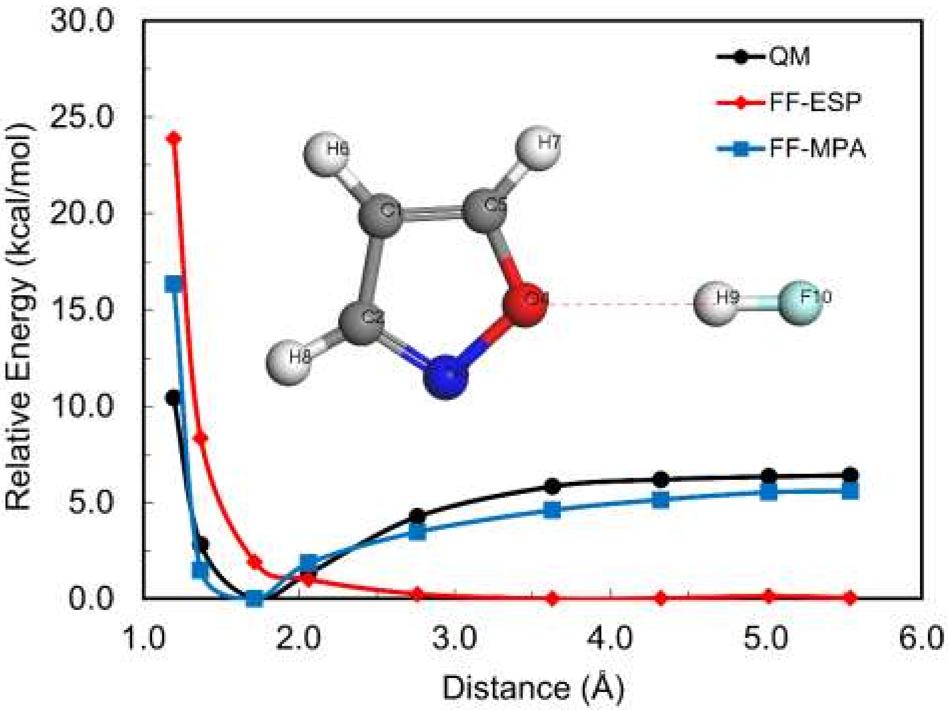

Figure S2: The comparison between the potential energies computed using QM (black), Dreiding FF using ESP (red), and Dreiding FF using MPA (blue) charges. The HF molecule is scanned with respect to the oxygen atom in the isoxazole molecule. The ESP fails to compute the charges correctly when intermolecular interaction of molecules becomes important inside the VDW surface.

Parameter Sets for PQEq and PQEq1

Table S1. The electronegativity (χ), idempotential (J), shell charge (-Z), atomic covalent radius (R_c=R_s), and spring force constant (K_s) parameters of the PQEq. The units of the parameters are given in the parentheses.

Atom	χ (eV)	J (eV)	Z	R_c=R_s (Å)	K_s (kcal/mol/Å^2)
H	4.52800	12.98410	1.00000	0.37100	2037.20061
He	9.66000	29.84000	1.00000	1.30000	1619.41057
Li	3.00600	4.77200	1.00000	1.55700	13.64832
Be	4.87700	8.88600	1.00000	1.24000	59.29709
B	5.11000	9.50000	1.00000	0.82200	109.59198
C	5.34300	10.12600	1.00000	0.75900	198.84054
N	6.89900	11.76000	1.00000	0.71500	301.87609
O	8.74100	13.36400	1.00000	0.66900	414.04451
F	10.87400	14.94800	1.00000	0.70600	596.16463
Ne	11.04000	21.10000	1.00000	1.76800	842.11732
Na	2.84300	4.59200	1.00000	2.08500	13.77286
Mg	3.95100	7.38600	1.00000	1.50000	31.32676
Al	4.06000	7.18000	1.00000	1.20100	48.83290
Si	4.16800	6.97400	1.00000	1.17600	60.04769
P	5.46300	8.00000	1.00000	1.10200	91.47760
S	6.92800	8.97200	1.00000	1.04700	114.50472
Cl	8.56400	9.89200	1.00000	0.99400	152.32280
Ar	9.46500	12.71000	1.00000	2.10800	202.34215
K	2.42100	3.84000	1.00000	2.58600	7.71165
Ca	3.23100	5.76000	1.00000	2.00000	14.56420
Sc	3.39500	6.16000	1.00000	1.75000	18.65526
Ti	3.47000	6.76000	1.00000	1.60700	22.74409
V	3.65000	6.82000	1.00000	1.47000	26.77933
Cr	3.41500	7.73000	1.00000	1.40200	28.62618
Mn	3.32500	8.21000	1.00000	1.53300	35.32593
Fe	3.76000	8.28000	1.00000	1.39300	39.53139
Co	4.10500	8.35000	1.00000	1.40600	44.27516
Ni	4.46500	8.41000	1.00000	1.39800	48.83290
Cu	3.72900	5.00200	1.00000	1.43400	53.55866
Zn	5.10600	8.57000	1.00000	1.40000	57.75021
Ga	3.64100	6.32000	1.00000	1.21100	40.89454
Ge	4.05100	6.87600	1.00000	1.18900	56.86022
As	5.18800	7.61800	1.00000	1.20400	77.04494
Se	6.42800	8.26200	1.00000	1.22400	88.08056
Br	7.79000	8.85000	1.00000	1.14100	108.87334

Atom	χ (eV)	J (eV)	Z	R_c=R_s (Å)	K_s (kcal/mol/Å^2)
Kr	8.50500	11.43000	1.00000	2.27000	133.65952
Rb	2.33100	3.69200	1.00000	2.77000	7.02929
Sr	3.02400	4.88000	1.00000	2.41500	12.03129
Y	3.83000	5.62000	1.00000	1.99800	14.62836
Zr	3.40000	7.10000	1.00000	1.75800	18.55104
Nb	3.55000	6.76000	1.00000	1.60300	21.15055
Mo	3.46500	7.51000	1.00000	1.53000	25.94248
Tc	3.29000	7.98000	1.00000	1.50000	29.12839
Ru	3.57500	8.03000	1.00000	1.50000	34.58997
Rh	3.97500	8.01000	1.00000	1.50900	38.61206
Pd	4.32000	8.00000	1.00000	1.54400	69.17994
Ag	4.43600	6.26800	1.00000	1.62200	48.97695
Cd	5.03400	7.91400	1.00000	1.60000	45.11735
In	3.50600	5.79200	1.00000	1.40400	32.55526
Sn	3.98700	6.24800	1.00000	1.35400	52.87639
Sb	4.89900	6.68400	1.00000	1.40400	50.31268
Te	5.81600	7.05200	1.00000	1.38000	60.37522
I	6.82200	7.52400	1.00000	1.33300	62.06798
Xe	7.59500	9.95000	1.00000	2.45900	82.11269
Cs	2.18300	3.42200	1.00000	2.98400	5.58842
Ba	2.81400	4.79200	1.00000	2.44200	8.36432
La	2.83550	5.48300	1.00000	2.07100	10.67729
Ce	2.77400	5.38400	1.00000	1.92500	11.21837
Pr	2.85800	5.12800	1.00000	2.00700	11.77531
Nd	2.86850	5.24100	1.00000	2.00700	10.57528
Pm	2.88100	5.34600	1.00000	2.00000	11.03202
Sm	2.91150	5.43900	1.00000	1.97800	11.52999
Eu	2.87850	5.57500	1.00000	2.22700	11.98786
Gd	3.16650	5.94900	1.00000	1.96800	14.13037
Tb	3.01800	5.66800	1.00000	1.95400	13.02211
Dy	3.05550	5.74300	1.00000	1.93400	13.55362
Ho	3.12700	5.78200	1.00000	1.92500	14.07050
Er	3.18650	5.82900	1.00000	1.91500	14.62836
Tm	3.25140	5.86580	1.00000	2.00000	15.23228
Yb	3.28890	5.93000	1.00000	2.15800	15.88822
Lu	2.96290	4.92580	1.00000	1.89600	15.16273
Hf	3.70000	6.80000	1.00000	1.75900	20.49776
Ta	5.10000	5.70000	1.00000	1.60500	25.34837
W	4.63000	6.62000	1.00000	1.53800	29.91565
Re	3.96000	7.84000	1.00000	1.60000	34.23337

Atom	χ (eV)	J (eV)	Z	R_c=R_s (Å)	K_s (kcal/mol/Å^2)
Os	5.14000	7.26000	1.00000	1.70000	39.06632
Ir	5.00000	8.00000	1.00000	1.86600	43.69259
Pt	4.79000	8.86000	1.00000	1.55700	51.08672
Au	4.89400	5.17200	1.00000	1.61800	57.25236
Hg	6.27000	8.32000	1.00000	1.60000	66.14815
Tl	3.20000	5.80000	1.00000	1.53000	43.69259
Pb	3.90000	7.06000	1.00000	1.44400	47.57360
Bi	4.69000	7.48000	1.00000	1.51400	44.87347
Po	4.21000	8.42000	1.00000	1.48000	48.83290
At	4.75000	9.50000	1.00000	1.47000	55.34395
Rn	5.37000	10.74000	1.00000	2.20000	62.65353
Fr	2.00000	4.00000	1.00000	2.30000	6.83259
Ra	2.84300	4.86800	1.00000	2.20000	8.67007
Ac	2.83500	5.67000	1.00000	2.10800	10.34466
Th	3.17500	5.81000	1.00000	2.01800	10.34466
Pa	2.98500	5.81000	1.00000	1.80000	13.07337
U	3.34100	5.70600	1.00000	1.71300	13.33589
Np	3.54900	5.43400	1.00000	1.80000	13.38967
Pu	3.24300	5.63800	1.00000	1.84000	13.55362
Am	2.98950	6.00700	1.00000	1.94200	14.25166
Cm	2.83150	6.37900	1.00000	1.90000	14.43755
Bk	3.19350	6.07100	1.00000	1.90000	14.62836
Cf	3.19700	6.20200	1.00000	1.90000	16.19823
Es	3.33300	6.17800	1.00000	1.90000	16.85603
Fm	3.40000	6.20000	1.00000	1.90000	13.95226
Md	3.47000	6.22000	1.00000	1.90000	18.24526
No	3.47500	6.35000	1.00000	1.90000	20.24779
Lr	3.50000	6.40000	1.00000	1.90000	N/A

Table S2. The electronegativity (χ), idempotential (J), shell charge ($-Z$), atomic covalent radius (R_c=R_s), and spring force constant (K_s) parameters of the PQEq1. For PQEq1, only χ and J parameters are optimized for the atoms shown in the table. The units of the parameters are given in the parentheses.

Atom	χ (eV)	J (eV)	Z	R_c=R_s (Å)	K_s (kcal/mol/Å^2)
H	4.72484	15.57338	1.00000	0.371	2037.20061
C	5.50813	9.81186	1.00000	0.759	198.84054
N	7.78778	10.80315	1.00000	0.715	301.87609
O	8.30811	14.66128	1.00000	0.669	414.04451
F	8.70340	17.27715	1.00000	0.706	596.16463
Si	4.80466	6.45956	1.00000	1.176	60.04769
P	6.52204	7.13703	1.00000	1.102	91.47760
S	8.19185	8.64528	1.00000	1.047	114.50472
Cl	8.20651	9.73890	1.00000	0.994	152.32280

Table S3. The absolute percent change of the optimized electronegativity (χ) and idempotential (J) in PQEq1 compare to PQEq.

Atom	χ_{PQEq} (eV)	χ_{PQEq1} (eV)	%$\Delta\chi/\chi$	J_{PQEq} (eV)	J_{PQEq1} (eV)	%$\Delta J/J$
H	4.52800	4.72484	4.35	12.98410	15.57338	19.94
C	5.34300	5.50813	3.09	10.12600	9.81186	3.10
N	6.89900	7.78778	12.88	11.76000	10.80315	8.14
O	8.74100	8.30811	4.95	13.36400	14.66128	9.71
F	10.87400	8.70340	19.96	14.94800	17.27715	15.58
Si	4.16800	4.80466	15.27	6.97400	6.45956	7.38
P	5.46300	6.52204	19.39	8.00000	7.13703	10.79
S	6.92800	8.19185	18.24	8.97200	8.64528	3.64
Cl	8.56400	8.20651	4.17	9.89200	9.73890	1.55

The Electric Dipole Scan Over the Molecular Test Set

Figure S3 shows the comparison between the electrostatic energies computed by QM, PQEq, and PQEq1 for the scan of the electric dipole at different distances for the first 4 of all 68 cases. The dipole scan directions are shown with the dotted lines on the molecular structure schematics for each case. We probe each molecule database structure with a pair of ±1 point charges separated by 1 Å to describe both dipole and higher order multipoles of the corresponding system. The QM energy is computed using the standard B3LYP hybrid flavor of DFT, including both the generalized gradient approximation and a component of the exact Hartree–Fock (HF) exchange[175-179]. These calculations were performed with the 6-311G(d,p) (or 6-311G**++) basis set[180].

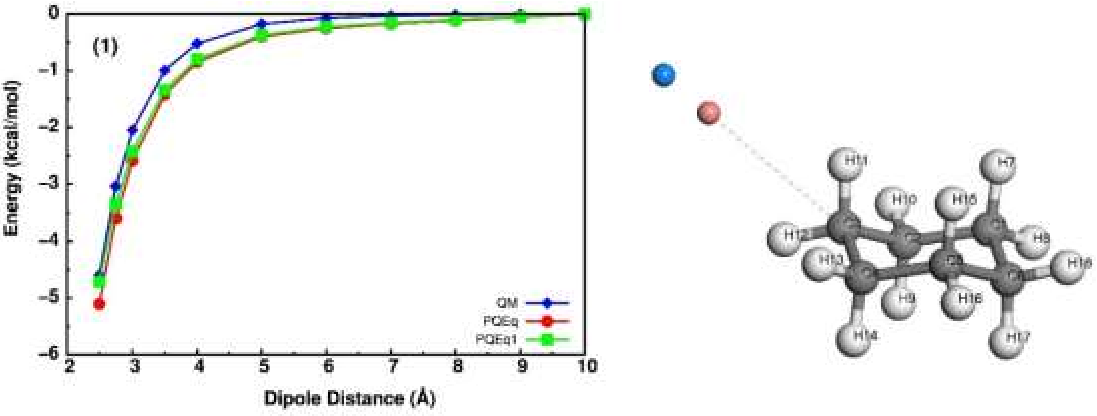

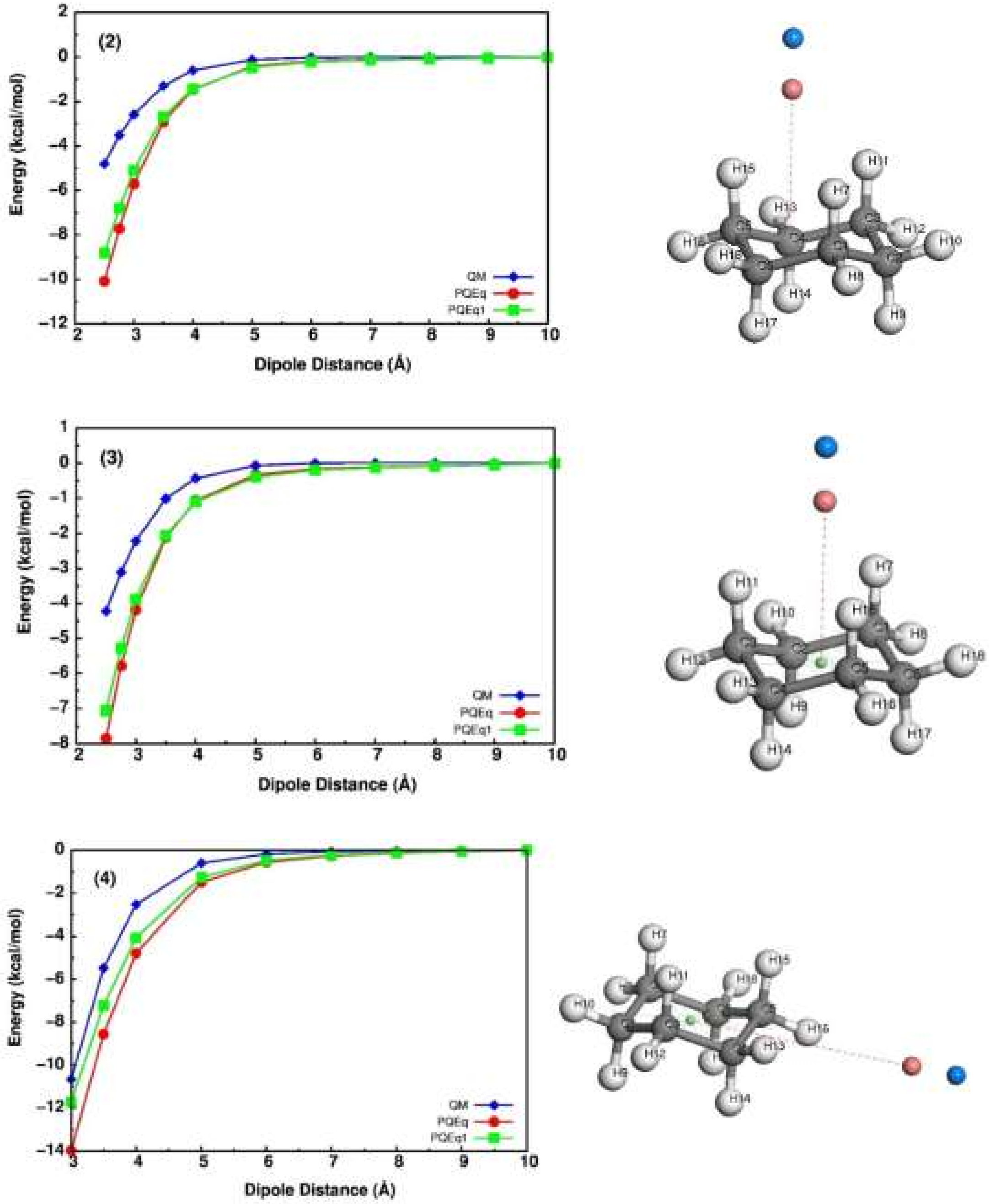

Figure S3. Electrostatic interaction energies of an electric dipole near the database molecular structures computed by QM (blue), PQEq (red), and PQE1 (green). Scan axes are selected along a variety of symmetry directions to provide insight about the polarization effect for the corresponding element including H, C, N, O, F, Si, P, S, and Cl. The molecular structure configuration with the scan direction (dotted line) of the electric dipole for each case is shown on the right side. The ±1 electric dipole is shown with small solid spheres. The positive (red) and negative (blue) heads of the dipole form an angle of 180° (dotted line) with the reference point.

PQEq and QEq versus Fixed Charge Calculation Models

Figure S4 compares the dipole electrostatic interaction energies (for the first 4 of 68 cases) from QM, PQEq, and PQEq1 with the results from ESP, MPA, OPLS, AMBER, QEq with variable charges, and QEq with fixed charges (denoted as QEq0). Here QEq and QEq0 refer to the QEq part of PQEq in which the shell polarization is turned off.

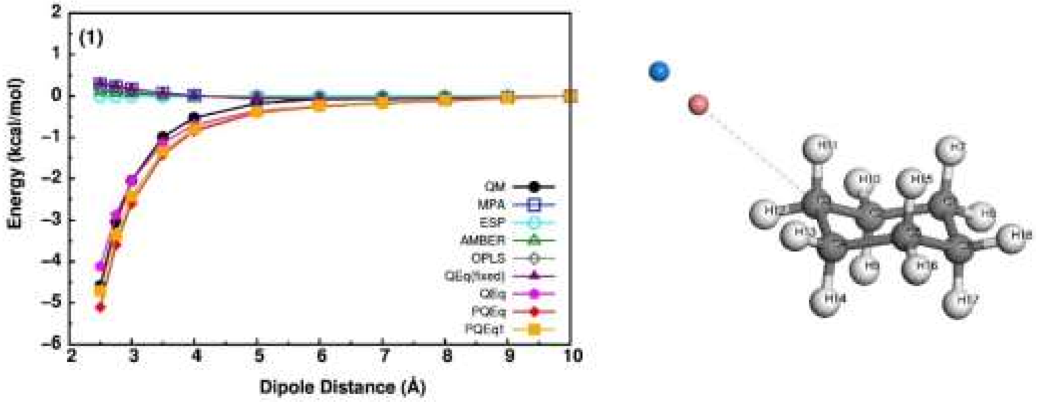

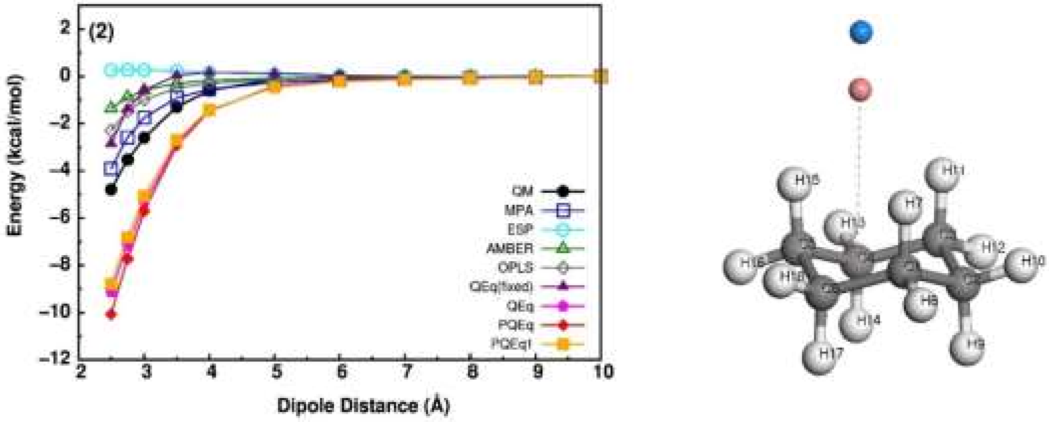

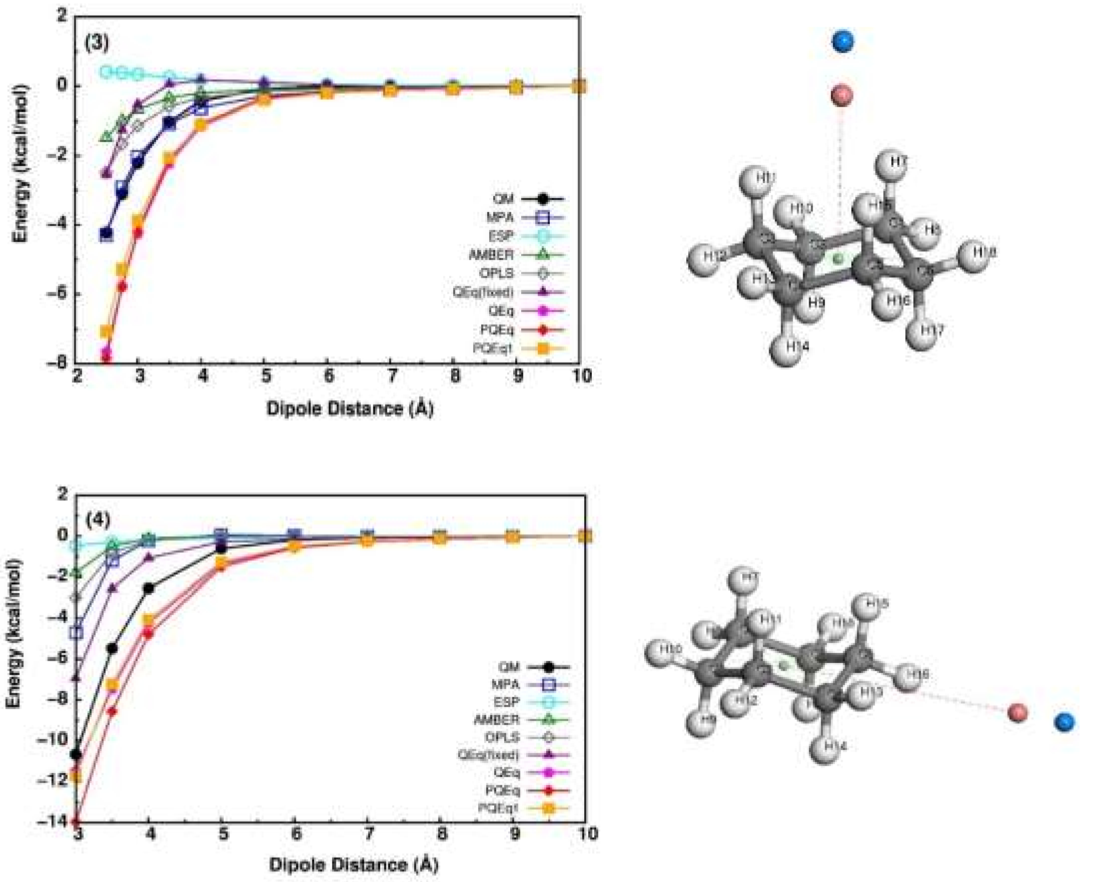

Figure S4. Electrostatic interaction energies as an electric dipole is brought up to molecular structures (68 cases) computed by QM, PQEq, and PQEq1, QEq0, compared with the interactions from fixed charge models: ESP, MPA, OPLS, AMBER, and QEq0. Here QEq and QEq0 is from the QEq part of the PQEq, with shell polarization turning off. The inset of each subfigure shows the molecular structure configuration with the scan direction (dotted line).

Additional data on the 68 training set structures, charges, and interaction energies is available through the supplementary material available at: doi: 10.1063/1.4978891.

Appendix E

TESTING PQEQ DAMPING

Undamped PQEq charges during high temperature (480K) simulations resulted in the runaway motion of lithium atoms. In order to address this issue, a damping scheme was implemented. Charges for a new timestep t are computed as a fraction λ of the computed charge, and a fraction (1- λ) of the charge from the previous step:

$$q_t = \lambda q_c + (1 - \lambda) q_{t-1} \tag{1}$$

Shell positions are updated using the same scheme:

$$\vec{r}_t = \lambda \vec{r}_c + (1 - \lambda) \vec{r}_{t-1} \tag{2}$$

In order to understand the effect of damping, a series of tests were run. The PQEq simulation at 480K/r=0.02/N=100 was extended for 500fs over a range of damping factors (λ=1, 0.1, 0.01, 0.001) and the trajectories of each lithium were recorded. To differentiate between charge and shell position damping, the first test was run using the QEq model ($\vec{r}_t = 0$):

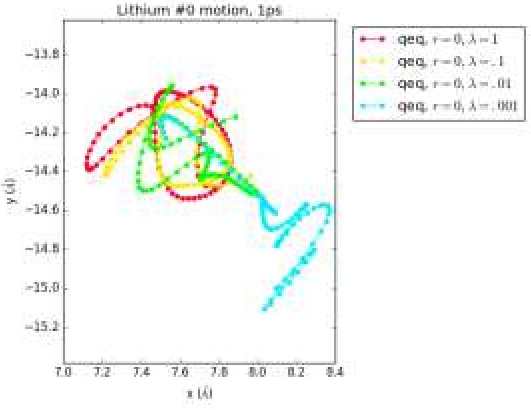

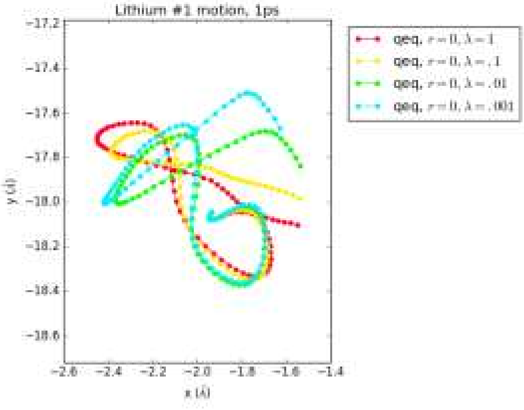

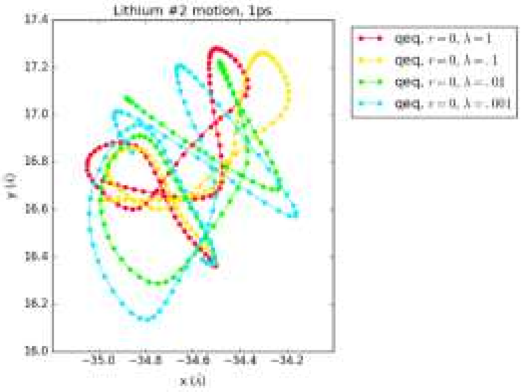
Lithium #2 motion, 1ps
17.4
17.2
17.0
16.8
16.6
16.4
16.2
16.0
y (Å)
−35.0
−34.8
−34.6
−34.4
−34.2
x (Å)
qeq, $r=0, \lambda=1$
qeq, $r=0, \lambda=.1$
qeq, $r=0, \lambda=.01$
qeq, $r=0, \lambda=.001$

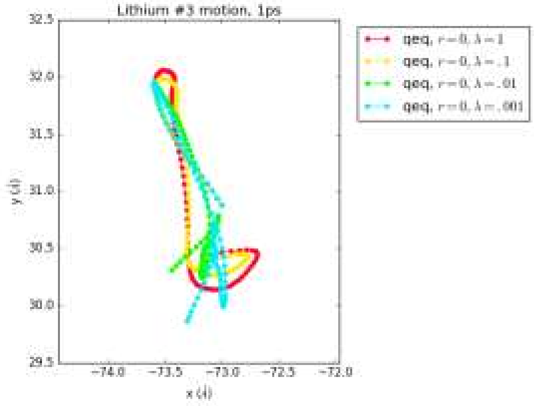
Lithium #3 motion, 1ps
32.5
32.0
31.5
31.0
30.5
30.0
29.5
y (Å)
−74.0
−73.5
−73.0
−72.5
−72.0
x (Å)
qeq, $r=0, \lambda=1$
qeq, $r=0, \lambda=.1$
qeq, $r=0, \lambda=.01$
qeq, $r=0, \lambda=.001$

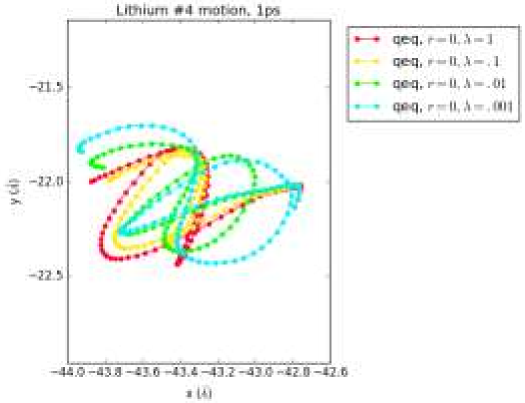
Lithium #4 motion, 1ps
−21.5
−22.0
−22.5
y (Å)
−44.0
−43.8
−43.6
−43.4
−43.2
−43.0
−42.8
−42.6
x (Å)
qeq, $r=0, \lambda=1$
qeq, $r=0, \lambda=.1$
qeq, $r=0, \lambda=.01$
qeq, $r=0, \lambda=.001$

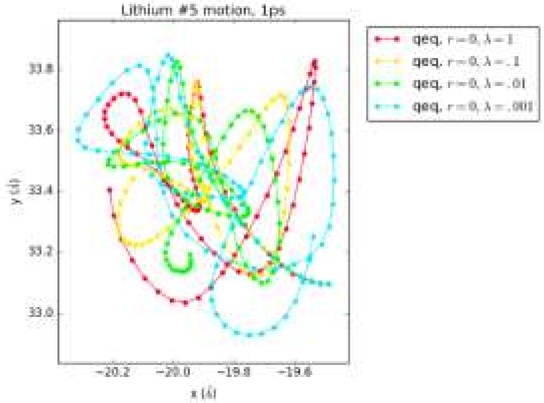
Lithium #5 motion, 1ps
33.8
33.6
33.4
33.2
33.0
y (Å)
−20.2
−20.0
−19.8
−19.6
x (Å)
qeq, $r=0, \lambda=1$
qeq, $r=0, \lambda=.1$
qeq, $r=0, \lambda=.01$
qeq, $r=0, \lambda=.001$

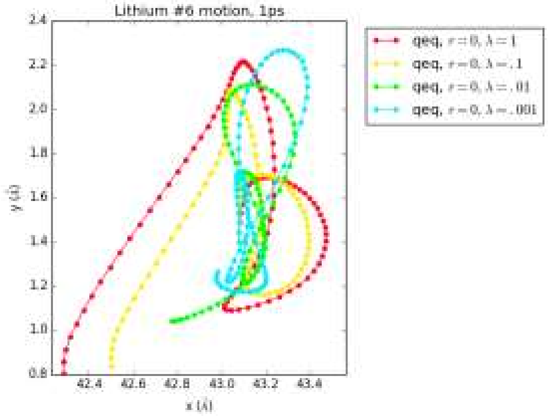
Lithium #6 motion, 1ps
2.4
2.2
2.0
1.8
1.6
1.4
1.2
1.0
0.8
y (Å)
42.4
42.6
42.8
43.0
43.2
43.4
x (Å)
qeq, $r=0, \lambda=1$
qeq, $r=0, \lambda=.1$
qeq, $r=0, \lambda=.01$
qeq, $r=0, \lambda=.001$

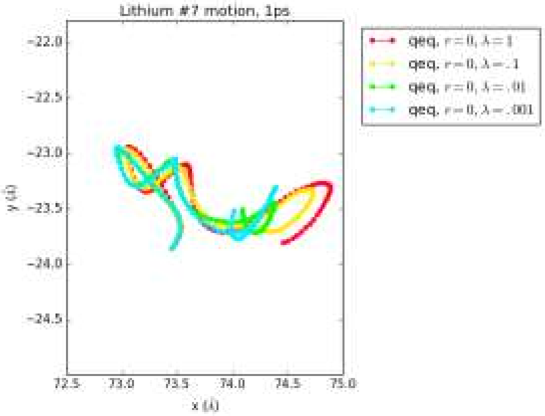
Lithium #7 motion, 1ps
−22.0
−22.5
−23.0
−23.5
−24.0
−24.5
y (Å)
72.5
73.0
73.5
74.0
74.5
75.0
x (Å)
qeq, $r=0, \lambda=1$
qeq, $r=0, \lambda=.1$
qeq, $r=0, \lambda=.01$
qeq, $r=0, \lambda=.001$

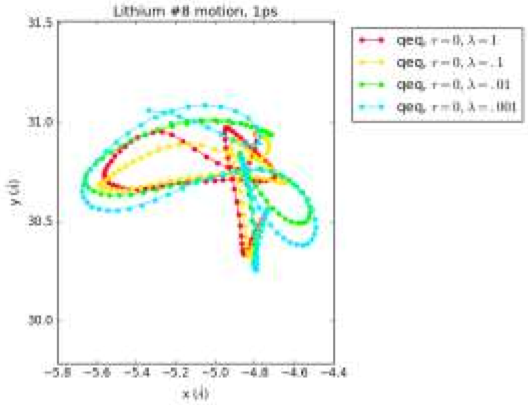
Lithium #8 motion, 1ps
qeq, $r=0, \lambda=1$
qeq, $r=0, \lambda=.1$
qeq, $r=0, \lambda=.01$
qeq, $r=0, \lambda=.001$
31.5
31.0
30.5
30.0
y (Å)
−5.8 −5.6 −5.4 −5.2 −5.0 −4.8 −4.6 −4.4
x (Å)

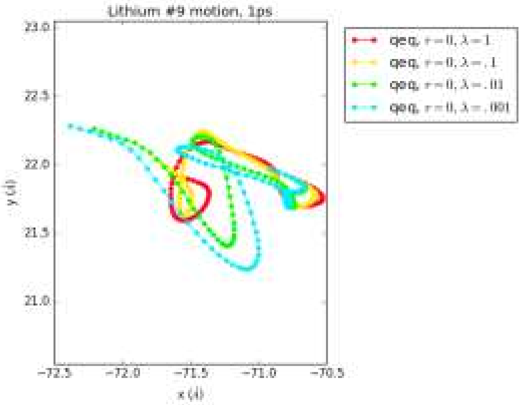
Lithium #9 motion, 1ps
qeq, $r=0, \lambda=1$
qeq, $r=0, \lambda=.1$
qeq, $r=0, \lambda=.01$
qeq, $r=0, \lambda=.001$
23.0
22.5
22.0
21.5
21.0
y (Å)
−72.5 −72.0 −71.5 −71.0 −70.5
x (Å)

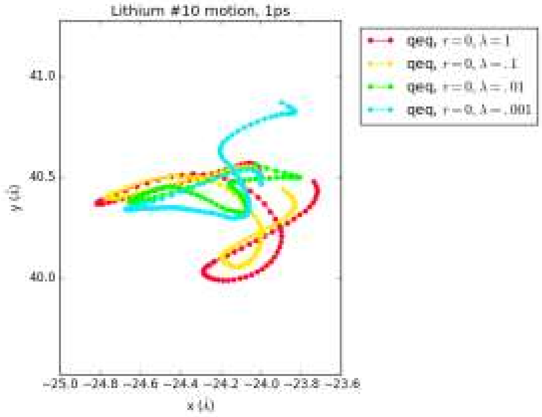
Lithium #10 motion, 1ps
qeq, $r=0, \lambda=1$
qeq, $r=0, \lambda=.1$
qeq, $r=0, \lambda=.01$
qeq, $r=0, \lambda=.001$
41.0
40.5
40.0
y (Å)
−25.0 −24.8 −24.6 −24.4 −24.2 −24.0 −23.8 −23.6
x (Å)

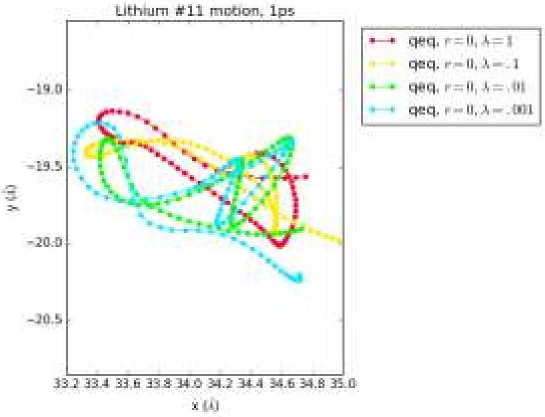
Lithium #11 motion, 1ps
qeq, $r=0, \lambda=1$
qeq, $r=0, \lambda=.1$
qeq, $r=0, \lambda=.01$
qeq, $r=0, \lambda=.001$
−19.0
−19.5
−20.0
−20.5
y (Å)
33.2 33.4 33.6 33.8 34.0 34.2 34.4 34.6 34.8 35.0
x (Å)

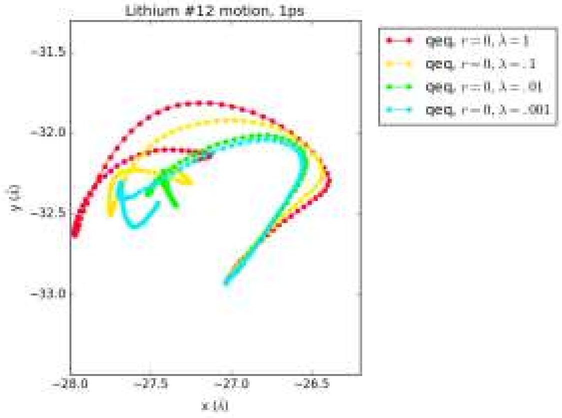
Lithium #12 motion, 1ps
qeq, $r=0, \lambda=1$
qeq, $r=0, \lambda=.1$
qeq, $r=0, \lambda=.01$
qeq, $r=0, \lambda=.001$
−31.5
−32.0
−32.5
−33.0
y (Å)
−28.0 −27.5 −27.0 −26.5
x (Å)

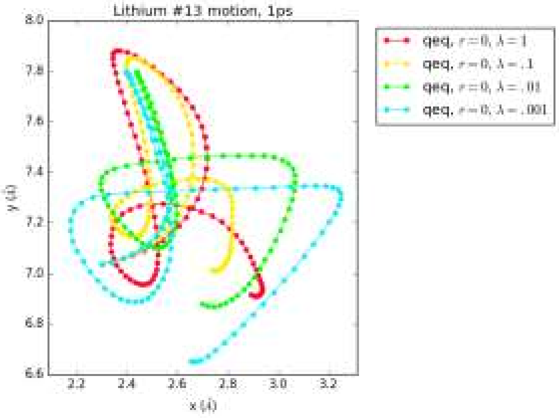
Lithium #13 motion, 1ps
qeq, $r=0, \lambda=1$
qeq, $r=0, \lambda=.1$
qeq, $r=0, \lambda=.01$
qeq, $r=0, \lambda=.001$
8.0
7.8
7.6
7.4
7.2
7.0
6.8
6.6
y (Å)
2.2 2.4 2.6 2.8 3.0 3.2
x (Å)

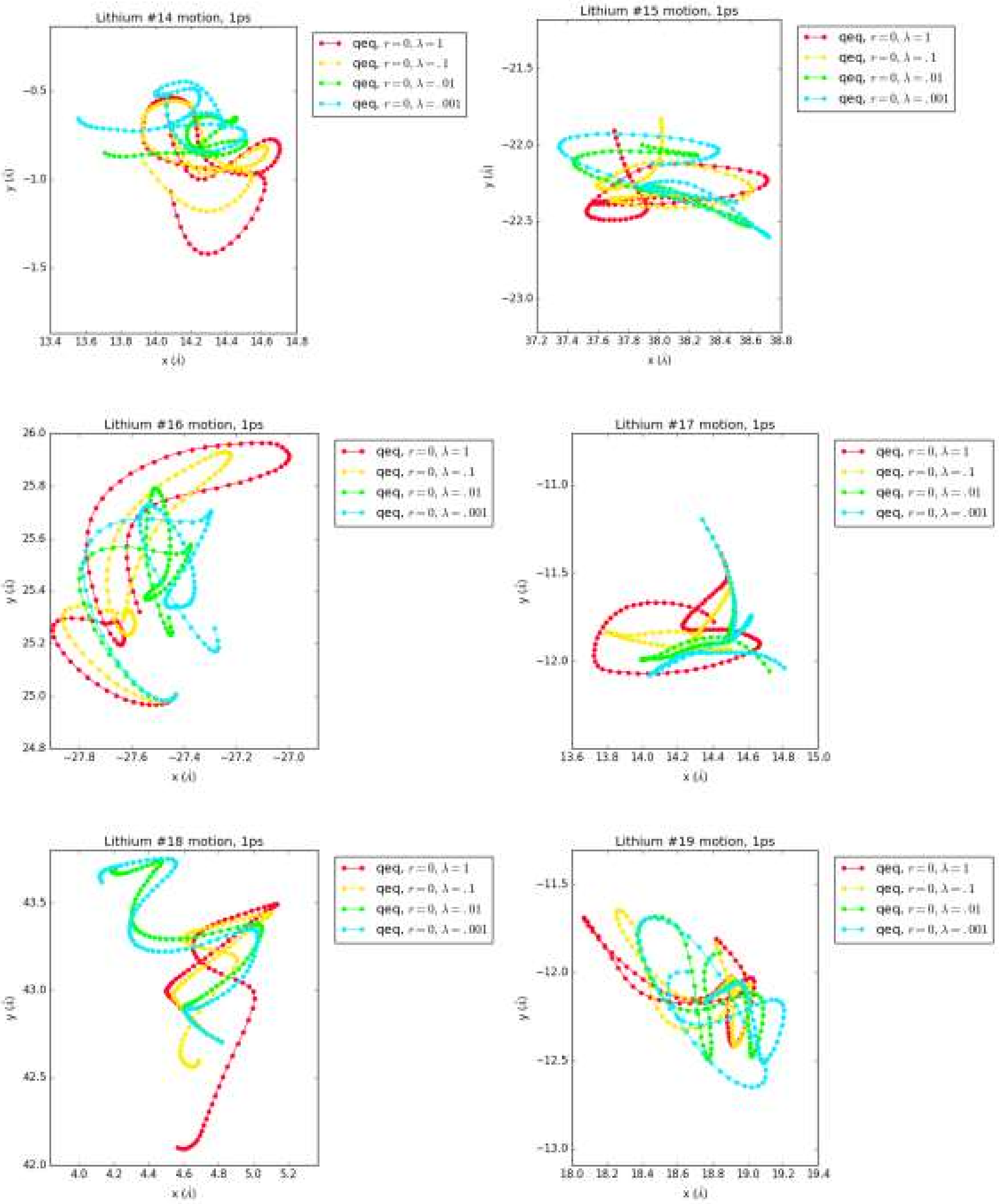

Figure S1. Lithium motion for each of the 20 lithium ions over a 500fs extension of the 480K/r=0.02/N=100 PQEq simulation using the QEq model ($\vec{r}_t = 0$). Trajectories are shown for a range of damping factors λ=1, 0.1, 0.01, 0.001. Lithium ions show qualitatively the same behavior in each case, suggesting that the damping of shell positions may be important.

For the QEq trajectories, qualitatively similar yet quantitatively different trajectories were observed for no damping (λ=1) and full damping (λ=0.001), suggesting that the damping of shell positions may also be important. An analysis of PQEq damping was then performed:

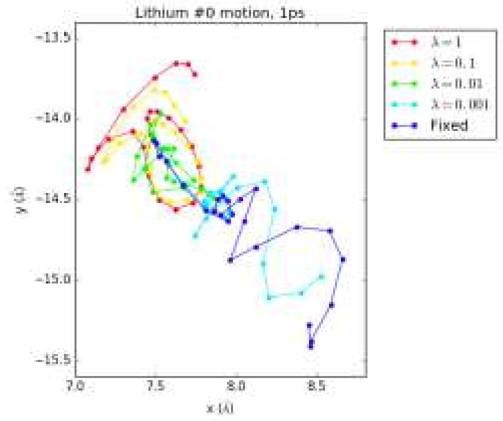

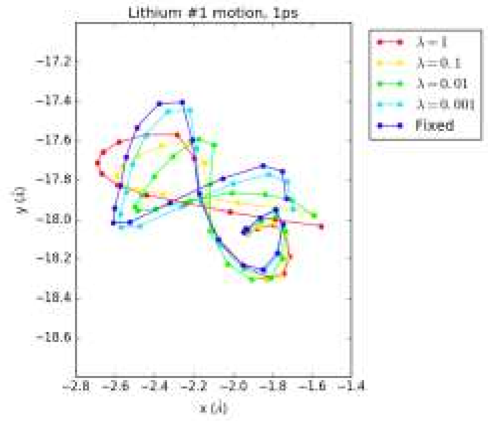

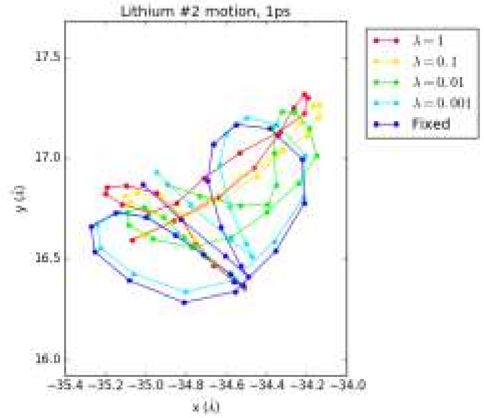

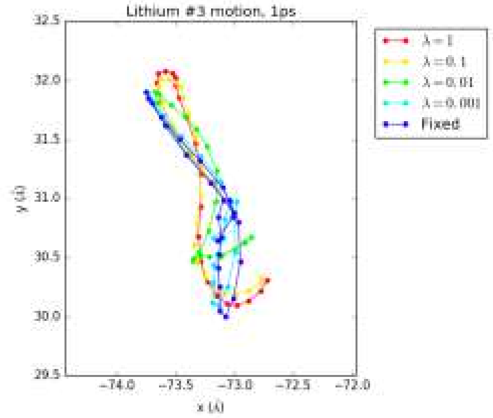

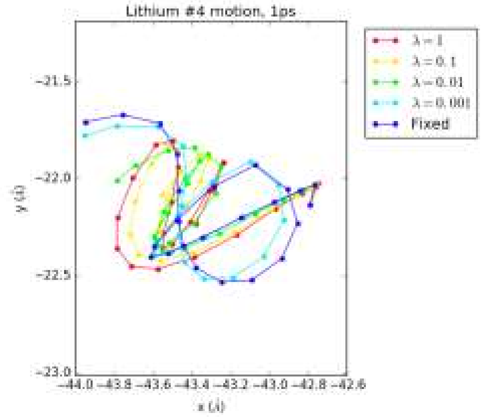

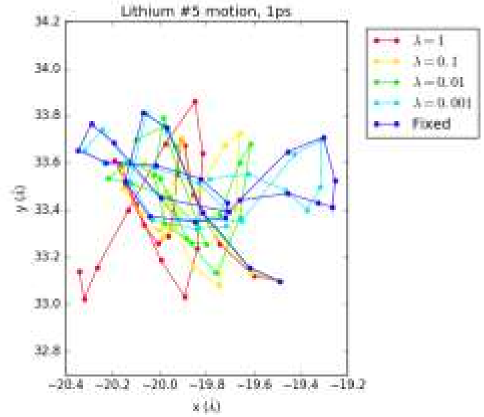

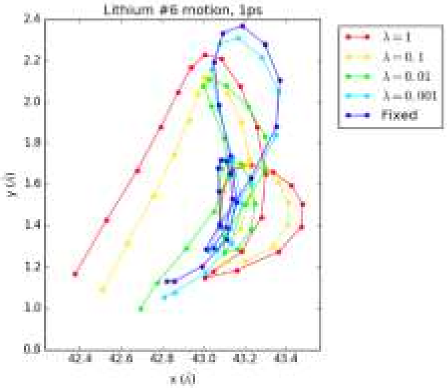
Lithium #6 motion, 1ps
y (Å)
x (Å)
0.0
1.0
1.2
1.4
1.6
1.8
2.0
2.2
2.4
42.4
42.6
42.8
43.0
43.2
43.4
$\lambda = 1$
$\lambda = 0.1$
$\lambda = 0.01$
$\lambda = 0.001$
Fixed

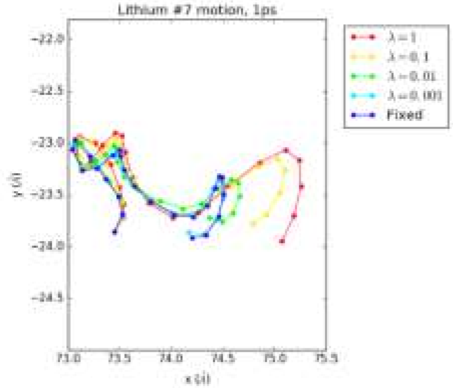
Lithium #7 motion, 1ps
y (Å)
x (Å)
−22.0
−22.5
−23.0
−23.5
−24.0
−24.5
73.0
73.5
74.0
74.5
75.0
75.5
$\lambda = 1$
$\lambda = 0.1$
$\lambda = 0.01$
$\lambda = 0.001$
Fixed

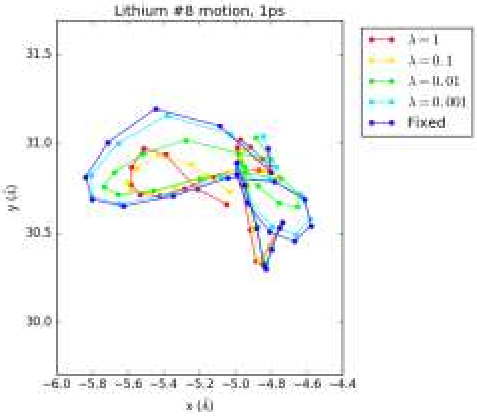
Lithium #8 motion, 1ps
y (Å)
x (Å)
31.5
31.0
30.5
30.0
−6.0
−5.8
−5.6
−5.4
−5.2
−5.0
−4.8
−4.6
−4.4
$\lambda = 1$
$\lambda = 0.1$
$\lambda = 0.01$
$\lambda = 0.001$
Fixed

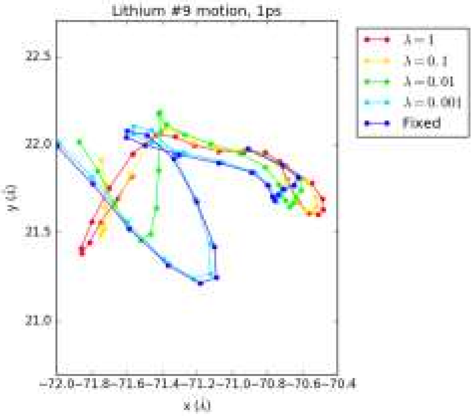
Lithium #9 motion, 1ps
y (Å)
x (Å)
22.5
22.0
21.5
21.0
−72.0
−71.8
−71.6
−71.4
−71.2
−71.0
−70.8
−70.6
−70.4
$\lambda = 1$
$\lambda = 0.1$
$\lambda = 0.01$
$\lambda = 0.001$
Fixed

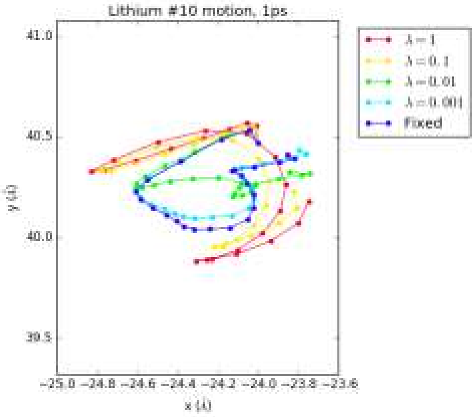
Lithium #10 motion, 1ps
y (Å)
x (Å)
41.0
40.5
40.0
39.5
−25.0
−24.8
−24.6
−24.4
−24.2
−24.0
−23.8
−23.6
$\lambda = 1$
$\lambda = 0.1$
$\lambda = 0.01$
$\lambda = 0.001$
Fixed

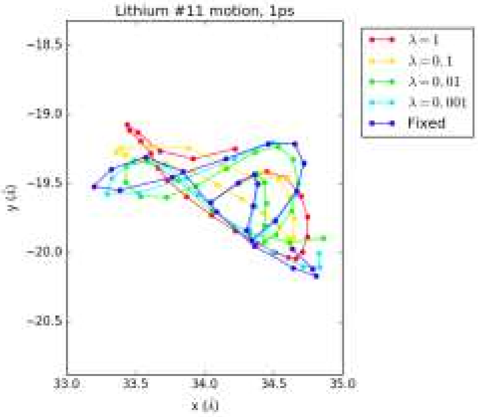
Lithium #11 motion, 1ps
y (Å)
x (Å)
−18.5
−19.0
−19.5
−20.0
−20.5
33.0
33.5
34.0
34.5
35.0
$\lambda = 1$
$\lambda = 0.1$
$\lambda = 0.01$
$\lambda = 0.001$
Fixed

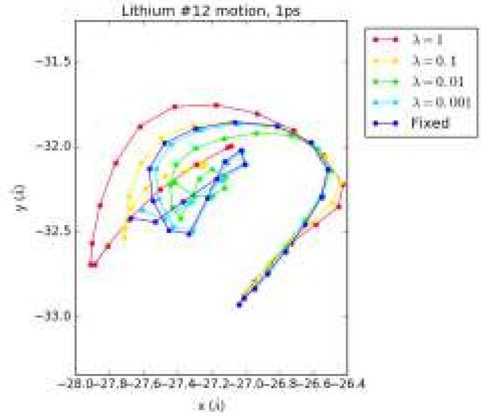
Lithium #12 motion, 1ps
λ = 1
λ = 0.1
λ = 0.01
λ = 0.001
Fixed
−31.5
−32.0
−32.5
−33.0
−28.0 −27.8 −27.6 −27.4 −27.2 −27.0 −26.8 −26.6 −26.4
x (Å)
y (Å)

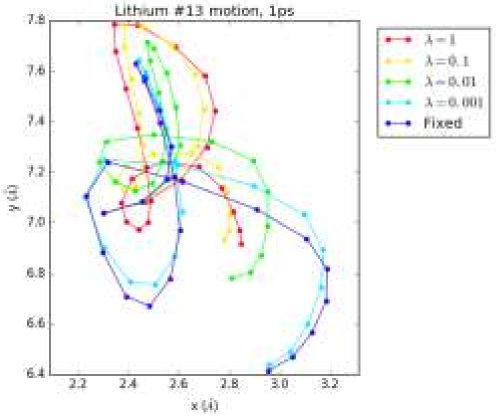
Lithium #13 motion, 1ps
λ = 1
λ = 0.1
λ = 0.01
λ = 0.001
Fixed
7.8
7.6
7.4
7.2
7.0
6.8
6.6
6.4
2.2 2.4 2.6 2.8 3.0 3.2
x (Å)
y (Å)

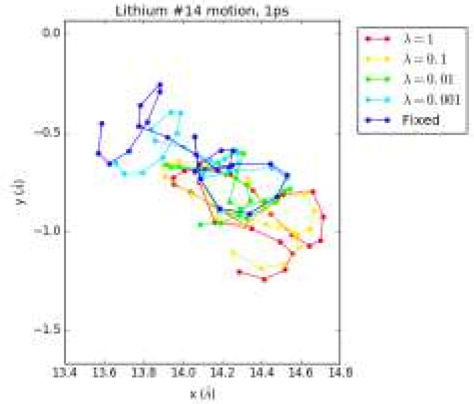
Lithium #14 motion, 1ps
λ = 1
λ = 0.1
λ = 0.01
λ = 0.001
Fixed
0.0
−0.5
−1.0
−1.5
13.4 13.6 13.8 14.0 14.2 14.4 14.6 14.8
x (Å)
y (Å)

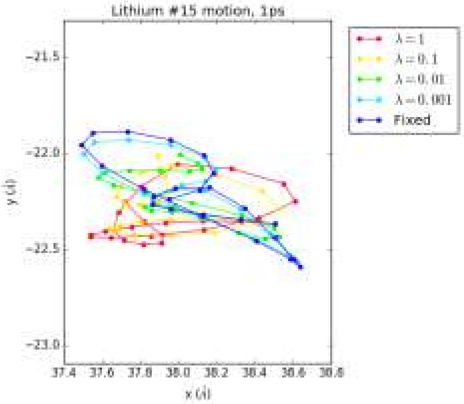
Lithium #15 motion, 1ps
λ = 1
λ = 0.1
λ = 0.01
λ = 0.001
Fixed
−21.5
−22.0
−22.5
−23.0
37.4 37.6 37.8 38.0 38.2 38.4 38.6 38.8
x (Å)
y (Å)

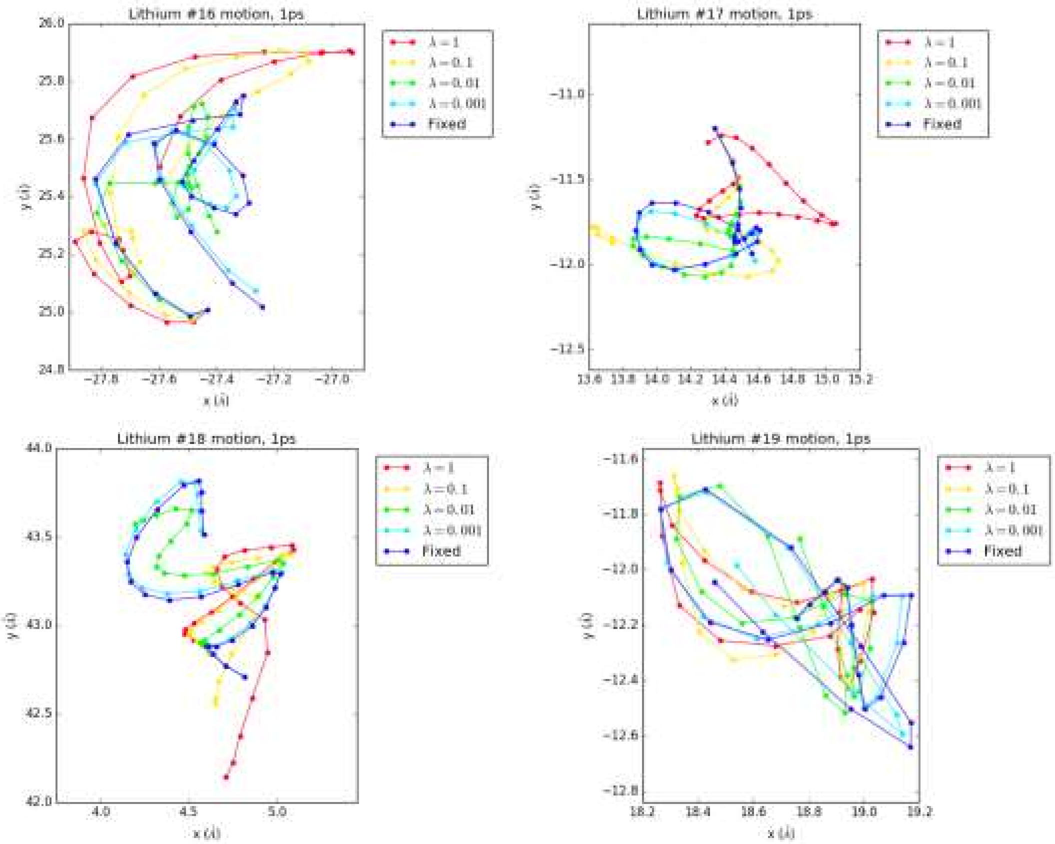

Figure S2. Lithium motion for each of the 20 lithium ions over a 500fs extension of the 480K/r=0.02/N=100 PQEq simulation using the PQEq model and one trajectory with fixed charges and shell positions. The undamped trajectories often diverge, suggesting that damping may be required.

For the PQEq trajectories, the undamped trajectories (λ=1) diverged significantly from the λ=0.001 and fixed charge and shell position trajectory. Additionally, in several cases, undamped lithium charges and shell positions results in large displacements (i.e. case 16), consistent with results from MD.

From these tests, λ=0.001 appears to be both stable and include effects beyond the fixed charge and shell model. This damping factor corresponds to a damping time of $t_{damp} = \frac{1}{\lambda}$ timesteps = 1ps. Using the diffusion relation, an effective damping length can be computed as $r_{damp} = \sqrt{6Dt_d}$ ~ 0.3Å. This allows for the damping of high frequency changes in lithium charges and shell positions, while allowing lithium charges to change after site updates. Empirically, this damping factor seems to solve the runaway lithium charge problem in both short and long molecular dynamics simulations. Thus, λ=0.001 was selected as the PQEq damping factor for the PEO-LiTFSI simulations.

References

1. Gorecki, W., Jeannin, M., Belorizky, E., Roux, C. & Armand, M. Physical properties of solid polymer electrolyte PEO (LiTFSI) complexes. *Journal of Physics: Condensed Matter* **7**, 6823 (1995).
2. Mao, G., Saboungi, M.-L., Price, D.L., Armand, M.B. & Howells, W. Structure of liquid PEO-LiTFSI electrolyte. *Physical review letters* **84**, 5536 (2000).
3. Buthelezi, T. & Glencoe/McGraw, H. *Chemistry : matter and change.* (Glencoe/McGraw-Hill, New York, N.Y.; 2013).
4. Shkrob, I.A., Zhu, Y., Marin, T.W. & Abraham, D. Reduction of carbonate electrolytes and the formation of solid-electrolyte interface (SEI) in Lithium-Ion Batteries. 2. Radiolytically induced polymerization of ethylene carbonate. *The Journal of Physical Chemistry C* **117**, 19270-19279 (2013).
5. Dufo-López, R., Lujano-Rojas, J.M. & Bernal-Agustín, J.L. Comparison of different lead–acid battery lifetime prediction models for use in simulation of stand-alone photovoltaic systems. *Applied Energy* **115**, 242-253 (2014).
6. Zhou, X. & Guo, Y.G. Highly disordered carbon as a superior anode material for room-temperature sodium-ion batteries. *ChemElectroChem* **1**, 83-86 (2014).
7. Kim, J.G. *et al.* A review of lithium and non-lithium based solid state batteries. *Journal of Power Sources* **282**, 299-322 (2015).
8. Jones, J., Anouti, M., Caillon-Caravanier, M., Willmann, P. & Lemordant, D. Lithium fluoride dissolution equilibria in cyclic alkylcarbonates and water. *Journal of Molecular Liquids* **153**, 146-152 (2010).
9. Kalhoff, J., Eshetu, G.G., Bresser, D. & Passerini, S. Safer Electrolytes for Lithium-Ion Batteries: State of the Art and Perspectives. *ChemSusChem* **8**, 2154-2175 (2015).
10. Li, Z., Huang, J., Liaw, B.Y., Metzler, V. & Zhang, J. A review of lithium deposition in lithium-ion and lithium metal secondary batteries. *Journal of power sources* **254**, 168-182 (2014).
11. Aurbach, D., Zinigrad, E., Cohen, Y. & Teller, H. A short review of failure mechanisms of lithium metal and lithiated graphite anodes in liquid electrolyte solutions. *Solid state ionics* **148**, 405-416 (2002).
12. Wang, X. *et al.* Improving cyclic stability of lithium cobalt oxide based lithium ion battery at high voltage by using trimethylboroxine as an electrolyte additive. *Electrochimica Acta* **173**, 804-811 (2015).
13. Schmitt, J., Maheshwari, A., Heck, M., Lux, S. & Vetter, M. Impedance change and capacity fade of lithium nickel manganese cobalt oxide-based batteries during calendar aging. *Journal of Power Sources* **353**, 183-194 (2017).
14. Xia, X., Gu, X.W. & Greer, J.R. in Meeting Abstracts 1915-1915 (The Electrochemical Society, 2015).
15. Xing, L.D. *et al.* Theoretical Insight into Oxidative Decomposition of Propylene Carbonate in the Lithium Ion Battery. *J Phys Chem B* **113**, 5181-5187 (2009).
16. Xing, L.D., Borodin, O., Smith, G.D. & Li, W.S. Density Functional Theory Study of the Role of Anions on the Oxidative Decomposition Reaction of Propylene Carbonate. *J Phys Chem A* **115**, 13896-13905 (2011).
17. Tasaki, K., Goldberg, A., Liang, J.-J. & Winter, M. New Insight into Differences in Cycling Behaviors of a Lithium-ion Battery Cell Between the Ethylene Carbonate-and Propylene Carbonate-Based Electrolytes. *ECS Transactions* **33**, 59-69 (2011).
18. Leggesse, E.G., Lin, R.T., Teng, T.-F., Chen, C.-L. & Jiang, J.-C. Oxidative decomposition of propylene carbonate in lithium ion batteries: a DFT study. *The Journal of Physical Chemistry A* **117**, 7959-7969 (2013).
19. Mayers, M., Kaminski, J. & Miller, T. Suppression of Dendrite Formation via Pulse Charging in Rechargeable Lithium Metal Batteries. *Journal of Physical Chemistry C* **116**, 26214-26221 (2012).
20. Seong, I.W., Hong, C.H., Kim, B.K. & Yoon, W.Y. The effects of current density and amount of discharge on dendrite formation in the lithium powder anode electrode. *Journal of Power Sources* **178**, 769-773 (2008).
21. Lee, H., Yanilmaz, M., Toprakci, O., Fu, K. & Zhang, X. A review of recent developments in membrane separators for rechargeable lithium-ion batteries. *Energy & Environmental Science* **7**, 3857-3886 (2014).
22. Devaux, D., Bouchet, R., Glé, D. & Denoyel, R. Mechanism of ion transport in PEO/LiTFSI complexes: Effect of temperature, molecular weight and end groups. *Solid State Ionics* **227**, 119-127 (2012).

23. Timachova, K., Watanabe, H. & Balsara, N.P. Effect of Molecular Weight and Salt Concentration on Ion Transport and the Transference Number in Polymer Electrolytes. *Macromolecules* **48**, 7882-7888 (2015).
24. Xue, Z., He, D. & Xie, X. Poly (ethylene oxide)-based electrolytes for lithium-ion batteries. *Journal of Materials Chemistry A* **3**, 19218-19253 (2015).
25. Long, L., Wang, S., Xiao, M. & Meng, Y. Polymer electrolytes for lithium polymer batteries. *Journal of Materials Chemistry A* **4**, 10038-10069 (2016).
26. Choudhury, S., Mangal, R., Agrawal, A. & Archer, L.A. A highly reversible room-temperature lithium metal battery based on crosslinked hairy nanoparticles. *Nature communications* **6**, 10101 (2015).
27. Duan, H. *et al.* In-situ plasticized polymer electrolyte with double-network for flexible solid-state lithium-metal batteries. *Energy Storage Materials* **10**, 85-91 (2018).
28. Pożyczka, K., Marzantowicz, M., Dygas, J. & Krok, F. Ionic conductivity and lithium transference number of poly (ethylene oxide): LiTFSI system. *Electrochimica Acta* **227**, 127-135 (2017).
29. Ibl, N. Some theoretical aspects of pulse electrolysis. *Surface Technology* **10**, 81-104 (1980).
30. Aryanfar, A. *et al.* Dynamics of lithium dendrite growth and inhibition: pulse charging experiments and Monte Carlo calculations. *The journal of physical chemistry letters* **5**, 1721-1726 (2014).
31. Islam, M. Einstein–Smoluchowski diffusion equation: a discussion. *Physica Scripta* **70**, 120 (2004).
32. Bazant, M.Z., Thornton, K. & Ajdari, A. Diffuse-charge dynamics in electrochemical systems. *Physical review E* **70**, 021506 (2004).
33. Chazalviel, J.-N. Electrochemical aspects of the generation of ramified metallic electrodeposits. *Physical review A* **42**, 7355 (1990).
34. Borodin, O. Polarizable force field development and molecular dynamics simulations of ionic liquids. *The Journal of Physical Chemistry B* **113**, 11463-11478 (2009).
35. Borodin, O. & Smith, G.D. Mechanism of ion transport in amorphous poly (ethylene oxide)/LiTFSI from molecular dynamics simulations. *Macromolecules* **39**, 1620-1629 (2006).
36. Xu, W. *et al.* Lithium metal anodes for rechargeable batteries. *Energy & Environmental Science* **7**, 513-537 (2014).
37. Armand, M. & Tarascon, J.-M. Building better batteries. *Nature* **451**, 652-657 (2008).
38. Ding, F. *et al.* Dendrite-free lithium deposition via self-healing electrostatic shield mechanism. *Journal of the American Chemical Society* **135**, 4450-4456 (2013).
39. Chandrashekar, S. *et al.* 7Li MRI of Li batteries reveals location of microstructural lithium. *Nature materials* **11**, 311-315 (2012).
40. Harry, K.J., Hallinan, D.T., Parkinson, D.Y., MacDowell, A.A. & Balsara, N.P. Detection of subsurface structures underneath dendrites formed on cycled lithium metal electrodes. *Nature materials* **13**, 69-73 (2014).
41. Rugolo, J. & Aziz, M.J. Electricity storage for intermittent renewable sources. *Energy & Environmental Science* **5**, 7151-7160 (2012).
42. Huskinson, B. *et al.* A metal-free organic-inorganic aqueous flow battery. *Nature* **505**, 195-198 (2014).
43. Goodenough, J.B. Rechargeable batteries: challenges old and new. *Journal of Solid State Electrochemistry* **16**, 2019-2029 (2012).
44. Nishida, T., Nishikawa, K., Rosso, M. & Fukunaka, Y. Optical observation of Li dendrite growth in ionic liquid. *Electrochimica acta* **100**, 333-341 (2013).
45. Williard, N., He, W., Hendricks, C. & Pecht, M. Lessons learned from the 787 dreamliner issue on lithium-ion battery reliability. *Energies* **6**, 4682-4695 (2013).
46. Xu, K. Nonaqueous liquid electrolytes for lithium-based rechargeable batteries. *Chemical reviews* **104**, 4303-4418 (2004).
47. Nishikawa, K. *et al.* In situ observation of dendrite growth of electrodeposited Li metal. *Journal of The Electrochemical Society* **157**, A1212-A1217 (2010).
48. Fleury, V. Branched fractal patterns in non-equilibrium electrochemical deposition from oscillatory nucleation and growth. *Nature* **390**, 145-148 (1997).
49. Ely, D.R. & García, R.E. Heterogeneous nucleation and growth of lithium electrodeposits on negative electrodes. *Journal of the Electrochemical Society* **160**, A662-A668 (2013).
50. Akolkar, R. Mathematical model of the dendritic growth during lithium electrodeposition. *Journal of Power Sources* **232**, 23-28 (2013).

51. Brissot, C., Rosso, M., Chazalviel, J.N. & Lascaud, S. In Situ Concentration Cartography in the Neighborhood of Dendrites Growing in Lithium/Polymer-Electrolyte/Lithium Cells. *Journal of the Electrochemical Society* **146**, 4393-4400 (1999).
52. Orsini, F. *et al.* In situ scanning electron microscopy (SEM) observation of interfaces within plastic lithium batteries. *Journal of power sources* **76**, 19-29 (1998).
53. Monroe, C. & Newman, J. Dendrite growth in lithium/polymer systems a propagation model for liquid electrolytes under galvanostatic conditions. *Journal of The Electrochemical Society* **150**, A1377-A1384 (2003).
54. Crowther, O. & West, A.C. Effect of electrolyte composition on lithium dendrite growth. *Journal of the Electrochemical Society* **155**, A806-A811 (2008).
55. Howlett, P., MacFarlane, D. & Hollenkamp, A. A sealed optical cell for the study of lithium-electrode|electrolyte interfaces. *Journal of power sources* **114**, 277-284 (2003).
56. Schweikert, N. *et al.* Suppressed lithium dendrite growth in lithium batteries using ionic liquid electrolytes: Investigation by electrochemical impedance spectroscopy, scanning electron microscopy, and in situ 7 Li nuclear magnetic resonance spectroscopy. *Journal of Power Sources* **228**, 237-243 (2013).
57. Basile, A., Hollenkamp, A.F., Bhatt, A.I. & O'Mullane, A.P. Extensive charge–discharge cycling of lithium metal electrodes achieved using ionic liquid electrolytes. *Electrochemistry communications* **27**, 69-72 (2013).
58. Rosso, M., Gobron, T., Brissot, C., Chazalviel, J.-N. & Lascaud, S. Onset of dendritic growth in lithium/polymer cells. *Journal of power sources* **97**, 804-806 (2001).
59. Stone, G. *et al.* Resolution of the modulus versus adhesion dilemma in solid polymer electrolytes for rechargeable lithium metal batteries. *Journal of The Electrochemical Society* **159**, A222-A227 (2012).
60. Bhattacharyya, R. *et al.* In situ NMR observation of the formation of metallic lithium microstructures in lithium batteries. *Nature materials* **9**, 504-510 (2010).
61. Ben-Jacob, E. & Garik, P. The formation of patterns in non-equilibrium growth. *Nature* **343**, 523-530 (1990).
62. Huggins, R. *Advanced batteries: materials science aspects*. (Springer Science & Business Media, 2008).
63. Bard, A.J., Faulkner, L.R., Leddy, J. & Zoski, C.G. *Electrochemical methods: fundamentals and applications*, Vol. 2. (wiley New York, 1980).
64. Jackson, J.D. *Classical electrodynamics*. (John Wiley & Sons, 2007).
65. Roy, S. Formation of dual diffusion layer by pulsing currents. *Industrial & Engineering Chemistry Research* **51**, 1756-1760 (2011).
66. Diggle, J., Despic, A. & Bockris, J.M. The mechanism of the dendritic electrocrystallization of zinc. *Journal of The Electrochemical Society* **116**, 1503-1514 (1969).
67. Wang, M. & Ming, N.-b. Concentration field oscillation in front of a dendrite tip in electrochemical deposition. *Physical Review A* **45**, 2493 (1992).
68. Norton, J.D., White, H.S. & Feldberg, S.W. Effect of the electrical double layer on voltammetry at microelectrodes. *Journal of physical chemistry* **94**, 6772-6780 (1990).
69. Alexe-Ionescu, A., Barbero, G., Bianco, S., Cicero, G. & Pirri, C. Electrical response of electrolytic cells limited by different types of electrodes. *Journal of Electroanalytical Chemistry* **669**, 21-27 (2012).
70. Macdonald, J.R. Theory of ac space-charge polarization effects in photoconductors, semiconductors, and electrolytes. *Physical Review* **92**, 4 (1953).
71. Hossain, R. & Adamiak, K. Dynamic properties of the electric double layer in electrolytes. *Journal of Electrostatics* **71**, 829-838 (2013).
72. Zhong, X. *et al.* In situ study the dependence of electrochemical migration of tin on chloride. *Electrochemistry Communications* **27**, 63-68 (2013).
73. Rosso, M. Electrodeposition from a binary electrolyte: new developments and applications. *Electrochimica Acta* **53**, 250-256 (2007).
74. Léger, C., Argoul, F. & Bazant, M.Z. Front dynamics during diffusion-limited corrosion of ramified electrodeposits. *The Journal of Physical Chemistry B* **103**, 5841-5851 (1999).
75. Tarascon, J.-M. & Armand, M. Issues and challenges facing rechargeable lithium batteries, in *Materials For Sustainable Energy: A Collection of Peer-Reviewed Research and Review Articles from Nature Publishing Group* 171-179 (World Scientific, 2011).
76. Etacheri, V., Marom, R., Elazari, R., Salitra, G. & Aurbach, D. Challenges in the development of advanced Li-ion batteries: a review. *Energy & Environmental Science* **4**, 3243-3262 (2011).

77. Miller III, T.F., Wang, Z.-G., Coates, G.W. & Balsara, N.P. Designing Polymer Electrolytes for Safe and High Capacity Rechargeable Lithium Batteries. *Accounts of Chemical Research* **50**, 590-593 (2017).
78. Aryanfar, A., Brooks, D.J., Colussi, A.J. & Hoffmann, M.R. Quantifying the dependence of dead lithium losses on the cycling period in lithium metal batteries. *Physical Chemistry Chemical Physics* **16**, 24965-24970 (2014).
79. Buriez, O. *et al.* Performance limitations of polymer electrolytes based on ethylene oxide polymers. *Journal of Power Sources* **89**, 149-155 (2000).
80. Panday, A. *et al.* Effect of molecular weight and salt concentration on conductivity of block copolymer electrolytes. *Macromolecules* **42**, 4632-4637 (2009).
81. Royston, E., Ghosh, A., Kofinas, P., Harris, M.T. & Culver, J.N. Self-assembly of virus-structured high surface area nanomaterials and their application as battery electrodes. *Langmuir* **24**, 906-912 (2008).
82. Hou, W.-H., Chen, C.-Y., Wang, C.-C. & Huang, Y.-H. The effect of different lithium salts on conductivity of comb-like polymer electrolyte with chelating functional group. *Electrochimica Acta* **48**, 679-690 (2003).
83. Liang, Y.-H., Wang, C.-C. & Chen, C.-Y. Synthesis and characterization of a new network polymer electrolyte containing polyether in the main chains and side chains. *European Polymer Journal* **44**, 2376-2384 (2008).
84. Snyder, J.F., Carter, R.H. & Wetzel, E.D. Electrochemical and mechanical behavior in mechanically robust solid polymer electrolytes for use in multifunctional structural batteries. *Chemistry of materials* **19**, 3793-3801 (2007).
85. Hayamizu, K., Aihara, Y. & Price, W.S. Correlating the NMR self-diffusion and relaxation measurements with ionic conductivity in polymer electrolytes composed of cross-linked poly (ethylene oxide-propylene oxide) doped with LiN (SO 2 CF 3) 2. *The Journal of Chemical Physics* **113**, 4785-4793 (2000).
86. Chaurasia, S.K., Singh, R.K. & Chandra, S. Ion–polymer and ion–ion interaction in PEO-based polymer electrolytes having complexing salt LiClO4 and/or ionic liquid,[BMIM][PF6]. *Journal of Raman Spectroscopy* **42**, 2168-2172 (2011).
87. Newman, G., Francis, R., Gaines, L. & Rao, B. Hazard investigations of LiClO4/dioxolane electrolyte. *Journal of The Electrochemical Society* **127**, 2025-2027 (1980).
88. Fullerton-Shirey, S.K. & Maranas, J.K. Effect of LiClO4 on the structure and mobility of PEO-based solid polymer electrolytes. *Macromolecules* **42**, 2142-2156 (2009).
89. Munshi, M. & Owens, B. Ionic transport in poly (ethylene oxide)(PEO)-LiX polymeric solid electrolyte. *Polymer journal* **20**, 577-586 (1988).
90. Henderson, W.A. Crystallization kinetics of glyme− LiX and PEO− LiX polymer electrolytes. *Macromolecules* **40**, 4963-4971 (2007).
91. Nitzan, A. & Ratner, M.A. Conduction in polymers: dynamic disorder transport. *The Journal of Physical Chemistry* **98**, 1765-1775 (1994).
92. Druger, S.D., Nitzan, A. & Ratner, M.A. Dynamic bond percolation theory: A microscopic model for diffusion in dynamically disordered systems. I. Definition and one-dimensional case. *The Journal of chemical physics* **79**, 3133-3142 (1983).
93. Maitra, A. & Heuer, A. Cation transport in polymer electrolytes: a microscopic approach. *Physical review letters* **98**, 227802 (2007).
94. Diddens, D., Heuer, A. & Borodin, O. Understanding the lithium transport within a Rouse-based model for a PEO/LiTFSI polymer electrolyte. *Macromolecules* **43**, 2028-2036 (2010).
95. Diddens, D. & Heuer, A. Lithium Ion Transport Mechanism in Ternary Polymer Electrolyte-Ionic Liquid Mixtures: A Molecular Dynamics Simulation Study. *ACS Macro Letters* **2**, 322-326 (2013).
96. Bowers, K.J. *et al.* in Proceedings of the 2006 ACM/IEEE conference on Supercomputing 84 (ACM, 2006).
97. Banks, J.L. *et al.* Integrated modeling program, applied chemical theory (IMPACT). *Journal of computational chemistry* **26**, 1752-1780 (2005).
98. Shin, H., Pascal, T.A., Goddard III, W.A. & Kim, H. Scaled Effective Solvent Method for Predicting the Equilibrium Ensemble of Structures with Analysis of Thermodynamic Properties of Amorphous Polyethylene Glycol–Water Mixtures. *The Journal of Physical Chemistry B* **117**, 916-927 (2013).
99. Ishizuka, R. & Matubayasi, N. Self-Consistent Determination of Atomic Charges of Ionic Liquid through a Combination of Molecular Dynamics Simulation and Density Functional Theory. *Journal of chemical theory and computation* **12**, 804-811 (2016).

100. Chirlian, L.E. & Francl, M.M. Atomic charges derived from electrostatic potentials: A detailed study. *J. Comput. Chem.* **8**, 894-905 (1987).
101. Mulliken, R.S. Electronic population analysis on LCAO–MO molecular wave functions. I. *The Journal of Chemical Physics* **23**, 1833-1840 (1955).
102. Cramer, C.J. *Essentials of computational chemistry: theories and models*. (John Wiley & Sons, 2013).
103. Rappé, A.K. & Goddard III, W.A. Charge equilibration for molecular dynamics simulations. *J. Phys. Chem.* **95**, 3358-3363 (1991).
104. Rappé, A.K., Casewit, C.J., Colwell, K., Goddard III, W.A. & Skiff, W. UFF, a full periodic table force field for molecular mechanics and molecular dynamics simulations. *J. Am. Chem. Soc.* **114**, 10024-10035 (1992).
105. Naserifar, S., Liu, L., Goddard III, W.A., Tsotsis, T.T. & Sahimi, M. Toward a process-based molecular model of SiC membranes. 1. Development of a reactive force field. *J. Phys. Chem. C* **117**, 3308-3319 (2013).
106. van Duin, A.C., Dasgupta, S., Lorant, F. & Goddard, W.A. ReaxFF: a reactive force field for hydrocarbons. *J. Phys. Chem. A* **105**, 9396-9409 (2001).
107. Bauer, B.A. & Patel, S. Recent applications and developments of charge equilibration force fields for modeling dynamical charges in classical molecular dynamics simulations. *Theor. Chem. Acc.* **131**, 1-15 (2012).
108. Illingworth, C.J. & Domene, C. in Proceedings of the Royal Society of London A: Mathematical, Physical and Engineering Sciences rspa. 2009.0014 (The Royal Society, 2009).
109. Jorgensen, W.L. Special issue on polarization. *J. Chem. Theory Comput.* **3**, 1877-1877 (2007).
110. Halgren, T.A. & Damm, W. Polarizable force fields. *Curr. Opin. Struct. Biol.* **11**, 236-242 (2001).
111. Lamoureux, G., MacKerell Jr, A.D. & Roux, B. A simple polarizable model of water based on classical drude oscillators. *J. Chem. Phys.* **119**, 5185-5197 (2003).
112. Xu, H., Stern, H.A. & Berne, B. Can water polarizability be ignored in hydrogen bond kinetics? *J. Phys. Chem. B* **106**, 2054-2060 (2002).
113. Yu, H. & van Gunsteren, W.F. Charge-on-spring polarizable water models revisited: from water clusters to liquid water to ice. *J. Chem. Phys.* **121**, 9549-9564 (2004).
114. Anisimov, V.M. *et al.* Determination of electrostatic parameters for a polarizable force field based on the classical Drude oscillator. *J. Chem. Theory Comput.* **1**, 153-168 (2005).
115. Lamoureux, G. & Roux, B. Modeling induced polarization with classical drude oscillators: Theory and molecular dynamics simulation algorithm. *J. Chem. Phys.* **119**, 3025-3039 (2003).
116. Lucas, T.R., Bauer, B.A. & Patel, S. Charge equilibration force fields for molecular dynamics simulations of lipids, bilayers, and integral membrane protein systems. *Biochim. Biophys. Acta, Biomembr.* **1818**, 318-329 (2012).
117. Patel, S., Mackerell, A.D. & Brooks, C.L. CHARMM fluctuating charge force field for proteins: II protein/solvent properties from molecular dynamics simulations using a nonadditive electrostatic model. *J. Comput. Chem.* **25**, 1504-1514 (2004).
118. Shi, Y. *et al.* Polarizable atomic multipole-based AMOEBA force field for proteins. *J. Chem. Theory Comput.* **9**, 4046-4063 (2013).
119. Baucom, J. *et al.* Molecular dynamics simulations of the d (CCAACGTTGG) 2 decamer in crystal environment: comparison of atomic point-charge, extra-point, and polarizable force fields. *J. Chem. Phys.* **121**, 6998-7008 (2004).
120. Warshel, A. & Levitt, M. Theoretical studies of enzymic reactions: dielectric, electrostatic and steric stabilization of the carbonium ion in the reaction of lysozyme. *J. Mol. Biol.* **103**, 227-249 (1976).
121. Cho, A.E., Guallar, V., Berne, B.J. & Friesner, R. Importance of accurate charges in molecular docking: quantum mechanical/molecular mechanical (QM/MM) approach. *J. Comput. Chem.* **26**, 915-931 (2005).
122. Friesner, R.A. & Guallar, V. Ab initio quantum chemical and mixed quantum mechanics/molecular mechanics (QM/MM) methods for studying enzymatic catalysis. *Annu. Rev. Phys. Chem.* **56**, 389-427 (2005).
123. Xie, W. & Gao, J. Design of a next generation force field: the X-POL potential. *J. Chem. Theory Comput.* **3**, 1890-1900 (2007).
124. Anisimov, V.M., Vorobyov, I.V., Roux, B. & MacKerell, A.D. Polarizable empirical force field for the primary and secondary alcohol series based on the classical Drude model. *J. Chem. Theory Comput.* **3**, 1927-1946 (2007).

125. Hernández-Cobos, J., Saint-Martin, H., Mackie, A., Vega, L. & Ortega-Blake, I. Water liquid-vapor equilibria predicted by refined ab initio derived potentials. *J. Chem. Phys.* **123**, 044506 (2005).
126. Saint-Martin, H., Hernández-Cobos, J., Bernal-Uruchurtu, M.I., Ortega-Blake, I. & Berendsen, H.J. A mobile charge densities in harmonic oscillators (MCDHO) molecular model for numerical simulations: the water–water interaction. *J. Chem. Phys.* **113**, 10899-10912 (2000).
127. Sprik, M. & Klein, M.L. A polarizable model for water using distributed charge sites. *J. Chem. Phys.* **89**, 7556-7560 (1988).
128. Yu, H., Geerke, D.P., Liu, H. & van Gunsteren, W.F. Molecular dynamics simulations of liquid methanol and methanol–water mixtures with polarizable models. *J. Comput. Chem.* **27**, 1494-1504 (2006).
129. Yu, H. & van Gunsteren, W.F. Accounting for polarization in molecular simulation. *Comput. Phys. Commun.* **172**, 69-85 (2005).
130. Gao, J. A molecular-orbital derived polarization potential for liquid water. *J. Chem. Phys.* **109**, 2346-2354 (1998).
131. Barnes, P., Finney, J., Nicholas, J. & Quinn, J. Cooperative effects in simulated water. *Nature* **282**, 459-464 (1979).
132. Stillinger, F.H. & David, C.W. Polarization model for water and its ionic dissociation products. *J. Chem. Phys.* **69**, 1473-1484 (1978).
133. Bucher, D. *et al.* Polarization effects and charge transfer in the KcsA potassium channel. *Biophys. Chem.* **124**, 292-301 (2006).
134. Guidoni, L., Torre, V. & Carloni, P. Water and potassium dynamics inside the KcsA K+ channel. *FEBS letters* **477**, 37-42 (2000).
135. Lamoureux, G., Harder, E., Vorobyov, I.V., Roux, B. & MacKerell, A.D. A polarizable model of water for molecular dynamics simulations of biomolecules. *Chem. Phys. Lett.* **418**, 245-249 (2006).
136. Gillan, M. Collective dynamics in super-ionic CaF2. II. Defect interpretation. *J. Phys. C: Solid State Phys.* **19**, 3517 (1986).
137. Kalinin, S.V., Morozovska, A.N., Chen, L.Q. & Rodriguez, B.J. Local polarization dynamics in ferroelectric materials. *Rep. Prog. Phys.* **73**, 056502 (2010).
138. Karasawa, N. & Goddard, W.A.I. Force fields, structures, and properties of poly (vinylidene fluoride) crystals. *Macromolecules* **25**, 7268-7281 (1992).
139. Zhang, Q. & Goddard, W. Charge and polarization distributions at the 90 degrees domain wall in barium titanate ferroelectric. *Applied Physics Letters* **89** (2006).
140. Borodin, O. & Smith, G.D. Development of many-body polarizable force fields for Li-battery applications: 2. LiTFSI-doped oligoether, polyether, and carbonate-based electrolytes. *J. Phys. Chem. B* **110**, 6293-6299 (2006).
141. Lebedev, N., Levanyuk, A. & Sigov, A. Polarized Defects and Anomalies of Properties of Crystals During Phase Transitions. *Zh. Eksp. Teor. Fiz.* **85**, 1423-1436 (1983).
142. Levanyuk, A.P. & Sigov, A.S. *Defects and Structural Phase Transitions.* (Gordon and Breach Science Publishers, New York, USA; 1988).
143. Mitchell, P. & Fincham, D. Shell model simulations by adiabatic dynamics. *J. Phys.: Condens. Matter* **5**, 1031 (1993).
144. Board, J. & Elliott, R. Shell model molecular dynamics calculations of the Raman spectra of molten NaI. *J. Phys.: Condens. Matter* **1**, 2427 (1989).
145. O'Sullivan, K. & Madden, P. Light scattering by alkali halides melts: a comparison of shell-model and rigid-ion computer simulation results. *J. Phys.: Condens. Matter* **3**, 8751 (1991).
146. Baker, C.M., Lopes, P.E., Zhu, X., Roux, B. & MacKerell Jr, A.D. Accurate calculation of hydration free energies using pair-specific Lennard-Jones parameters in the CHARMM Drude polarizable force field. *J. Chem. Theory Comput.* **6**, 1181-1198 (2010).
147. Mayer, A., Lambin, P. & Langlet, R. Charge-dipole model to compute the polarization of fullerenes. *Appl. Phys. Lett.* **89**, 063117 (2006).
148. Misquitta, A.J. & Stone, A.J. Accurate induction energies for small organic molecules: 1. Theory. *J. Chem. Theory Comput.* **4**, 7-18 (2008).
149. Misquitta, A.J. & Stone, A.J. Dispersion energies for small organic molecules: first row atoms. *Mol. Phys.* **106**, 1631-1643 (2008).

150. Misquitta, A.J., Stone, A.J. & Price, S.L. Accurate induction energies for small organic molecules. 2. Development and testing of distributed polarizability models against SAPT (DFT) energies. *J. Chem. Theory Comput.* **4**, 19-32 (2008).
151. Welch, G.W., Karamertzanis, P.G., Misquitta, A.J., Stone, A.J. & Price, S.L. Is the induction energy important for modeling organic crystals? *J. Chem. Theory Comput.* **4**, 522-532 (2008).
152. Cieplak, P., Dupradeau, F.-Y., Duan, Y. & Wang, J. Polarization effects in molecular mechanical force fields. *J. Phys.: Condens. Matter* **21**, 333102 (2009).
153. Khoruzhii, O. *et al.* Polarizable Force Fields for Proteins, in *Protein Modelling* 91-134 (Springer, 2014).
154. Rick, S.W. & Stuart, S.J. Potentials and algorithms for incorporating polarizability in computer simulations. *Rev. Comput. Chem.* **18**, 89-146 (2002).
155. Harder, E. *et al.* OPLS3: a force field providing broad coverage of drug-like small molecules and proteins. *Journal of Chemical Theory and Computation* **12**, 281-296 (2015).
156. Jorgensen, W.L., Maxwell, D.S. & Tirado-Rives, J. Development and testing of the OPLS all-atom force field on conformational energetics and properties of organic liquids. *Journal of the American Chemical Society* **118**, 11225-11236 (1996).
157. Jorgenson, W. & Tirado-Rives, J. The OPLS (optimized potentials for liquid simulations) potential functions for proteins, energy minimizations for crystals of cyclic peptides and crambin. *J. Am. Chem. Soc* **110**, 1657-1666 (1988).
158. Kaminski, G.A., Friesner, R.A., Tirado-Rives, J. & Jorgensen, W.L. Evaluation and reparametrization of the OPLS-AA force field for proteins via comparison with accurate quantum chemical calculations on peptides. *J. Phys. Chem. B* **105**, 6474-6487 (2001).
159. Cornell, W.D. *et al.* A second generation force field for the simulation of proteins, nucleic acids, and organic molecules. *J. Am. Chem. Soc.* **117**, 5179-5197 (1995).
160. Salomon-Ferrer, R., Case, D.A. & Walker, R.C. An overview of the Amber biomolecular simulation package. *Wiley Interdiscip. Rev. Comput. Mol. Sci.* **3**, 198-210 (2013).
161. Wang, J., Wolf, R.M., Caldwell, J.W., Kollman, P.A. & Case, D.A. Development and testing of a general amber force field. *J. Comput. Chem.* **25**, 1157-1174 (2004).
162. Best, R.B. *et al.* Optimization of the additive CHARMM all-atom protein force field targeting improved sampling of the backbone ϕ, ψ and side-chain $\chi1$ and $\chi2$ dihedral angles. *J. Chem. Theory Comput.* **8**, 3257-3273 (2012).
163. Mackerell, A.D. Empirical force fields for biological macromolecules: overview and issues. *J. Comput. Chem.* **25**, 1584-1604 (2004).
164. MacKerell Jr, A.D. *et al.* All-atom empirical potential for molecular modeling and dynamics studies of proteins†. *J. Phys. Chem. B* **102**, 3586-3616 (1998).
165. Dick Jr, B. & Overhauser, A. Theory of the dielectric constants of alkali halide crystals. *Phys. Rev.* **112**, 90 (1958).
166. Drude, P., Mann, C. & Millikan, R. The theory of optics (1902). *New York etc.: Longmans, Green, and Co* **1** (2008).
167. *CRC Handbook of Chemistry and Physics, 89th Edition (Internet Version 2009)*, Edn. 89. (CRC Press/Taylor and Francis, Boca Raton, FL; 2008).
168. Applequist, J., Carl, J.R. & Fung, K.-K. Atom dipole interaction model for molecular polarizability. Application to polyatomic molecules and determination of atom polarizabilities. *J. Am. Chem. Soc.* **94**, 2952-2960 (1972).
169. Mulliken, R.S. Electronic structures of molecules XI. Electroaffinity, molecular orbitals and dipole moments. *J. Chem. Phys.* **3**, 573-585 (1935).
170. Nakano, A. Parallel multilevel preconditioned conjugate-gradient approach to variable-charge molecular dynamics. *Comput. Phys. Commun.* **104**, 59-69 (1997).
171. Aktulga, H.M., Fogarty, J.C., Pandit, S.A. & Grama, A.Y. Parallel reactive molecular dynamics: Numerical methods and algorithmic techniques. *Parallel Computing* **38**, 245-259 (2012).
172. Aktulga, H.M., Pandit, S.A., van Duin, A.C. & Grama, A.Y. Reactive molecular dynamics: Numerical methods and algorithmic techniques. *SIAM J. Sci. Comput.* **34**, C1-C23 (2012).
173. Plimpton, S. Fast parallel algorithms for short-range molecular dynamics. *J. Comput. Phys.* **117**, 1-19 (1995).
174. Barrett, R. *et al. Templates for the solution of linear systems: building blocks for iterative methods*, Vol. 43. (Siam, 1994).

175. Becke, A.D. Density-functional exchange-energy approximation with correct asymptotic behavior. *Phys. Rev. A* **38**, 3098 (1988).

176. Becke, A.D. Density-functional thermochemistry. III. The role of exact exchange. *J. Chem. Phys.* **98**, 5648-5652 (1993).

177. Lee, C., Yang, W. & Parr, R.G. Development of the Colle-Salvetti correlation-energy formula into a functional of the electron density. *Phys. Rev. B* **37**, 785 (1988).

178. Slater, J.C. *The self-consistent field for molecules and solids*, Vol. 4. (McGraw-Hill New York, 1974).

179. Vosko, S.H., Wilk, L. & Nusair, M. Accurate spin-dependent electron liquid correlation energies for local spin density calculations: a critical analysis. *Can. J. Phys.* **58**, 1200-1211 (1980).

180. Frisch, M.J., Pople, J.A. & Binkley, J.S. Self-consistent molecular orbital methods 25. Supplementary functions for Gaussian basis sets. *J. Chem. Phys.* **80**, 3265-3269 (1984).

181. Zhao, Y. & Truhlar, D.G. The M06 suite of density functionals for main group thermochemistry, thermochemical kinetics, noncovalent interactions, excited states, and transition elements: two new functionals and systematic testing of four M06-class functionals and 12 other functionals. *Theor. Chem. Acc.* **120**, 215-241 (2008).

182. Perdew, J.P., Burke, K. & Ernzerhof, M. Generalized gradient approximation made simple. *Phys. Rev. Lett.* **77**, 3865 (1996).

183. Hariharan, P.C. & Pople, J.A. The influence of polarization functions on molecular orbital hydrogenation energies. *Theor. Chim. Acta* **28**, 213-222 (1973).

184. Hehre, W.J., Ditchfield, R. & Pople, J.A. Self—consistent molecular orbital methods. XII. Further extensions of gaussian—type basis sets for use in molecular orbital studies of organic molecules. *J. Chem. Phys.* **56**, 2257-2261 (1972).

185. Krishnan, R., Binkley, J.S., Seeger, R. & Pople, J.A. Self-consistent molecular orbital methods. XX. A basis set for correlated wave functions. *J. Chem. Phys.* **72**, 650-654 (1980).

186. Wang, J. *et al.* Development of polarizable models for molecular mechanical calculations II: induced dipole models significantly improve accuracy of intermolecular interaction energies. *J. Phys. Chem. B* **115**, 3100-3111 (2011).

187. An, Q., Liu, Y., Zybin, S.V., Kim, H. & Goddard III, W.A. Anisotropic shock sensitivity of cyclotrimethylene trinitramine (RDX) from compress-and-shear reactive dynamics. *J. Phys. Chem. C* **116**, 10198-10206 (2012).

188. Liu, L., Liu, Y., Zybin, S.V., Sun, H. & Goddard III, W.A. ReaxFF-lg: Correction of the ReaxFF reactive force field for London dispersion, with applications to the equations of state for energetic materials. *J. Phys. Chem. A* **115**, 11016-11022 (2011).

189. Nelson, M.T. *et al.* NAMD: a parallel, object-oriented molecular dynamics program. *Int. J. High Perform. Comput. Appl.* **10**, 251-268 (1996).

190. Brooks, B.R. *et al.* CHARMM: a program for macromolecular energy, minimization, and dynamics calculations. *J. Comput. Chem.* **4**, 187-217 (1983).

191. Bowers, K.J. *et al.* in SC 2006 Conference, Proceedings of the ACM/IEEE 43-43 (IEEE, 2006).

192. Naserifar, S., Brooks, D.J., Goddard III, W.A. & Cvicek, V. Polarizable charge equilibration model for predicting accurate electrostatic interactions in molecules and solids. *The Journal of Chemical Physics* **146**, 124117 (2017).

193. Nimon, E.S. & Churikov, A.V. Electrochemical behaviour of Li□ Sn, Li□ Cd and Li□ Sn□ Cd alloys in propylene carbonate solution. *Electrochimica acta* **41**, 1455-1464 (1996).

194. Bowers, K. *et al.* Scalable Algorithms for Molecular Dynamics Simulations on Commodity Clusters. *ACM/IEEE SC 2006 Conference (SC'06)*, 43-43 (2006).

195. Shivakumar, D. *et al.* Prediction of absolute solvation free energies using molecular dynamics free energy perturbation and the OPLS force field. *Journal of chemical theory and computation* **6**, 1509-1519 (2010).

196. Guo, Z. *et al.* Probing the α-Helical Structural Stability of Stapled p53 Peptides: Molecular Dynamics Simulations and Analysis. *Chem. Biol. Drug Des.* **75**, 348-359 (2010).

197. Banks, J.L. *et al.* Integrated Modeling Program, Applied Chemical Theory (IMPACT). *Journal of Computational Chemistry* **26**, 1752-1780 (2005).

198. McQuarrie, D.A. *Statistical Mechanics*. (University Science Books, Mill Valley, CA; 2000).

199. Martyna, G.J., Tobias, D.J. & Klein, M.L. Constant pressure molecular dynamics algorithms. *Journal of Chemical Physics* **101**, 4177-4177 (1994).

200. Shin, H., Pascal, T.A., Goddard, W.A. & Kim, H. Scaled effective solvent method for predicting the equilibrium ensemble of structures with analysis of thermodynamic properties of amorphous polyethylene glycol-water mixtures. *Journal of Physical Chemistry B* **117**, 916-927 (2013).
201. Bos, A., Pünt, I., Wessling, M. & Strathmann, H. CO 2-induced plasticization phenomena in glassy polymers. *Journal of Membrane Science* **155**, 67-78 (1999).
202. Willard, A.P. & Chandler, D. Instantaneous liquid interfaces. *The Journal of Physical Chemistry B* **114**, 1954-1958 (2010).
203. Julin, J. *et al.* Mass accommodation of water: Bridging the gap between molecular dynamics simulations and kinetic condensation models. *Journal of Physical Chemistry A* **117**, 410-420 (2013).
204. Julin, J., Winkler, P.M., Donahue, N.M., Wagner, P.E. & Riipinen, I. Near-Unity Mass Accommodation Coefficient of Organic Molecules of Varying Structure. *Environmental Science & Technology* **48**, 12083-12089 (2014).
205. Lancaster, D.K., Johnson, A.M., Burden, D.K., Wiens, J.P. & Nathanson, G.M. Inert gas scattering from liquid hydrocarbon microjets. *Journal of Physical Chemistry Letters* **4**, 3045-3049 (2013).
206. Bauer, B.A., Lucas, T.R., Meninger, D.J. & Patel, S. Water permeation through DMPC lipid bilayers using polarizable charge equilibration force fields. *Chemical physics letters* **508**, 289-294 (2011).
207. Alexander, W.a., Zhang, J., Murray, V.J., Nathanson, G.M. & Minton, T.K. Kinematics and dynamics of atomic-beam scattering on liquid and self-assembled monolayer surfaces. *Faraday Discussions* **157**, 355-374 (2012).
208. Donaldson, D.J. Adsorption of Atmospheric Gases at the Air−Water Interface. I. NH 3. *Journal of Physical Chemistry A* **103**, 62-70 (1999).
209. Ogasawara, H., Horimoto, N. & Kawai, M. Ammonia adsorption by hydrogen bond on ice and its solvation. *Journal of Chemical Physics* **112**, 8229-8232 (2000).
210. Youngs, T.G. & Hardacre, C. Application of static charge transfer within an ionic-liquid force field and its effect on structure and dynamics. *ChemPhysChem* **9**, 1548-1558 (2008).
211. Webb, M.A. *et al.* Systematic Computational and Experimental Investigation of Lithium-Ion Transport Mechanisms in Polyester-Based Polymer Electrolytes. *ACS Central Science* **1**, 198-205 (2015).
212. Soniat, M. *et al.* Predictive simulation of non-steady-state transport of gases through rubbery polymer membranes. *Polymer* (2017).
213. Bader, R.F. *Atoms in molecules*. (Wiley Online Library, 1990).
214. Bayly, C.I., Cieplak, P., Cornell, W. & Kollman, P.A. A well-behaved electrostatic potential based method using charge restraints for deriving atomic charges: the RESP model. *J. Phys. Chem.* **97**, 10269-10280 (1993).
215. Breneman, C.M. & Wiberg, K.B. Determining atom-centered monopoles from molecular electrostatic potentials. The need for high sampling density in formamide conformational analysis. *J. Comput. Chem.* **11**, 361-373 (1990).
216. Campaná, C., Mussard, B. & Woo, T.K. Electrostatic potential derived atomic charges for periodic systems using a modified error functional. *J. Chem. Theory Comput.* **5**, 2866-2878 (2009).
217. Cioslowski, J. A new population analysis based on atomic polar tensors. *J. Am. Chem. Soc.* **111**, 8333-8336 (1989).
218. Cornell, W.D., Cieplak, P., Bayly, C.I. & Kollmann, P.A. Application of RESP charges to calculate conformational energies, hydrogen bond energies, and free energies of solvation. *J. Am. Chem. Soc.* **115**, 9620-9631 (1993).
219. Cox, S. & Williams, D. Representation of the molecular electrostatic potential by a net atomic charge model. *J. Comput. Chem.* **2**, 304-323 (1981).
220. Cusachs, L.C. & Politzer, P. On the problem of defining the charge on an atom in a molecule. *Chem. Phys. Lett.* **1**, 529-531 (1968).
221. Fonseca Guerra, C., Handgraaf, J.W., Baerends, E.J. & Bickelhaupt, F.M. Voronoi deformation density (VDD) charges: Assessment of the Mulliken, Bader, Hirshfeld, Weinhold, and VDD methods for charge analysis. *J. Comput. Chem.* **25**, 189-210 (2004).
222. Li, J., Xing, J., Cramer, C.J. & Truhlar, D.G. Accurate dipole moments from Hartree–Fock calculations by means of class IV charges. *J. Chem. Phys.* **111**, 885-892 (1999).
223. Li, J., Zhu, T., Cramer, C.J. & Truhlar, D.G. New class IV charge model for extracting accurate partial charges from wave functions. *J. Phys. Chem. A* **102**, 1820-1831 (1998).
224. Löwdin, P.-O. On the nonorthogonality problem. *Adv. Quantum Chem.* **5**, 185-199 (1970).

225. Manz, T.A. & Sholl, D.S. Chemically meaningful atomic charges that reproduce the electrostatic potential in periodic and nonperiodic materials. *J. Chem. Theory Comput.* **6**, 2455-2468 (2010).
226. Reed, A.E., Weinstock, R.B. & Weinhold, F. Natural population analysis. *J. Chem. Phys.* **83**, 735-746 (1985).
227. Storer, J.W., Giesen, D.J., Cramer, C.J. & Truhlar, D.G. Class IV charge models: A new semiempirical approach in quantum chemistry. *J. Comput.-Aided Mol. Des.* **9**, 87-110 (1995).
228. Thompson, J.D., Xidos, J.D., Sonbuchner, T.M., Cramer, C.J. & Truhlar, D.G. More reliable partial atomic charges when using diffuse basis sets. *PhysChemComm* **5**, 117-134 (2002).
229. Williams, D.E. Representation of the molecular electrostatic potential by atomic multipole and bond dipole models. *J. Comput. Chem.* **9**, 745-763 (1988).
230. Winget, P., Thompson, J.D., Xidos, J.D., Cramer, C.J. & Truhlar, D.G. Charge Model 3: A class IV charge model based on hybrid density functional theory with variable exchange. *J. Phys. Chem. A* **106**, 10707-10717 (2002).
231. Oostenbrink, C., Villa, A., Mark, A.E. & van Gunsteren, W.F. A biomolecular force field based on the free enthalpy of hydration and solvation: the GROMOS force-field parameter sets 53A5 and 53A6. *J. Comput. Chem.* **25**, 1656-1676 (2004).
232. van Gunsteren, W.F. *et al.* Biomolecular simulation: the {GROMOS96} manual and user guide. (1996).
233. Bakowies, D. & Thiel, W. Hybrid models for combined quantum mechanical and molecular mechanical approaches. *J. Phys. Chem.* **100**, 10580-10594 (1996).
234. Braga, S.F. *et al.* Structure and dynamics of carbon nanoscrolls. *Nano Lett.* **4**, 881-884 (2004).
235. Gama, C.I. *et al.* Sulfation patterns of glycosaminoglycans encode molecular recognition and activity. *Nat. Chem. Biol.* **2**, 467-473 (2006).
236. Jaramillo-Botero, A., Naserifar, S. & Goddard III, W.A. General multiobjective force field optimization framework, with application to reactive force fields for silicon carbide. *J. Chem. Theory Comput.* **10**, 1426-1439 (2014).
237. Maiti, P.K., Cagin, T., Lin, S.-T. & Goddard, W.A. Effect of solvent and pH on the structure of PAMAM dendrimers. *Macromolecules* **38**, 979-991 (2005).
238. Naserifar, S., Goddard III, W.A., Liu, L., Tsotsis, T.T. & Sahimi, M. Toward a process-based molecular model of SiC membranes. 2. Reactive dynamics simulation of the pyrolysis of polymer precursor to form amorphous SiC. *J. Phys. Chem. C* **117**, 3320-3329 (2013).
239. Rick, S.W., Stuart, S.J. & Berne, B.J. Dynamical fluctuating charge force fields: Application to liquid water. *J. Chem. Phys.* **101**, 6141-6156 (1994).
240. Tung, R.T. Chemical bonding and Fermi level pinning at metal-semiconductor interfaces. *Phys. Rev. Lett.* **84**, 6078 (2000).
241. Vaidehi, N. *et al.* Prediction of structure and function of G protein-coupled receptors. *Proc. Natl. Acad. Sci.* **99**, 12622-12627 (2002).
242. Zhang, Q. *et al.* Adhesion and nonwetting-wetting transition in the Al/α− Al 2 O 3 interface. *Phys. Rev. B* **69**, 045423 (2004).
243. Lindahl, E., Hess, B. & Van Der Spoel, D. GROMACS 3.0: a package for molecular simulation and trajectory analysis. *J. Mol. Model. Ann.* **7**, 306-317 (2001).
244. Whitfield, T.W. *et al.* Theoretical study of aqueous solvation of K+ comparing ab initio, polarizable, and fixed-charge models. *J. Chem. Theory Comput.* **3**, 2068-2082 (2007).
245. Yu, H. *et al.* Simulating monovalent and divalent ions in aqueous solution using a Drude polarizable force field. *J. Chem. Theory Comput.* **6**, 774-786 (2010).
246. Banks, J.L. *et al.* Parametrizing a polarizable force field from ab initio data. I. The fluctuating point charge model. *J. Chem. Phys.* **110**, 741-754 (1999).
247. Bryce, R.A., Vincent, M.A., Malcolm, N.O., Hillier, I.H. & Burton, N.A. Cooperative effects in the structuring of fluoride water clusters: ab initio hybrid quantum mechanical/molecular mechanical model incorporating polarizable fluctuating charge solvent. *J. Chem. Phys.* **109**, 3077-3085 (1998).
248. Chen, B., Potoff, J.J. & Siepmann, J.I. Adiabatic nuclear and electronic sampling Monte Carlo simulations in the Gibbs ensemble: Application to polarizable force fields for water. *J. Phys. Chem. B* **104**, 2378-2390 (2000).
249. Cho, K.-H., Kang, Y.K., No, K.T. & Scheraga, H.A. A fast method for calculating geometry-dependent net atomic charges for polypeptides. *J. Phys. Chem. B* **105**, 3624-3634 (2001).

250. Gasteiger, J. & Marsili, M. Iterative partial equalization of orbital electronegativity—a rapid access to atomic charges. *Tetrahedron* **36**, 3219-3228 (1980).
251. Gong, L. Development and applications of the ABEEM fluctuating charge molecular force field in the ion-containing systems. *Sci. China. Chem.* **55**, 2471-2484 (2012).
252. Mortier, W.J., Ghosh, S.K. & Shankar, S. Electronegativity-equalization method for the calculation of atomic charges in molecules. *Journal of the American Chemical Society* **108**, 4315-4320 (1986).
253. Mortier, W.J., Van Genechten, K. & Gasteiger, J. Electronegativity equalization: application and parametrization. *Journal of the American Chemical Society* **107**, 829-835 (1985).
254. Nistor, R.A., Polihronov, J.G., Müser, M.H. & Mosey, N.J. A generalization of the charge equilibration method for nonmetallic materials. *The Journal of chemical physics* **125**, 094108 (2006).
255. No, K.T., Grant, J.A., Jhon, M.S. & Scheraga, H.A. Determination of net atomic charges using a modified partial equalization of orbital electronegativity method. 2. Application to ionic and aromatic molecules as models for polypeptides. *J. Phys. Chem.* **94**, 4740-4746 (1990).
256. Olano, L.R. & Rick, S.W. Fluctuating charge normal modes: An algorithm for implementing molecular dynamics simulations with polarizable potentials. *J. Comput. Chem.* **26**, 699-707 (2005).
257. Patel, S. & Brooks, C.L. CHARMM fluctuating charge force field for proteins: I parameterization and application to bulk organic liquid simulations. *J. Comput. Chem.* **25**, 1-16 (2004).
258. Ribeiro, M.C. & Almeida, L.C. Fluctuating charge model for polyatomic ionic systems: a test case with diatomic anions. *J. Chem. Phys.* **110**, 11445-11448 (1999).
259. Rick, S.W. Simulations of ice and liquid water over a range of temperatures using the fluctuating charge model. *J. Chem. Phys.* **114**, 2276-2283 (2001).
260. Stern, H.A., Rittner, F., Berne, B.J. & Friesner, R.A. Combined fluctuating charge and polarizable dipole models: Application to a five-site water potential function. *J. Chem. Phys.* **115**, 2237-2251 (2001).
261. Verstraelen, T. *et al.* The significance of parameters in charge equilibration models. *J. Chem. Theory Comput.* **7**, 1750-1764 (2011).
262. Wang, S. & Cann, N. Polarizable and flexible model for ethanol. *J. Chem. Phys.* **126**, 214502 (2007).
263. Wilmer, C.E. & Snurr, R.Q. Towards rapid computational screening of metal-organic frameworks for carbon dioxide capture: Calculation of framework charges via charge equilibration. *Chem. Eng. J.* **171**, 775-781 (2011).
264. York, D.M. & Yang, W. A chemical potential equalization method for molecular simulations. *The Journal of chemical physics* **104**, 159-172 (1996).
265. Donchev, A.G. *et al.* Assessment of performance of the general purpose polarizable force field QMPFF3 in condensed phase. *J. Comput. Chem.* **29**, 1242-1249 (2008).
266. Engkvist, O., Åstrand, P.-O. & Karlström, G. Accurate intermolecular potentials obtained from molecular wave functions: Bridging the gap between quantum chemistry and molecular simulations. *Chem. Rev.* **100**, 4087-4108 (2000).
267. Gordon, M.S., Smith, Q.A., Xu, P. & Slipchenko, L.V. Accurate first principles model potentials for intermolecular interactions. *Annu. Rev. Phys. Chem.* **64**, 553-578 (2013).
268. Gresh, N., Cisneros, G.A., Darden, T.A. & Piquemal, J.-P. Anisotropic, polarizable molecular mechanics studies of inter-and intramolecular interactions and ligand-macromolecule complexes. A bottom-up strategy. *J. Chem. Theory Comput.* **3**, 1960-1986 (2007).
269. Kaminski, G.A., Stern, H.A., Berne, B.J. & Friesner, R.A. Development of an accurate and robust polarizable molecular mechanics force field from ab initio quantum chemistry. *J. Phys. Chem. A* **108**, 621-627 (2004).
270. Ponder, J.W. *et al.* Current status of the AMOEBA polarizable force field. *J. Phys. Chem. B* **114**, 2549-2564 (2010).
271. Ren, P., Wu, C. & Ponder, J.W. Polarizable atomic multipole-based molecular mechanics for organic molecules. *J. Chem. Theory Comput.* **7**, 3143-3161 (2011).
272. Stone, A. Distributed multipole analysis, or how to describe a molecular charge distribution. *Chem. Phys. Lett.* **83**, 233-239 (1981).
273. Stone, A. Distributed polarizabilities. *Mol. Phys.* **56**, 1065-1082 (1985).
274. Wang, Z.X. *et al.* Strike a balance: optimization of backbone torsion parameters of AMBER polarizable force field for simulations of proteins and peptides. *J. Comput. Chem.* **27**, 781-790 (2006).
275. Xie, W., Pu, J., MacKerell, A.D. & Gao, J. Development of a polarizable intermolecular potential function (PIPF) for liquid amides and alkanes. *J. Chem. Theory Comput.* **3**, 1878-1889 (2007).

276. FIELD, B.M.J. Hybrid quantum mechanical/molecular mechanical fluctuating charge models for condensed phase simulations. *Mol. Phys.* **91**, 835-846 (1997).
277. Gao, J. Toward a molecular orbital derived empirical potential for liquid simulations. *J. Phys. Chem. B* **101**, 657-663 (1997).
278. Madden, P.A., Heaton, R., Aguado, A. & Jahn, S. From first-principles to material properties. *J. Mol. Struct. THEOCHEM* **771**, 9-18 (2006).
279. Murphy, R.B., Philipp, D.M. & Friesner, R.A. A mixed quantum mechanics/molecular mechanics (QM/MM) method for large-scale modeling of chemistry in protein environments. *J. Comput. Chem.* **21**, 1442-1457 (2000).
280. Senn, H.M. & Thiel, W. QM/MM methods for biomolecular systems. *Angew. Chem. Int. Ed.* **48**, 1198-1229 (2009).
281. Antila, H.S. & Salonen, E. Polarizable force fields. *Biomolecular Simulations: Methods and Protocols*, 215-241 (2013).
282. No, K.T., Grant, J.A. & Scheraga, H.A. Determination of net atomic charges using a modified partial equalization of orbital electronegativity method. 1. Application to neutral molecules as models for polypeptides. *J. Phys. Chem.* **94**, 4732-4739 (1990).
283. Verstraelen, T., Van Speybroeck, V. & Waroquier, M. The electronegativity equalization method and the split charge equilibration applied to organic systems: Parametrization, validation, and comparison. *J. Chem. Phys.* **131**, 044127 (2009).
284. Zheng, C. & Zhong, C. Estimation of framework charges in covalent organic frameworks using connectivity-based atom contribution method. *J. Phys. Chem. C* **114**, 9945-9951 (2010).
285. Oda, A. & Takahashi, O. Parameter determination for the charge equilibration method including third- and fourth-order terms applied to non-metallic compounds. *Chem. Phys. Lett.* **495**, 155-159 (2010).
286. Applequist, J. An atom dipole interaction model for molecular optical properties. *Acc. Chem. Res.* **10**, 79-85 (1977).
287. Thole, B.T. Molecular polarizabilities calculated with a modified dipole interaction. *Chem. Phys.* **59**, 341-350 (1981).
288. Lopes, P.E. *et al.* Polarizable force field for peptides and proteins based on the classical drude oscillator. *J. Chem. Theory Comput.* **9**, 5430-5449 (2013).
289. Ren, P. & Ponder, J.W. Consistent treatment of inter-and intramolecular polarization in molecular mechanics calculations. *J. Comput. Chem.* **23**, 1497-1506 (2002).
290. Ren, P. & Ponder, J.W. Polarizable atomic multipole water model for molecular mechanics simulation. *The Journal of Physical Chemistry B* **107**, 5933-5947 (2003).
291. Schnieders, M.J., Baker, N.A., Ren, P. & Ponder, J.W. Polarizable atomic multipole solutes in a Poisson-Boltzmann continuum. *J. Chem. Phys.* **126**, 124114 (2007).
292. Chelli, R. & Procacci, P. A transferable polarizable electrostatic force field for molecular mechanics based on the chemical potential equalization principle. *J. Chem. Phys.* **117**, 9175-9189 (2002).
293. Paricaud, P., Předota, M., Chialvo, A.A. & Cummings, P.T. From dimer to condensed phases at extreme conditions: Accurate predictions of the properties of water by a Gaussian charge polarizable model. *J. Chem. Phys.* **122**, 244511 (2005).
294. Cramer, C.J. Essential of Computational chemistry. *Wiley, England* (2004).
295. Mayo, S.L., Olafson, B.D. & Goddard, W.A. DREIDING: a generic force field for molecular simulations. *J. Phys. Chem.* **94**, 8897-8909 (1990).
296. Francl, M.M. & Chirlian, L.E. The pluses and minuses of mapping atomic charges to electrostatic potentials. *Rev. Comput. Chem.* **14**, 1-31 (2000).
297. Lipkowitz, K.B. & Boyd, D.B. *Reviews in Computational Chemistry:* Volume 13**. (Wiley Online Library, 1997).